Parton distributions

Graeme Watt

Parton distributions

A thesis presented for the degree of

Doctor of Philosophy

by

Graeme Watt

Institute for Particle Physics Phenomenology
Department of Physics
University of Durham

November 2004

Parton distributions

A thesis presented for the degree of Doctor of Philosophy by

Graeme Watt

November 2004

Abstract

Parton distributions, $a(x, \mu^2)$, are essential ingredients for almost all theoretical calculations at hadron colliders. They give the number densities of the colliding partons (quarks and gluons) inside their parent hadrons at a given momentum fraction x and scale μ^2. The scale dependence of the parton distributions is given by DGLAP evolution, while the x dependence must be determined from a global analysis of deep-inelastic scattering (DIS) and related hard-scattering data.

In Part I we introduce 'doubly-unintegrated' parton distributions, $f_a(x, z, k_t^2, \mu^2)$, which additionally depend on the splitting fraction z and the transverse momentum k_t associated with the last evolution step. We show how these distributions can be used to calculate cross sections for inclusive jet production in DIS and compare the predictions to data taken at the HERA ep collider. We then calculate the transverse momentum distributions of W and Z bosons at the Tevatron $p\bar{p}$ collider and of Standard Model Higgs bosons at the forthcoming LHC.

In Part II we study diffractive DIS, which is characterised by a large rapidity gap between the slightly deflected proton and the products of the virtual photon dissociation. We perform a novel QCD analysis of recent HERA data and extract diffractive parton distributions. The results of this analysis are used to investigate the effect of absorptive corrections in inclusive DIS. These absorptive corrections are due to the recombination of partons within the proton and are found to enhance the size of the gluon distribution at small x. We discuss the problem that the gluon distribution decreases with decreasing x at low scales while the sea quark distribution increases with decreasing x, whereas Regge theory predicts that both should have the same small-x behaviour. Our study hints at the possible importance of power corrections at low scales of around 1 GeV.

Declaration

I declare that no material in this thesis has previously been submitted for a degree at this or any other university.

The research presented in this thesis has been carried out in collaboration with Professors A. D. Martin and M. G. Ryskin, and has been published in the following papers:

- G. Watt, A. D. Martin and M. G. Ryskin,
  "Unintegrated parton distributions and inclusive jet production at HERA,"
  Eur. Phys. J. C **31** (2003) 73 [arXiv:hep-ph/0306169].

- G. Watt, A. D. Martin and M. G. Ryskin,
  "Unintegrated parton distributions and electroweak boson production at hadron colliders," Phys. Rev. D **70** (2004) 014012 [Erratum-ibid. D **70** (2004) 079902] [arXiv:hep-ph/0309096].

- A. D. Martin, M. G. Ryskin and G. Watt,
  "A QCD analysis of diffractive deep-inelastic scattering data,"
  Eur. Phys. J. C **37** (2004) 285 [arXiv:hep-ph/0406224].

- A. D. Martin, M. G. Ryskin and G. Watt,
  "Simultaneous QCD analysis of diffractive and inclusive DIS data,"
  Phys. Rev. D **70** (2004) 091502 [arXiv:hep-ph/0406225].

Acknowledgements

Firstly, I am indebted to my supervisor, Professor Alan Martin, for his kindness, enthusiasm, and encouragement given throughout my time in Durham. It has been a great privilege to work with a man of such experience and to be the last of those fortunate enough to be supervised by him.

I am equally grateful to my main collaborator, Professor Misha Ryskin, whose great insight underpinned my study. He was extremely patient in explaining novel concepts multiple times until I finally understood, at least in part. His almost limitless knowledge and absolute conviction in his work meant that there was never a question that he could not answer.

Fellow students Michael Dinsdale, Darren Forde, George Georgiou and James Haestier proved to be friendly office mates over the course of the three years.

My Ph.D. was funded by a studentship from the UK Particle Physics and Astronomy Research Council. I was twice the recipient of a Nick Brown Memorial Bursary to attend the CTEQ Summer School in May 2003 and the Lund Small-x Workshop in May 2004. DESY provided financial support for me to attend the HERA-LHC Workshop in June 2004. The IPPP provided financial support for me to attend the Physics at Colliders summer school in July 2003 and the Diffraction 2004 Workshop in September 2004.

Lastly, I am grateful to my parents for their support over the years.

Contents

Abstract ii

Declaration iii

Acknowledgements iv

I Unintegrated parton distributions 1

1 Parton evolution and factorisation 2

1.1 Colour factors and running coupling 3

1.2 Deep-inelastic *ep* scattering 5

1.2.1 Operator product expansion 6

1.3 DGLAP evolution and collinear factorisation 7

1.3.1 Global parton analysis 13

1.3.2 Parton showers 14

1.4 BFKL evolution and k_t-factorisation 15

1.5 CCFM evolution and k_t-factorisation 17

1.5.1 Angular ordering 18

1.5.2 The CCFM equation 19

2 UPDFs and inclusive jet production at HERA 22

2.1 Unintegrated parton distributions from integrated ones 24

2.2 (z, k_t)-factorisation in deep-inelastic scattering 27

2.2.1 Generalising k_t-factorisation 31

2.2.2 Motivation for the (z, k_t)-factorisation formula 33

2.2.3 Derivation of splitting kernels 36

2.3 Application to inclusive jet production in DIS 40

2.3.1 Collinear factorisation approach at LO 42

2.3.2 (z, k_t)-factorisation approach at LO 47

2.3.3 Towards a NLO (z, k_t)-factorisation approach 49

2.3.4 An estimate of the NNLO contribution 53
2.4 Description of HERA inclusive jet production data 54
2.4.1 Comparison with ZEUS data at high Q^2 54
2.4.2 Comparison with H1 data at low Q^2 56
2.5 Summary 60

3 UPDFs and electroweak bosons at hadron colliders 62
3.1 (z, k_t)-factorisation at hadron-hadron colliders 64
3.2 Application to the P_T distributions of electroweak bosons 69
3.3 The K-factors 73
3.4 Numerical results 75
3.4.1 W and Z boson production at the Tevatron 75
3.4.2 Standard Model Higgs boson production at the LHC 81
3.5 Summary 82

II Diffractive PDFs and absorptive corrections 85

4 Diffractive deep-inelastic scattering 86
4.1 Regge theory 86
4.2 What is diffraction? 89
4.3 Diffractive DIS kinematics 90
4.4 Diffractive structure function 92
4.5 Collinear factorisation in DDIS 92
4.6 'Resolved' Pomeron model 93
4.7 The Pomeron in QCD 95
4.7.1 Two-gluon exchange 95
4.7.2 Two-quark exchange 106

5 A QCD analysis of diffractive deep-inelastic scattering data 112
5.1 New perturbative QCD approach to DDIS 114
5.2 Description of DDIS data 117
5.2.1 ... with a 'dummy' gluon distribution 118
5.2.2 ... with MRST gluon and sea quark distributions 120
5.3 Diffractive parton distributions 123

6 Absorptive corrections in deep-inelastic scattering 128
6.1 Gluon recombination at small x 129
6.2 Absorptive corrections to F_2 131

6.2.1 Connection to GLRMQ approach 132
6.3 Theoretical calculation of F_2^{DGLAP} 135
6.4 Simultaneous QCD analysis of DDIS and DIS data 138
6.5 Diversion: Multi-Pomeron exchange 146
6.6 Positive input gluons at 1 GeV^2 149
6.7 Pomeron-like sea quarks but valence-like gluons? 151
6.8 Back to diffractive PDFs 152
6.9 Discussion and summary 155

Part I

Unintegrated parton distributions

Chapter 1

Parton evolution and factorisation

The theory of the strong interaction is quantum chromodynamics (QCD), where the fundamental entities are quarks and gluons. However, the initial-state particles collided in particle physics experiments—such as the HERA and Tevatron colliders and the forthcoming LHC—are not quarks and gluons, but hadrons. Therefore, it is essential to know the momentum distributions of the partons (quarks and gluons) inside the colliding hadrons in order to relate theoretical QCD calculations with experimental data. These parton distribution functions (PDFs) are the subject of this thesis.

The conventional collinear factorisation approach expresses hadronic observables as the convolution of the PDFs with partonic hard-scattering coefficients, computed assuming that the hard scattering is initiated by a parton collinear to its parent hadron. The separation of parton emissions associated with the initial hadron or with the hard scattering is provided via a factorisation scale. The scale dependence of the PDFs is governed by Dokshitzer-Gribov-Lipatov-Altarelli-Parisi (DGLAP) [1–5] evolution. Both the DGLAP splitting kernels and the hard-scattering coefficients are calculable as perturbation series in the running strong coupling. This formalism is often applied unquestioned, with a huge amount of effort expounded on calculating higher-order corrections to the perturbation series. In this thesis, we study simple modifications to standard DGLAP evolution.

In Part I, we introduce PDFs which depend on the transverse momentum, relative to the parent hadron, of the parton initiating the hard scattering. We use these *unintegrated* PDFs to calculate the transverse momentum distributions of final-state particles produced in deep-inelastic scattering (DIS) and hadron-hadron collisions.

In Part II, we study a subset of DIS events known as *diffractive*. We perform a novel QCD analysis of recent diffractive DIS data taken at the HERA collider, and extract diffractive PDFs. We then use this diffractive DIS analysis to calculate the

effect of absorptive corrections on the DGLAP evolution of PDFs, arising from the recombination of partons within the proton.

In this introductory chapter we concentrate on only a few aspects of perturbative QCD phenomenology which are particularly relevant to the research presented in later chapters. For more details, the reader is referred to the textbooks [6–19] and review articles [20–27].

1.1 Colour factors and running coupling

First we give the formulae used for calculating colour factors throughout this thesis. We use the convention that indices $a, b, \ldots$ run over the $N_C = 3$ colour degrees of freedom of the quark fields, while indices $A, B, \ldots$ run over the $(N_C^2 - 1) = 8$ colour degrees of freedom of the gluon field. The $SU(N_C)$ generators t^A satisfy the following properties:

$$[t^A, t^B] = \mathrm{i} f^{ABC} t^C, \tag{1.1}$$

$$t^A_{ab} t^B_{ba} \equiv \mathrm{Tr}(t^A t^B) = T_R\, \delta^{AB} \qquad \text{with} \quad T_R \equiv \frac{1}{2}, \tag{1.2}$$

$$t^A_{ab} t^A_{bc} = C_F\, \delta_{ac} \qquad \text{with} \quad C_F \equiv \frac{N_C^2 - 1}{2N_C} = \frac{4}{3}, \tag{1.3}$$

$$f^{ABC} f^{ABD} = C_A\, \delta^{CD} \qquad \text{with} \quad C_A \equiv N_C = 3. \tag{1.4}$$

The scale dependence of the running coupling α_S is given by the renormalisation group equation,

$$\ln \frac{Q^2}{\mu^2} = \int_{\alpha_S(\mu^2)}^{\alpha_S(Q^2)} \frac{\mathrm{d}\alpha_S}{\beta(\alpha_S)} = \int_{\alpha_S(\mu^2)}^{\alpha_S(Q^2)} \mathrm{d}\alpha_S \left\{ -b\,\alpha_S^2 \left[1 + b'\alpha_S + \mathcal{O}(\alpha_S^2) \right] \right\}^{-1}, \tag{1.5}$$

where the one- and two-loop coefficients are

$$b = \frac{(11\, C_A - 2\, n_f)}{12\pi} = \frac{(33 - 2\, n_f)}{12\pi}, \tag{1.6}$$

$$b' = \frac{(17\, C_A^2 - 5\, C_A\, n_f - 3\, C_F\, n_f)}{2\pi(11\, C_A - 2\, n_f)} = \frac{(153 - 19\, n_f)}{2\pi(33 - 2\, n_f)}, \tag{1.7}$$

and n_f is the number of active quark flavours.[1] At leading order (LO), where we

[1] The discovery of 'asymptotic freedom' in 1973, meaning that the strong interaction gets weaker at small distances, earned Gross, Politzer, and Wilczek the 2004 Nobel Prize.

keep only the first (one-loop) term on the right-hand side (RHS) of (1.5),

$$\alpha_S(Q^2) = \frac{\alpha_S(\mu^2)}{1 + b\,\alpha_S(\mu^2)\ln(Q^2/\mu^2)}, \tag{1.8}$$

while at next-to-leading order (NLO), where we also keep the second (two-loop) term on the RHS of (1.5),

$$\frac{1}{\alpha_S(Q^2)} - \frac{1}{\alpha_S(\mu^2)} + b' \ln\left\{\frac{\alpha_S(Q^2)\,[1 + b'\alpha_S(\mu^2)]}{\alpha_S(\mu^2)\,[1 + b'\alpha_S(Q^2)]}\right\} = b\,\ln\frac{Q^2}{\mu^2}. \tag{1.9}$$

These equations (1.8) and (1.9) allow $\alpha_S(Q^2)$ to be calculated if the coupling is known at some reference scale μ. Typically, $\mu = M_Z$ and $\alpha_S(M_Z^2)$ is extracted from experimental data. An alternative approach is to introduce a parameter $\Lambda_{\rm QCD}$ instead of $\alpha_S(\mu^2)$, defined as the scale at which the coupling would diverge, that is,

$$\alpha_S(\mu^2) \to \infty \quad \text{as} \quad \mu \to \Lambda^+_{\rm QCD}. \tag{1.10}$$

With this definition, (1.8) becomes

$$\alpha_S(Q^2) = \frac{1}{b\ln(Q^2/\Lambda^2_{\rm QCD})}, \tag{1.11}$$

while (1.9) becomes

$$\frac{1}{\alpha_S(Q^2)} + b' \ln\left[\frac{b'\alpha_S(Q^2)}{1 + b'\alpha_S(Q^2)}\right] = b\,\ln\frac{Q^2}{\Lambda^2_{\rm QCD}}. \tag{1.12}$$

This last equation (1.12) can be solved approximately for $\alpha_S(Q^2)$ by expanding in inverse powers of $\ln(Q^2/\Lambda^2_{\rm QCD})$:

$$\alpha_S(Q^2) = \frac{1}{b\ln(Q^2/\Lambda^2_{\rm QCD})} + \frac{b'}{b^2\ln^2(Q^2/\Lambda^2_{\rm QCD})}\left(\ln\frac{b'}{b} - \ln\ln\frac{Q^2}{\Lambda^2_{\rm QCD}}\right) + \mathcal{O}\left(\frac{1}{\ln^3(Q^2/\Lambda^2_{\rm QCD})}\right). \tag{1.13}$$

Redefining $\Lambda_{\rm QCD}$ to absorb the term proportional to $\ln(b'/b)$ we obtain

$$\alpha_S(Q^2) \simeq \frac{1}{b\ln(Q^2/\Lambda^2_{\rm QCD})}\left[1 - \frac{b'}{b}\frac{\ln\ln(Q^2/\Lambda^2_{\rm QCD})}{\ln(Q^2/\Lambda^2_{\rm QCD})}\right]. \tag{1.14}$$

Note that $\Lambda_{\rm QCD}$ depends on the number of active flavours, n_f, with the dependence

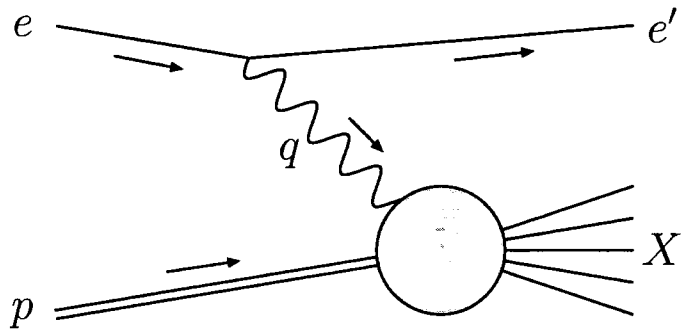

Figure 1.1: Deep-inelastic ep scattering mediated by a virtual photon γ^*.

determined by ensuring that $\alpha_S(Q^2)$ is continuous across the flavour thresholds, that is,

$$\alpha_S(m_c^2)\big|_{n_f=3} = \alpha_S(m_c^2)\big|_{n_f=4}\,, \qquad \alpha_S(m_b^2)\big|_{n_f=4} = \alpha_S(m_b^2)\big|_{n_f=5}\,. \tag{1.15}$$

Due to the various ambiguities involved in specifying $\Lambda_{\rm QCD}$, such as the flavour dependence, the renormalisation scheme dependence, and whether it is defined according to (1.11), (1.12), or (1.14), it is better to specify the absolute value of the running coupling by giving $\alpha_S(\mu^2)$ at some reference scale μ, usually at $\mu = M_Z$.

1.2 Deep-inelastic ep scattering

Deep-inelastic ep scattering is mediated by exchange of a virtual photon with momentum[2] $q = e - e'$, where e and e' are the momenta of the initial and final electrons, see Fig. 1.1. The virtual photon (γ^*) has spacelike virtuality $q^2 \equiv -Q^2$. We neglect the proton mass assuming that $m_p \ll Q$, and assume that Q^2 is sufficiently small that Z boson exchange can be neglected. The ep centre-of-mass (CM) energy squared is $s \equiv (e+p)^2 = 2\,e\cdot p$, where p is the momentum of the initial proton. The Bjorken-x variable is $x_B \equiv Q^2/(2\,p\cdot q)$. The $\gamma^* p$ CM energy squared is $W^2 \equiv (q+p)^2 = Q^2(1/x_B - 1)$.

The total $ep \to eX$ cross section can be written as a contraction of a leptonic tensor (representing $e \to e\gamma^*$) and a hadronic tensor (representing $\gamma^* p \to X$). The hadronic tensor, $W^{\mu\nu}$, can be written in terms of two independent structure functions, after utilising gauge, Lorentz, and time-reversal invariance, parity conservation

[2]'Momentum' always refers to 4-momentum throughout this thesis.

and assuming unpolarised beams. The final result is

$$\frac{\mathrm{d}^2\sigma^{ep}}{\mathrm{d}x_B\,\mathrm{d}Q^2} = \frac{2\pi\alpha_{\mathrm{em}}^2(Q^2)}{x_B\,Q^4}\left\{\left[1+(1-y)^2\right]F_T(x_B,Q^2)+2(1-y)\,F_L(x_B,Q^2)\right\}, \tag{1.16}$$

where $y \equiv (q\cdot p)/(e\cdot p) = Q^2/(x_B\,s)$. The subscripts T and L on the structure functions $F_{T,L}$ denote the separate contributions from a virtual photon with transverse and longitudinal polarisations respectively. Analogous to (1.8) the very weak running of the electromagnetic coupling is taken to be

$$\alpha_{\mathrm{em}}(Q^2) = \frac{\alpha}{1-\frac{\alpha}{3\pi}\ln(Q^2/m_e^2)}, \tag{1.17}$$

where $\alpha \simeq 1/137$ is the fine-structure constant and m_e is the electron mass.

The structure functions of the proton are related to the γ^*p cross sections by

$$F_{T,L} = \frac{Q^2}{4\pi^2\alpha_{\mathrm{em}}}\sigma_{T,L}^{\gamma^*p}, \tag{1.18}$$

$$F_2(x_B,Q^2) \equiv F_T(x_B,Q^2)+F_L(x_B,Q^2), \tag{1.19}$$

so the ep cross section can be obtained from the γ^*p cross sections by

$$\frac{\mathrm{d}^2\sigma^{ep}}{\mathrm{d}y\,\mathrm{d}Q^2} = \frac{\alpha_{\mathrm{em}}(Q^2)}{2\pi y\,Q^2}\left\{\left[1+(1-y)^2\right]\sigma_T^{\gamma^*p}+2(1-y)\,\sigma_L^{\gamma^*p}\right\}. \tag{1.20}$$

1.2.1 Operator product expansion

The hadronic tensor governing the γ^*p interaction, also known as the forward Compton amplitude, is

$$W^{\mu\nu} = \mathrm{i}\int \mathrm{d}^4x\, e^{\mathrm{i}q\cdot x}\,\langle p|T\left\{J^\mu(x)J^\nu(0)\right\}|p\rangle, \tag{1.21}$$

that is, it involves taking the Fourier transform of the proton matrix element of a time-ordered product of currents. An alternative strategy to the parton model for calculating $W^{\mu\nu}$ is to expand this product as a series of local operators. This is known as the operator product expansion (OPE).[3] The most important terms in the operator product of two currents J^μ come from products of two quark currents $\bar{q}\gamma^\mu q$ with quarks of the same flavour. The relative size of contributions from the OPE to DIS is controlled by the *twist* of the operator, defined by $t = d - s$, where d is the (mass) dimension and s is the spin of the operator. A given operator of twist

[3] See, for example, Chapter 18 of [6] for more details.

t is suppressed by at least a factor

$$\left(\frac{1}{Q}\right)^{t-2}. \tag{1.22}$$

The dimensions of quark and gluon operators are 3/2 and 2 respectively, while their spins are 1/2 and 1 respectively. Thus the leading contribution from two quark operators is twist-two ('leading-twist') while the leading contribution from four gluon or four quark operators is twist-four ('higher-twist'). Note that a contribution suppressed by $(1/Q)^{t-2}$ does not necessarily originate from an operator of twist t. For example, a contribution behaving like $1/Q^2$ could be either a sub-leading twist-two contribution or a leading twist-four contribution.

1.3 DGLAP evolution and collinear factorisation

It is convenient to use a Sudakov decomposition, whereby a general momentum k can be expanded in a basis of the proton momentum p, a lightlike 4-vector $q' \equiv q + x_B\, p$, and a transverse component $k_\perp$, which satisfy the relations

$$p^2 = 0 = q'^2, \quad p \cdot k_\perp = 0 = q' \cdot k_\perp, \quad k_\perp^2 = -k_t^2, \quad p \cdot q' = \frac{Q^2}{2x_B}. \tag{1.23}$$

We define the plus and minus components of a 4-vector k as $k^\pm \equiv k^0 \pm k^3$. In the Breit frame

$$p = (p^+, p^-, \boldsymbol{p_t}) = (Q/x_B, 0, \mathbf{0}), \qquad q' = (0, Q, \mathbf{0}), \qquad k_\perp = (0, 0, \boldsymbol{k_t}). \tag{1.24}$$

We adopt a physical[4] (axial) gluon gauge, where only the two transverse gluon polarisations propagate. The numerator of a gluon propagator with momentum k in an axial gauge is

$$d_{\mu\nu}(k, n) = -g_{\mu\nu} + \frac{k_\mu\, n_\nu + n_\mu\, k_\nu}{k \cdot n} - n^2 \frac{k_\mu\, k_\nu}{(k \cdot n)^2}. \tag{1.25}$$

Although the propagator is more complicated in an axial gauge than in covariant gauges, for example the Feynman gauge where $d_{\mu\nu} = -g_{\mu\nu}$, a physical gauge has the distinct advantage that ghost fields are not required to cancel the unphysical gluon polarisations. Choosing a lightlike gauge-fixing vector $n = q'$ gives the light-cone

[4]For more information on physical gauges, see [21, 28].

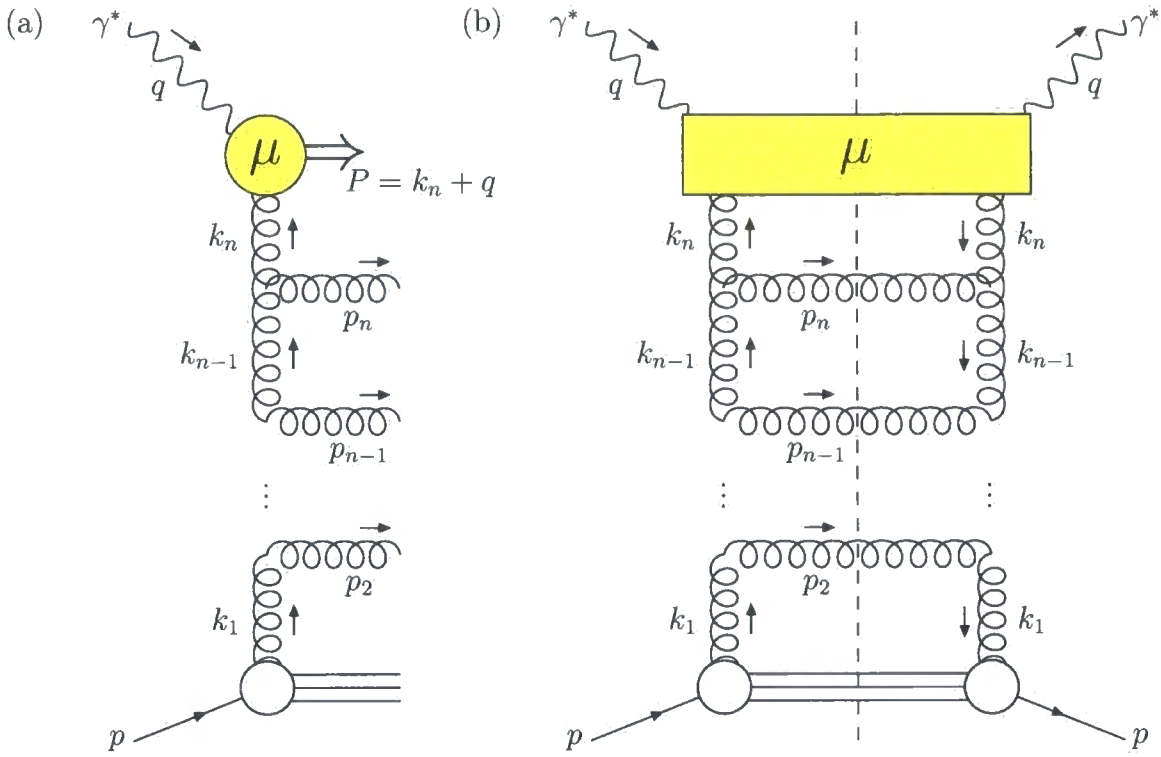

Figure 1.2: (a) The parton evolution chain, simplified so that all the partons in the chain are gluons. (b) The evolution ladder, given by the amplitude of diagram (a) multiplied by its complex conjugate. The horizontal gluons cut by the dashed line are on-shell, $p_i^2 = 0$.

gauge,

$$d_{\mu\nu}(k, q') = -g_{\mu\nu} + \frac{k_\mu\, q'_\nu + q'_\mu\, k_\nu}{k \cdot q'}. \tag{1.26}$$

For the special case when k possesses only a plus (p) component, then $d_{\mu\nu}(k, q') = -g^{\perp}_{\mu\nu}$, where $g^{\perp}_{\mu\nu}$ is the transverse part of the metric, that is,

$$g^{\perp}_{\mu\nu} = g_{\mu\nu} - \frac{p_\mu\, q'_\nu + q'_\mu\, p_\nu}{p \cdot q'}. \tag{1.27}$$

In an axial gluon gauge, the logarithmic scaling violations of the proton structure function $F_2(x_B, Q^2)$ are given by multiparton emission diagrams, such as that shown in Fig. 1.2(a), with strongly-ordered transverse momenta along the evolution chain. The shaded circle at the top of Fig. 1.2(a) indicates some hard subprocess with an associated factorisation scale μ. The ladder diagram representing the amplitude of Fig. 1.2(a) multiplied by its complex conjugate is shown in Fig. 1.2(b). Using a Sudakov decomposition of the momenta of the propagator partons,

$$k_i = x_i\, p - \beta_i\, q' + k_{i\perp}, \tag{1.28}$$

where the Sudakov (light-cone) variables $x_i, \beta_i \in [0,1]$. In the infinite momentum frame, the plus momentum fractions $x_i = k_i^+/p^+$ become the longitudinal momentum fractions of the proton. The emitted partons along the evolution chain have momenta

$$p_i = k_{i-1} - k_i = (x_{i-1} - x_i)\, p + (\beta_i - \beta_{i-1})\, q' + p_{i\perp}, \tag{1.29}$$

where $p_{i\perp} = k_{i-1\perp} - k_{i\perp}$, while the total momentum going into the hard subprocess at the top of the ladder is

$$P \equiv k_n + q = (x_n - x_B)\, p + (1 - \beta_n)\, q' + k_{n\perp}. \tag{1.30}$$

Since the outgoing partons must be on-shell ($p_i^2 = 0$), we have

$$(\beta_i - \beta_{i-1}) = \frac{x_B}{x_{i-1}(1 - z_i)} \frac{p_{i,t}^2}{Q^2}, \tag{1.31}$$

where $z_i \equiv x_i/x_{i-1}$, and the Sudakov variables of the propagator partons obey the ordering

$$\ldots > x_{n-1} > x_n > x_B, \qquad \ldots < \beta_{n-1} < \beta_n < 1. \tag{1.32}$$

The kinematics we have discussed so far are completely general, and also hold for the different types of parton evolution we will discuss later. We now consider the approximation made in DGLAP evolution, where transverse momenta are assumed to be strongly ordered,

$$\mu^2 \gg k_{n,t}^2 \gg k_{n-1,t}^2 \gg \ldots \gg k_{2,t}^2 \gg k_{1,t}^2 \gg k_0^2, \tag{1.33}$$

where k_0 is an infrared cutoff. Schematically, neglecting the running of the strong coupling, the diagram in Fig. 1.2(b) with n propagators gives a contribution proportional to

$$(\alpha_S)^n \int_{k_0^2}^{\mu^2} \frac{\mathrm{d}k_{n,t}^2}{k_{n,t}^2} \int_{k_0^2}^{k_{n,t}^2} \frac{\mathrm{d}k_{n-1,t}^2}{k_{n-1,t}^2} \cdots \int_{k_0^2}^{k_{2,t}^2} \frac{\mathrm{d}k_{1,t}^2}{k_{1,t}^2} \sim \frac{1}{n!} \left(\alpha_S \ln \mu^2\right)^n, \tag{1.34}$$

The leading logarithmic approximation (LLA) includes a sum of all such terms.

We write the momentum of the last parton in the evolution chain, which initiates the hard scattering, as $k_n \equiv k = x\,p - \beta\, q' + k_\perp$. Since this parton has $k_t \ll \mu$, it can be taken to be approximately collinear with the proton, $k = x\,p$. We write $a(x, \mu^2)$ as a shorthand for the PDFs of the proton, $xq(x, \mu^2)$ or $xg(x, \mu^2)$. We neglect non-perturbative power-suppressed contributions of $\mathcal{O}([\Lambda_{\mathrm{QCD}}/\mu]^p)$, where the power $p > 0$. These contributions should be negligible as long as $\mu \gg \Lambda_{\mathrm{QCD}}$,

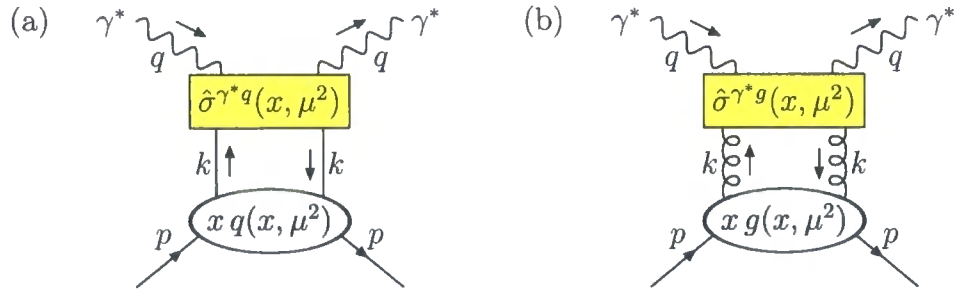

Figure 1.3: Illustration of collinear factorisation. The hard scattering is initiated by either (a) a quark or (b) a gluon with momentum $k = x\,p$.

where $\Lambda_{\rm QCD}$ is typically a few hundred MeV. The collinear factorisation formula, illustrated in Figure 1.3, expresses the hadronic ($\gamma^* p$) cross section in terms of the PDFs, $a(x, \mu^2)$, and the partonic ($\gamma^* a$) cross sections:

$$\sigma^{\gamma^* p} = \sum_{a=q,g} \int_{x_B}^{1} \frac{\mathrm{d}x}{x}\, a(x, \mu^2)\, \hat{\sigma}^{\gamma^* a}(x, \mu^2). \tag{1.35}$$

The partonic cross section $\hat{\sigma}$ is calculable as a perturbation series in α_S,

$$\hat{\sigma} = \alpha_S^r \left[\hat{\sigma}^{\rm LO} + \alpha_S\, \hat{\sigma}^{\rm NLO} + \alpha_S^2\, \hat{\sigma}^{\rm NNLO} + \ldots\right], \tag{1.36}$$

where r is the smallest power of α_S contributing to a specific process. For example, $r = 0$ for inclusive DIS, but $r = 1$ for inclusive jet production. For inclusive DIS, the usual choice of scale is given by the photon virtuality, $\mu = Q$. Currently, $\hat{\sigma}^{\rm LO}$ and $\hat{\sigma}^{\rm NLO}$ have been calculated for a large number of processes. By contrast, the next-to-next-to-leading order (NNLO) partonic cross section, $\hat{\sigma}^{\rm NNLO}$, is only known for a few simple processes, such as inclusive DIS and Drell-Yan (and related) processes in hadron-hadron collisions, but calculations of $\hat{\sigma}^{\rm NNLO}$ will increasingly become available over the next few years.

The partonic cross section,

$$\mathrm{d}\hat{\sigma} = \mathrm{d}\Phi\, |\mathcal{M}|^2 / F, \tag{1.37}$$

is calculated for an on-shell incoming parton with momentum $k = x\,p$, neglecting the minus and transverse components of k. The squared matrix element, $|\mathcal{M}|^2$, is calculated from the Feynman rules,[5] summing over all outgoing helicities and colours and averaging over all incoming helicities and colours. This averaging is

[5]In fact, by the optical theorem, $\mathrm{d}\Phi\, |\mathcal{M}|^2$ can be written down directly from the imaginary part of the forward scattering amplitude, using 'cut' diagrams with slightly modified Feynman rules. Here, we prefer to keep the two factors distinct.

often denoted explicitly by the notation $\langle|\mathcal{M}|^2\rangle$, $\overline{|\mathcal{M}|^2}$, or $\overline{\sum}|\mathcal{M}|^2$. Throughout this thesis, $|\mathcal{M}|^2$ will always denote implicitly an averaging over all incoming helicities and colours. The Lorentz-invariant phase space for a subprocess with final state particles of momenta p_i is

$$\mathrm{d}\Phi = (2\pi)^4\delta^{(4)}\left(k+q-\sum_i p_i\right)\prod_i \frac{\mathrm{d}^3\boldsymbol{p_i}}{2E_i\,(2\pi)^3}, \tag{1.38}$$

and the flux factor for a collinear collision between the virtual photon and the incoming parton is

$$F = 4\,k\cdot q = 4x\,p\cdot q. \tag{1.39}$$

Since

$$\int \mathrm{d}^4p_i\;\delta(p_i^2-m_i^2)\,\Theta(E_i) = \int \mathrm{d}^3\boldsymbol{p_i}\;\frac{1}{2E_i}, \tag{1.40}$$

the phase space element (1.38) can be written

$$\mathrm{d}\Phi = (2\pi)^4\delta^{(4)}\left(k+q-\sum_i p_i\right)\prod_i \frac{\mathrm{d}^4p_i}{(2\pi)^3}\;\delta(p_i^2-m_i^2)\,\Theta(E_i). \tag{1.41}$$

Beyond LO, the calculation of $\hat{\sigma}$ gives rise to both ultraviolet and infrared divergences. Usually, dimensional regularisation is used to regulate them both, where the entire calculation is performed in $4-2\epsilon$ dimensions, then the divergences appear as poles in ϵ. The ultraviolet divergences are subtracted according to a particular renormalisation scheme, while the infrared divergences are subtracted according to a particular factorisation scheme. Both the renormalisation and factorisation schemes are usually taken to be the modified minimal subtraction ($\overline{MS}$) scheme. For more details, see [29] in [10].

The scale dependence of the PDFs is governed by the DGLAP equation,

$$\frac{\partial a(x,\mu^2)}{\partial \ln\mu^2} = \frac{\alpha_S(\mu^2)}{2\pi}\sum_{b=q,g}\int_x^1 \mathrm{d}z\,P_{ab}\left(z,\alpha_S(\mu^2)\right)\,b\left(\frac{x}{z},\mu^2\right), \tag{1.42}$$

where the splitting kernels P_{ab} correspond to a $b\to ac$ branching in the evolution chain, and are expansions in α_S,

$$P_{ab}\left(z,\alpha_S\right) = P_{ab}^{\mathrm{LO}}(z) + \alpha_S P_{ab}^{\mathrm{NLO}}(z) + \alpha_S^2 P_{ab}^{\mathrm{NNLO}}(z) + \ldots. \tag{1.43}$$

Here, the NLO kernels correspond to $\mathcal{O}(\alpha_S)$ corrections to each rung of the evolution ladder, while the NNLO kernels corresponds to $\mathcal{O}(\alpha_S^2)$ corrections. Note however, that the assumption of strongly-ordered transverse momenta between each

'rung' remains, so that the parton initiating the hard subprocess still has negligible transverse momentum even after including higher-order corrections to the splitting kernels. The LO and NLO kernels have been known for more than 20 years, while the calculation of the NNLO kernels has only recently been completed [30,31]. The LO DGLAP splitting kernels are

$$P_{qq}^{\mathrm{LO}}(z) = C_F \left[\frac{1+z^2}{(1-z)_+} + \frac{3}{2}\delta(1-z) \right], \tag{1.44}$$

$$P_{gq}^{\mathrm{LO}}(z) = C_F \frac{1+(1-z)^2}{z}, \tag{1.45}$$

$$P_{qg}^{\mathrm{LO}}(z) = T_R \left[z^2 + (1-z)^2 \right], \tag{1.46}$$

$$P_{gg}^{\mathrm{LO}}(z) = 2\,C_A \left[\frac{z}{(1-z)_+} + \frac{1-z}{z} + z(1-z) \right] + \frac{1}{6}\left(11\,C_A - 4\,n_f\,T_R\right)\delta(1-z). \tag{1.47}$$

Here, the 'plus' distribution is defined such that

$$\int_0^1 \mathrm{d}z \, \frac{f(z)}{(1-z)_+} = \int_0^1 \mathrm{d}z \, \frac{f(z)-f(1)}{1-z}, \tag{1.48}$$

which encapsulates the cancellation between the real and virtual soft singularities. The real parts of the LO kernels are derived in Section 2.2.3. The coefficients of the virtual parts, proportional to $\delta(1-z)$, can be obtained from quark number conservation

$$\int_0^1 \mathrm{d}z \; P_{qq}^{\mathrm{LO}}(z) = 0, \tag{1.49}$$

and momentum conservation

$$\int_0^1 \mathrm{d}z \; z \left[P_{qq}^{\mathrm{LO}}(z) + P_{gq}^{\mathrm{LO}}(z) \right] = 0, \quad \int_0^1 \mathrm{d}z \; z \left[2n_f P_{qg}^{\mathrm{LO}}(z) + P_{gg}^{\mathrm{LO}}(z) \right] = 0. \tag{1.50}$$

For a consistent calculation, the order in α_S of the partonic cross section and the splitting kernel used in the evolution should match. For example, NLO partonic cross sections should be convoluted with PDFs evolved with NLO DGLAP splitting kernels.

Extending the lower limit of the integral to 0 in (1.42), with the understanding that $b(x/z, \mu^2) \equiv 0$ for $z < x$, and inserting the LO splitting kernels, $P_{ab}^{\mathrm{LO}}(z)$, we

obtain

$$\frac{\partial\, a(x,\mu^2)}{\partial \ln \mu^2} = \frac{\alpha_S(\mu^2)}{2\pi} \sum_{b=q,g} \left[\int_x^1 \mathrm{d}z\, P_{ab}(z)\, b\left(\frac{x}{z}, \mu^2\right) - a(x,\mu^2) \int_0^1 \mathrm{d}\zeta\, \zeta\, P_{ba}(\zeta) \right], \tag{1.51}$$

where the 'unregularised' LO DGLAP splitting kernels are

$$P_{qq}(z) = C_F \frac{1+z^2}{1-z}, \tag{1.52}$$

$$P_{gq}(z) = P_{qq}(1-z) = C_F \frac{1+(1-z)^2}{z}, \tag{1.53}$$

$$P_{qg}(z) = P_{gq}(1-z) = T_R \left[z^2 + (1-z)^2\right], \tag{1.54}$$

$$P_{gg}(z) = P_{gg}(1-z) = 2\, C_A \left[\frac{z}{1-z} + \frac{1-z}{z} + z(1-z) \right]. \tag{1.55}$$

The two terms on the RHS of (1.51) correspond to real emission and virtual contributions respectively. The first (real) term describes the number density increase of partons with plus momentum fraction x from the splitting of parent partons with plus momentum fraction x/z. The second (virtual) term describes the number density decrease of partons with plus momentum fraction x splitting to partons with plus momentum fraction ζx. The extra factor of ζ in the virtual term avoids double-counting the s- and t-channel partons. The factor ζ is equivalent to a factor of a half when integrating over ζ and summing over b.

1.3.1 Global parton analysis

Formally, the PDFs are defined in terms of the expectation values of suitable renormalised quantum mechanical operators (see, for example, [32]). Since the PDFs contain non-perturbative physics, they cannot be computed completely using perturbation theory. In principle, lattice QCD could be used to calculate the PDFs (see, for example, [33]). In practice, however, the PDFs are determined using experimental data, primarily inclusive DIS data, but also data from hadron-hadron colliders such as inclusive jet production. The situation is similar to that for the running coupling α_S, where the scale dependence is known from the renormalisation group equation (1.5), but an absolute value $\alpha_S(M_Z^2)$ must be determined from experiment. In the case of PDFs, the scale dependence is known from the DGLAP equation (1.42), but the x dependence must be determined from experiment. The PDFs are parameterised at some starting scale Q_0^2. The distributions $a(x, Q_0^2)$ are then evolved up to higher scales and predictions calculated with the collinear factorisation formula (1.35) are compared with data. The parameters in the starting

distributions are adjusted until the optimum fit is obtained. Currently, the two major groups performing *global* parton analysis to DIS and related hard-scattering data are MRST [34] and CTEQ [35]. We will look in more detail at how these fits are done in Part II of this thesis.

1.3.2 Parton showers

The DGLAP formalism is amenable to implementation in a parton shower algorithm (see, for example, Chapter 5 of [8]). As we will see in Section 2.2.2, in the limit of strongly-ordered transverse momenta the partonic cross section for n parton branchings, where the nth parton branching is $b \to ac$, factorises as

$$\mathrm{d}\hat{\sigma}_n^{\gamma^* b} = \mathrm{d}\Phi_n^{\gamma^* b} \, |\mathcal{M}_n^{\gamma^* b}|^2 \, / \, F^{\gamma^* b} = \frac{\mathrm{d}x_n}{x_n} \frac{\mathrm{d}k_{n,t}^2}{k_{n,t}^2} \, z_n \frac{\alpha_S(k_{n,t}^2)}{2\pi} \, P_{ab}(z_n) \, \mathrm{d}\hat{\sigma}_{n-1}^{\gamma^* a}. \tag{1.56}$$

This procedure can be used recursively to generate a parton shower, as implemented in the Monte Carlo event generators HERWIG [36] and PYTHIA [37]. In a parton shower, the transverse momenta of successive emissions are ordered, but not *strongly* ordered, that is, (1.33) becomes

$$\mu^2 > k_{n,t}^2 > k_{n-1,t}^2 > \ldots > k_{2,t}^2 > k_{1,t}^2 > k_0^2. \tag{1.57}$$

Such a procedure accounts for all $(\alpha_S \ln \mu^2)^n$ terms. Note that the evolution variable is not restricted to being the transverse momentum. Since the branching formula (1.56) contains a factor

$$\frac{\mathrm{d}x_n}{x_n} \frac{\mathrm{d}k_{n,t}^2}{k_{n,t}^2} = \frac{\mathrm{d}z_n}{z_n} \frac{\mathrm{d}k_{n,t}^2}{k_{n,t}^2} = \frac{\mathrm{d}z_n}{z_n} \frac{\mathrm{d}[k_{n,t}^2 \, f(z_n)]}{[k_{n,t}^2 \, f(z_n)]}, \tag{1.58}$$

then the evolution variable can be taken to be $[k_{n,t}^2 \, f(z_n)]$, for any reasonable function $f(z_n)$. For example, the evolution variable used in HERWIG is related to the angle of parton emission, allowing angular ordering due to colour coherence (see Section 1.5.1) to be built in from the outset. By contrast, the evolution variable used in PYTHIA is the parton virtuality, and so angular ordering must be imposed as an additional constraint. By accounting for angular ordering and momentum conservation along the evolution chain, an accuracy approaching next-to-leading logarithmic (NLL) can be obtained, that is, where all terms like $\alpha_S(\alpha_S \ln \mu^2)^{n-1}$ are included in addition to the LLA terms.

1.4 BFKL evolution and k_t-factorisation

We now consider *semihard* processes [23] where $x_B \ll 1$. Since $W^2 = Q^2(1/x_B - 1) \simeq Q^2/x_B$, the small-$x_B$ limit is also referred to as the high-energy limit, $W \gg Q$. The hard scale Q is much less than the $\gamma^* p$ CM energy W, but still large enough for perturbative QCD to be applicable, that is, $Q \gg \Lambda_{\rm QCD}$. In this regime, gluons are the predominant partons. The gluons emitted from the evolution chain take away the major part of the plus momenta of the propagating gluons, so $(1 - z_i) \sim 1$.

Consider what happens if, in addition to strongly-ordered transverse momenta, we also have strongly-ordered plus momenta,

$$x_B \ll x_n \ll x_{n-1} \ll \ldots \ll x_2 \ll x_1 \ll 1, \tag{1.59}$$

along the evolution chain. In this limit the gluon splitting kernel $P_{gg}(z_i) \simeq 2C_A/z_i$ and the parton branching equation (1.56) becomes

$$\mathrm{d}\hat{\sigma}_n^{\gamma^* b} = \frac{\mathrm{d}x_n}{x_n} \frac{\mathrm{d}k_{n,t}^2}{k_{n,t}^2} \frac{\alpha_S(k_{n,t}^2)}{2\pi} 2C_A \, \mathrm{d}\hat{\sigma}_{n-1}^{\gamma^* a}. \tag{1.60}$$

In addition to the factor of $(\alpha_S \ln \mu^2)^n$ coming from the integration over successive transverse momenta we have an additional factor

$$\int_{x_B}^1 \frac{\mathrm{d}x_n}{x_n} \int_{x_n}^1 \frac{\mathrm{d}x_{n-1}}{x_{n-1}} \ldots \int_{x_2}^1 \frac{\mathrm{d}x_1}{x_1} \sim \frac{1}{n!} \left(\ln \frac{1}{x_B} \right)^n, \tag{1.61}$$

so the total contribution in the so-called double leading logarithmic approximation (DLLA) contains all terms proportional to $[\alpha_S \ln(\mu^2) \ln(1/x_B)]^n$. However, there are additional $[\alpha_S \ln(1/x_B)]^n$ terms which are not accompanied by a factor $[\ln(\mu^2)]^n$, corresponding to the situation where the plus momenta are strongly ordered along the evolution chain, but the transverse momenta are not. The LL Balitsky-Fadin-Kuraev-Lipatov (BFKL) equation [38–40] sums all $[\alpha_S \ln(1/x_B)]^n$ terms. The dominance of ladder diagrams such as that in Figure 1.2 is now only true if the triple-gluon vertices are replaced by non-local effective vertices and the t-channel gluons are replaced by so-called 'reggeised' gluons with modified propagators, which account for virtual radiative corrections.

Since transverse momentum is not strongly ordered in the BFKL formalism, the parton entering the subprocess at the top of the evolution ladder has non-negligible transverse momentum. Therefore, instead of the conventional PDFs, $a(x, \mu^2)$, used in collinear factorisation, it is necessary to define PDFs which depend on this transverse momentum. Recall that, at least at LO, the number of partons in the proton

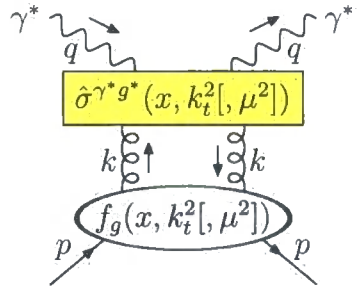

Figure 1.4: Illustration of k_t-factorisation. The gluon initiating the hard scattering has momentum $k = x\,p + k_\perp$. The unintegrated gluon distribution $f_g(x, k_t^2)$ satisfies BFKL evolution. For CCFM evolution there is an extra argument μ^2 related to the maximum angle for gluon emission.

with (plus) momentum fraction between x and $x + \mathrm{d}x$, integrated over transverse momentum k_t between zero and the factorisation scale μ, is

$$a(x, \mu^2)\,\frac{\mathrm{d}x}{x}. \tag{1.62}$$

By analogy, we define *unintegrated* parton distribution functions (UPDFs), $f_a(x, k_t^2[, \mu^2])$, such that the number of partons with plus momentum fraction between x and $x+\mathrm{d}x$ and transverse momentum squared between k_t^2 and $k_t^2 + \mathrm{d}k_t^2$ is

$$f_a(x, k_t^2[, \mu^2])\,\frac{\mathrm{d}x}{x}\,\frac{\mathrm{d}k_t^2}{k_t^2}. \tag{1.63}$$

Thus the UPDFs should satisfy the normalisation relation,

$$a(x, \mu^2) = \int_0^{\mu^2} \frac{\mathrm{d}k_t^2}{k_t^2}\, f_a(x, k_t^2[, \mu^2]). \tag{1.64}$$

At small x only the unintegrated gluon distribution need be considered. The unintegrated gluon distribution $f_g(x, k_t^2)$ satisfies BFKL evolution. For CCFM evolution, considered in Section 1.5.2, there is an extra argument μ^2 related to the maximum angle for gluon emission. Compared to the collinear factorisation approach to calculate hadronic cross sections, there is an additional convolution over k_t:

$$\sigma^{\gamma^* p} = \int_{x_B}^1 \frac{\mathrm{d}x}{x} \int_0^\infty \frac{\mathrm{d}k_t^2}{k_t^2}\, f_g(x, k_t^2)\, \hat{\sigma}^{\gamma^* g^*}(x, k_t^2). \tag{1.65}$$

This approach is called k_t-factorisation [41, 42] or the semihard approach [23, 43], illustrated in Fig. 1.4.[6] The partonic cross section $\hat{\sigma}^{\gamma^* g^*}$ is taken off-shell, indicated

[6]For a review of the k_t-factorisation approach, see [26, 27].

by the notation 'g^*'. It is given by (1.37), calculated with the incoming gluon having momentum $k = x\,p + k_\perp$ and virtuality $k^2 = -k_t^2$. Since the flux factor is not well-defined, it is taken to be the usual on-shell flux factor, $F = 4x\,p\cdot q$. The summation over the incoming gluon polarisations is performed using

$$\sum_\lambda \varepsilon_\mu(k,\lambda)\,\varepsilon_\nu^*(k,\lambda) = 2\,\frac{k_{\perp\mu}k_{\perp\nu}}{k_t^2}. \tag{1.66}$$

The LL BFKL equation, which governs the x dependence of the unintegrated gluon distribution, is

$$\frac{\partial f_g(x,k_t^2)}{\partial \ln(1/x)} = \bar{\alpha}_S\,k_t^2\int_0^\infty \frac{\mathrm{d}k_t'^2}{k_t'^2}\left[\frac{f_g(x,k_t'^2)-f_g(x,k_t^2)}{|k_t'^2-k_t^2|}+\frac{f_g(x,k_t^2)}{(4k_t'^4+k_t^4)^{1/2}}\right], \tag{1.67}$$

where $\bar{\alpha}_S \equiv C_A\,\alpha_S/\pi$. The NLL BFKL corrections, which sum all $\alpha_S[\alpha_S\ln(1/x_B)]^{n-1}$ terms, have also been calculated [44, 45], and were found to be larger than the LL BFKL contribution, giving cross sections that were not even positive-definite. However, resumming additional collinearly-enhanced contributions stabilises the result (see, for example, [47]).[7]

1.5 CCFM evolution and k_t-factorisation

The (true) rapidity of an outgoing particle of mass m_i with momentum

$$p_i = (p_i^+, p_i^-, \boldsymbol{p_{i,t}}) = (p_i^+, [m_i^2+p_{i,t}^2]/p_i^+, \boldsymbol{p_{i,t}}) \tag{1.68}$$

is

$$\eta_i \equiv \frac{1}{2}\ln\frac{p_i^+}{p_i^-}. \tag{1.69}$$

Rapidity has the useful property that it is additive under boosts in the z direction. The pseudorapidity of a particle is defined as

$$\eta_i^{\text{pseudo}} \equiv -\ln\tan(\theta_i/2), \tag{1.70}$$

[7] It has been found in [46] that predictions for the transverse momentum distribution of gluons calculated using either resummed NLL BFKL or LO DGLAP do not differ significantly, provided that the initial and final virtualities are not too close to each other.

where θ_i is the angle of the 3-momentum of the particle relative to the z axis. Rapidity and pseudorapidity are related by

$$\sinh \eta_i^{\text{pseudo}} = \left(\sqrt{1 + \frac{m_i^2}{k_{i,t}^2}} \right) \sinh \eta_i, \tag{1.71}$$

so the distinction disappears in the limit that $m_i \ll k_{i,t}$. For a pedagogical discussion of light-cone variables, rapidity and pseudorapidity, see [48].

1.5.1 Angular ordering

Colour coherence effects impose the angular ordering of the gluons emitted from the evolution chain, originating from the destructive interference between the gluon emission amplitudes (see, for example, [8, 11]). The angle θ_i between the direction of the emitted gluons, with momenta p_i, and the proton beam direction should increase as we move towards the hard scattering at the top of the evolution ladder. To be more precise, the ordering is in the rapidity variable (1.69), which should reduce as we move towards the hard subprocess. Of course, angular ordering (or pseudorapidity ordering) and rapidity ordering are equivalent in all evolution steps prior to the last, since the emitted partons are massless. The smallest allowed rapidity, η_{min}, is fixed by the rapidity of the subprocess, which usually has some finite invariant mass, so that the rapidity and pseudorapidity are not equal in this case. We will refer to 'angular ordering' throughout this thesis, but the reader should bear in mind that it is really rapidity ordering which is implied.

It is convenient to introduce a variable $\xi_i \equiv p_i^-/p_i^+$. Then the rapidities of the emitted gluons are

$$\eta_i = -\frac{1}{2} \ln \xi_i \qquad [= -\ln \tan(\theta_i/2)], \tag{1.72}$$

and the 'angular ordering',

$$\ldots > \eta_{n-1} > \eta_n > \eta_{\text{min}}, \tag{1.73}$$

is equivalent to an ordering in ξ_i,

$$\ldots < \xi_{n-1} < \xi_n < \Xi, \tag{1.74}$$

where

$$\Xi \equiv \frac{P^-}{P^+} = \frac{(1 - \beta_n)}{x_n/x_B - 1} \tag{1.75}$$

provides the smallest allowed rapidity, $\eta_{\min} = -(1/2)\ln\Xi$. From (1.29) and (1.31),

$$\xi_i = \frac{p_i^-}{p_i^+} = \left(\frac{x_B\, p_{i,t}/Q}{x_{i-1}(1-z_i)}\right)^2 = \left(\frac{x_B\,\overline{p}_i}{x_{i-1}Q}\right)^2, \tag{1.76}$$

where we have defined the rescaled *transverse* momenta $\overline{p}_i$ of the emitted gluons to be

$$\overline{p}_i \equiv \frac{p_{i,t}}{1-z_i} = \frac{x_{i-1}}{x_B} Q\sqrt{\xi_i}. \tag{1.77}$$

In angular-ordered evolution, the factorisation scale μ plays the rôle of the maximum rescaled transverse momentum, so

$$\mu = \frac{x_n}{x_B} Q\sqrt{\Xi}. \tag{1.78}$$

Therefore, the angular ordering (1.74) can be written as

$$\ldots, \qquad z_{n-1}\,\overline{p}_{n-1} < \overline{p}_n, \qquad z_n\,\overline{p}_n < \mu. \tag{1.79}$$

These angular-ordering constraints are automatically satisfied by both DGLAP evolution (with strongly-ordered transverse momenta) and BFKL evolution (with strongly-ordered plus momenta).

1.5.2 The CCFM equation

The Catani-Ciafaloni-Fiorani-Marchesini (CCFM) equation [49–52] resums large logarithms of $1/(1-z)$ in addition to those of $1/z$ summed by the BFKL equation. Moreover, angular ordering of emitted gluons due to colour coherence is imposed, as given by (1.79). For large and small z, CCFM evolution becomes similar to DGLAP and BFKL evolution respectively. In the small-x_B regime, k_t-factorisation can again be used, where the cross section is written in terms of an off-shell partonic cross section and an unintegrated gluon distribution, $f_g(x, k_t^2, \mu^2)$:

$$\sigma^{\gamma^* p} = \int_{x_B}^1 \frac{\mathrm{d}x}{x} \int_0^\infty \frac{\mathrm{d}k_t^2}{k_t^2}\, f_g(x, k_t^2, \mu^2)\, \hat{\sigma}^{\gamma^* g^*}(x, k_t^2, \mu^2). \tag{1.80}$$

The extra argument with respect to (1.65) is the factorisation scale μ, given by (1.78), which is related to the smallest rapidity allowed for gluon emission. The

differential form of the CCFM equation, as given in [52,53], is

$$\frac{\partial}{\partial \ln \mu^2}\left(\frac{f_g(x,k_t^2,\mu^2)}{\Delta_s(\mu^2,Q_0^2)}\right) = \int_x^{1-Q_0/\mu} \mathrm{d}z\, \frac{P_{gg}\left(z,(\mu/z)^2,k_t^2\right)}{\Delta_s(\mu^2,Q_0^2)}\, f_g\left(x/z,k_t'^2,(\mu/z)^2\right), \tag{1.81}$$

where Q_0 is an infrared cutoff, $\boldsymbol{k_t'} \equiv \boldsymbol{k_t} + [(1-z)\mu/z]\hat{\boldsymbol{n}}$, and the azimuthal integration over the direction of the two-dimensional unit vector $\hat{\boldsymbol{n}}$ is understood. It is important to note that (1.81) is an evolution equation in the angular variable $\mu/x = (Q/x_B)\sqrt{\Xi}$ rather in μ itself. The gluon Sudakov form factor in the DLLA is

$$\Delta_s(\mu^2,Q_0^2) = \exp\left[-\int_{Q_0^2}^{\mu^2}\frac{\mathrm{d}q^2}{q^2}\int_0^{1-Q_0/q}\mathrm{d}z\,\frac{\bar{\alpha}_S}{1-z}\right]. \tag{1.82}$$

The splitting function is

$$P_{gg}\left(z,(\mu/z)^2,k_t^2\right) = \bar{\alpha}_S\left[\frac{1}{(1-z)} + \frac{1}{z}\Delta_{ns}(z,(\mu/z)^2,k_t^2)\right], \tag{1.83}$$

where the non-Sudakov form factor,

$$\Delta_{ns}(z,(\mu/z)^2,k_t^2) = \exp\left[-\bar{\alpha}_S\int_z^1\frac{\mathrm{d}z'}{z'}\int^{k_t^2}\frac{\mathrm{d}q^2}{q^2}\Theta\left(q-z'\frac{\mu}{z}\right)\right], \tag{1.84}$$

regularises the $1/z$ divergence in the splitting function (1.83) in a similar way that the Sudakov form factor regularises the $1/(1-z)$ divergence.

The CCFM equation (1.81) has been used as the basis for the Monte Carlo event generators SMALLX [54,55] and CASCADE [53,56]. A reformulation of the CCFM equation known as the linked dipole chain (LDC) model is implemented in the Monte Carlo program LDCMC [57,58].

In the context of the CASCADE event generator, attempts have been made to modify the CCFM equation (1.81) to include the full LO DGLAP splitting function. However, naïvely making the replacement

$$\frac{1}{1-z} \to \frac{1}{1-z} - 2 + z(1-z) \tag{1.85}$$

in the gluon splitting function (1.83) leads to negative branching probabilities [26]. A positive definite branching probability can be obtained by making the replacements [26,27,59]

$$\frac{1}{1-z} \to \frac{z}{1-z} + z(1-z)/2, \qquad \frac{1}{z} \to \frac{1-z}{z} + z(1-z)/2, \tag{1.86}$$

in the gluon splitting function (1.83) and the Sudakov form factor (1.82), with a similar replacement for $1/z'$ in the non-Sudakov form factor (1.84).

Ideally, we would like to construct UPDFs with an analytic solution which include both quarks and gluons in the evolution, the correct angular ordering, the complete LO DGLAP splitting functions, and which are not restricted to the small-x_B domain. We will do this in the next chapter.

Chapter 2

Unintegrated parton distributions and inclusive jet production at HERA

The UPDFs depend on two hard scales, k_t and μ, and so the evolution is much more complicated than conventional DGLAP evolution. For example, the unintegrated gluon distribution, $f_g(x, k_t^2, \mu^2)$, satisfies the CCFM evolution equation based on angular ordering of gluon emissions along the chain, in the approximation where only the $1/z$ and $1/(1-z)$ singular terms of the splitting function $P_{gg}(z)$ are kept. So far, working with this equation has only proved possible with Monte Carlo event generators [53–56].

However, in [60–62] it was shown that it is possible to obtain the two-scale unintegrated distributions, $f_a(x, k_t^2, \mu^2)$, from single-scale distributions, $h_a(x, k_t^2)$, with the dependence on the second scale μ introduced only in the *last step* of the evolution. We call this the Kimber-Martin-Ryskin (KMR) procedure.[1] In [61], two alternatives for the evolution of $h_a(x, k_t^2)$ were considered:

(i) pure DGLAP evolution, or

(ii) a unified evolution equation [65] which embodies both the leading $\ln k_t^2$ (DGLAP) and $\ln(1/x)$ (BFKL) effects, as well as including a major part of the sub-leading $\ln(1/x)$ contributions.

As expected, the gluon and sea quark distributions, $f_a(x, k_t^2, \mu^2)$, extended into the $k_t > \mu$ region, and indeed populated this domain more and more as x decreased. An interesting result was that the UPDFs obtained via the unified BFKL-DGLAP evolution of prescription (ii) were not very different from those based on the simpler

[1] Alternative formalisms are given in [63, 64].

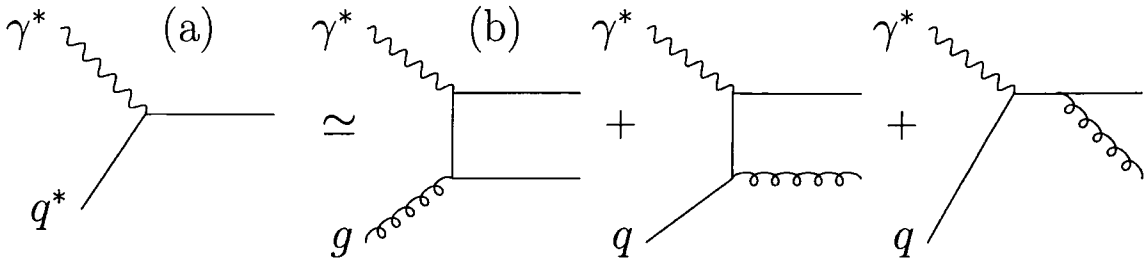

Figure 2.1: A schematic diagram of inclusive jet production in DIS at LO which shows the approximate equality between (a) the formalism based on the doubly-unintegrated quark distribution, where the incoming quark is off-shell with finite transverse momentum, and (b) the conventional QCD approach using integrated PDFs, where the incoming partons are on-shell with zero transverse momentum.

DGLAP evolution of (i). It was concluded that the imposition of the angular-ordering constraint in the last step of the evolution was more important than including BFKL effects. Here, we pay particular attention to probing the unintegrated quark distribution at larger values of x, so prescription (i) will certainly be a good approximation.

In this chapter, we refine and extend the KMR last-step procedure [61] for determining the UPDFs. First we note that in [61] angular ordering was imposed on both quark and gluon emissions; we correct this and only impose angular ordering on gluon emissions. Second, the KMR procedure was based on k_t-factorisation or the semihard approach in which the unintegrated parton distribution is convoluted with an off-shell partonic cross section where the incoming parton has virtuality $-k_t^2$. This is only valid for gluons in the high-energy approximation where $z \to 0$, with z the fraction of the plus momentum of the parent parton carried by the unintegrated parton. Here, we generalise the notion of k_t-factorisation and show that it is more accurate to calculate observables using 'doubly-unintegrated' parton distribution functions (DUPDFs), $f_a(x, z, k_t^2, \mu^2)$, where the off-shell parton now has virtuality $-k_t^2/(1-z)$.

In Section 2.1 we describe how the UPDFs, $f_a(x, k_t^2, \mu^2)$, can be determined from the conventional integrated PDFs $a(x, \mu^2)$. Then in Section 2.2 we define the DUPDFs, $f_a(x, z, k_t^2, \mu^2)$, and show how k_t-factorisation is generalised to '(z, k_t)-factorisation'. The most direct way to test the DUPDFs is via inclusive jet production in DIS. Inclusive jet production, particularly in the current jet region, probes the doubly-unintegrated quark distribution in a similar way that inclusive DIS probes

the integrated quark densities. The idea is that the LO diagram at $\mathcal{O}(\alpha_S^0)$ computed using (z, k_t)-factorisation will reproduce, to a good approximation, the results of the conventional LO QCD diagrams at $\mathcal{O}(\alpha_S)$ computed using collinear factorisation. This approximate equality is shown schematically in Fig. 2.1. The respective formalisms are presented in Section 2.3 and their predictions for inclusive jet production are compared with each other, and also with recent HERA data, in Section 2.4. These sections not only compare the LO predictions, but also extend the comparisons to NLO.

2.1 Unintegrated parton distributions from integrated ones

The KMR proposal [61] to determine the UPDFs was to relax the DGLAP strong ordering in the last evolution step only, that is, $\ldots \ll k_{n-1,t} \ll k_t \sim \mu$, where we have omitted the subscript n on the k_t of the last propagator. This procedure is expected to account for the major part of the conventional NLL terms, that is, terms like $\alpha_S(\alpha_S \ln \mu^2)^{n-1}$, compared to the usual LLA where only terms like $(\alpha_S \ln \mu^2)^n$ are included. The procedure is as follows. We start from the LO DGLAP equation in the form (1.51) evaluated at a scale k_t:

$$\frac{\partial\, a(x,k_t^2)}{\partial \ln k_t^2} = \frac{\alpha_S(k_t^2)}{2\pi} \sum_{b=q,g} \left[\int_x^1 \mathrm{d}z\, P_{ab}(z)\, b\left(\frac{x}{z}, k_t^2\right) - a(x,k_t^2) \int_0^1 \mathrm{d}\zeta\, \zeta\, P_{ba}(\zeta) \right]. \quad (2.1)$$

The virtual (loop) contributions may be resummed to all orders by the Sudakov form factor,

$$T_a(k_t^2,\mu^2) \equiv \exp\left(- \int_{k_t^2}^{\mu^2} \frac{\mathrm{d}\kappa_t^2}{\kappa_t^2} \frac{\alpha_S(\kappa_t^2)}{2\pi} \sum_{b=q,g} \int_0^1 \mathrm{d}\zeta\, \zeta\, P_{ba}(\zeta) \right), \quad (2.2)$$

which gives the probability of evolving from a scale k_t to a scale μ without parton emission. Differentiating, we obtain

$$\frac{1}{T_a(k_t^2,\mu^2)} \frac{\partial\, T_a(k_t^2,\mu^2)}{\partial \ln k_t^2} = \frac{\alpha_S(k_t^2)}{2\pi} \sum_{b=q,g} \int_0^1 \mathrm{d}\zeta\, \zeta\, P_{ba}(\zeta), \quad (2.3)$$

so that the LO DGLAP equation (2.1) can be written in the form

$$\frac{\partial\, a(x,k_t^2)}{\partial \ln k_t^2} = \frac{\alpha_S(k_t^2)}{2\pi} \sum_{b=q,g} \int_x^1 \mathrm{d}z\, P_{ab}(z)\, b\left(\frac{x}{z}, k_t^2\right) - \frac{a(x,k_t^2)}{T_a(k_t^2,\mu^2)} \frac{\partial\, T_a(k_t^2,\mu^2)}{\partial \ln k_t^2}. \quad (2.4)$$

We define the UPDFs to be

$$\begin{aligned} f_a(x,k_t^2,\mu^2) &\equiv \frac{\partial}{\partial \ln k_t^2}\left[\, a(x,k_t^2)\, T_a(k_t^2,\mu^2)\,\right] \\ &= T_a(k_t^2,\mu^2)\,\frac{\partial\, a(x,k_t^2)}{\partial \ln k_t^2} + a(x,k_t^2)\,\frac{\partial\, T_a(k_t^2,\mu^2)}{\partial \ln k_t^2} \\ &= T_a(k_t^2,\mu^2)\,\frac{\alpha_S(k_t^2)}{2\pi}\sum_b \int_x^1 \mathrm{d}z\, P_{ab}(z)\, b\left(\frac{x}{z},k_t^2\right). \end{aligned} \tag{2.5}$$

This definition is meaningful for $k_t > \mu_0$, where $\mu_0 \sim 1$ GeV is the minimum scale for which DGLAP evolution of the conventional PDFs, $a(x,\mu^2)$, is valid. Integrating over transverse momentum up to the factorisation scale we find that

$$\begin{aligned} \int_{\mu_0^2}^{\mu^2} \frac{\mathrm{d}k_t^2}{k_t^2}\, f_a(x,k_t^2,\mu^2) &= \left[\, a(x,k_t^2)\, T_a(k_t^2,\mu^2)\,\right]_{k_t=\mu_0}^{k_t=\mu} \\ &= a(x,\mu^2) - a(x,\mu_0^2)\, T_a(\mu_0^2,\mu^2), \end{aligned} \tag{2.6}$$

since $T_a(\mu^2,\mu^2) = 1$. Thus, the normalisation condition (1.64) will be exactly satisfied if we define

$$\left.\frac{1}{k_t^2}\, f_a(x,k_t^2,\mu^2)\right|_{k_t<\mu_0} = \frac{1}{\mu_0^2}\, a(x,\mu_0^2)\, T_a(\mu_0^2,\mu^2), \tag{2.7}$$

so that the density of partons in the proton is constant for $k_t < \mu_0$ at fixed x and μ.

So far, we have ignored the singular behaviour of the unregularised splitting kernels, $P_{qq}(z)$ and $P_{gg}(z)$, at $z = 1$, corresponding to soft gluon emission. These soft singularities cancel between the real and virtual parts of the DGLAP equation (2.1). After resumming the virtual part to all orders in the Sudakov form factor (2.2) the singularities must be regulated for the unintegrated distributions to be defined. The singularities indicate a physical effect that we have not yet accounted for. Here, it is the angular ordering caused by colour coherence, implying a cutoff on the splitting fraction z for those splitting kernels where a real gluon is emitted in the s-channel.

We now apply the angular-ordering constraints of Section 1.5.1 specifically to the last evolution step. For all other evolution steps, the strong ordering in transverse momentum automatically ensures angular ordering. The condition $z_n\,\overline{p}_n < \mu$ (1.79) implies

$$z\,\frac{k_t}{1-z} < \mu \qquad \Longleftrightarrow \qquad z < \frac{\mu}{\mu + k_t}, \tag{2.8}$$

where, as before, we have dropped the subscript n specifying the last evolution step. Recall from (1.78) that μ is entirely determined from the kinematics of the

subprocess at the top of the evolution ladder,

$$\mu = Q\frac{x}{x_B}\sqrt{\Xi} = Q\frac{x}{x_B}\sqrt{\frac{1-\beta}{x/x_B - 1}}. \tag{2.9}$$

Equation (2.8) applies only to those splitting functions in the real part of the DGLAP equation associated with gluon emission in the s-channel. By unitarity the same form of the cutoff must be chosen in the virtual part. We define $\zeta_{\max} = 1 - \zeta_{\min} = \mu/(\mu + \kappa_t)$ and insert $\Theta(\zeta_{\max} - \zeta)$ into the Sudakov form factor for those splitting functions where a gluon is emitted in the s-channel and $\Theta(\zeta - \zeta_{\min})$ where a gluon is emitted in the t-channel. Note that there is no 'coherence' effect for quark (fermion) emission and therefore the phase space available for quark emission is not restricted by the angular-ordering condition (2.8).[2]

The precise expressions for the unintegrated quark and gluon distributions are

$$f_q(x,k_t^2,\mu^2) = T_q(k_t^2,\mu^2)\,\frac{\alpha_S(k_t^2)}{2\pi}\int_x^1 \mathrm{d}z\,\left[P_{qq}(z)\,\frac{x}{z}q\left(\frac{x}{z},k_t^2\right)\,\Theta\left(\frac{\mu}{\mu+k_t}-z\right) + P_{qg}(z)\,\frac{x}{z}g\left(\frac{x}{z},k_t^2\right)\right] \tag{2.10}$$

and

$$f_g(x,k_t^2,\mu^2) = T_g(k_t^2,\mu^2)\,\frac{\alpha_S(k_t^2)}{2\pi}\int_x^1 \mathrm{d}z\,\left[\sum_q P_{gq}(z)\,\frac{x}{z}q\left(\frac{x}{z},k_t^2\right) + P_{gg}(z)\,\frac{x}{z}g\left(\frac{x}{z},k_t^2\right)\,\Theta\left(\frac{\mu}{\mu+k_t}-z\right)\right]. \tag{2.11}$$

The exponent of the quark Sudakov form factor can be simplified using the fact that $P_{gq}(1-\zeta) = P_{qq}(\zeta)$. Then

$$\begin{aligned}\int_0^{\zeta_{\max}} \mathrm{d}\zeta\,\zeta\,P_{qq}(\zeta) + \int_{\zeta_{\min}}^1 \mathrm{d}\zeta\,\zeta\,P_{gq}(\zeta) &= \frac{1}{2}\left[\int_0^{\zeta_{\max}} \mathrm{d}\zeta\,P_{qq}(\zeta) + \int_{\zeta_{\min}}^1 \mathrm{d}\zeta\,P_{gq}(\zeta)\right] \\ &= \int_0^{\zeta_{\max}} \mathrm{d}\zeta\,P_{qq}(\zeta),\end{aligned} \tag{2.12}$$

so that

$$T_q(k_t^2,\mu^2) = \exp\left(-\int_{k_t^2}^{\mu^2}\frac{\mathrm{d}\kappa_t^2}{\kappa_t^2}\,\frac{\alpha_S(\kappa_t^2)}{2\pi}\int_0^{\zeta_{\max}}\mathrm{d}\zeta\,P_{qq}(\zeta)\right). \tag{2.13}$$

[2]This is in contrast to [61], where a cutoff on the splitting fraction was applied both to quark and gluon emissions. Also, in [61], the scale μ was treated as a free parameter, which was chosen to be the hard scale of the subprocess, or a combination of hard scales. Here we fix μ using (2.9).

Similarly, the exponent of the gluon Sudakov form factor can be simplified by exploiting the symmetry $P_{qg}(1-\zeta) = P_{qg}(\zeta)$. We have

$$\sum_q \int_0^1 \mathrm{d}\zeta\, \zeta\, P_{qg}(\zeta) = 2n_f \int_0^1 \mathrm{d}\zeta\, \frac{1}{2} P_{qg}(\zeta) = n_f \int_0^1 \mathrm{d}\zeta\, P_{qg}(\zeta), \tag{2.14}$$

so that the gluon Sudakov form factor is

$$T_g(k_t^2, \mu^2) = \exp\left(- \int_{k_t^2}^{\mu^2} \frac{\mathrm{d}\kappa_t^2}{\kappa_t^2} \frac{\alpha_S(\kappa_t^2)}{2\pi} \left(\int_{\zeta_{\min}}^{\zeta_{\max}} \mathrm{d}\zeta\, \zeta\, P_{gg}(\zeta) + n_f \int_0^1 \mathrm{d}\zeta\, P_{qg}(\zeta) \right) \right). \tag{2.15}$$

Sample plots of the unintegrated gluon distribution at $\mu^2 = 100\ \mathrm{GeV}^2$ are shown in Fig. 2.2, using the MRST2001 LO [66] and CTEQ6L1 [35] PDFs as input. We use the one-loop expression for α_S (1.11). The results when using the MRST99 NLO [67] parton set and the two-loop expression (1.14) for α_S are also shown, cf. Fig. 3 of [61]. For the remainder of this thesis, we use MRST2001 LO PDFs as input unless otherwise specified. Sample plots of the unintegrated quark distributions are shown in Fig. 2.3. Note that the charm and bottom quark distributions are zero for $k_t^2 < m_{c,b}^2$.

It is important to note that the starting point of our derivation is the LO DGLAP equation (2.1), with LO DGLAP splitting kernels and one-loop running coupling. Therefore, in order for the normalisation (1.64) to be satisfied, it is essential that we use a LO parton set where the integrated PDFs have been determined using the same splitting kernels and running coupling. In [61], the MRST99 parton set was used, which has been determined using NLO DGLAP splitting kernels and two-loop running coupling, therefore (1.64) was found not to be satisfied. Also, in [61] the angular-ordering constraints were not correctly applied and the Sudakov form factor $T_a(\mu_0^2, \mu^2)$ was omitted from (2.7). The refined prescription now gives (almost) exactly the normalisation of (1.64), as shown in Fig. 2.4. The small differences, especially for the unintegrated gluon, are due to the fact that the angular ordering constraints are not applied in the conventional global analyses which determine the integrated PDFs.

2.2 (z, k_t)-factorisation in deep-inelastic scattering

We have defined UPDFs, $f_a(x, k_t^2, \mu^2)$, valid for all values of x with both quarks and gluons included in the evolution. This was done by assuming that the transverse momentum of the parton initiating the hard scattering is generated entirely in the

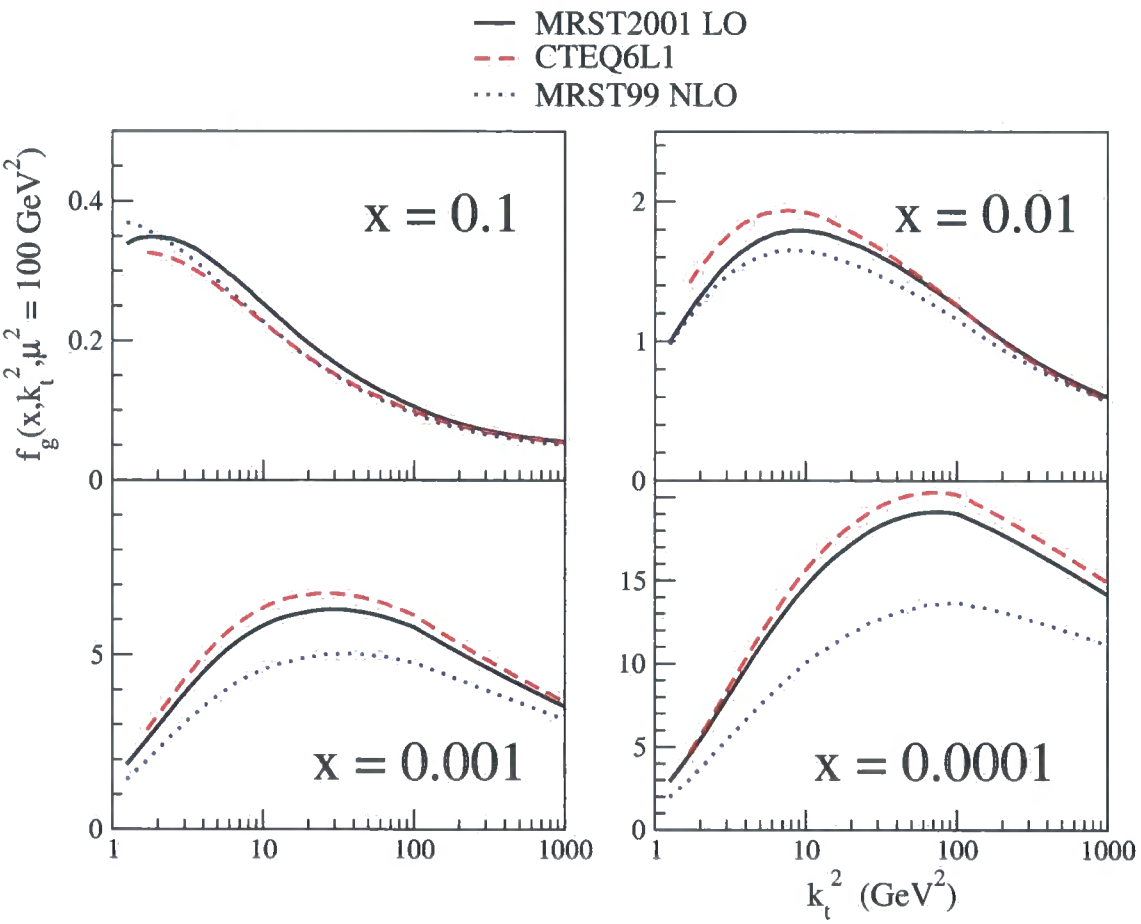

Figure 2.2: Sample plots of the unintegrated gluon distribution with MRST2001 LO, CTEQ6L1 and MRST99 NLO PDFs as input.

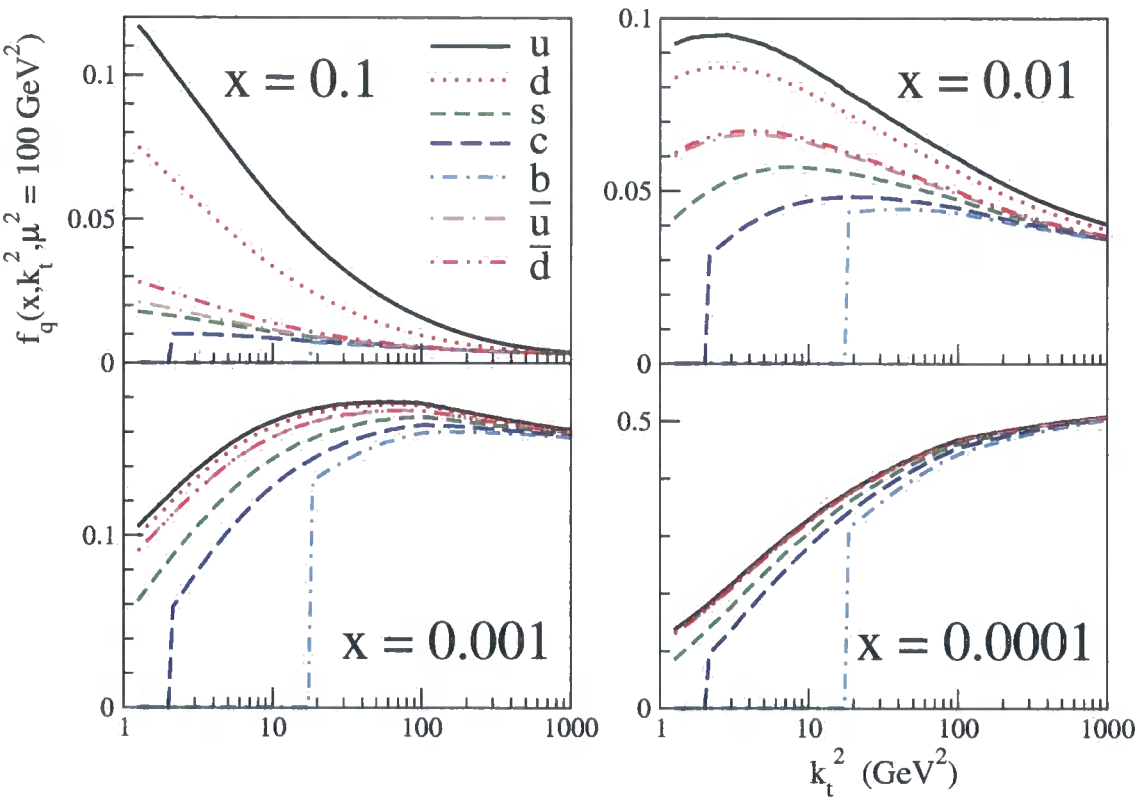

Figure 2.3: Sample plots of the unintegrated quark distributions with MRST2001 LO PDFs as input.

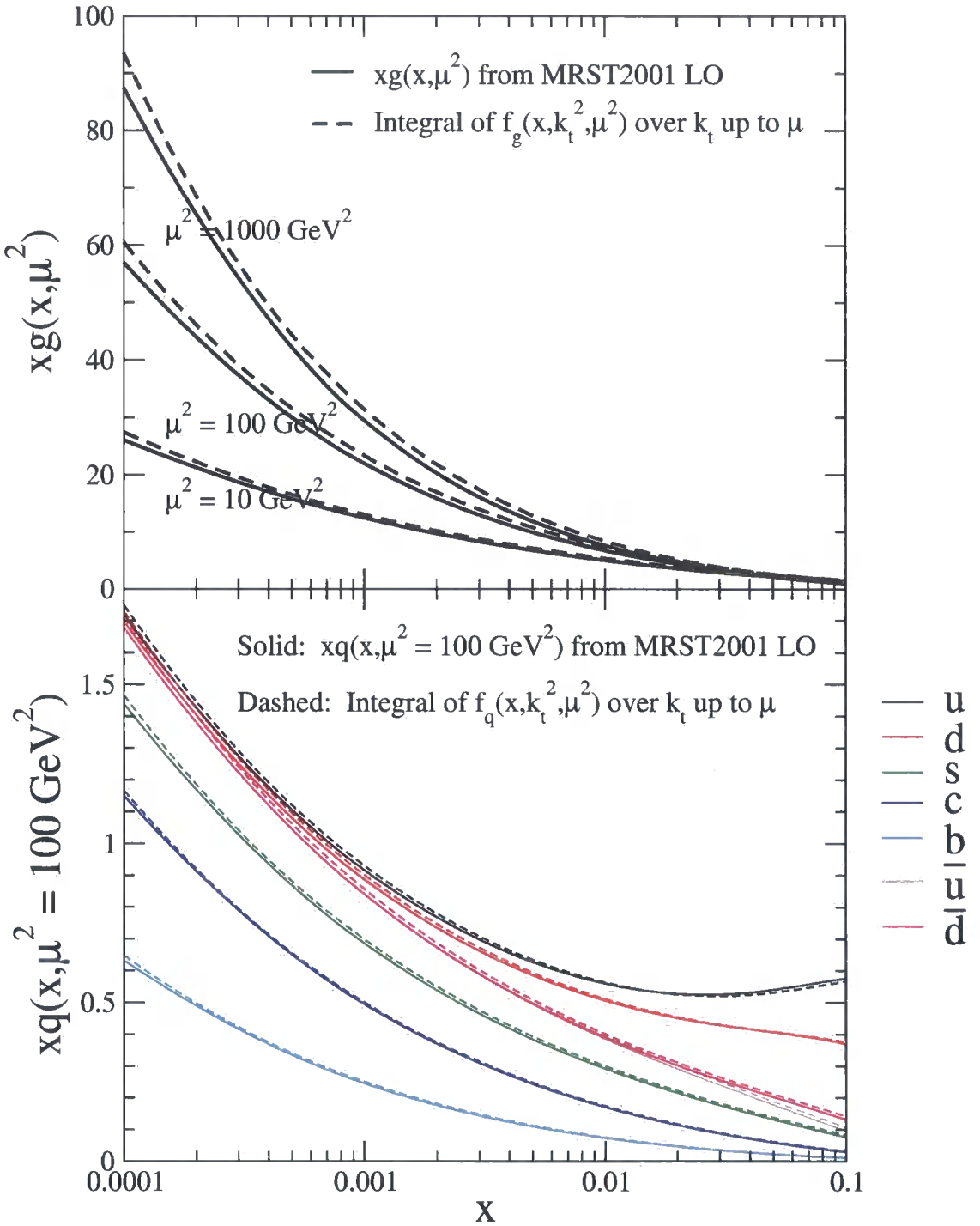

Figure 2.4: UPDFs integrated over k_t (dashed lines) compared to the integrated PDFs (solid lines).

last evolution step and then imposing constraints from angular ordering to regulate the soft gluon singularities. It now remains to specify the prescription for calculating observables such as cross sections.

The penultimate parton in the evolution chain has momentum $k_{n-1} = (x/z)\,p$. In the final evolution step, it splits into a parton with momentum $k_n \equiv k = x\,p - \beta\,q' + k_\perp$ and an emitted parton of momentum $p_n = k_{n-1} - k_n$. The Sudakov variable β is specified by the on-shell condition, $p_n^2 = 0$, which gives

$$\beta = \frac{x_B}{x}\,\frac{z}{(1-z)}\,\frac{k_t^2}{Q^2}\,. \tag{2.16}$$

Hence $k^2 = -k_t^2/(1-z)$. The rapidity of the emitted parton is

$$\eta^{\text{Breit}} = \frac{1}{2}\ln\frac{p_n^+}{p_n^-} = \frac{1}{2}\ln\frac{x\,(1-z)}{x_B\,z\,\beta}. \tag{2.17}$$

In the small-x regime, where gluons dominate, the main contribution comes from the $z \to 0$ limit, where $k \simeq x\,p + k_\perp$, $k^2 \simeq -k_t^2$, and the emitted gluon has a large positive rapidity. In this case, observables can be calculated from the k_t-factorisation prescription (1.80). At small x, we would expect that the leading $\ln(1/x)$ terms would need to be resummed. However, in [61] it was found that the unintegrated gluon based on a unified BFKL-DGLAP equation was very similar to the unintegrated gluon calculated purely from the DGLAP equation, as in Section 2.1.

In [61] the k_t-factorisation approach was used to calculate the unintegrated gluon contribution to the proton structure function $F_2(x_B, Q^2)$ via the subprocess $\gamma^* g^* \to q\bar{q}$. The unintegrated quark contribution was included via a LLA calculation of the process $\gamma^* q^* \to qg$. In [60] the normal on-shell partonic cross section was evaluated with off-shell kinematics to estimate the cross section for prompt photon hadroproduction. Again, the z dependence of the hard-scattering coefficient was neglected.

2.2.1 Generalising k_t-factorisation

Clearly, it is desirable to formulate a more general prescription for the calculation of cross sections using UPDFs. This prescription should be valid for both quarks and gluons and without taking the limit $z \to 0$. The 'partonic cross section' will necessarily have some z dependence, therefore we must consider parton distributions, $f_a(x, z, k_t^2, \mu^2)$, *doubly*-unintegrated over both z and k_t^2, satisfying the normalisation

conditions

$$\int_x^1 \mathrm{d}z\, f_a(x, z, k_t^2, \mu^2) = f_a(x, k_t^2, \mu^2) \tag{2.18}$$

and

$$\int_x^1 \mathrm{d}z \int_0^{\mu^2} \frac{\mathrm{d}k_t^2}{k_t^2}\, f_a(x, z, k_t^2, \mu^2) = a(x, \mu^2). \tag{2.19}$$

These normalisation conditions are only satisfied for fixed x and μ, independent of the integration variables z or k_t. Apart from the angular-ordering constraints, the distributions may be obtained from (2.5):

$$f_a(x, z, k_t^2, \mu^2) = T_a(k_t^2, \mu^2)\, \frac{\alpha_S(k_t^2)}{2\pi} \sum_b P_{ab}(z)\, b\left(\frac{x}{z}, k_t^2\right). \tag{2.20}$$

The explicit forms, including the constraints, follow from (2.10) and (2.11):

$$f_q(x, z, k_t^2, \mu^2) = T_q(k_t^2, \mu^2)\, \frac{\alpha_S(k_t^2)}{2\pi} \left[P_{qq}(z)\, \frac{x}{z} q\left(\frac{x}{z}, k_t^2\right) \Theta\left(\frac{\mu}{\mu + k_t} - z\right) + P_{qg}(z)\, \frac{x}{z} g\left(\frac{x}{z}, k_t^2\right) \right] \tag{2.21}$$

and

$$f_g(x, z, k_t^2, \mu^2) = T_g(k_t^2, \mu^2)\, \frac{\alpha_S(k_t^2)}{2\pi} \left[\sum_q P_{gq}(z)\, \frac{x}{z} q\left(\frac{x}{z}, k_t^2\right) + P_{gg}(z)\, \frac{x}{z} g\left(\frac{x}{z}, k_t^2\right) \Theta\left(\frac{\mu}{\mu + k_t} - z\right) \right]. \tag{2.22}$$

The universal factorisation formula involving these DUPDFs, analogous to (1.80), is

$$\sigma^{\gamma^* p} = \sum_a \int_{x_B}^1 \frac{\mathrm{d}x}{x} \int_x^1 \mathrm{d}z \int_0^\infty \frac{\mathrm{d}k_t^2}{k_t^2}\, f_a(x, z, k_t^2, \mu^2)\, \hat{\sigma}^{\gamma^* a^*}(x, z, k_t^2, \mu^2), \tag{2.23}$$

where $\hat{\sigma}^{\gamma^* a^*}$ are now the partonic cross sections for an incoming parton with (plus) momentum fraction x and transverse momentum k_t, which has split from a parent parton with (plus) momentum fraction x/z and zero transverse momentum. We will refer to this generalised form of k_t-factorisation as '(z, k_t)-factorisation'.

There will be an effective upper bound on the k_t integration from kinematics, but note that there is no restriction to the domain $k_t < \mu$, as in conventional DGLAP calculations. For $k_t > \mu$, the Sudakov form factors $T_a(k_t^2, \mu^2)$ are defined to be 1.

Taking the limit $z \to 0$ of $\hat{\sigma}^{\gamma^* g^*}(x, z, k_t^2, \mu^2)$ in (2.23) we essentially recover the

conventional k_t-factorisation prescription of (1.80). Alternatively, in the limit $k_t \to 0$, we recover the conventional collinear factorisation prescription.

Note that $f_a(x, z, k_t^2, \mu^2)$ is undefined for $k_t < \mu_0 \sim 1$ GeV and also that (2.7) no longer applies since there is now a z dependence involved. To approximate the $k_t < \mu_0$ contribution of (2.23), we choose to take the collinear limit $k_t \to 0$ in the hard-scattering coefficients, so that

$$\hat{\sigma}^{\gamma^* a^*}(x, z, k_t^2, \mu^2)\big|_{k_t<\mu_0} = \lim_{k_t \to 0} \hat{\sigma}^{\gamma^* a^*}(x, z, k_t^2, \mu^2) \equiv \hat{\sigma}^{\gamma^* a}(x, \mu^2). \tag{2.24}$$

We then make the replacement

$$\int_x^1 \mathrm{d}z \int_0^{\mu_0^2} \frac{\mathrm{d}k_t^2}{k_t^2} f_a(x, z, k_t^2, \mu^2) = a(x, \mu_0^2)\, T_a(\mu_0^2, \mu^2), \tag{2.25}$$

so that the (z, k_t)-factorisation formula (2.23) becomes

$$\sigma^{\gamma^* p} = \sum_a \int_{x_B}^1 \frac{\mathrm{d}x}{x} \left[a(x, \mu_0^2)\, T_a(\mu_0^2, \mu^2)\, \hat{\sigma}^{\gamma^* a}(x, \mu^2) + \int_x^1 \mathrm{d}z \int_{\mu_0^2}^\infty \frac{\mathrm{d}k_t^2}{k_t^2} f_a(x, z, k_t^2, \mu^2)\, \hat{\sigma}^{\gamma^* a^*}(x, z, k_t^2, \mu^2) \right]. \tag{2.26}$$

In the first term, the limit $k_t \to 0$ must also be taken in the expressions determining x and μ. In the following, we will use (2.23) for brevity, with the understanding that the $k_t < \mu_0$ region is to be dealt with as in (2.26).

2.2.2 Motivation for the (z, k_t)-factorisation formula

At this stage, it is perhaps unclear exactly how we should calculate the partonic cross sections, $\hat{\sigma}^{\gamma^* a^*}(x, z, k_t^2, \mu^2)$, since the incoming parton is now off-shell with virtuality $k^2 = -k_t^2/(1-z)$, and so the usual k_t-factorisation approach does not apply. This issue can be clarified by starting with the collinear factorisation formula one rung down. That is,

$$\sigma^{\gamma^* p} = \sum_{b=q,g} \int_x^1 \frac{\mathrm{d}(x/z)}{(x/z)}\, b(x/z, k_t^2)\, \hat{\sigma}^{\gamma^* b}(x/z, k_t^2), \tag{2.27}$$

where we have chosen the factorisation scale to be k_t, and b is the penultimate parton in the evolution chain of Fig. 1.2, so that $\hat{\sigma}^{\gamma^* b}$ incorporates the last evolution step. From Fig. 1.2 we see that the parton b, with momentum $k_{n-1} = (x/z)\, p$, splits into a parton of type a with momentum $k_n \equiv k = x\, p - \beta\, q' + k_\perp$, which then goes on

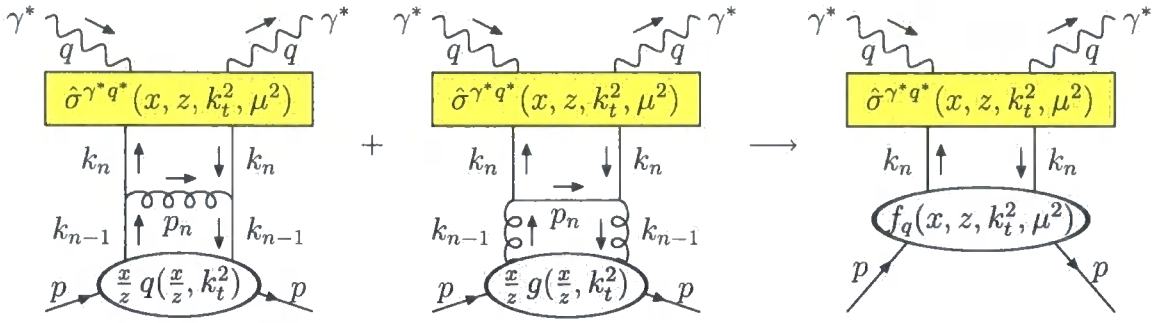

Figure 2.5: Illustration of (z, k_t)-factorisation for the doubly-unintegrated quark distribution, $f_q(x, z, k_t^2, \mu^2)$, shown in the final diagram. In the first two diagrams the penultimate parton in the DGLAP evolution chain, with momentum $k_{n-1} = (x/z)\, p$, splits into a quark with momentum $k_n \equiv k = x\, p - \beta\, q' + k_\perp$.

to initiate the hard subprocess at a scale μ given by (2.9). To derive formula (2.23) we need to show that the partonic cross section $\hat{\sigma}^{\gamma^* b}$ can be factorised to give a partonic cross section for the $\gamma^* a^*$ subprocess, $\hat{\sigma}^{\gamma^* a^*}$, with the remainder being absorbed into the definition of the DUPDF, $f_a(x, z, k_t^2, \mu^2)$. This idea is illustrated in Fig. 2.5 for the doubly-unintegrated quark distribution, and in Fig. 2.6 for the doubly-unintegrated gluon distribution.

The squared matrix element can be factorised if we assume the LLA, so that only the leading $1/k_t^2$ term is kept and terms not giving a logarithmic divergence in the collinear limit are neglected. We find that

$$|\mathcal{M}^{\gamma^* b}|^2 = 16\pi^2 \frac{(1-z)}{z k_t^2} \frac{\alpha_S(k_t^2)}{2\pi} \sum_a P_{ab}(z)\, |\mathcal{M}^{\gamma^* a^*}|^2 \;\times\; [1 + \mathcal{O}(\beta)]\,, \tag{2.28}$$

where $|\mathcal{M}^{\gamma^* a^*}|^2$ represents the squared matrix element of the $\gamma^* a^*$ subprocess, containing one power of α_S less than $|\mathcal{M}^{\gamma^* b}|^2$. We have used this method to derive the form of all four splitting kernels, $P_{ab}(z)$ (see Section 2.2.3). It is crucial that we adopt a physical gauge for the gluon so that the splitting kernels are obtained from only the ladder-type diagrams.

The extra terms of (2.28) are proportional to β and so are negligible for either $k_t \to 0$ or $z \to 0$. Away from these limits, it is far from obvious that these 'beyond LLA' terms will be small, a necessary condition for the factorisation to hold. We will observe that the main effect of the extra terms is to suppress the contribution from large z for gluon emission. In our approach, we achieve the same effect with angular ordering, so the extra terms may be neglected. We will provide some numerical

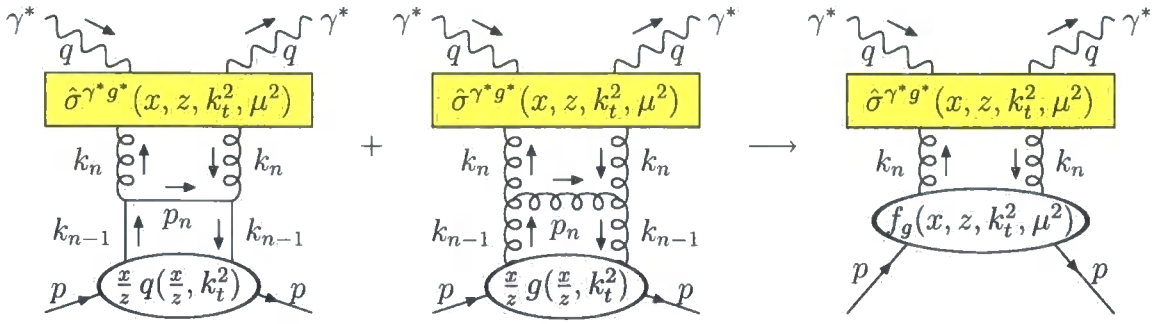

Figure 2.6: Illustration of (z, k_t)-factorisation for the doubly-unintegrated gluon distribution, $f_g(x, z, k_t^2, \mu^2)$, shown in the final diagram. In the first two diagrams the penultimate parton in the DGLAP evolution chain, with momentum $k_{n-1} = (x/z)\, p$, splits into a gluon with momentum $k_n \equiv k = x\, p - \beta\, q' + k_\perp$.

evidence to justify this in Section 2.4.1.

In (2.28), $|\mathcal{M}^{\gamma^* a^*}|^2$ should also be evaluated in the LLA for the factorisation to hold, so terms proportional to k_t^2 should be neglected when calculating this. This amounts to the replacement $k \to x\, p$ in the numerator of $|\mathcal{M}^{\gamma^* a^*}|^2$, but not in the propagator virtualities in the denominator. For example, if $a = g$, the unintegrated gluon, we make the replacement $d_{\mu\nu}(k, q') \to d_{\mu\nu}(x\, p, q') = -g^\perp_{\mu\nu}$ in the sum over initial gluon polarisations. If $a = q$, the unintegrated quark, we make the replacement $k \to x\, p$ in the trace. Of course, x may have some k_t dependence from kinematics, so some terms beyond the LLA are included in this respect. In Section 3.4.2, we will briefly discuss the possibility of evaluating $|\mathcal{M}^{\gamma^* a^*}|^2$ with $k \to x\, p + k_\perp$, as in the k_t-factorisation prescription.

The phase space $\mathrm{d}\Phi^{\gamma^* b}$ can be factorised easily to give the phase space $\mathrm{d}\Phi^{\gamma^* a^*}$:

$$\begin{aligned}
\mathrm{d}\Phi^{\gamma^* b} &= \mathrm{d}\Phi^{\gamma^* a^*} \times \frac{1}{(2\pi)^3}\, \mathrm{d}^4 p_n\, \delta(p_n^2) = \mathrm{d}\Phi^{\gamma^* a^*} \times \frac{1}{(2\pi)^3}\, \mathrm{d}^4 k\, \delta(p_n^2) \\
&= \mathrm{d}\Phi^{\gamma^* a^*} \times \frac{1}{16\pi^2}\, \mathrm{d}x\, \mathrm{d}\beta\, \mathrm{d}k_t^2\, \frac{z}{x(1-z)}\, \delta\left(\beta - \frac{x_B}{x}\, \frac{z}{(1-z)}\, \frac{k_t^2}{Q^2}\right) \\
&= \mathrm{d}\Phi^{\gamma^* a^*} \times \frac{1}{16\pi^2}\, \mathrm{d}x\, \mathrm{d}k_t^2\, \frac{z}{x(1-z)},
\end{aligned} \tag{2.29}$$

where we have used $\mathrm{d}^4 k = p \cdot q\ \mathrm{d}x\, \mathrm{d}\beta\, \mathrm{d}^2 \boldsymbol{k_t}$ and $\mathrm{d}^2 \boldsymbol{k_t} = k_t\, \mathrm{d}k_t\, \mathrm{d}\phi = \pi \mathrm{d}k_t^2$, after integrating over the azimuthal angle ϕ. The β integration absorbs the delta function, determining β as given by (2.16).

The partonic flux factor $F^{\gamma^* a^*}$ is not well defined since the parton a is off-shell and non-collinear with the photon. As in conventional k_t-factorisation, we define it

to be[3]

$$F^{\gamma^* a^*} \equiv z\, F^{\gamma^* b} = z\, 4\, k_{n-1} \cdot q = 4x\, p \cdot q. \tag{2.30}$$

Finally, we have the relationship

$$\mathrm{d}\hat{\sigma}^{\gamma^* b} = \mathrm{d}\Phi^{\gamma^* b}\, |\mathcal{M}^{\gamma^* b}|^2 \,/\, F^{\gamma^* b} = \frac{\mathrm{d}x}{x}\, \frac{\mathrm{d}k_t^2}{k_t^2}\, z \frac{\alpha_S(k_t^2)}{2\pi} \sum_a P_{ab}(z)\, \mathrm{d}\hat{\sigma}^{\gamma^* a^*}. \tag{2.31}$$

To calculate the hadronic cross section, we insert (2.31) into (2.27)

$$\begin{aligned} \mathrm{d}\sigma^{\gamma^* p} &= \sum_{b=q,g} \frac{\mathrm{d}(x/z)}{(x/z)}\, b(x/z, k_t^2)\, \mathrm{d}\hat{\sigma}^{\gamma^* b} \\ &= \sum_{b=q,g} \frac{\mathrm{d}z}{z}\, \frac{\mathrm{d}x}{x}\, \frac{\mathrm{d}k_t^2}{k_t^2}\, z \frac{\alpha_S(k_t^2)}{2\pi} \sum_a P_{ab}(z)\, b(x/z, k_t^2)\, \mathrm{d}\hat{\sigma}^{\gamma^* a^*} \\ &\to \sum_a \frac{\mathrm{d}x}{x}\, \mathrm{d}z\, \frac{\mathrm{d}k_t^2}{k_t^2}\, f_a(x, z, k_t^2, \mu^2)\, \mathrm{d}\hat{\sigma}^{\gamma^* a^*}(x, z, k_t^2, \mu^2), \end{aligned} \tag{2.32}$$

where in the last step we recognise the 'real' part of the DUPDFs given in (2.20). The (z, k_t)-factorisation formula (2.23) follows easily.

2.2.3 Derivation of splitting kernels

Here, we derive the four LO DGLAP splitting kernels from the relevant Feynman diagrams shown in Fig. 2.7. The presentation is similar to that given in Chapter 1 of [11]. In all four cases, we shall show that the squared matrix element factorises in the LLA as

$$|\mathcal{M}^{\gamma^* b}|^2 \overset{\text{LLA}}{\approx} 16\pi^2 \frac{(1-z)}{z k_t^2} \frac{\alpha_S(k_t^2)}{2\pi} P_{ab}(z)\, |\mathcal{M}^{\gamma^* a^*}|^2. \tag{2.33}$$

$P_{qq}(z)$:

The squared matrix element corresponding to Fig. 2.7(a) is

$$|\mathcal{M}^{\gamma^* q}|^2 = \frac{1}{2} C_{ac}\, \frac{g^2}{k^4}\, \mathrm{Tr}[X_{ac}\, \not{k} \gamma^\mu \not{l} \gamma^\nu \not{k}]\, d_{\mu\nu}(l-k, q'), \tag{2.34}$$

where $g^2 = 4\pi\alpha_S(k_t^2)$ and the colour factor is

$$C_{ac} = \frac{1}{N_C} t^A_{ab} t^A_{bc} = \frac{C_F}{N_C} \delta_{ac}. \tag{2.35}$$

[3]Choosing another definition for the flux factor is a NLL effect.

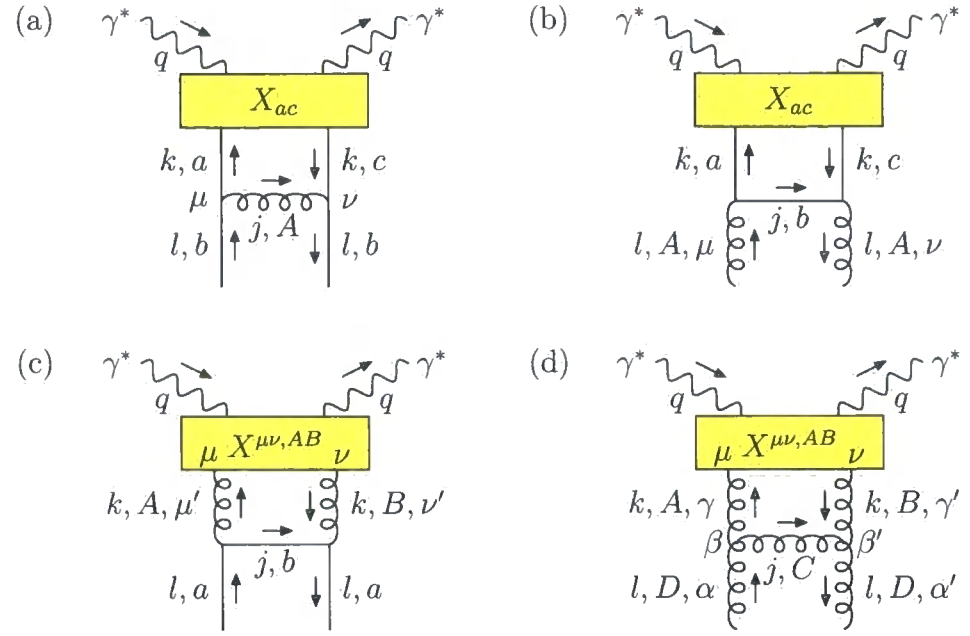

Figure 2.7: Cut diagrams giving the LO DGLAP splitting kernels: (a) $P_{qq}(z)$, (b) $P_{qg}(z)$, (c) $P_{gq}(z)$, (d) $P_{gg}(z)$. Here, j, k, l, q are momenta, $a, b, c = 1, \ldots, N_C$ and $A, B, C, D = 1, \ldots, (N_C^2 - 1)$ are colour indices, and $\alpha, \beta, \gamma, \mu, \nu, \alpha', \beta', \gamma', \mu', \nu'$ are Lorentz indices. In each case, the box labelled X contains additional Lorentz and colour structure.

Simplifying the trace using identities such as $\not{k}\not{l} = -\not{l}\not{k} + 2k \cdot l$ gives

$$\begin{aligned}\mathrm{Tr}[X_{ac}\,\not{k}\gamma^\mu\not{l}\gamma^\nu\not{k}]\; d_{\mu\nu}(l-k,q') = -2k^2\mathrm{Tr}[X_{ac}\,(\not{l}-\not{k})] - \frac{k^2}{(l-k)\cdot q'} \\ \times\left\{2l\cdot q'\,\mathrm{Tr}[X_{ac}\,\not{k}] + 2k\cdot q'\,\mathrm{Tr}[X_{ac}\,\not{l}] - k^2\,\mathrm{Tr}[X_{ac}\,\not{q}']\right\}. \quad (2.36)\end{aligned}$$

To extract the LLA contribution we must only keep the terms proportional to k^2 in this expression, neglecting 'beyond LLA' terms such as those proportional to k^4. To this accuracy, we may replace $\not{l}$ with $\not{k}/z$ on the RHS of (2.36). Thus,

$$\mathrm{Tr}[X_{ac}\,\not{k}\gamma^\mu\not{l}\gamma^\nu\not{k}]\; d_{\mu\nu}(l-k,q') \overset{\mathrm{LLA}}{\approx} -2k^2\,\mathrm{Tr}[X_{ac}\,\not{k}]\left(\frac{1-z}{z}+\frac{2}{1-z}\right). \quad (2.37)$$

Substituting into (2.34) we obtain

$$\begin{aligned}|\mathcal{M}^{\gamma^* q}|^2 &\overset{\mathrm{LLA}}{\approx} 16\pi^2\frac{(1-z)}{zk_t^2}\frac{\alpha_S(k_t^2)}{2\pi}\left(C_F\frac{1+z^2}{1-z}\right)\left(\frac{1}{2}\mathrm{Tr}[X_{ac}\,\not{k}]\frac{1}{N_C}\delta_{ac}\right) \\ &\equiv 16\pi^2\frac{(1-z)}{zk_t^2}\frac{\alpha_S(k_t^2)}{2\pi}P_{qq}(z)\;|\mathcal{M}^{\gamma^* q^*}|^2,\end{aligned} \quad (2.38)$$

where $|\mathcal{M}^{\gamma^* q^*}|^2$ should be evaluated with $k = x\,p$ in order not to lose the logarithmic divergence.

$P_{qg}(z)$:

The squared matrix element corresponding to Fig. 2.7(b) is

$$|\mathcal{M}^{\gamma^* g}|^2 = \frac{1}{2} C_{ac}\, \frac{g^2}{k^4}\, \mathrm{Tr}[X_{ac}\, \not{k} \gamma^\mu (\not{l} - \not{k}) \gamma^\nu \not{k}]\; d_{\mu\nu}(l, q'), \tag{2.39}$$

where $d_{\mu\nu}(l, q') = -g^{\perp}_{\mu\nu}$ and the colour factor is

$$C_{ac} = \frac{1}{(N_C^2 - 1)} t^A_{ab} t^A_{bc} = \frac{C_F}{(N_C^2 - 1)} \delta_{ac} = \frac{T_R}{N_C} \delta_{ac}. \tag{2.40}$$

Using the identity $\gamma^\mu (\not{l} - \not{k}) \gamma^\nu \; (-g^{\perp}_{\mu\nu}) = 2(\not{l} - \not{k}_\parallel)$, we obtain

$$\mathrm{Tr}[X_{ac}\, \not{k} \gamma^\mu (\not{l} - \not{k}) \gamma^\nu \not{k}]\; (-g^{\perp}_{\mu\nu}) = -2k^2 \mathrm{Tr}[X_{ac}\, (\not{l} - \not{k}_\parallel)] + 2k^2 (1 - 2z) \mathrm{Tr}[X_{ac}\, \not{k}]. \tag{2.41}$$

As before, within the LLA we can replace $\not{l}$ by $\not{k}/z$ and $\not{k}_\parallel$ by $\not{k}$, so that

$$\mathrm{Tr}[X_{ac}\, \not{k} \gamma^\mu (\not{l} - \not{k}) \gamma^\nu \not{k}]\; (-g^{\perp}_{\mu\nu}) \overset{\text{LLA}}{\approx} -2k^2\, \mathrm{Tr}[X_{ac}\, \not{k}] \left(\frac{1 - z}{z} - 1 + 2z \right). \tag{2.42}$$

Substituting into (2.39) we obtain

$$\begin{aligned} |\mathcal{M}^{\gamma^* g}|^2 &\overset{\text{LLA}}{\approx} 16\pi^2 \frac{(1 - z)}{z k_t^2} \frac{\alpha_S(k_t^2)}{2\pi}\; (T_R[z^2 + (1 - z)^2])\; \left(\frac{1}{2} \mathrm{Tr}[X_{ac}\, \not{k}] \frac{1}{N_C} \delta_{ac} \right) \\ &\equiv 16\pi^2 \frac{(1 - z)}{z k_t^2} \frac{\alpha_S(k_t^2)}{2\pi} P_{qg}(z)\; |\mathcal{M}^{\gamma^* q^*}|^2, \end{aligned} \tag{2.43}$$

where again $|\mathcal{M}^{\gamma^* q^*}|^2$ should be evaluated with $k = x\,p$ in order not to lose the logarithmic divergence.

$P_{gq}(z)$:

The squared matrix element corresponding to Fig. 2.7(c) is

$$|\mathcal{M}^{\gamma^* q}|^2 = \frac{1}{2} \mathcal{C}^{AB}\, \frac{g^2}{k^4}\, X^{\mu\nu, AB}\, \mathrm{Tr}[(\not{l} - \not{k}) \gamma^{\mu'} \not{l} \gamma^{\nu'}]\; d_{\mu\mu'}(k, q')\, d_{\nu\nu'}(k, q'), \tag{2.44}$$

where the colour factor is

$$\mathcal{C}^{AB} = \frac{1}{N_C} t^A_{ab} t^B_{ba} = \frac{1}{N_C} \mathrm{Tr}[t^A t^B] = \frac{T_R}{N_C} \delta^{AB} = \frac{C_F}{(N_C^2 - 1)} \delta^{AB}. \tag{2.45}$$

Evaluating the trace, we obtain

$$\mathrm{Tr}[(\not{l}-\not{k})\gamma^{\mu'}\not{l}\gamma^{\nu'}]\, d_{\mu\mu'}(k,q')\, d_{\nu\nu'}(k,q') = 4\Big[(l-k)^{\mu'} d_{\mu\mu'}(k,q')\; l^{\nu'} d_{\nu\nu'}(k,q') + l^{\mu'} d_{\mu\mu'}(k,q')\; (l-k)^{\nu'} d_{\nu\nu'}(k,q') + \frac{k^2}{2} d_{\mu\mu'}(k,q') d_{\nu\nu'}(k,q')\Big]. \quad (2.46)$$

Now in the first two terms of (2.46) we can replace

$$\begin{aligned} l^{\mu} d_{\mu\nu}(k,q') &= \frac{1}{z}\left(k^{\mu} + \beta q'^{\mu} - k_{\perp}^{\mu}\right)\left(-g_{\mu\nu} + \frac{k_{\mu} q'_{\nu} + q'_{\mu} k_{\nu}}{k\cdot q'}\right) \\ &= \frac{1}{z}\left(k_{\perp\nu} + \frac{z k^2}{k\cdot q'} q'_{\nu}\right) \overset{\text{LLA}}{\approx} \frac{1}{z} k_{\perp\nu}, \end{aligned} \quad (2.47)$$

and

$$k^{\mu} d_{\mu\nu}(k,q') = \frac{k^2}{k\cdot q'} q'_{\nu} \overset{\text{LLA}}{\approx} 0, \quad (2.48)$$

while in the third term of (2.46) we can replace

$$d_{\mu\nu}(k,q') \overset{\text{LLA}}{\approx} d_{\mu\nu}(x\,p,q') = -g^{\perp}_{\mu\nu}. \quad (2.49)$$

Averaging over the azimuthal angle,

$$\left\langle k_{\perp\mu} k_{\perp\nu}\right\rangle \equiv \int_0^{2\pi} \frac{\mathrm{d}\phi}{2\pi}\, k_{\perp\mu} k_{\perp\nu} = -\frac{1}{2} k_t^2 g^{\perp}_{\mu\nu} = \frac{1}{2} k^2 (1-z) g^{\perp}_{\mu\nu}, \quad (2.50)$$

we obtain

$$\mathrm{Tr}[(\not{l}-\not{k})\gamma^{\mu'}\not{l}\gamma^{\nu'}]\, d_{\mu\mu'}(k,q')\, d_{\nu\nu'}(k,q') \overset{\text{LLA}}{\approx} 4k^2 g^{\perp}_{\mu\nu}\left(\frac{1-z}{z^2} + \frac{1}{2}\right), \quad (2.51)$$

and substituting into (2.44) gives

$$\begin{aligned} |\mathcal{M}^{\gamma^* q}|^2 &\overset{\text{LLA}}{\approx} 16\pi^2 \frac{(1-z)}{z k_t^2} \frac{\alpha_S(k_t^2)}{2\pi}\left(C_F \frac{1+(1-z)^2}{z}\right)\left(X^{\mu\nu,AB}(-g^{\perp}_{\mu\nu}/2)\,\frac{\delta^{AB}}{(N_C^2-1)}\right) \\ &\equiv 16\pi^2 \frac{(1-z)}{z k_t^2} \frac{\alpha_S(k_t^2)}{2\pi} P_{gq}(z)\; |\mathcal{M}^{\gamma^* g^*}|^2, \end{aligned} \quad (2.52)$$

where again $|\mathcal{M}^{\gamma^* g^*}|^2$ should be evaluated with $k = x\,p$ in order not to lose the logarithmic divergence.

$P_{gg}(z)$:

The squared matrix element corresponding to Fig. 2.7(d) is

$$\begin{aligned}|\mathcal{M}^{\gamma^* g}|^2 = \frac{1}{2}C^{AB}\,\frac{g^2}{k^4}\,X^{\mu\nu,AB}\,d_{\mu\gamma}(k,q')\,d_{\nu\gamma'}(k,q')\,d_{\alpha\alpha'}(l,q')\,d_{\beta\beta'}(l-k,q')\\ \times\left[(2l-k)^{\gamma}g^{\alpha\beta}+(2k-l)^{\alpha}g^{\beta\gamma}-(k+l)^{\beta}g^{\gamma\alpha}\right]\\ \times(-1)\left[(2l-k)^{\gamma'}g^{\alpha'\beta'}+(2k-l)^{\alpha'}g^{\beta'\gamma'}-(k+l)^{\beta'}g^{\gamma'\alpha'}\right],\end{aligned} \tag{2.53}$$

where the colour factor is

$$C^{AB}=\frac{1}{(N_C^2-1)}f^{ACD}f^{BCD}=\frac{C_A}{(N_C^2-1)}\delta^{AB}. \tag{2.54}$$

Using the FORM [68] program to evaluate (2.53), substituting

$$g_{\mu\nu}\to g^{\perp}_{\mu\nu}+\frac{p_\mu q'_\nu+q'_\mu p_\nu}{p\cdot q'}, \tag{2.55}$$

and keeping only the LLA terms proportional to $g^{\perp}_{\mu\nu}$, we obtain

$$\begin{aligned}|\mathcal{M}^{\gamma^* g}|^2 &\overset{\text{LLA}}{\approx} 16\pi^2\frac{(1-z)}{zk_t^2}\frac{\alpha_S(k_t^2)}{2\pi}\left(2C_A\frac{(1-z+z^2)^2}{z(1-z)}\right)\left(X^{\mu\nu,AB}(-g^{\perp}_{\mu\nu}/2)\,\frac{\delta^{AB}}{(N_C^2-1)}\right)\\ &\equiv 16\pi^2\frac{(1-z)}{zk_t^2}\frac{\alpha_S(k_t^2)}{2\pi}P_{gg}(z)\;|\mathcal{M}^{\gamma^* g^*}|^2,\end{aligned} \tag{2.56}$$

where again $|\mathcal{M}^{\gamma^* g^*}|^2$ should be evaluated with $k = xp$ in order not to lose the logarithmic divergence.

2.3 Application to inclusive jet production in DIS

The simplest process that we can consider to illustrate the use of the DUPDFs is current jet production in DIS. The subprocess is simply $\gamma^* q^* \to q$ at the top of the evolution chain. In the normal collinear factorisation approach, this diagram gives the parton model prediction for the structure function $F_2(x_B, Q^2)$. Indeed, measurements of $F_2(x_B, Q^2)$ are used to determine the integrated quark distribution $q(x, \mu^2)$. In the new (z, k_t)-factorisation framework of Section 2.2, where the incoming quark has transverse momentum $\boldsymbol{k_t}$, we produce a current jet with transverse momentum $\boldsymbol{k_t}$ and transverse energy $E_T = k_t$. The parton emitted in the last evolution step will emerge with transverse momentum $-\boldsymbol{k_t}$ and transverse energy $E_T = k_t$.

The inclusive jet cross section counts all jets passing the required cuts. Having calculated the ep cross section from (1.20), we need the differential cross section with respect to the transverse energy E_T and the rapidity η:

$$\frac{\mathrm{d}^4\sigma^{ep}}{\mathrm{d}y\,\mathrm{d}Q^2\,\mathrm{d}E_T\,\mathrm{d}\eta} = \frac{\mathrm{d}^2\sigma^{ep}}{\mathrm{d}y\,\mathrm{d}Q^2} \sum_i \delta(E_T - E_T(j_i))\,\delta(\eta - \eta(j_i)), \tag{2.57}$$

where the sum is over jets with momenta j_i, transverse energy $E_T(j_i)$ and rapidity $\eta(j_i)$. Experimental data are usually given in bins of y, Q^2, E_T, and η, which we need to integrate over to obtain a prediction:

$$\begin{aligned}\sigma^{ep} &= \int_{y_{\min}}^{y_{\max}} \mathrm{d}y \int_{Q^2_{\min}}^{Q^2_{\max}} \mathrm{d}Q^2 \int_{E_{T,\min}}^{E_{T,\max}} \mathrm{d}E_T \int_{\eta_{\min}}^{\eta_{\max}} \mathrm{d}\eta\, \frac{\mathrm{d}^4\sigma^{ep}}{\mathrm{d}y\,\mathrm{d}Q^2\,\mathrm{d}E_T\,\mathrm{d}\eta} \\ &= \int_{y_{\min}}^{y_{\max}} \mathrm{d}y \int_{Q^2_{\min}}^{Q^2_{\max}} \mathrm{d}Q^2\, \frac{\mathrm{d}^2\sigma^{ep}}{\mathrm{d}y\,\mathrm{d}Q^2} \sum_i \Theta\left(\eta(j_i) - \eta_{\min}\right) \Theta\left(\eta_{\max} - \eta(j_i)\right) \\ &\qquad \times \Theta\left(E_T(j_i) - E_{T,\min}\right) \Theta\left(E_{T,\max} - E_T(j_i)\right).\end{aligned} \tag{2.58}$$

The differential cross sections are easily obtained by dividing by the size of the bin, for example,

$$\frac{\mathrm{d}\sigma^{ep}}{\mathrm{d}E_T} = \sigma^{ep}/(E_{T,\max} - E_{T,\min}). \tag{2.59}$$

In Section 2.2 we gave the general prescription for calculating the cross section. Recall that it was necessary to consider the DUPDFs, $f_a(x, z, k_t^2, \mu^2)$, to keep the precise kinematics in the subprocess, without taking the limit $z \to 0$. We now check that this prescription reproduces with good accuracy the conventional LO QCD calculation with integrated partons, where all $\mathcal{O}(\alpha_S)$ diagrams are included, not just the ones which give the leading $\mathrm{d}k_t^2/k_t^2$ term. With the (z, k_t)-factorisation approach, in addition to the jets produced in the hard subprocess, we must also count the parton emitted in the last evolution step with transverse energy $E_T = k_t$ and rapidity given by (2.17).

We also explain how the prescription may be extended to higher orders in perturbation theory. The conventional NLO QCD diagrams are at $\mathcal{O}(\alpha_S^2)$. These include all real and virtual $\mathcal{O}(\alpha_S)$ corrections to the LO QCD diagrams. The hard-scattering coefficients obtained from these diagrams are convoluted with NLO integrated PDFs, $a(x, \mu^2)$, satisfying the DGLAP equation with two-loop α_S and NLO splitting kernels. Several codes are available which include these NLO QCD calculations, for example, DISASTER++ [69], DISENT [70], JETVIP [71], MEPJET [72], and NLOJET++ [73]. There is no longer a one-to-one correspondence between partons and jets. The momenta of the outgoing partons should be passed through a jet al-

gorithm to assign the partons to jets. At NLO in the (z, k_t)-factorisation approach, we continue to use the LO doubly-unintegrated partons constructed in Section 2.1 and only calculate the $\mathcal{O}(\alpha_S)$ diagrams expected to dominate.

The procedure involved in going from $\sigma^{\gamma^* p}$ to σ^{ep}, via (1.20) and (2.58), is the same in all the theoretical approaches we describe, therefore in the following sections we only describe how to calculate $\sigma^{\gamma^* p}$.

2.3.1 Collinear factorisation approach at LO

In the collinear approximation, the LO QCD Feynman diagrams are at $\mathcal{O}(\alpha_S)$. These are the boson-gluon fusion process, $\gamma^* g \to q\bar{q}$, and the QCD Compton process, $\gamma^* q \to qg$, illustrated in Fig. 2.1(b). These partonic processes give rise to two jets with equal transverse energy and opposite transverse momentum. There is a one-to-one correspondence between partons and jets. There are no singularities to be regulated and no cutoff is imposed on gluon emission.

We now explain a few of the details involved since this calculation offers valuable insights into the (z, k_t)-factorisation approach. The cut diagrams are illustrated in Fig. 2.8. Note that the direction of fermion number flow is not indicated in these diagrams. The arrows indicate only the direction of the labelled momentum and this is taken to be the same for both quarks and antiquarks. The contribution from diagrams (a) to (f) to $\sigma^{\gamma^* p}$ need to be added together. Diagrams (a) to (d) have the same kinematics, so we calculate them first. We label the momenta by

$$\begin{aligned} &q = q' - x_B\, p, \qquad l = \frac{x}{z}\, p, \qquad k = x\, p - \beta\, q' + k_\perp, \\ &j_1 = k + q = (x - x_B)\, p + (1 - \beta)\, q' + k_\perp, \qquad j_2 = l - k = \frac{x}{z}(1 - z)\, p + \beta\, q' - k_\perp, \end{aligned} \tag{2.60}$$

with $x \geq x_B$. The 2-body phase space is

$$\mathrm{d}\Phi^{\gamma^* a} = (2\pi)^4\, \delta^{(4)}(l + q - j_1 - j_2)\, \frac{\mathrm{d}^4 j_1}{(2\pi)^3}\, \delta(j_1^2)\, \frac{\mathrm{d}^4 j_2}{(2\pi)^3}\, \delta(j_2^2) \;=\; \frac{\mathrm{d}^4 k}{4\pi^2}\, \delta(j_1^2)\, \delta(j_2^2). \tag{2.61}$$

The two delta functions can be used to determine β and x:

$$\beta = \frac{x_B\, z\, r}{x\,(1 - z)} \quad \text{and} \quad x_\pm = \frac{x_B}{2(1 - z)} \left(1 - z + r \pm \sqrt{(1 - z + r)^2 - 4rz(1 - z)}\right), \tag{2.62}$$

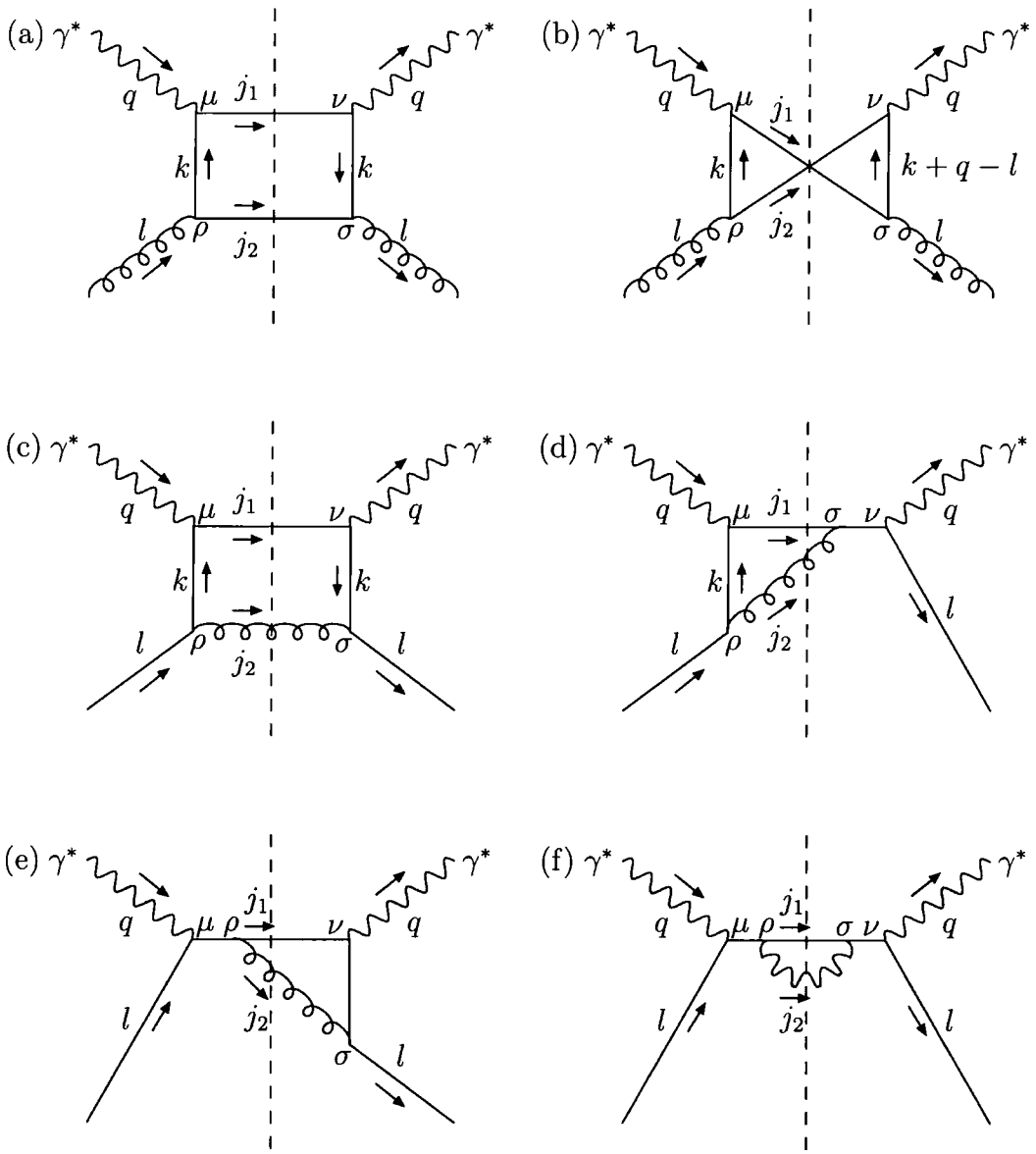

Figure 2.8: Cut diagrams contributing to inclusive jet production in LO QCD.

where $r \equiv k_t^2/Q^2$. The flux factor is $F^{\gamma^* a} = 4\, l \cdot q$, so that

$$\frac{\mathrm{d}\Phi^{\gamma^* a}}{F^{\gamma^* a}} = \frac{\mathrm{d}k_t^2}{16\pi}\left(\frac{x_B}{Q^2}\right)^2 \sum_{x=x_\pm} \frac{z^2}{x^2(1-z)}\frac{1}{1-x_B\beta/x}. \tag{2.63}$$

In practice, the condition $x \geq x_B$ ensures that only the $x = x_+$ solution contributes.

The squared matrix elements of all six diagrams can be written in the form

$$|\mathcal{M}_{T,L}^{\gamma^* a}|^2 = \frac{1}{2} e^2 g^2\, M^{\mu\nu}\, \varepsilon_\mu(q,\lambda)\varepsilon_\nu^*(q,\lambda), \tag{2.64}$$

where λ is either T or L and the initial factor of $1/2$ is to average over the helicity of the incoming parton. Appropriate scales have been chosen for the two running couplings, $e^2 = 4\pi\alpha_{\mathrm{em}}(Q^2)$ and $g^2 = 4\pi\alpha_S(k_t^2)$. We have

$$\text{(a)}\quad M^{\mu\nu} = \left(\sum_q e_q^2\right) T_R \frac{1}{k^4}\mathrm{Tr}\left[\not{k}\gamma^\rho \not{j}_2 \gamma^\sigma \not{k}\gamma^\nu \not{j}_1 \gamma^\mu\right] d_{\rho\sigma}(l,q'), \tag{2.65}$$

$$\text{(b)}\quad M^{\mu\nu} = \left(\sum_q e_q^2\right) T_R \frac{1}{k^2}\frac{1}{(k+q-l)^2}\mathrm{Tr}\left[\not{k}\gamma^\rho \not{j}_2 \gamma^\nu (\not{k}+\not{q}-\not{l})\gamma^\sigma \not{j}_1 \gamma^\mu\right] d_{\rho\sigma}(l,q'), \tag{2.66}$$

$$\text{(c)}\quad M^{\mu\nu} = e_q^2 C_F \frac{1}{k^4}\mathrm{Tr}\left[\not{k}\gamma^\rho \not{l}\gamma^\sigma \not{k}\gamma^\nu \not{j}_1 \gamma^\mu\right] d_{\rho\sigma}(j_2,q'), \tag{2.67}$$

$$\text{(d)}\quad M^{\mu\nu} = e_q^2 C_F \frac{1}{k^2}\frac{1}{(l+q)^2}\mathrm{Tr}\left[\not{k}\gamma^\rho \not{l}\gamma^\nu (\not{l}+\not{q})\gamma^\sigma \not{j}_1 \gamma^\mu\right] d_{\rho\sigma}(j_2,q'). \tag{2.68}$$

For diagrams (e) and (f) of Fig. 2.8, the momenta can be parameterised as

$$\begin{aligned} q = q' - x_B\, p, \qquad l = X\, p, \qquad j_1 &= \xi\, p + b\, q' + k_\perp, \\ j_2 = l + q - j_1 &= (X - x_B - \xi)\, p + (1-b)\, q' - k_\perp, \end{aligned} \tag{2.69}$$

with $0 \leq \xi \leq X - x_B \leq 1$ and $0 \leq b \leq 1$. This time the 2-body phase space determines

$$b = x_B r/\xi, \qquad \xi_\pm = \frac{1}{2}\left\{X - x_B \pm \sqrt{(X-x_B)(X-(1+4r)x_B)}\right\}. \tag{2.70}$$

Dividing the phase space by the flux factor gives

$$\frac{\mathrm{d}\Phi^{\gamma^* q}}{F^{\gamma^* q}} = \frac{\mathrm{d}k_t^2}{16\pi}\left(\frac{x_B}{Q^2}\right)^2 \sum_{\xi=\xi_\pm} \frac{1}{X\xi}\frac{1}{|1-b(X-x_B)/\xi|}, \tag{2.71}$$

and the squared matrix elements are

$$\text{(e)}\quad M^{\mu\nu} = e_q^2 C_F \frac{1}{(l+q)^2}\frac{1}{(j_1-q)^2}\mathrm{Tr}\left[\not{l}\gamma^\sigma(\not{j}_1-\not{q})\gamma^\nu \not{j}_1\gamma^\rho(\not{l}+\not{q})\gamma^\mu\right] d_{\rho\sigma}(j_2,q'), \tag{2.72}$$

$$\text{(f)}\quad M^{\mu\nu} = e_q^2 C_F \frac{1}{(l+q)^2}\frac{1}{(l+q)^2}\mathrm{Tr}\left[\not{l}\gamma^\nu(\not{l}+\not{q})\gamma^\sigma \not{j}_1\gamma^\rho(\not{l}+\not{q})\gamma^\mu\right] d_{\rho\sigma}(j_2,q'). \tag{2.73}$$

Averaging over the transverse photon polarisations in (2.64), we have

$$\varepsilon_\mu(q,T)\,\varepsilon_\nu^*(q,T) \to -\frac{1}{2}g_{\mu\nu}^{\perp}, \tag{2.74}$$

while demanding that the longitudinal polarisation vector is normalised, $[\varepsilon(q,L)]^2 = 1$, and satisfies the Lorentz condition, $q\cdot\varepsilon(q,L)=0$, leads to

$$\varepsilon_\mu(q,L) = \frac{1}{Q}(2x_B p_\mu + q_\mu). \tag{2.75}$$

Gauge invariance ensures that the q_μ term does not contribute to the squared matrix element if all diagrams are included, courtesy of the Ward identity

$$q_\mu M^{\mu\nu} = 0 = q_\nu M^{\mu\nu}. \tag{2.76}$$

Therefore, we are free to neglect the q_μ term of (2.75) from the outset, so that

$$\varepsilon_\mu(q,L)\,\varepsilon_\nu^*(q,L) \to \frac{4x_B^2}{Q^2}p_\mu p_\nu. \tag{2.77}$$

Finally, the contribution to the $\gamma^* p$ cross section from Fig. 2.8 (a), (b), (c), and (d), calculated with the aid of the FORM [68] program, is

$$\sigma_{T,L}^{\gamma^* p} = \sum_q \frac{4\pi^2\alpha_{\mathrm{em}}e_q^2}{Q^2}\int_x^1 \mathrm{d}z \int_0^\infty \frac{\mathrm{d}k_t^2}{k_t^2}\sum_{x=x_\pm}\frac{x_B/x}{1-x_B\beta/x}\frac{\alpha_S(k_t^2)}{2\pi}$$
$$\times\left\{P_{qg}(z)\frac{x}{z}g(\frac{x}{z},\mu^2)\left[C_{T,L}^a + C_{T,L}^b\right] + P_{qq}(z)\frac{x}{z}q(\frac{x}{z},\mu^2)\left[C_{T,L}^c + C_{T,L}^d\right]\right\}, \tag{2.78}$$

while the contribution from diagrams (e) and (f) is

$$\sigma_{T,L}^{\gamma^* p} = \sum_q \frac{4\pi^2\alpha_{\mathrm{em}}e_q^2}{Q^2}\int_{x_B}^1 \mathrm{d}X \int_0^\infty \frac{\mathrm{d}k_t^2}{k_t^2}\frac{x_B}{X}\frac{k_t^2}{Q^2}\sum_{\xi=\xi_\pm}\frac{x_B/\xi}{|1-b(X-x_B)/\xi|}\frac{\alpha_S(k_t^2)}{2\pi}$$
$$\times C_F X q(X,\mu^2)\left[C_{T,L}^e + C_{T,L}^f\right], \tag{2.79}$$

where the coefficients are

$$C_T^a = 1 - \frac{\beta\,(x + 2\,x_B\,z - 4\,x\,z - 2\,x_B\,z^2 + 4\,x\,z^2)}{x\,(1 - 2\,z + 2\,z^2)}, \qquad C_L^a = \frac{8\,\beta(1-\beta)\,x_B\,(1-z)\,z}{x\,(1 - 2\,z + 2\,z^2)},$$

$$C_T^b = A\,(x - 2\,\beta\,x - 2\,\beta\,x_B\,z - 2\,x\,z + 4\,\beta\,x\,z), \qquad C_L^b = 8\,A\,\beta\,(1-\beta)\,x_B\,z,$$

$$C_T^c = 1 - \frac{\beta\,(x + x_B\,z - x\,z - x_B\,z^2 + 2\,x\,z^2)}{x\,(1 + z^2)}, \qquad C_L^c = \frac{4\,\beta(1-\beta)\,x_B\,(1-z)\,z}{x\,(1 + z^2)},$$

$$C_T^d = \frac{-\beta\,x\,z\,(1-z)}{(x - x_B\,z)\,(1 + z^2)}, \qquad C_L^d = 0,$$

$$C_T^e = \frac{-b\,\xi\,(\xi + x_B)}{(X - x_B)\,(X - x_B - \xi)\,(\xi + (1-b)\,x_B)}, \qquad C_L^e = 0,$$

$$C_T^f = \frac{\xi}{(X - x_B)^2}, \qquad C_L^f = 0, \tag{2.80}$$

where

$$A \equiv \frac{\beta\,(1-z)}{(x + x_B\,z - \beta\,x_B\,z - x\,z)(1 - 2\,z + 2\,z^2)}. \tag{2.81}$$

Note that for high E_T jet production in LO QCD there are no infrared singularities from either on-shell propagators or soft gluon emission. We will take the factorisation scale to be $\mu = E_T = k_t$, in order to compare directly with the approach based on DUPDFs. The inclusive jet cross section calculated using (2.78) and (2.79) was found to be in agreement with the LO QCD predictions of the DISENT [70] and JETVIP [71] programs.

At this point it is an interesting check to take the DGLAP limit, so that we insert $\Theta(\mu - k_t)$ and take the limit $k_t \to 0$, so that the only contributions come from the ladder-type diagrams of Fig. 2.8 (a) and (c), and

$$\sigma_T^{\gamma^* p} = \sum_q \frac{4\pi^2 \alpha_{\rm em} e_q^2}{Q^2} \int_x^1 \mathrm{d}z \int_0^{\mu^2} \frac{\mathrm{d}k_t^2}{k_t^2} \frac{\alpha_S(k_t^2)}{2\pi} \left\{ P_{qg}(z)\,\frac{x}{z} g(\frac{x}{z}, \mu^2) + P_{qq}(z)\,\frac{x}{z} q(\frac{x}{z}, \mu^2) \right\}, \tag{2.82}$$

with $x = x_B$ and $\sigma_L^{\gamma^* p} = 0$. At lowest order,

$$F_2(x_B, \mu^2) = \frac{Q^2}{4\pi^2 \alpha_{\rm em}} \left(\sigma_T^{\gamma^* p} + \sigma_L^{\gamma^* p} \right) = \sum_q e_q^2 x\, q(x, \mu^2), \tag{2.83}$$

leading to the well-known logarithmic scaling violation of F_2, or equivalently the 'real' part of the DGLAP equation for the (integrated) quark distribution,

$$\frac{\partial\, q(x, \mu^2)}{\partial \ln \mu^2} = \frac{\alpha_S(\mu^2)}{2\pi} \int_x^1 \frac{\mathrm{d}z}{z} \left\{ P_{qg}(z)\, g(\frac{x}{z}, \mu^2) + P_{qq}(z)\, q(\frac{x}{z}, \mu^2) \right\}, \tag{2.84}$$

where the conventional choice of scale is $\mu = Q$. Of course, for high E_T jet production, it is not appropriate to take the limit $k_t \to 0$.

Let us anticipate how this calculation would be treated in terms of DUPDFs, where we would want to factor out the emission with momentum j_2 in Fig. 2.8 (a) and (c) into the doubly-unintegrated quark distribution, $f_q(x, z, k_t^2, \mu^2)$. For this to be possible, we must assume that $\mathcal{C}_T^a = 1 = \mathcal{C}_T^c$, and neglect all other contributions. The diagrams in Fig. 2.8 (d), (e), and (f) come from the subprocess $\gamma^* q \to qg$, where the gluon is radiated off the final quark line. Such diagrams are strongly suppressed in an axial gluon gauge, due to one or more of the propagators having very large virtualities, and can be neglected. Similarly, for the crossed quark box diagram of Fig. 2.8 (b). Numerically, the terms proportional to β in diagrams (a) and (c) are found to be very small. The one exception is the term proportional to β in $\mathcal{C}_T^c$. This is negative and increasingly important as z increases; that is, it is a destructive interference term. In the case of the doubly-unintegrated quark distribution, the same effect is obtained with an explicit constraint from angular ordering, so the term proportional to β is redundant. We will look at this in more detail in Section 2.4.1.

Ultimately, we will need to resort to explicit numerical comparison of (z, k_t)-factorisation with the conventional collinear factorisation approach in order to demonstrate the approximate equivalence of the two methods.

2.3.2 (z, k_t)-factorisation approach at LO

Within the new (z, k_t)-factorisation framework developed in Section 2.2 the LO diagram is simply $\gamma^* q^* \to q$, illustrated in Fig. 2.1(a), where the incoming quark has momentum $k = x\,p - \beta\,q' + k_\perp$. The partonic cross section contained in (2.23) is

$$\mathrm{d}\hat{\sigma}_{T,L}^{\gamma^* q^*}(x, z, k_t^2, \mu^2) = \mathrm{d}\Phi^{\gamma^* q^*}\, |\mathcal{M}_{T,L}^{\gamma^* q^*}|^2 \,/\, F^{\gamma^* q^*}, \tag{2.85}$$

where $F^{\gamma^* q^*} = 4x\,p \cdot q = 2x\,Q^2/x_B$. Labelling the current jet by

$$P = k + q = (x - x_B)\,p + (1 - \beta)\,q' + k_\perp, \tag{2.86}$$

where $x \geq x_B$, the 1-body phase space is

$$\begin{aligned} \mathrm{d}\Phi^{\gamma^* q^*} &= (2\pi)^4 \delta^{(4)}(k + q - P)\,\frac{\mathrm{d}^4 P}{(2\pi)^3}\,\delta(P^2) \;=\; 2\pi\,\delta(P^2) \\ &= 2\pi\,\frac{x_B}{Q^2} \sum_{i=\pm} \frac{1}{1 - x_B\beta/x}\,\delta(x - x_i), \end{aligned} \tag{2.87}$$

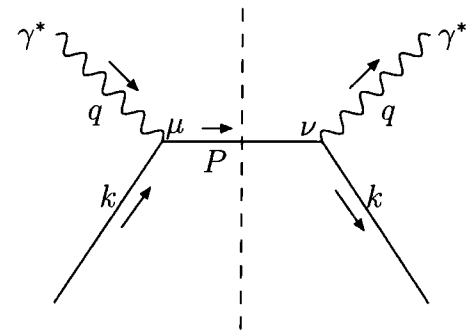

Figure 2.9: Cut diagram contributing at LO in the (z, k_t)-factorisation approach.

where $x_\pm$ is given by (2.62) with $r \equiv k_t^2/Q^2$. Again, the condition $x \geq x_B$ means that only the $x = x_+$ solution contributes. The rapidity of the current jet in the Breit frame is

$$\eta_P^{\text{Breit}} = \frac{1}{2} \ln \frac{P^+}{P^-} = \frac{1}{2} \ln \frac{x/x_B - 1}{1 - \beta}. \tag{2.88}$$

The squared matrix element, given by the cut diagram of Fig. 2.9, is

$$|\mathcal{M}_{T,L}^{\gamma^* q^*}|^2 = \frac{1}{2} e^2 e_q^2 \, \text{Tr}\left[\not{k} \, \gamma^\nu \, (\not{k} + \not{q}) \, \gamma^\mu \right] \, \varepsilon_\mu(q, \lambda) \, \varepsilon_\nu^*(q, \lambda), \tag{2.89}$$

where λ is either T or L. We use the same formulae, (2.74) and (2.77), to sum over the photon polarisations as before.

Note that our approach is not gauge invariant since we do not include the complete set of cut diagrams shown in Fig. 2.8. Rather, we only keep the leading $\mathrm{d}k_t^2/k_t^2$ term coming from Fig. 2.8 (a) and (c). We rely on using a physical gluon gauge where the neglected diagrams are suppressed. We represent this approach by Fig. 2.9, where the incoming quark is off-shell with virtuality $-k_t^2/(1-z)$. Strictly speaking, the Ward identity (2.76) does not apply to Fig. 2.9. To show this we define the trace Tr[...] of (2.89) to be $M^{\mu\nu}$. Then, with $k = x\,p$,

$$q_\mu M^{\mu\nu} = 4Q^2 \left(\frac{x}{x_B} - 1 \right) \neq 0, \tag{2.90}$$

unless $x = x_B$ which is not true for non-zero k_t due to the relation (2.62).

For example, the q_μ term of the longitudinal photon polarisation vector (2.75) gives rise to large cancellations between the contributions from Fig. 2.8 (a) and (b) to ensure that the Ward identity is satisfied. When the diagram of Fig. 2.8(b) is neglected, as in Fig. 2.9, the q_μ term in $\varepsilon_\mu(q, L)$ gives a much too large σ_L. Therefore, we should not include the q_μ term in $\varepsilon_\mu(q, L)$; this is equivalent to an appropriate choice for the photon gauge.

According to the prescription given in Section 2.2 we should only keep the leading

$\mathrm{d}k_t^2/k_t^2$ term in the squared matrix element and so terms explicitly of $\mathcal{O}(k_t^2)$ should be neglected when calculating $|\mathcal{M}_{T,L}^{\gamma^* q^*}|^2$. This amounts to the substitution $k = xp$ in the trace (2.89), leading to

$$|\mathcal{M}_T^{\gamma^* q^*}|^2 = 4\pi\alpha_{\mathrm{em}}\, e_q^2\, Q^2\, \frac{x}{x_B}, \qquad |\mathcal{M}_L^{\gamma^* q}|^2 = 0. \tag{2.91}$$

The partonic cross sections are then

$$\hat{\sigma}_T^{\gamma^* q^*}(x, z, k_t^2, \mu^2) = \frac{4\pi^2\alpha_{\mathrm{em}}}{Q^2}\frac{x_B}{1 - x_B\beta/x}\,\delta(x - x_+)e_q^2, \qquad \hat{\sigma}_L^{\gamma^* q^*}(x, z, k_t^2, \mu^2) = 0. \tag{2.92}$$

Inserting into (2.23) we obtain the hadronic cross sections

$$\sigma_T^{\gamma^* p} = \frac{4\pi^2\alpha_{\mathrm{em}}}{Q^2}\int_x^1 \mathrm{d}z \int_0^\infty \frac{\mathrm{d}k_t^2}{k_t^2}\,\frac{x_B/x}{1 - x_B\beta/x}\sum_q e_q^2 f_q(x, z, k_t^2, \mu^2), \qquad \sigma_L^{\gamma^* p} = 0, \tag{2.93}$$

with $x = x_+$. Again, it is an interesting check to take the collinear limit, $k_t \to 0$, so that we insert $\Theta(\mu - k_t)$ and take $\mu = Q$. Then, $x \to x_B$, $\beta \to 0$, and by the normalisation condition (2.19) we recover the parton model prediction for the proton structure function $F_2 = F_T + F_L$:

$$F_2(x_B, Q^2) = \frac{Q^2}{4\pi^2\alpha_{\mathrm{em}}}(\sigma_T^{\gamma^* p} + \sigma_L^{\gamma^* p}) = \sum_q e_q^2\, x_B\, q(x_B, Q^2). \tag{2.94}$$

Alternatively, taking the limit $z \to 0$ of x and β in (2.93), then using the normalisation (2.18), gives

$$F_2(x_B, \mu^2) = \int_0^\infty \frac{\mathrm{d}k_t^2}{k_t^2}\,\frac{x_B}{x}\sum_q e_q^2 f_q(x, k_t^2, \mu^2), \tag{2.95}$$

with $x = x_B(1 + k_t^2/Q^2)$.

2.3.3 Towards a NLO (z, k_t)-factorisation approach

It is beyond the scope of this work to perform a full NLO calculation within the framework of (z, k_t)-factorisation. Rather, at this exploratory stage, we aim to produce a simplified description using the LO DUPDFs and computing only the $\mathcal{O}(\alpha_S)$ diagrams expected to be dominant. The major loop corrections are already accounted for by the Sudakov form factor (2.2). The diagram where a gluon is radiated from the final quark line is strongly suppressed in a physical gauge. This leaves the cut diagrams of Fig. 2.10 as the only contributions which should be

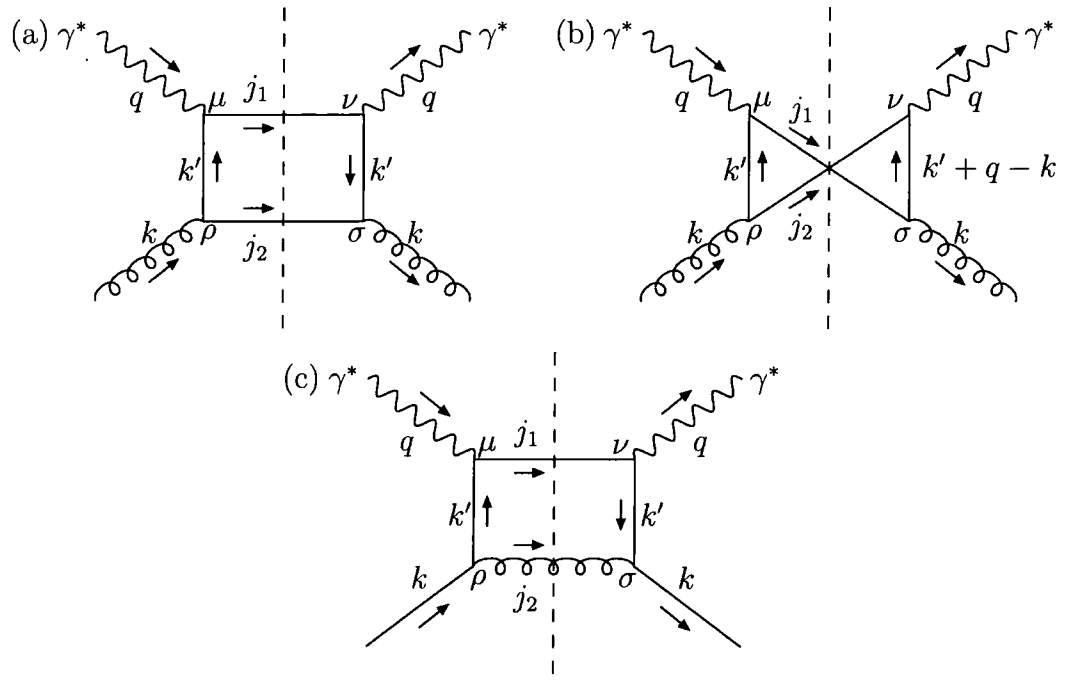

Figure 2.10: Cut diagrams contributing at 'NLO' in the (z, k_t)-factorisation approach.

included. It is debatable whether or not the crossed box diagram of Fig. 2.10(b) should be included. We choose to include it, although it gives only a relatively small contribution to the cross section.

All diagrams in Fig. 2.10 have the same kinematics. An initial parton, with momentum $k = x\,p - \beta\,q' + k_\perp$, splits to a quark with momentum $k' = x'\,p - \beta'\,q' + k'_\perp$, which goes on to interact with the photon. The outgoing partons have momentum $j_1 = k' + q$ and $j_2 = k - k'$ where $x_B \leq x' \leq x \leq 1$ and $0 \leq \beta \leq \beta' \leq 1$. Note that the diagrams of Fig. 2.10 naturally include the LO contribution of Fig. 2.9 in the limit that $k_t \ll k'_t$. Therefore, the LO contribution does not have to be added in explicitly.

The KTJET package [74], together with the CLHEP package [75], were used to cluster the three outgoing partons into jets. The jet algorithm was run in the inclusive mode, in the ΔR scheme and E_T recombination scheme, in order to mirror the analyses of the experimental data considered in Section 2.4. It is necessary to pass the algorithm the complete 4-vectors of the outgoing partons with momenta

$$j_1 = (x' - x_B)\,p + (1 - \beta')\,q' + k'_\perp = \begin{pmatrix} \frac{Q}{2}\left[x'/x_B - \beta'\right] \\ k'_t \cos(\phi_{k'x}) \\ k'_t \sin(\phi_{k'x}) \\ \frac{Q}{2}\left[x'/x_B - 2 + \beta'\right] \end{pmatrix}, \qquad (2.96)$$

$$j_2 = (x - x')\,p + (\beta' - \beta)\,q' + k_\perp - k'_\perp = \begin{pmatrix} \frac{Q}{2}\left[(x - x')/x_B + \beta' - \beta\right] \\ \left|\boldsymbol{k_t} - \boldsymbol{k'_t}\right| \cos(\phi_{kk'x}) \\ \left|\boldsymbol{k_t} - \boldsymbol{k'_t}\right| \sin(\phi_{kk'x}) \\ \frac{Q}{2}\left[(x - x')/x_B - \beta' + \beta\right] \end{pmatrix}, \tag{2.97}$$

$$p_n = \frac{x}{z}(1 - z)\,p + \beta\,q' - k_\perp = \begin{pmatrix} \frac{Q}{2}\left[\frac{x}{z}(1 - z)/x_B + \beta\right] \\ -k_t \cos(\phi_{kx}) \\ -k_t \sin(\phi_{kx}) \\ \frac{Q}{2}\left[\frac{x}{z}(1 - z)/x_B - \beta\right] \end{pmatrix}, \tag{2.98}$$

where $\phi_{k'x}$ is the angle between $\boldsymbol{k'_t}$ and the x axis, $\phi_{kk'x}$ is the angle between $(\boldsymbol{k_t} - \boldsymbol{k'_t})$ and the x axis, and ϕ_{kx} is the angle between $\boldsymbol{k_t}$ and the x axis. Together with $\phi_{kk'}$, the angle between $\boldsymbol{k_t}$ and $\boldsymbol{k'_t}$, only two of these angles are independent. These are chosen to be $\phi_{kk'}$ and ϕ_{kx}, which are averaged over by introducing two additional integrations into (2.58):

$$\int_0^{2\pi} \frac{\mathrm{d}\phi_{kk'}}{2\pi} \int_0^{2\pi} \frac{\mathrm{d}\phi_{kx}}{2\pi}. \tag{2.99}$$

The other two angles are given by

$$\phi_{k'x} = \phi_{kx} + \phi_{kk'}, \qquad \phi_{kk'x} = \phi_{kx} + \cos^{-1}\left(\frac{k_t - k'_t \cos(\phi_{kk'})}{\left|\boldsymbol{k_t} - \boldsymbol{k'_t}\right|}\right). \tag{2.100}$$

We find that the 2-body phase space divided by the flux factor is given by

$$\frac{\mathrm{d}\Phi^{\gamma^* a}}{F^{\gamma^* a}} = \frac{\mathrm{d}k_t'^2}{16\pi x}\left(\frac{x_B}{Q^2}\right)^2 \sum_{x'=x'_\pm} \left|x - x_B\beta - (1 - \beta)x' - (x - x_B)\beta'\right|^{-1}, \tag{2.101}$$

where $\beta' = \beta + (x_B R)/(x - x')$, and

$$x'_\pm = \frac{1}{2(1 - \beta)}\Big\{x(1 - \beta) + x_B(1 - \beta - R) + x_B r' \\ \pm\sqrt{\left[x_B(1 - \beta + R) - x(1 - \beta)\right]^2 + x_B r'\left[x_B r' - 2\left(x(1 - \beta) - x_B(1 - \beta - R)\right)\right]}\Big\},$$

with $r' \equiv k_t'^2/Q^2$ and $R \equiv \left|\boldsymbol{k_t} - \boldsymbol{k'_t}\right|^2/Q^2$.

The cut diagrams representing the squared matrix elements are shown in Fig. 2.10. Again, we write

$$\left|\mathcal{M}^{\gamma^* a}_{T,L}\right|^2 = \frac{1}{2} e^2 g^2 M^{\mu\nu}\, \varepsilon_\mu(q, \lambda)\varepsilon^*_\nu(q, \lambda), \tag{2.102}$$

where λ is either T or L and the initial factor of $1/2$ is to average over the helicity of the incoming parton. We take $e^2 = 4\pi\alpha(Q^2)$ and $g^2 = 4\pi\alpha_S(\mu_R^2)$, with $\mu_R =$

$\max(k_t, k_t')$. We have

$$\text{(a)}\quad M^{\mu\nu} = \left(\sum_q e_q^2\right) T_R \frac{1}{k'^4} \mathrm{Tr}\left[\not{k}'\gamma^\rho \not{j}_2 \gamma^\sigma \not{k}'\gamma^\nu \not{j}_1 \gamma^\mu\right] d_{\rho\sigma}(k, q'), \tag{2.103}$$

$$\text{(b)}\quad M^{\mu\nu} = \left(\sum_q e_q^2\right) T_R \frac{1}{k'^2} \frac{1}{(k'+q-k)^2} \mathrm{Tr}\left[\not{k}'\gamma^\rho \not{j}_2 \gamma^\nu (\not{k}' + \not{q} - \not{k})\gamma^\sigma \not{j}_1 \gamma^\mu\right] d_{\rho\sigma}(k, q'), \tag{2.104}$$

$$\text{(c)}\quad M^{\mu\nu} = e_q^2 C_F \frac{1}{k'^4} \mathrm{Tr}\left[\not{k}'\gamma^\rho \not{k}\gamma^\sigma \not{k}'\gamma^\nu \not{j}_1 \gamma^\mu\right] d_{\rho\sigma}(j_2, q'). \tag{2.105}$$

In order to keep only the leading $\mathrm{d}k_t^2/k_t^2$ term, we make the replacement $k \to x\,p$ in the numerator of these expressions, but not in the virtualities in the denominator. Inserting the partonic cross sections into (2.23) we finally obtain

$$\begin{aligned}\sigma_{T,L}^{\gamma^* p} = \sum_q \frac{4\pi^2 \alpha_{\mathrm{em}}\, e_q^2}{Q^2} \left(\frac{x_B}{Q^2}\right) \int_0^1 \mathrm{d}x \int_x^1 \mathrm{d}z \int_0^\infty \frac{\mathrm{d}k_t^2}{k_t^2} \int_0^\infty \mathrm{d}k_t'^2\, \frac{x_B}{x}\, \frac{\alpha_S(\mu_R^2)}{2\pi} \\ \times \sum_{x'=x'_\pm} |x - x_B\beta - (1-\beta)x' - (x - x_B)\beta'|^{-1} \\ \times \left\{T_R\, f_g(x, z, k_t^2, \mu^2)\, \left[C_{T,L}^a + C_{T,L}^b\right] + C_F\, f_q(x, z, k_t^2, \mu^2)\, C_{T,L}^c\right\},\end{aligned} \tag{2.106}$$

where the coefficients are

$$\begin{aligned}C_T^a &= \frac{(1 - 2\beta'\,(1-\beta'))\; x\; (x' - x_B) + (\beta'\,(x_B - 2\,x') + x')\; ((1-\beta')\; x_B + (2\,\beta' - 1)\; x')}{x\,((1-\beta')\; x_B - x')^2}, \\ C_L^a &= \frac{4\;(1-\beta')\;\beta'\, x_B\;(x' - x_B + \beta'\;(x + x_B - 2\,x'))}{x\,((1-\beta')\; x_B - x')^2}, \\ C_T^b &= \frac{(1-\beta')\;(x' - x_B)\;((1 - 2\,\beta')\; x + 2\;(\beta'\;(2\,x' - x_B) - x'))}{x\;(x' - (1-\beta')\; x_B)\;((1 + \beta - \beta')\;(x - x') + (1 + \beta - \beta' + R)\; x_B)}, \\ C_L^b &= \frac{8\,(1-\beta')^2\,\beta'\, x_B\;(x' - x_B)}{x\;(x' - (1-\beta')\; x_B)\;((1 + \beta - \beta')\;(x - x') + (1 + \beta - \beta' + R)\; x_B)}, \\ C_T^c &= \frac{(1 - 2\,\beta'\,(1-\beta'))\; x\;(x' - x_B) + x'\;\left((2\,\beta' - 1)\; x_B + \left(1 - 2\,\beta'^2\right)\; x'\right)}{(x - x')\;((1-\beta')\; x_B - x')^2}, \\ C_L^c &= \frac{4\;(1-\beta')\;\beta'^2\, x_B}{((1-\beta')\; x_B - x')^2}.\end{aligned} \tag{2.107}$$

Inspection of the coefficient C_T^c reveals a pole at $z' \equiv x'/x = 1$, corresponding to soft gluon emission. We can regulate this singularity by appealing to angular ordering.

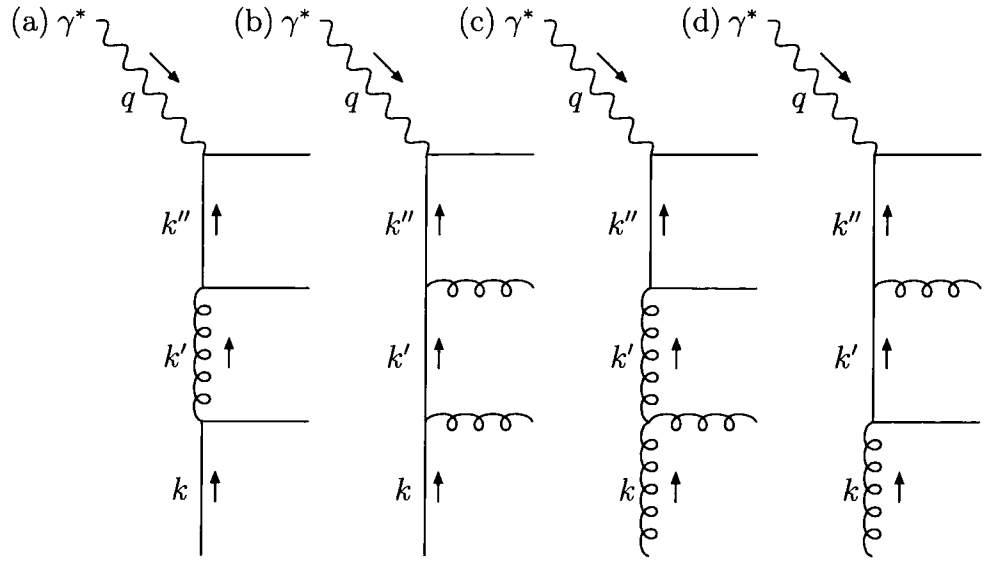

Figure 2.11: Feynman diagrams contributing at 'NNLO' in the (z, k_t)-factorisation approach.

The rapidity of the gluon, with momentum j_2, should be greater than the rapidity of the quark, with momentum j_1:

$$\eta_{j_2}^{\text{Breit}} > \eta_{j_1}^{\text{Breit}} \quad \Longleftrightarrow \quad z' < \frac{\mu'}{\mu' + |\boldsymbol{k_t} - \boldsymbol{k_t'}|}, \qquad \text{with} \qquad \mu' \equiv Q\frac{x'}{x_B}\sqrt{\frac{1-\beta'}{x'/x_B - 1}}. \tag{2.108}$$

This condition applies only to the diagram where a quark radiates a gluon, Fig. 2.10(c), and not to the diagrams where a gluon radiates a quark, Fig. 2.10 (a) and (b).

2.3.4 An estimate of the NNLO contribution

The NNLO diagrams have not yet been calculated in the collinear approximation (NNLO QCD). As we will explain in Section 2.4, the 'NLO' calculation of Section 2.3.3 gives reasonable agreement with conventional NLO QCD. It is possible that a simplified 'NNLO' (z, k_t)-factorisation calculation may provide an estimate of whether the NNLO QCD corrections are likely to be important, especially at low E_T and low Q^2 in the forward region, where there is a discrepancy between NLO QCD and the data.

The four contributing diagrams, all of which have the same kinematics (phase space), are shown in Fig. 2.11. Diagrams (a) and (b) are the doubly-unintegrated quark contribution, while diagrams (c) and (d) are the doubly-unintegrated gluon contribution. Encouraged by the fact that the crossed quark box of Fig. 2.10(b) gives only a small contribution, we may neglect the interference cut graphs arising

from Fig. 2.11 as a first approximation, leaving only four squared matrix elements to be calculated.

This simplified approach provides an approximation of QCD, in which only ladder-type diagrams remain. The soft gluon singularities are regulated by angular ordering. There are no infrared singularities remaining. We can add an arbitrary number of rungs to the ladder and the answer will be finite. However, with more rungs, the number of neglected interference terms grows; it is likely that the approximate treatment of these terms by imposing angular-ordering constraints will spoil the accuracy of the method if too many rungs are added.

2.4 Description of HERA inclusive jet production data

Data are available for inclusive jet production in DIS measured at the HERA collider. We may therefore check how well the simpler (z, k_t)-factorisation approach is able to reproduce the conventional collinear factorisation approach, and at the same time see how well these calculations describe the data.

Recall from Section 2.3 that at LO the (z, k_t)-factorisation approach is based on the simple $\gamma^* q^* \to q$ subprocess driven by the doubly-unintegrated quark distribution, $f_q(x, z, k_t^2, \mu^2)$, retaining the full kinematics. On the other hand, in the LO QCD description the subprocesses are $\gamma^* g \to q\bar{q}$ and $\gamma^* q \to gq$ evaluated with collinear kinematics and conventional integrated PDFs, $g(x, Q^2)$ and $q(x, Q^2)$.

A computer program was written to calculate the conventional LO QCD prediction and the LO and 'NLO' predictions of the new (z, k_t)-factorisation approach. The GNU Scientific Library [76] implementation of the VEGAS algorithm [77] was used to perform multidimensional Monte Carlo integration.

2.4.1 Comparison with ZEUS data at high Q^2

We now compare our predictions to the experimental data obtained by the ZEUS Collaboration [78]. This data was taken during 1996 and 1997, when HERA collided protons of energy $E_p = 820$ GeV with positrons of energy $E_e = 27.5$ GeV at a CM energy of $\sqrt{s} = \sqrt{4E_pE_e} \simeq 300$ GeV. Rather than make cuts on the variable $y = Q^2/(x_B s)$, ZEUS make cuts on $\cos\gamma$, one of the angles used in reconstructing the kinematical variables using the double-angle-method, where

$$\cos\gamma = \frac{x_B(1-y)E_p - yE_e}{x_B(1-y)E_p + yE_e}. \tag{2.109}$$

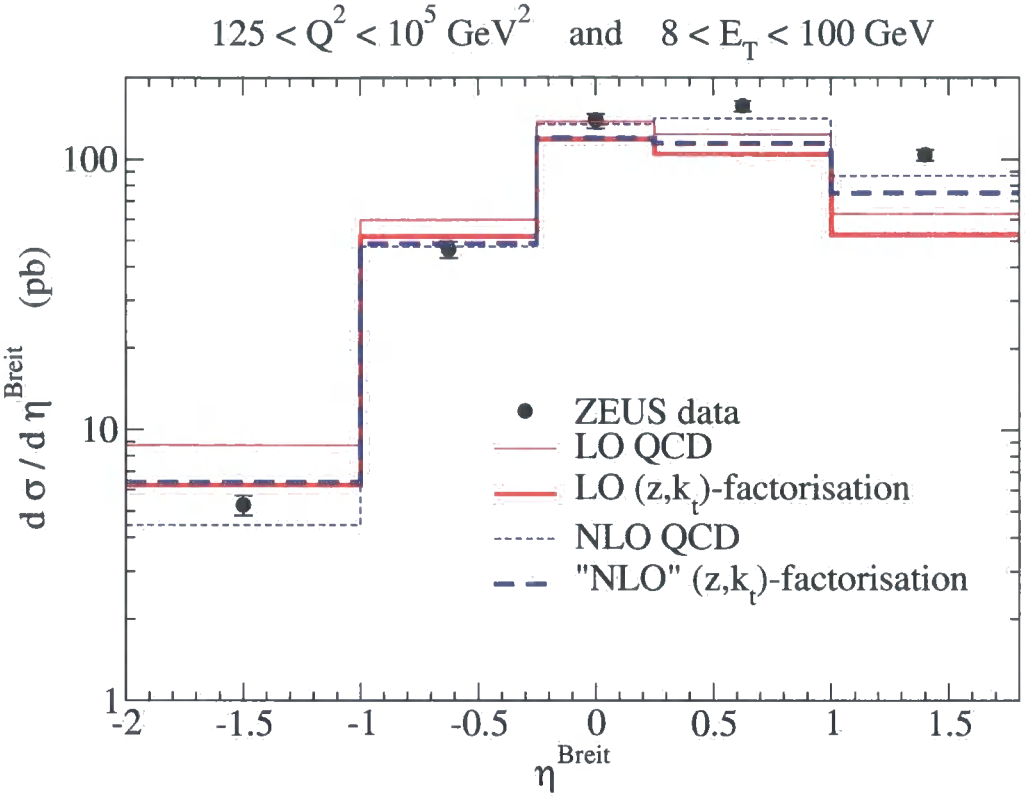

Figure 2.12: Comparison with ZEUS inclusive jet production data [78] at high Q^2. The feint and bold lines correspond, respectively, to the predictions of the conventional QCD approach and the (z, k_t)-factorisation approach based on DUPDFs.

In the parton model, $\gamma^* q \to q$, the angle γ corresponds to the direction of the scattered quark. In (2.58) we therefore set $y_{\min} = 0$ and $y_{\max} = 1$ and demand instead that $\cos\gamma$ satisfies the ZEUS experimental cuts, $-0.7 < \cos\gamma < 0.5$.

In Fig. 2.12 we show the rapidity distribution, $\mathrm{d}\sigma/\mathrm{d}\eta^{\mathrm{Breit}}$, integrated over Q^2 from 125 to 10^5 GeV^2 and over E_T from 8 to 100 GeV. The parton-to-hadron correction factors given in Table 3 of the ZEUS paper [78] have been applied to the theory predictions. For the results presented, we used MRST2001 LO PDFs [66] as input. The NLO QCD predictions have been taken from the plot in Fig. 3b) of [78]; these were obtained with the DISENT program [70] using MRST99 PDFs [67], a renormalisation scale of E_T, and a factorisation scale of Q. The statistical, systematic and jet-energy-scale uncertainties have been added in quadrature to estimate the total experimental uncertainty. All the theory predictions give a reasonably good description of the data. The NLO predictions generally give a slightly better description than the LO predictions. For the (z, k_t)-factorisation approach, the 'NLO' corrections are only significant in the forward region.

Note from Fig. 2.12 that the LO (z, k_t)-factorisation predictions are slightly larger than the data in the current jet (negative rapidity) region. One possible explanation for this is provided by a colour coherence phenomenon known as the 'drag effect' (see, for example, [11]), a consequence of which is that the current jet is pulled towards the proton direction. A constant 1 GeV shift in the z component of the current jet momentum is found to shift the rapidity distribution to obtain slightly better agreement with the experimental data.

To test the assertion that the angular-ordering constraint mimics the major neglected terms in the LO QCD calculation of Section 2.3.1, we can replace $P_{qg}(z)$ by $P_{qg}(z)\,(\mathcal{C}^a + \mathcal{C}^b)$ and $P_{qq}(z)$ by $P_{qq}(z)\,\mathcal{C}^c$ in the real part of the doubly-unintegrated quark (2.21), where the coefficients $\mathcal{C}$ were given in (2.80). The inclusive jet cross section calculated in this manner, with separate coefficients for the T and L contributions, is found to be almost unchanged, as seen in Fig. 2.13, providing evidence that the 'beyond LLA' terms in the conventional LO QCD calculation have much the same effect as an explicit angular-ordering constraint.

In order to verify that the extra z convolution of (z, k_t)-factorisation with respect to k_t-factorisation is important, we also repeated the calculation taking the limit $z \to 0$ in the partonic cross section. The parton emitted in the last evolution step then goes in the proton direction and is not counted in the inclusive jet cross section. In general, the predictions are much worse, even in the current jet region, providing evidence that the extra z convolution of our method is important.

2.4.2 Comparison with H1 data at low Q^2

The H1 Collaboration have measured the inclusive jet cross section in DIS at high Q^2 [79] and at low Q^2 [80]. Here, we focus on the latter, where $Q^2 = 5$ to 100 GeV^2. In this region, the NLO QCD corrections to LO QCD are larger than at high Q^2, and the advantages of our approach become more apparent. Again, this data was taken during 1996 and 1997.

The H1 Collaboration use the electron method to reconstruct the kinematical variables, so cuts are imposed directly on the variable y, namely $0.2 < y < 0.6$. We therefore set $y_{\min} = 0.2$ and $y_{\max} = 0.6$ in (2.58). Also, H1 present their data in rapidity bins in the LAB frame rather than the Breit frame, so we need to be able to calculate the rapidity in the LAB frame.

In the Breit frame, we write the momenta of the incoming and outgoing positron as $e = a_e\, p + b_e\, q' + e_\perp$ and $e' = e - q$ respectively. The on-shell conditions $e^2 = 0 = e'^2$ imply that $e_t^2 = a_e b_e Q^2/x_B$ and $e \cdot q = -Q^2/2$. In the LAB frame, we write the initial proton and positron momenta as $p^{\text{LAB}} = (E_p, 0, 0, E_p)$ and $e^{\text{LAB}} = (E_e, 0, 0, -E_e)$,

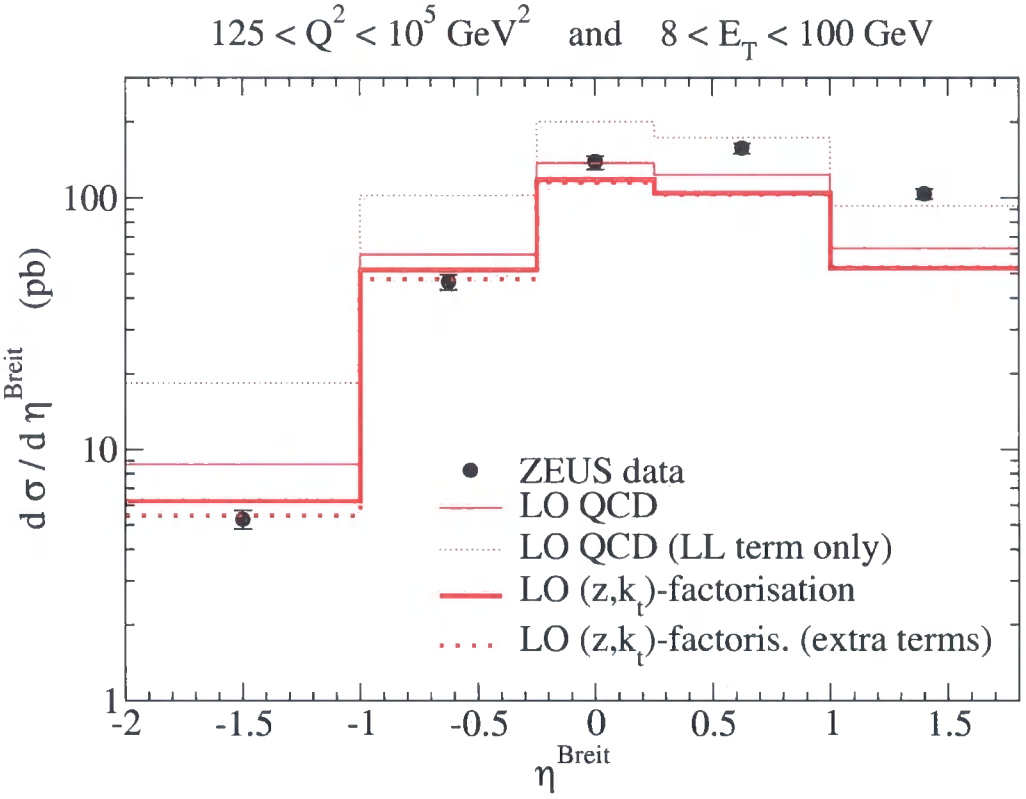

Figure 2.13: Effect of including additional terms beyond the leading logarithmic dk_t^2/k_t^2 term. Without an explicit angular-ordering constraint, as in LO QCD, the extra terms have a large effect, as seen by the difference between the dotted and solid feint lines. With an explicit angular-ordering constraint, as in LO (z, k_t)-factorisation, the extra terms have little effect, as seen by the difference between the solid and dotted bold lines.

where $E_p = 820$ GeV, $E_e = 27.5$ GeV, and $p^{\text{LAB}} \cdot e^{\text{LAB}} = 2E_pE_e = p \cdot e$. Taking dot products of e with p and q' determines b_e and a_e respectively:

$$b_e = 4E_pE_e\frac{x_B}{Q^2}, \qquad a_e = x_B(b_e - 1), \tag{2.110}$$

so

$$e_t^2 = 4E_pE_ex_B\left(4E_pE_e\frac{x_B}{Q^2} - 1\right). \tag{2.111}$$

The momentum of an outgoing parton can be written $j = a_j\,p + b_j\,q' + j_\perp$ and $j^{\text{LAB}} = a_j^{\text{LAB}}\,p^{\text{LAB}} + b_j^{\text{LAB}}\,e^{\text{LAB}} + j_\perp^{\text{LAB}}$ in the Breit and LAB frames respectively. We have

$$\begin{aligned} e \cdot j &= (a_eb_j + b_ea_j)\,p \cdot q' + e_\perp \cdot j_\perp \\ &= [b_e(a_j + b_jx_B) - x_Bb_j]\,p \cdot q' - \boldsymbol{e_t} \cdot \boldsymbol{j_t} \\ &= \left[4E_pE_e\frac{x_B}{Q^2}(a_j + x_Bb_j) - x_Bb_j\right]p \cdot q' - e_tj_t\cos\phi_{ej}, \end{aligned} \tag{2.112}$$

where ϕ_{ej} is the angle between $\boldsymbol{e_t}$ and $\boldsymbol{j_t}$. Taking dot products of j^{LAB} with p^{LAB} and e^{LAB} determines a_j^{LAB} and b_j^{LAB} in terms of $e \cdot j$ and $p \cdot j$:

$$a_j^{\text{LAB}} = \frac{e \cdot j}{p \cdot e}, \qquad b_j^{\text{LAB}} = \frac{p \cdot j}{p \cdot e} = b_j\frac{p \cdot q'}{p \cdot e}. \tag{2.113}$$

The rapidity in the LAB frame is then

$$\begin{aligned} \eta_j^{\text{LAB}} &= \frac{1}{2}\ln\left(\frac{a_j^{\text{LAB}}}{b_j^{\text{LAB}}}\frac{E_p}{E_e}\right) = \frac{1}{2}\ln\left(\frac{e \cdot j}{b_j\,p \cdot q'}\frac{E_p}{E_e}\right) \\ &= \frac{1}{2}\ln\left[\left(4E_pE_e\frac{x_B}{Q^2}\left(\frac{a_j}{b_j} + x_B\right) - x_B - \frac{2x_B}{b_jQ^2}e_tj_t\cos\phi_{ej}\right)\frac{E_p}{E_e}\right]. \end{aligned} \tag{2.114}$$

It is necessary to average the cross section over the azimuthal angle ϕ_{ej} between the initial positron and the outgoing jet in the transverse plane. For the 'NLO' (z, k_t)-factorisation calculation, the jet momenta are not necessarily the same as the momenta of the outgoing partons. It is necessary to pass the momenta through a jet algorithm. Rather than use (2.114) to determine η^{LAB}, which would require an additional azimuthal averaging, it is simpler to explicitly transform the momenta from the Breit to the LAB frame, then to calculate the rapidities of the resultant momenta. This is done by first boosting along the z axis to transform the momenta from the Breit frame to the γ^*p CM frame. The momenta are then transformed from the γ^*p CM frame to the LAB frame using the method described in Section 6.2 of [62], which involves boosts along the z and x axes followed by rotations about the y and z axes. The final rotation about the z-axis does not change the rapidity

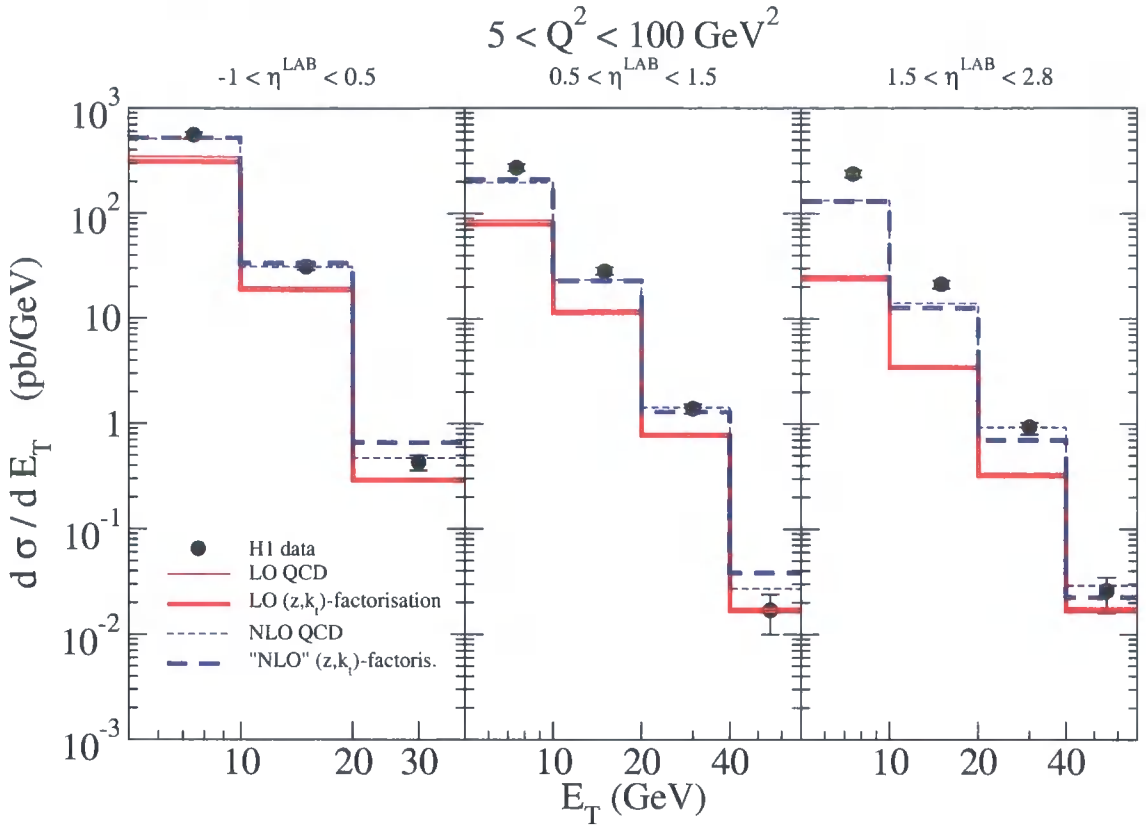

Figure 2.14: Comparison with H1 inclusive jet production data [80] at low Q^2. The predictions of the (z, k_t)-factorisation approach based on DUPDFs (which is much simpler to implement) are in good agreement with the conventional QCD approach. In some bins the predictions of the latter approach are hidden beneath the bold lines of the (z, k_t)-factorisation approach, at the respective order.

or the transverse energy and may be omitted. It was checked numerically that this method is equivalent to the method of (2.114).

In Fig. 2.14 we show $\mathrm{d}\sigma/\mathrm{d}E_T$ integrated over Q^2 between 5 and 100 GeV^2 in three rapidity intervals. For the results presented, we used the MRST2001 LO PDFs [66] as input. The NLO QCD predictions have been taken from the plot in Fig. 1 of the H1 paper [80]; these were obtained with the `DISENT` program [70] using CTEQ5M PDFs [81], a renormalisation scale of E_T and a factorisation scale of Q. The hadronisation correction factors used in [80] have been applied to all the theory predictions. The statistical and systematic uncertainties have been added in quadrature to estimate the total experimental uncertainty.

The LO (z, k_t)-factorisation calculation is in excellent agreement with conventional LO QCD, but neither describe the data well, especially in the forward rapidity region. The 'NLO' (z, k_t)-factorisation calculation is in very good agreement with conventional NLO QCD, although the agreement gets slightly worse as E_T

increases.[4] Deviations of the data from NLO QCD are seen only at small E_T in the forward region. Here, the NLO corrections are quite large and it is likely that NNLO corrections or resolved virtual photon contributions are important in this region. Again, taking the limit $z \to 0$ makes the (z, k_t)-factorisation predictions much worse, showing that it is important to keep the precise kinematics.

2.5 Summary

In this chapter, we have presented a method for determining UPDFs, $f_a(x, k_t^2, \mu^2)$, from the conventional (integrated) PDFs, by considering the last DGLAP evolution step separately, and imposing angular-ordering constraints on gluon emission. To include the precise kinematics in the hard subprocess initiated by the final parton in the evolution ladder, it is necessary to consider DUPDFs, $f_a(x, z, k_t^2, \mu^2)$. We gave a prescription, called (z, k_t)-factorisation, for the computation of cross sections using these distributions. This prescription is a natural generalisation of the k_t-factorisation approach.

We used (z, k_t)-factorisation to estimate the cross section for inclusive jet production at HERA at lowest order. Using the same LO DUPDFs, we then carried out a 'NLO' calculation which included the dominant Feynman diagrams with the soft gluon singularities being regulated by angular ordering.

We showed that at $\mathcal{O}(\alpha_S^0)$ the predictions of the approach based on DUPDFs, with exact kinematics, are close to the conventional LO QCD calculation at $\mathcal{O}(\alpha_S)$. The relative simplicity of the former approach is shown schematically in Fig. 2.1. Similarly, at $\mathcal{O}(\alpha_S)$ the predictions of the approach based on DUPDFs are close to the conventional NLO QCD calculation at $\mathcal{O}(\alpha_S^2)$.

It was seen that the NLO corrections are large in the forward region at low E_T and low Q^2 where the agreement with the data is poor. It is possible that the simplified (z, k_t)-factorisation approach might help to evaluate the rôle of the conventional NNLO QCD calculation. Alternatively, the resolved photon contribution is known to be important in the regime where E_T is much greater than Q. It would be better to calculate the resolved photon contribution in terms of the DUPDFs of the photon.[5]

By reorganising the perturbative expansion in α_S to keep only the most impor-

[4] In two bins the 'NLO' (z, k_t)-factorisation predictions are significantly higher than the NLO QCD predictions. This is due to the jet algorithm applied, which increases the 'NLO' (z, k_t)-factorisation predictions by more than a factor of two in these two bins only, compared to the result when no jet algorithm is applied.

[5] In Ref. [82], for example, the KMR prescription was applied to obtain the unintegrated gluon distribution of the photon.

tant terms, our method provides a simple but effective way of estimating exclusive (and inclusive) observables.

The logical next step is to show that DUPDFs can be applied to pp and $p\bar{p}$ collisions. The simplest calculation is the transverse momentum distributions of produced W and Z bosons. We will carry out this calculation in the next chapter.

Chapter 3

Unintegrated parton distributions and electroweak boson production at hadron colliders

At present, it is not straightforward to describe the transverse momentum (P_T) distributions of electroweak bosons produced in hadron-hadron collisions. In the usual collinear approximation, the transverse momentum of the incoming partons is neglected and so, for the Born level subprocesses $q_1\, q_2 \rightarrow V$ (where $V = \gamma^*, W, Z$) or $g_1\, g_2 \rightarrow H$, the transverse momentum of the final electroweak boson is zero. Therefore, initial-state QCD radiation is necessary to generate the P_T distributions. Both the LO and NLO differential cross sections diverge for $P_T \ll M_{V,H}$, with terms proportional to $\ln(M_{V,H}/P_T)$ appearing due to soft and collinear gluon emission, requiring resummation to achieve a finite P_T distribution.

Traditional calculations combine fixed-order perturbation theory at high P_T with either analytic resummation or numerical parton shower formalisms at low P_T, with some matching criterion to decide when to switch between the two. In addition, a parameterisation is needed to account for non-perturbative effects at the lowest P_T values. Analytic resummation can be performed either in the transverse momentum space (see, for example, [83]) or in the Fourier conjugate impact parameter space (see, for example, [84]).

An alternate description is provided in terms of UPDFs, where each incoming parton carries its own transverse momentum k_t, so that the subprocesses $q_1\, q_2 \rightarrow V$ and $g_1\, g_2 \rightarrow H$ already generate the LO P_T distributions in the k_t-factorisation approach. It has been shown in [85, 86] that UPDFs obtained from an approximate solution of the CCFM evolution equation embody the conventional soft gluon resummation formulae.

The UPDFs that we use are obtained from the familiar DGLAP-evolved PDFs determined from a global parton analysis of deep-inelastic and related hard-scattering data. The transverse momentum of the parton is generated entirely in the *last* evolution step [60–63]. Angular-ordering constraints are imposed which regulate the singularities arising from soft gluon emission, while the virtual terms in the DGLAP equation are resummed into Sudakov form factors. In Chapter 2 it was shown that it is necessary to extend the 'last-step' formalism of [61] to consider DUPDFs in order to preserve the exact kinematics. It was demonstrated that the main features of conventional higher order calculations can be accounted for within a much simpler theoretical framework, named (z, k_t)-factorisation.[1]

Strictly speaking, the integrated PDFs used as input to the last evolution step should themselves be determined from a new global fit to data using the (z, k_t)-factorisation approach. For the present work, we take the input PDFs from a global fit to data using the conventional collinear approximation [66]. This treatment is adequate for these initial investigations. However, we expect it to lower our predictions for quark-initiated processes by $\sim$10% compared to the case where the input PDFs are determined from a global fit using the (z, k_t)-factorisation approach. We will illustrate this point in Section 3.4 by comparing predictions for the proton structure function F_2 in the collinear approximation and in the (z, k_t)-factorisation formalism.

The 'last-step' prescription has some features in common with the initial-state parton shower algorithms implemented in Monte Carlo event generators (for a recent review, see [87]) such as the DGLAP-based HERWIG [36] and PYTHIA [37] programs and the CCFM-based CASCADE [56] program. The main advantage of our approach is that we use simple analytic formulae which implement the crucial physics in a transparent way, without the additional details or tuning which are frequently introduced in Monte Carlo programs. The P_T distributions are generated entirely from known and universal DUPDFs. For example, fits to Z production data at the Tevatron using parton showers favour a large intrinsic partonic transverse momentum $\langle k_t \rangle \approx 2$ GeV, while confinement of partons inside the proton would imply a $\langle k_t \rangle \approx 0.3$ GeV [88–90].

The DGLAP-based parton showers used in [36, 37] are theoretically justified only in the limit of strongly-ordered transverse momenta, since only the collinear divergent part of the squared matrix element is kept in each parton branching. Similarly, the CCFM-based parton shower used in [56] is strictly justified only in

[1]The idea is an extension of the original DDT formula [21]; however, in comparison with [21] we go beyond the double leading logarithmic approximation (DLLA) and account for the precise kinematics of the two incoming partons, as well as the angular ordering of emitted gluons.

the limit of strongly-ordered angles, which reduces to the limit of strongly-ordered transverse momenta as long as x is not too small. In this limit, the transverse momentum generated in all evolution steps prior to the last is negligible. Therefore, neglecting transverse momentum in every evolution step prior to the last should be a good approximation to the parton shower algorithms in which finite transverse momentum is generated at *every* evolution step.

The goal of the present chapter is to demonstrate that the P_T distributions of electroweak bosons can be successfully generated by DUPDFs. We do not aim to produce a *better* description of the data than existing calculations, but rather a *simpler* analytic description which reproduces the main features. With this approach, it is easy to see the physical origin of the P_T distributions and to identify the most important Feynman diagrams. Since the DUPDFs are universal—that is, they apply equally well to all hard hadronic processes—it is important to check them in a new kinematic domain.

One topical application is the prediction of the cross section for diffractive Higgs boson production at the LHC [91], which is driven by the unintegrated[2] gluon distribution $f_g(x, k_t^2, \mu^2)$, where μ is the hard scale of the subprocess. At the moment, the only possibility to check the behaviour of UPDFs in the domain $k_t \ll \mu$ is to compare predictions with the observed P_T distributions of W and Z bosons produced at the Tevatron. We will show that the doubly-unintegrated quark distributions, generated directly from the known integrated PDFs under the 'last-step' prescription, satisfactorily describe these data, including the region of interest, $P_T \ll M_{W,Z}$.

In Section 3.1 we describe the formalism for (z, k_t)-factorisation at hadron-hadron colliders, and in Section 3.2 we apply it to calculate the P_T distributions of electroweak bosons at LO. An estimate of the dominant higher-order corrections is made in Section 3.3 and numerical results are given in Section 3.4.

3.1 (z, k_t)-factorisation at hadron-hadron colliders

We now extend the formalism of Chapter 2, which concerned deep-inelastic scattering, to hadron-hadron collisions. The basic idea is illustrated in Fig. 3.1(a), which shows only one of the possible configurations. All permutations of quarks and gluons must be included. The arrows show the direction of the labelled momenta. The blobs represent the familiar integrated PDFs. The transverse momenta of the two incoming partons to the subprocess, represented by the rectangles labelled $\hat{\sigma}^{q_1^* q_2^*}$ in Fig. 3.1, are generated by a single parton emission in the last evolution step.

[2]To be precise, the *skewed* unintegrated gluon distribution is required. However, in the relevant

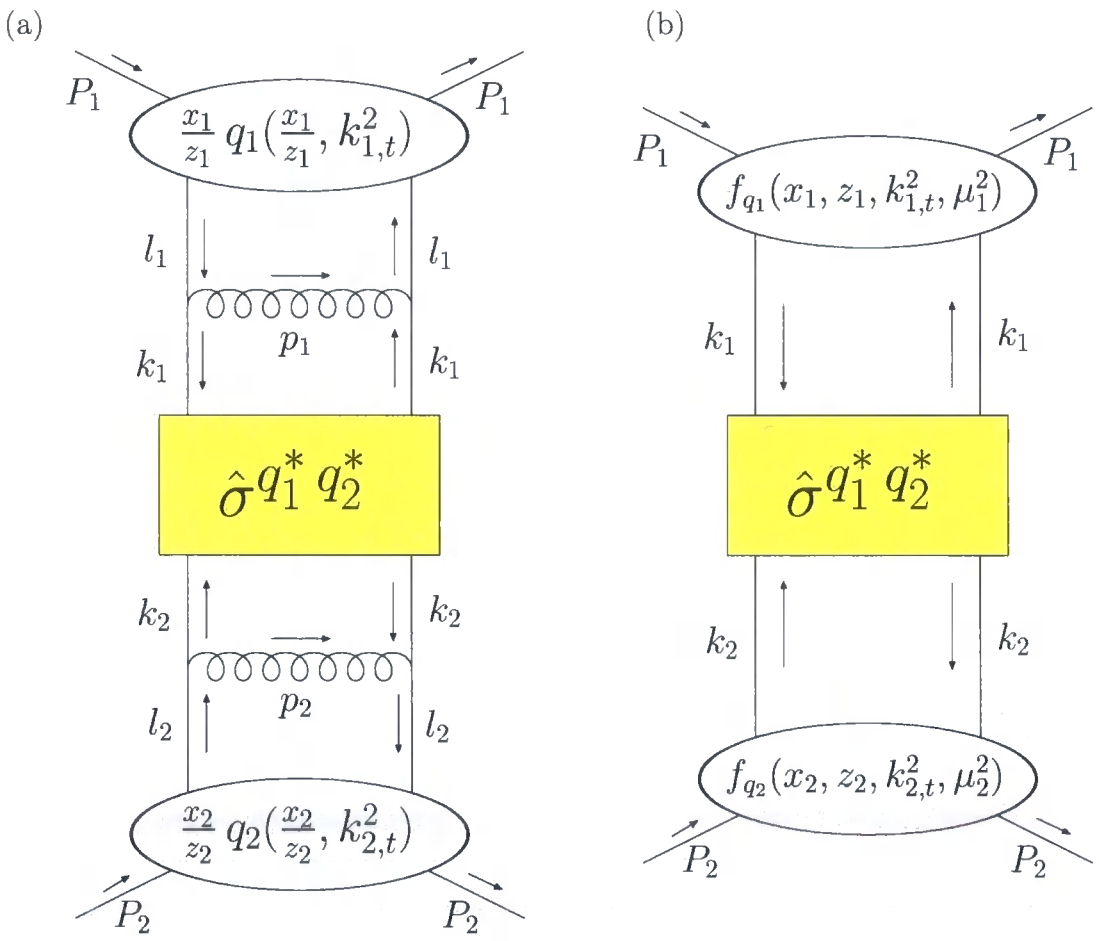

Figure 3.1: Illustration of (z, k_t)-factorisation at hadron-hadron colliders. (a) The transverse momentum of each parton entering the subprocess is generated by a single parton emission in the last evolution step. (b) The last evolution step is factorised into $f_{q_i}(x_i, z_i, k_{i,t}^2, \mu_i^2)$, where $i = 1, 2$.

We use a Sudakov decomposition of the momenta of the two incoming partons,

$$k_i = x_i P_i - \beta_i P_j + k_{i\perp}, \tag{3.1}$$

where $(i,j) = (1,2)$ or $(2,1)$. We work in the CM frame of the colliding hadrons and neglect the hadron masses so that the squared CM energy is $s \equiv (P_1+P_2)^2 \simeq 2\, P_1 \cdot P_2$. Then,

$$P_1 = (P_1^+, P_1^-, P_{1\perp}) = \sqrt{s}\,(1,0,\mathbf{0}), \qquad P_2 = \sqrt{s}\,(0,1,\mathbf{0}) \qquad k_{i\perp} = (0,0,\boldsymbol{k_{i,t}}). \tag{3.2}$$

The penultimate propagators in the evolution ladder have momenta $l_i = (x_i/z_i)\, P_i$, so that the partons emitted in the last step have momenta

$$p_i = l_i - k_i = \frac{x_i}{z_i}(1-z_i)\, P_i + \beta_i P_j - k_{i\perp}. \tag{3.3}$$

The on-shell condition for the emitted partons, $p_i^2 = 0$, determines

$$\beta_i = \frac{z_i\, r_i}{x_i\,(1-z_i)}, \tag{3.4}$$

where $r_i \equiv k_{i,t}^2/s$, so that the two incoming partons have virtuality $k_i^2 = -k_{i,t}^2/(1-z_i)$. The total momentum going into the subprocess labelled $\hat{\sigma}^{q_1^* q_2^*}$ in Fig. 3.1 is

$$q \equiv k_1 + k_2 = (x_1 - \beta_2)\, P_1 + (x_2 - \beta_1)\, P_2 + q_\perp, \tag{3.5}$$

where $q_\perp = k_{1\perp} + k_{2\perp}$. The kinematic variables obey the ordering

$$0 < \beta_j < x_i < z_i < 1. \tag{3.6}$$

Analogous to (1.35), the collinear factorisation formula for hadron-hadron collisions is

$$\sigma = \sum_{a_1, a_2} \int_0^1 \frac{\mathrm{d}x_1}{x_1} \int_0^1 \frac{\mathrm{d}x_2}{x_2}\, a_1(x_1,\mu^2)\, a_2(x_2,\mu^2)\, \hat{\sigma}^{a_1 a_2}, \tag{3.7}$$

where μ is the factorisation scale and the partonic cross sections $\hat{\sigma}^{a_1 a_2}$ are calculated with on-shell incoming partons with momenta $k_i = x_i P_i$. As in Chapter 2, we relax the DGLAP approximation of strongly-ordered transverse momenta in the last evolution step only.

If p_i are gluon momenta, then we must additionally impose angular-ordering[3]

small-x domain the skewed effect can be included by the Shuvaev prescription [92–94].

[3]We remind the reader that 'angular ordering' is a misnomer. It is rapidity ordering which

constraints due to colour coherence,

$$\xi_1 < \Xi < \xi_2, \tag{3.8}$$

where $\xi_i \equiv p_i^- / p_i^+$ and $\Xi \equiv q^- / q^+$. That is, the subprocess separates gluons emitted from each of the two hadrons. This condition leads to a suppression of soft gluon emission,

$$z_i < \frac{\mu_i}{\mu_i + k_{i,t}}, \tag{3.9}$$

with $\mu_1 \equiv x_1 \sqrt{s\,\Xi}$ and $\mu_2 \equiv x_2 \sqrt{s\,/\,\Xi}$.

The integrated PDFs, $a_i(x_i, \mu^2)$, of (3.7) are replaced by DUPDFs, $f_{a_i}(x_i, z_i, k_{i,t}^2, \mu_i^2)$, requiring additional convolutions over the splitting fractions z_i and the transverse momenta $k_{i,t}^2$, giving the (z, k_t)-factorisation formula

$$\sigma = \sum_{a_1, a_2} \int_0^1 \frac{\mathrm{d}x_1}{x_1} \int_0^1 \frac{\mathrm{d}x_2}{x_2} \int_{x_1}^1 \mathrm{d}z_1 \int_{x_2}^1 \mathrm{d}z_2 \int_0^\infty \frac{\mathrm{d}k_{1,t}^2}{k_{1,t}^2} \int_0^\infty \frac{\mathrm{d}k_{2,t}^2}{k_{2,t}^2} \times f_{a_1}(x_1, z_1, k_{1,t}^2, \mu_1^2)\, f_{a_2}(x_2, z_2, k_{2,t}^2, \mu_2^2)\, \hat{\sigma}^{a_1^* a_2^*}. \tag{3.10}$$

Here, the '*' indicates that the incoming partons, with momenta k_i given by (3.1), are off-shell with virtuality $k_i^2 = -k_{i,t}^2/(1 - z_i)$. This formula (3.10) is represented schematically in Fig. 3.1(b) for the case where the off-shell partons a_1^* and a_2^* are both quarks. The partonic cross sections in (3.10) are given by

$$\mathrm{d}\hat{\sigma}^{a_1^* a_2^*} = \mathrm{d}\Phi^{a_1^* a_2^*}\, |\mathcal{M}^{a_1^* a_2^*}|^2 \,/\, F^{a_1^* a_2^*}, \tag{3.11}$$

where the flux factor $F^{a_1^* a_2^*} = 2\, x_1\, x_2\, s$. The last evolution steps in Fig. 3.1(a) factorise from the rest of the diagram, to give the LO DGLAP splitting kernels, in the leading logarithmic approximation (LLA) where only the $\mathrm{d}k_{i,t}^2/k_{i,t}^2$ term is kept. Therefore, $|\mathcal{M}^{a_1^* a_2^*}|^2$ is calculated with the replacement $k_i \to x_i\, P_i$ in the numerator in order to keep only this collinear divergent term. However, any propagator virtualities appearing in the denominator of $|\mathcal{M}^{a_1^* a_2^*}|^2$ may be evaluated with the full kinematics, as may the phase space element $\mathrm{d}\Phi^{a_1^* a_2^*}$.

For this approach to work, it is vital that the $\mathrm{d}k_{i,t}^2/k_{i,t}^2$ term is obtained *only* from ladder-type diagrams like that in Fig. 3.1(a), and not from interference (non-ladder) diagrams. This is true if we use a physical gauge for the gluon, where only the two transverse polarisations propagate. For hadron-hadron collisions, the natural choice

should be applied.

is the planar gauge where the sum over gluon polarisations is performed using

$$d_{\mu\nu}(k, n) = -g_{\mu\nu} + \frac{k_\mu n_\nu + n_\mu k_\nu}{k \cdot n}, \tag{3.12}$$

where we take the gauge-fixing vector $n = x_1 P_1 + x_2 P_2$. Note that $n^2 = x_1 x_2 s \neq 0$, unlike the light-cone gauge of (1.26). Such a gauge choice ensures that the $\mathrm{d}k_{i,t}^2/k_{i,t}^2$ term is obtained from ladder-type diagrams on *both* sides of the subprocess represented by the rectangle in Fig. 3.1(a).

A related requirement is that terms beyond the leading $\mathrm{d}k_{i,t}^2/k_{i,t}^2$ term, coming from non-ladder diagrams, for example, give a negligible contribution. Such terms are proportional to the Sudakov variable β_i (3.4) and hence vanish in the limit that $z_i \to 0$ or $k_{i,t} \to 0$. Away from these limits it is not obvious that these 'beyond LLA' terms will be small, a necessary condition for the factorisation to hold. For the case of inclusive jet production in DIS and working in an axial gluon gauge, it was observed in Chapter 2 that the main effect of the extra terms was to suppress soft gluon emission. When the angular-ordering constraint (3.9) was applied, the extra terms were found to make a negligible difference to the cross section, see Fig. 2.13. For hadron-hadron collisions, although the number of possible non-ladder diagrams is larger, it is therefore reasonable to expect that the extra terms will have little numerical effect, at least for $k_{i,t}$ less than the hard scale of the subprocess. A similar argument is made to justify the approximation made in the DGLAP-based parton showers used in Monte Carlo simulations, where only the collinear divergent part of the squared matrix element for each parton branching is kept and angular ordering is imposed in all evolution steps to account for some of the missing terms. Here, we are more conservative and apply this approximation to the *last* evolution step only.

The DUPDFs in (3.10) are only defined for $k_{i,t} > \mu_0$, where $\mu_0 \sim 1$ GeV is the minimum scale for which DGLAP evolution of the integrated PDFs is valid. The approximation of the $k_{i,t} < \mu_0$ contribution made in Chapter 2 was to take the limit $k_{i,t} \to 0$ in the kinematic variables (and in $\hat{\sigma}^{a_1^* a_2^*}$), then to make the replacement

$$\int_{x_i}^1 \mathrm{d}z_i \int_0^{\mu_0^2} \frac{\mathrm{d}k_{i,t}^2}{k_{i,t}^2} f_{a_i}(x_i, z_i, k_{i,t}^2, \mu_i^2) = a_i(x_i, \mu_0^2)\, T_{a_i}(\mu_0^2, \mu_i^2), \tag{3.13}$$

where $T_{a_i}(\mu_0^2, \mu_i^2)$ are the Sudakov form factors (2.13) or (2.15). This replacement ensures that the normalisation conditions (2.19) are satisfied. A better approximation, which retains the $k_{i,t}$ dependence, is to take the limit $z_i \to 0$ in the kinematic

variables, then to make the replacement

$$\int_{x_i}^{1} \mathrm{d}z_i \, f_{a_i}(x_i, z_i, k_{i,t}^2, \mu_i^2) \equiv f_{a_i}(x_i, k_{i,t}^2, \mu_i^2) = \frac{k_{i,t}^2}{\mu_0^2} \, a_i(x_i, \mu_0^2) \, T_{a_i}(\mu_0^2, \mu_i^2), \tag{3.14}$$

where we have used (2.7). The requirement that $f_{a_i}(x_i, k_{i,t}^2, \mu_i^2) \sim k_{i,t}^2$ as $k_{i,t}^2 \to 0$ is a consequence of gauge invariance [23, 95].

A more complicated extrapolation of the DUPDFs for $k_t < \mu_0$, which allows both the k_t and z dependence to be retained in the kinematic variables, is to assume the polynomial form

$$f_a(x, z, k_t^2, \mu^2) = \frac{k_t^2}{\mu_0^2} \left[A(x, z, \mu^2) + \frac{k_t^2}{\mu_0^2} \, B(x, z, \mu^2) \right]. \tag{3.15}$$

The two coefficients A and B can be determined to ensure continuity at $k_t = \mu_0$ and the correct normalisation (3.13), leading to

$$A(x, z, \mu^2) = -f_a(x, z, \mu_0^2, \mu^2) + 2\, a(x, \mu_0^2) \, T_a(\mu_0^2, \mu^2) \,/\, (1 - x), \tag{3.16}$$

$$B(x, z, \mu^2) = 2\, f_a(x, z, \mu_0^2, \mu^2) - 2\, a(x, \mu_0^2) \, T_a(\mu_0^2, \mu^2) \,/\, (1 - x). \tag{3.17}$$

If (3.15) becomes negative, which is possible for $k_t \ll \mu_0$, then $f_a(x, z, k_t^2, \mu^2)$ is simply set to zero.

This extrapolation of the perturbative formulae accounts for some non-perturbative 'intrinsic' k_t of the initial partons, which is often parameterised by a Gaussian distribution with $\langle k_t \rangle \lesssim \mu_0$. Numerical results are insensitive to the precise form (3.13), (3.14), or (3.15) used for the $k_t < \mu_0$ contribution. However, for the rest of this chapter we will use the form (3.15) which ensures continuity at $k_t = \mu_0$.

3.2 Application to the P_T distributions of electroweak bosons

Perhaps the simplest application of (z, k_t)-factorisation at hadron-hadron colliders is electroweak boson production, where at LO the subprocess is simply $q_1^* \, q_2^* \to V$, illustrated in Fig. 3.2, or $g_1^* \, g_2^* \to H$, illustrated in Fig. 3.3. In the collinear approximation, these diagrams give the Born level estimate of the total cross section σ. When each parton carries finite transverse momentum $\boldsymbol{k}_{i,t}$, the final electroweak boson has transverse momentum $\boldsymbol{q_t} = \boldsymbol{k_{1,t}} + \boldsymbol{k_{2,t}}$, so we can calculate the P_T distribution

$$\frac{\mathrm{d}\sigma}{\mathrm{d}P_T} = \sigma \, \delta(q_t - P_T), \tag{3.18}$$

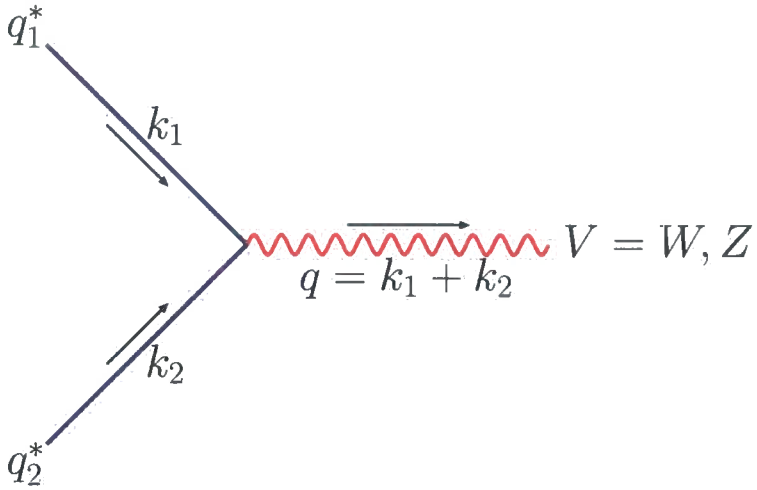

Figure 3.2: LO Feynman diagram contributing to the P_T distributions of W or Z bosons in the (z, k_t)-factorisation approach.

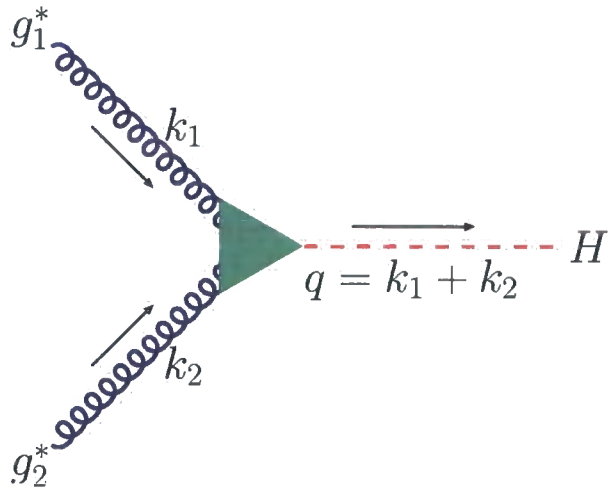

Figure 3.3: LO Feynman diagram contributing to the P_T distribution of SM Higgs bosons in the (z, k_t)-factorisation approach. The triangle represents the effective ggH vertex in the limit $M_H \ll 2m_t$.

with σ given by the (z, k_t)-factorisation formula (3.10).

The squared matrix element for W production is

$$|\mathcal{M}(q_1^* q_2^* \to W)|^2 = \frac{1}{4N_C}\left(\frac{g_W}{2\sqrt{2}}\right)^2 |V_{q_1q_2}|^2 \,\mathrm{Tr}[\not{k}_1\gamma^\mu(1-\gamma^5)\not{k}_2\gamma^\nu(1-\gamma^5)]\left(-g_{\mu\nu}+\frac{q_\mu q_\nu}{M_W^2}\right)$$
$$= \frac{\sqrt{2}}{N_C} G_F M_W^2 |V_{q_1q_2}|^2 x_1 x_2 s, \tag{3.19}$$

where $N_C = 3$ is the number of colours, $g_W^2 = 8M_W^2 G_F/\sqrt{2}$ is the weak charge squared, G_F is the Fermi coupling constant, and $|V_{q_1q_2}|^2$ is the Cabibbo-Kobayashi-Maskawa (CKM) matrix element squared. For Z production the corresponding result is

$$|\mathcal{M}(q_1^* q_2^* \to Z)|^2 = \frac{1}{4N_C}\left(\frac{g_W}{2\cos\theta_W}\right)^2 \mathrm{Tr}[\not{k}_1\gamma^\mu(V_q - A_q\gamma^5)\not{k}_2\gamma^\nu(V_q - A_q\gamma^5)]\left(-g_{\mu\nu}+\frac{q_\mu q_\nu}{M_Z^2}\right)$$
$$= \frac{\sqrt{2}}{N_C} G_F M_Z^2 (V_q^2 + A_q^2) x_1 x_2 s, \tag{3.20}$$

where $\cos\theta_W = M_W/M_Z$ is the weak mixing angle, $V_q = T_q^3 - 2e_q \sin^2\theta_W$ is the vector coupling, $A_q = T_q^3$ is the axial vector coupling, and T_q^3 is the weak isospin ($T_{u,c,t}^3 = +1/2$, $T_{d,s,b}^3 = -1/2$). The phase space element is

$$\mathrm{d}\Phi(q_1^* q_2^* \to V) = (2\pi)^4 \delta^{(4)}(k_1 + k_2 - q)\frac{\mathrm{d}^4 q}{(2\pi)^3}\delta(q^2 - M_V^2) = 2\pi\,\delta(q^2 - M_V^2), \tag{3.21}$$

and the flux factor is $F(q_1^* q_2^* \to V) = 4k_1 \cdot k_2 = 2x_1x_2s$.

The partonic differential cross sections for W or Z production are then

$$\frac{\mathrm{d}\hat{\sigma}}{\mathrm{d}P_T}(q_1^* q_2^* \to V) = \frac{\pi}{N_C}\sqrt{2}\,G_F M_V^2 V_V^2\,\delta(q^2 - M_V^2)\,\delta(q_t - P_T), \tag{3.22}$$

where $V_W^2 \equiv |V_{q_1q_2}|^2$ and $V_Z^2 \equiv V_q^2 + A_q^2$.

The dominant mechanism for SM Higgs production in hadron-hadron collisions is by gluon-gluon fusion via a top quark loop. For the case where $M_H \ll 2m_t$, the well-known effective ggH vertex can be derived from the Lagrangian [96, 97]

$$\mathcal{L}_{\mathrm{eff}} = -\frac{1}{4}\left(1 - \frac{\alpha_S(M_H^2)}{3\pi}\frac{H}{v}\right) G_{\mu\nu}^A G^{A\mu\nu}, \tag{3.23}$$

where $v^2 = (\sqrt{2}\,G_F)^{-1}$, $G_{\mu\nu}^A$ is the gluon field strength tensor, and H is the Higgs

field. The squared matrix element is then

$$|\mathcal{M}(g_1^* g_2^* \to H)|^2 = \frac{1}{4(N_C^2-1)} \left(\sqrt{2} G_F \frac{\alpha_S^2(M_H^2)}{9\pi^2}\right) \times (k_1 \cdot k_2\, g^{\mu\nu} - k_2^\mu k_1^\nu)\,(k_1 \cdot k_2\, g^{\rho\sigma} - k_2^\rho k_1^\sigma)\; d_{\mu\rho}(k_1, n) d_{\nu\sigma}(k_2, n)$$
$$= \sqrt{2} G_F \frac{\alpha_S(M_H^2)}{576\pi^2} (x_1\, x_2\, s)^2\,, \tag{3.24}$$

where the sum over gluon polarisations is performed using the planar gauge (3.12). The phase space element and the flux factor for SM Higgs production are the same as for $q_1^* q_2^* \to V$, leading to the partonic differential cross section

$$\frac{\mathrm{d}\hat{\sigma}}{\mathrm{d}P_T}(g_1^* g_2^* \to H) = \frac{\sqrt{2}\, G_F\, x_1\, x_2\, s}{576\,\pi}\, \alpha_S^2(M_H^2)\; \delta(q^2 - M_H^2)\; \delta(q_t - P_T). \tag{3.25}$$

For $q^2 = x_1\, x_2\, s$ and $q_t = 0$, these expressions (3.22) and (3.25) are exactly as in the collinear approximation. The difference arises when we consider the precise kinematics

$$q^2 = s\,[(x_1 - \beta_2)(x_2 - \beta_1) - R]\,, \qquad R \equiv q_t^2/s, \tag{3.26}$$
$$q_t^2 = |\boldsymbol{k_{1,t}} + \boldsymbol{k_{2,t}}|^2 = k_{1,t}^2 + k_{2,t}^2 + 2\, k_{1,t}\, k_{2,t}\, \cos\phi. \tag{3.27}$$

Applying the (z, k_t)-factorisation formula (3.10), the first delta function in (3.22) and (3.25) can be used to do the x_2 integration in (3.10), while the second delta function can be used to do the $k_{2,t}$ integration. In addition, we need to average over the azimuthal angle ϕ between $\boldsymbol{k_{1,t}}$ and $\boldsymbol{k_{2,t}}$.

The final hadronic differential cross sections for W or Z production are

$$\frac{\mathrm{d}\sigma}{\mathrm{d}P_T} = \frac{\pi}{N_C} \sqrt{2}\, G_F\, \tau \sum_{x_2 = x_2^\pm} \sum_{k_{2,t} = k_{2,t}^\pm} \int_0^1 \frac{\mathrm{d}x_1}{x_1} \int_{x_1}^1 \mathrm{d}z_1 \int_{x_2}^1 \mathrm{d}z_2 \int_0^\infty \frac{\mathrm{d}k_{1,t}^2}{k_{1,t}^2} \int_0^{2\pi} \frac{\mathrm{d}\phi}{2\pi}$$
$$\times \frac{2\, P_T\, \Theta(k_{2,t})}{k_{2,t} |k_{2,t} + k_{1,t} \cos\phi|} \frac{1}{x_1\, x_2 - \beta_1\, \beta_2} \sum_{q_1, q_2} V_V^2\, f_{q_1}(x_1, z_1, k_{1,t}^2, \mu_1^2)\, f_{q_2}(x_2, z_2, k_{2,t}^2, \mu_2^2), \tag{3.28}$$

with $\tau \equiv M_V^2/s$, $k_{2,t}^\pm \equiv -k_{1,t} \cos\phi \pm \sqrt{P_T^2 - k_{1,t}^2 \sin^2\phi}$, and

$$x_2^\pm \equiv \frac{1}{2x_1} \left\{ \bar{\tau} + R + x_1\beta_1 + \frac{z_2 r_2}{1 - z_2} \pm \sqrt{\left(\bar{\tau} + R + x_1\beta_1 + \frac{z_2 r_2}{1 - z_2}\right)^2 - 4 x_1 \beta_1 \frac{z_2 r_2}{1 - z_2}} \right\}. \tag{3.29}$$

In practice, the kinematic constraints (3.6) mean that the $x_2 = x_2^-$ solution does not contribute. The corresponding result for SM Higgs production is

$$\frac{\mathrm{d}\sigma}{\mathrm{d}P_T} = \frac{\sqrt{2}\,G_F}{576\,\pi}\,\alpha_S^2(M_H^2) \sum_{x_2=x_2^\pm} \sum_{k_{2,t}=k_{2,t}^\pm} \int_0^1 \frac{\mathrm{d}x_1}{x_1} \int_{x_1}^1 \mathrm{d}z_1 \int_{x_2}^1 \mathrm{d}z_2 \int_0^\infty \frac{\mathrm{d}k_{1,t}^2}{k_{1,t}^2} \int_0^{2\pi} \frac{\mathrm{d}\phi}{2\pi}$$
$$\times \frac{2\,P_T\,\Theta(k_{2,t})}{k_{2,t}|k_{2,t} + k_{1,t}\cos\phi|} \frac{x_1\,x_2}{x_1\,x_2 - \beta_1\,\beta_2}\, f_g(x_1, z_1, k_{1,t}^2, \mu_1^2)\, f_g(x_2, z_2, k_{2,t}^2, \mu_2^2), \quad (3.30)$$

where $\tau \equiv M_H^2/s$, and $k_{2,t}^\pm$ and $x_2^\pm$ are as above. Note that we have taken the ggH vertex in the $M_H \ll 2m_t$ limit. For $M_H < 2m_t$, the correction to the total cross section due to the top quark mass can be approximated [8] by a factor

$$\left[1 + \left(\frac{M_H}{2m_t}\right)^2\right]^2. \quad (3.31)$$

The $k_{i,t} < \mu_0$ contributions of (3.28) and (3.30) are accounted for using the approximation (3.15).[4]

3.3 The K-factors

In the collinear approximation, higher order QCD corrections to the LO diagrams, $q_1\,q_2 \to V$ or $g_1\,g_2 \to H$, are known to be significant when calculating the total cross section. The ratio of the corrected result to the leading order result is the so-called K-factor. A part of these higher order corrections is kinematic in nature, arising from real parton emission, which we have already accounted for at LO in the (z, k_t)-factorisation approach (see Fig. 3.1). Another part comes from the logarithmic loop corrections which have already been included in the Sudakov form factors (2.13) and (2.15). However, we need to include the non-logarithmic loop corrections arising, for example, from the gluon vertex correction to Figs. 3.2 and 3.3.

A large part of these non-logarithmic corrections have a semi-classical nature and may be obtained from the analytic continuation of the double logarithm in the Sudakov form factors in going from spacelike (DIS) to timelike (Drell-Yan) electroweak boson momenta [98–100]. In the soft ($\zeta \to 1$) and collinear ($k_t, \kappa_t \ll \mu$) limits, the

[4]Other contributions in the region $k_{i,t} < \mu_0$, such as the inclusion of additional intrinsic partonic transverse momentum with $\langle k_t \rangle \approx 0.3$ GeV, would only affect the P_T distributions at very low $P_T \lesssim 1$ GeV.

Sudakov form factors (2.13) and (2.15) can be written

$$T_a(k_t^2,\mu^2) \simeq \exp\left(-\int_{k_t^2}^{\mu^2}\frac{\mathrm{d}\kappa_t^2}{\kappa_t^2}\,\frac{\alpha_S(\kappa_t^2)}{2\pi}\,C_a\,\ln\frac{\mu^2}{\kappa_t^2}\right), \tag{3.32}$$

where $C_q \equiv C_F$ and $C_g \equiv C_A$. Accounting for the running coupling $\alpha_S(\kappa_t^2)$ given by (1.11) and performing the κ_t integral, we obtain the Sudakov form factors in the DLLA,

$$T_a(k_t^2,\mu^2) \simeq \exp\left(-\frac{C_a}{2\,\pi\,b}\,L\ln L\right), \tag{3.33}$$

where $L \equiv \ln(\mu^2/\Lambda^2_{\mathrm{QCD}})$ and $b = (33-2n_f)/(12\pi)$.

Replacing μ^2 by $-\mu^2$, we obtain the π^2-enhanced part of the K-factors via

$$K(a_1^*\,a_2^* \to V,H) \simeq \left|\frac{T_a(k_t^2,-\mu^2)}{T_a(k_t^2,\mu^2)}\right|^2. \tag{3.34}$$

Using the identity $\ln(-\mu^2) = \ln\mu^2 + \mathrm{i}\pi$ and the Mercator series $\ln(1+x) = x - x^2/2 + \ldots$, then

$$\ln\ln(-\mu^2) = \ln\left[\ln\mu^2\left(1+\frac{\mathrm{i}\pi}{\ln\mu^2}\right)\right] = \ln\ln\mu^2 + \left[\frac{\mathrm{i}\pi}{\ln\mu^2} - \frac{1}{2}\left(\frac{\mathrm{i}\pi}{\ln\mu^2}\right)^2 + \ldots\right]. \tag{3.35}$$

The final results for the K-factors are[5]

$$K(q_1^*\,q_2^* \to V) \simeq \left|\frac{T_q(k_t^2,-\mu^2)}{T_q(k_t^2,\mu^2)}\right|^2 \simeq \exp\left(C_F\,\frac{\alpha_S(\mu^2)}{2\,\pi}\,\pi^2\right) \tag{3.36}$$

and

$$K(g_1^*\,g_2^* \to H) \simeq \left|\frac{T_g(k_t^2,-\mu^2)}{T_g(k_t^2,\mu^2)}\right|^2 \simeq \exp\left(C_A\,\frac{\alpha_S(\mu^2)}{2\,\pi}\,\pi^2\right). \tag{3.37}$$

A particular scale choice $\mu^2 = P_T^{4/3}\,M_{V,H}^{2/3}$ has been found to eliminate certain subleading logarithms in the Sudakov form factors [102]. Therefore, we choose this scale to evaluate $\alpha_S(\mu^2)$ in (3.36) and (3.37).

[5]Note the extra factor of 1/2 in the exponents of (3.36) and (3.37) compared to [101], where the Mercator series was truncated after only the first term.

3.4 Numerical results

3.4.1 W and Z boson production at the Tevatron

The P_T distributions of produced W and Z bosons were measured by the CDF [103] and DØ [104, 105] Collaborations during the Tevatron Run 1, in $p\bar{p}$ collisions at a CM energy of $\sqrt{s} = 1.8$ TeV. Measurements were made of $W \to e\nu$ and $Z \to ee$ decays; therefore, we must multiply the theoretical predictions for W or Z production by the appropriate leptonic branching ratios.[6] We use the MRST2001 LO PDFs [66] as input, with $\mu_0^2 = 1.25$ GeV^2. As in Chapter 2, the GNU Scientific Library [76] implementation of the VEGAS algorithm [77] was used to perform multidimensional Monte Carlo integration. The LO predictions for the P_T distributions (3.28), integrated over bins of 1 GeV, are shown by the dashed lines in Figs. 3.4, 3.5 and 3.6. The integrated luminosity uncertainty (3.9% for CDF or 4.4% for DØ) is not included in the error bars for the plotted data. The LO predictions multiplied by the K-factor (3.36) are shown by the solid lines. Although the K-factor makes up the major part of the discrepancy, we see that the solid lines in Figs. 3.4, 3.5, and 3.6 still underestimate the precise measurements at small P_T to some extent. Normalising to the total measured cross sections (248 pb, 221 pb, and 2310 pb) by factors 1.23, 1.10, and 1.08 respectively, as shown by the dotted lines in Figs. 3.4, 3.5, and 3.6, gives a very good description of the data over the entire P_T range.

Although it makes sense to take μ_0^2 as low as possible, the insensitivity of the P_T distributions to the $k_t < \mu_0$ treatment can be demonstrated by taking $\mu_0^2 = 2.5$ GeV^2. The P_T distributions obtained are practically identical to those with $\mu_0^2 = 1.25$ GeV^2, with less than a 0.5% change in the total cross sections.

Notice that the predicted P_T distribution of Z bosons peaks about 0.5–1.0 GeV below the CDF data (Fig. 3.4). One possible explanation for this is provided by non-perturbative power corrections, part of which may be interpreted as a negative correction of about -3 GeV^2 to the factorisation scale at which the integrated PDFs are evaluated [107]. Such a shift in the factorisation scale is found to move the peak of the P_T distribution about 0.2 GeV in the direction of the CDF data, with a slightly larger normalisation factor of 1.24. The inclusion of small-x broadening in the Collins-Soper-Sterman [108] resummation formalism, which has been observed to improve the agreement with semi-inclusive DIS data [109], has been predicted to have a negligible effect on the W and Z P_T distributions integrated over rapidity at the Tevatron Run 2 ($\sqrt{s} = 1.96$ TeV) [110].

In Fig. 3.7 we show the importance of the extra z_i convolutions of (z, k_t)-

[6] BR($W \to e\nu$) = 0.1072 and BR($Z \to ee$) = 0.03363 [106].

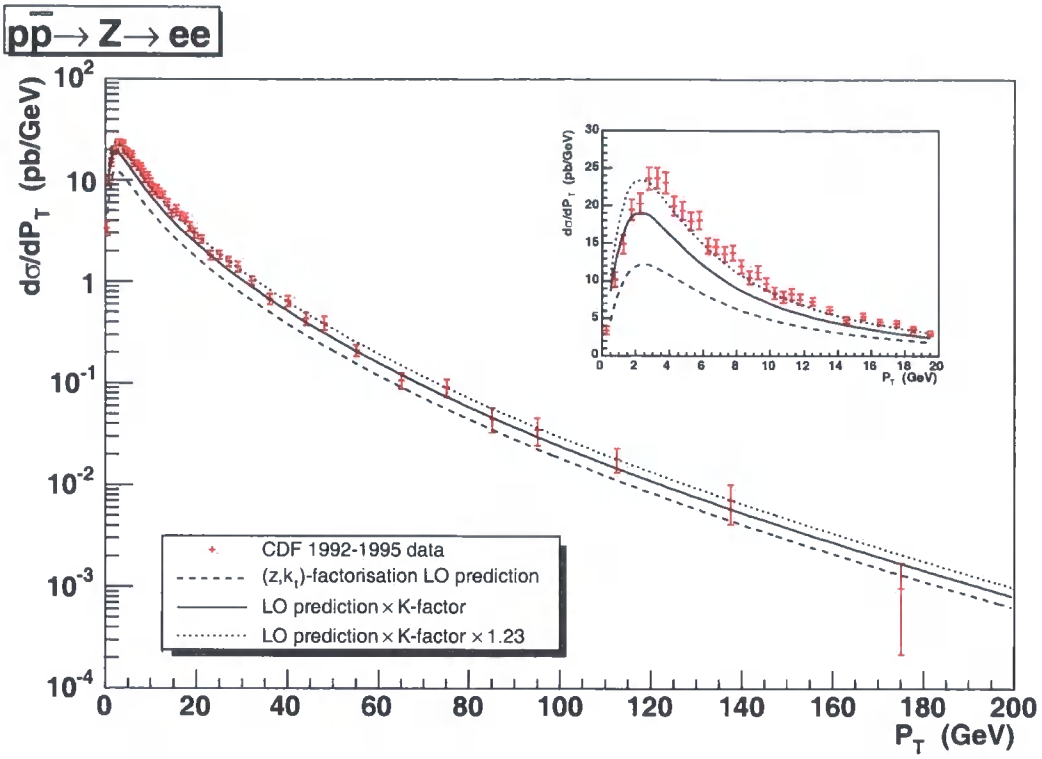

Figure 3.4: P_T distribution of Z bosons compared to CDF data [103].

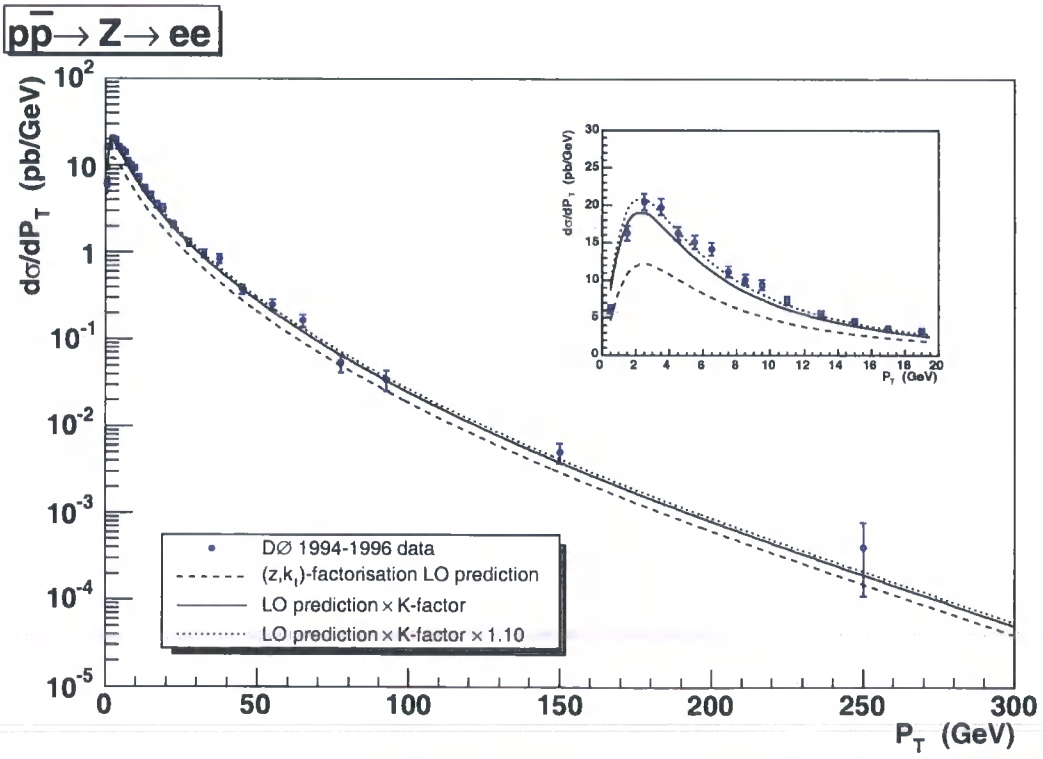

Figure 3.5: P_T distribution of Z bosons compared to DØ data [104].

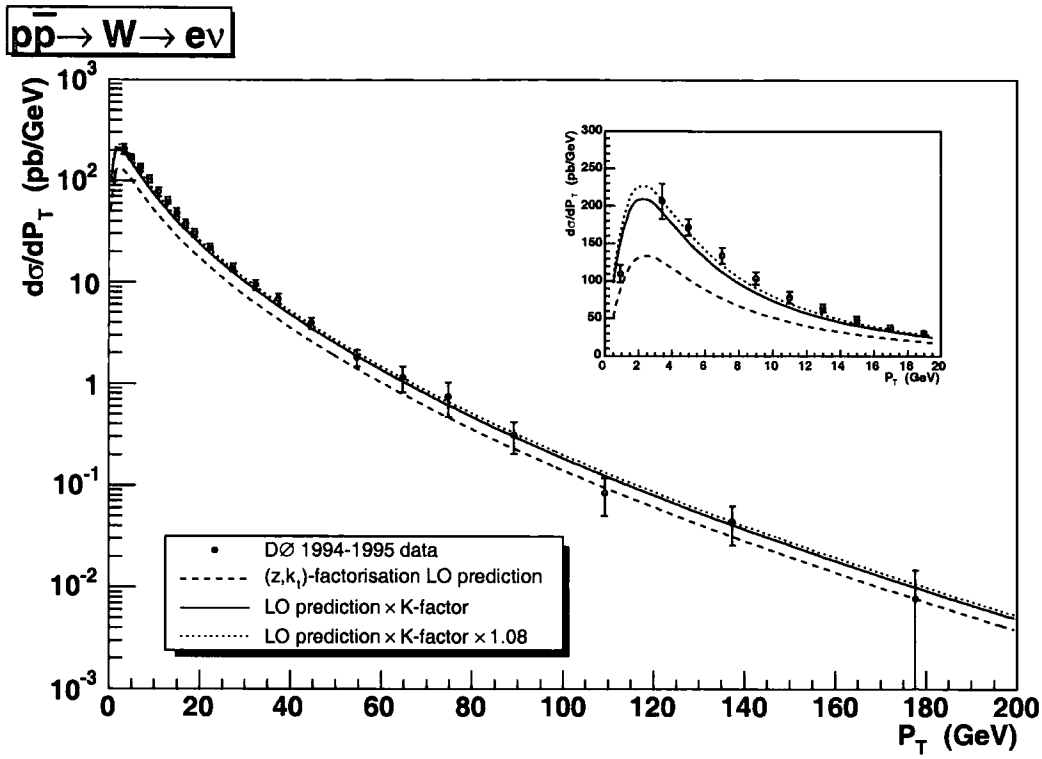

Figure 3.6: P_T distribution of W bosons compared to DØ data [105].

factorisation with respect to k_t-factorisation by taking $z_i \to 0$ in the kinematic variables. In this limit, $\beta_i \to 0$ and the integrals of the DUPDFs over z_i in (3.28) give the UPDFs, $f_{q_i}(x_i, k_{i,t}^2, \mu_i^2)$. At small P_T there is little difference from the result obtained with the full kinematics, since at small P_T the major contribution comes from small $z_i \ll 1$ parton branching. However, at large P_T the difference is significant and the $z_i \to 0$ prediction overestimates the data. In Fig. 3.8 we show the prediction for the P_T distribution of W bosons using CTEQ6L1 PDFs [35] as input (with $\mu_0^2 = 1.69$ GeV^2) rather than the MRST2001 LO PDFs [66]; the difference is negligible over the whole P_T range.

The small residual discrepancy between the solid lines in Figs. 3.4, 3.5, and 3.6 and the data is easily understood. Note that the MRST2001 LO PDFs [66] have been determined by a global fit to data using the conventional collinear approximation. A more precise treatment would fit the integrated PDFs, used as input to the last evolution step, to the proton structure function F_2, for example, using the (z, k_t)-factorisation formalism at LO. We would expect this treatment to give slightly larger integrated PDFs than the conventional sets by a factor of ≈ 1.1 and so eliminate the small discrepancy between the (z, k_t)-factorisation predictions and the data.

Alternatively, it was found in the last chapter that the major higher order corrections to the inclusive jet cross section in DIS could be accounted for by adding extra

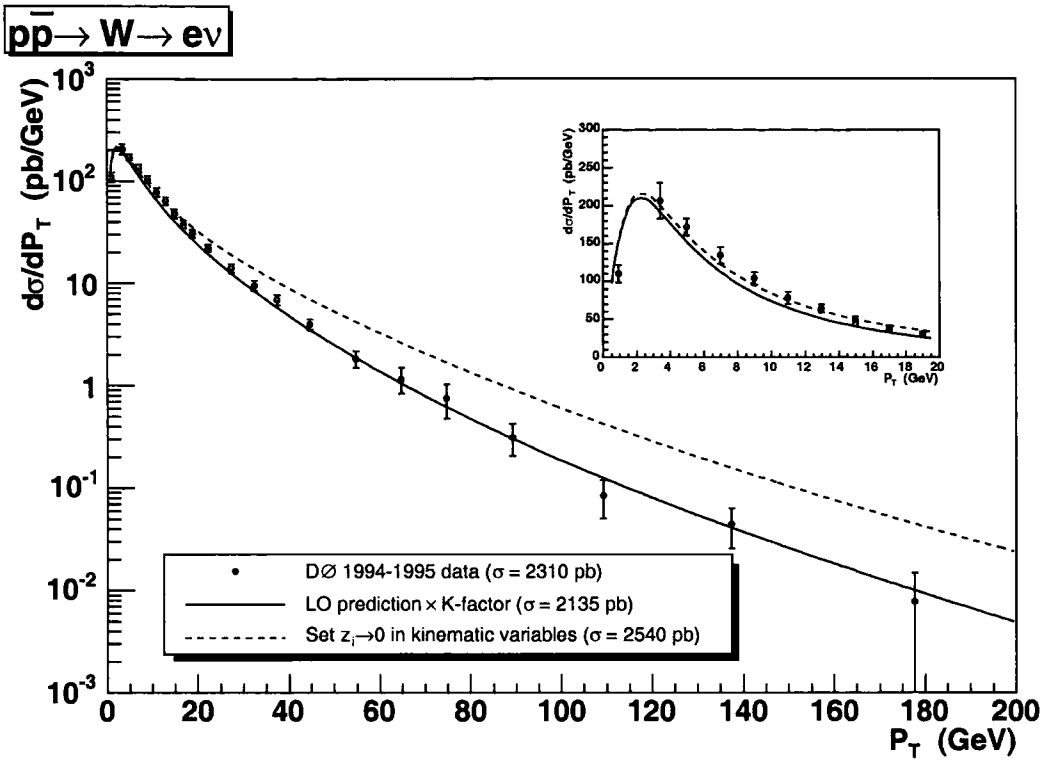

Figure 3.7: Effect of taking $z_i \to 0$ in the kinematic variables on the P_T distribution of W bosons compared to DØ data [105].

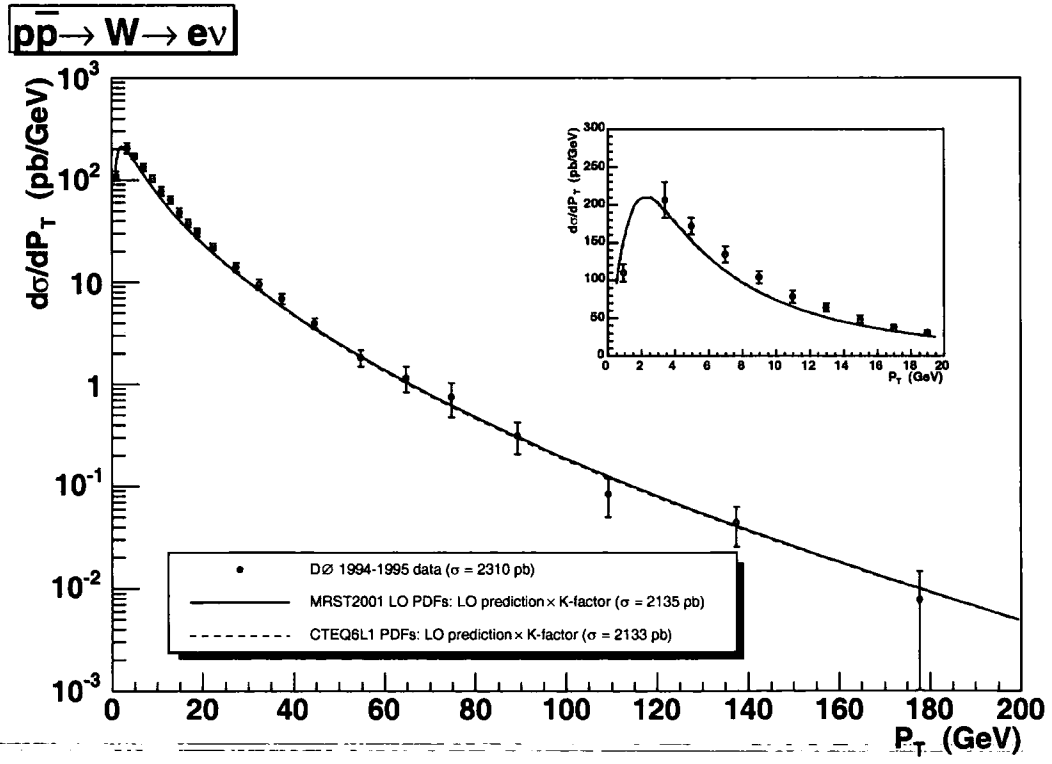

Figure 3.8: Effect of using CTEQ6L1 PDFs [35] rather than MRST2001 LO PDFs [66] on the P_T distribution of W bosons compared to DØ data [105].

parton emissions to the LO diagram, $\gamma^* q^* \to q$. In an axial gluon gauge, ladder-type diagrams gave the dominant contributions. Thus, it is likely that calculating the $\mathcal{O}(\alpha_S)$ subprocesses $q_1^* q_2^* \to gV$ and $q_i^* g_j^* \to qV$ using the (z, k_t)-factorisation prescription would account for any significant higher order corrections not already included and so reduce the observed discrepancy without refitting the input integrated PDFs.

Proton structure function $F_2(x_B, Q^2)$

These reasons for the small discrepancies discussed in the previous two paragraphs can be illustrated by considering the proton structure function $F_2(x_B, Q^2)$, which is plotted for two Q^2 values in Fig. 3.9. In the collinear approximation, the LO prediction for this observable comes from $\gamma^* q \to q$,

$$F_2(x_B, Q^2) = \sum_q e_q^2 \, x_B q(x_B, Q^2), \tag{3.38}$$

indicated by the solid lines in Fig. 3.9, which gives a good description of the data points since this data set was included in the MRST2001 LO global fit. The LO (z, k_t)-factorisation prediction comes from $\gamma^* q^* \to q$ and may be obtained from (2.93):

$$F_2(x_B, Q^2) = \sum_q e_q^2 \, x_B q(x_B, \mu_0^2) \, T_q(\mu_0^2, Q^2) + \int_x^1 \mathrm{d}z \int_{\mu_0^2}^{\infty} \frac{\mathrm{d}k_t^2}{k_t^2} \, \frac{x_B/x}{1 - x_B\beta/x} \sum_q e_q^2 f_q(x, z, k_t^2, \mu^2), \tag{3.39}$$

where the Sudakov variables $x = x_+$ and β are given in (2.62) and the factorisation scale μ is given in (2.9). The predictions of this formula are shown as the dashed lines in Fig. 3.9, while the first term of (3.39), representing the non-perturbative contributions from $k_t < \mu_0$, is also shown separately as the dotted lines. There is a clear difference between the predictions of (3.38) and (3.39), which increases as x_B decreases, due to the extra kinematic factor in the second term of (3.39). This difference would be eliminated by fitting the input integrated PDFs using (3.39). Alternatively, a 'NLO' prediction for F_2 may be calculated from the subprocesses $\gamma^* g^* \to q\bar{q}$ and $\gamma^* q^* \to qg$, and can be obtained from (2.106). Here, a lower limit of μ_0 is taken in the k_t' integration, and the $k_t' < \mu_0$ contribution is instead accounted for using the first term of (3.39). It is seen that these 'NLO' predictions, shown as the dot-dashed lines in Fig. 3.9, give almost the same results as (3.38).

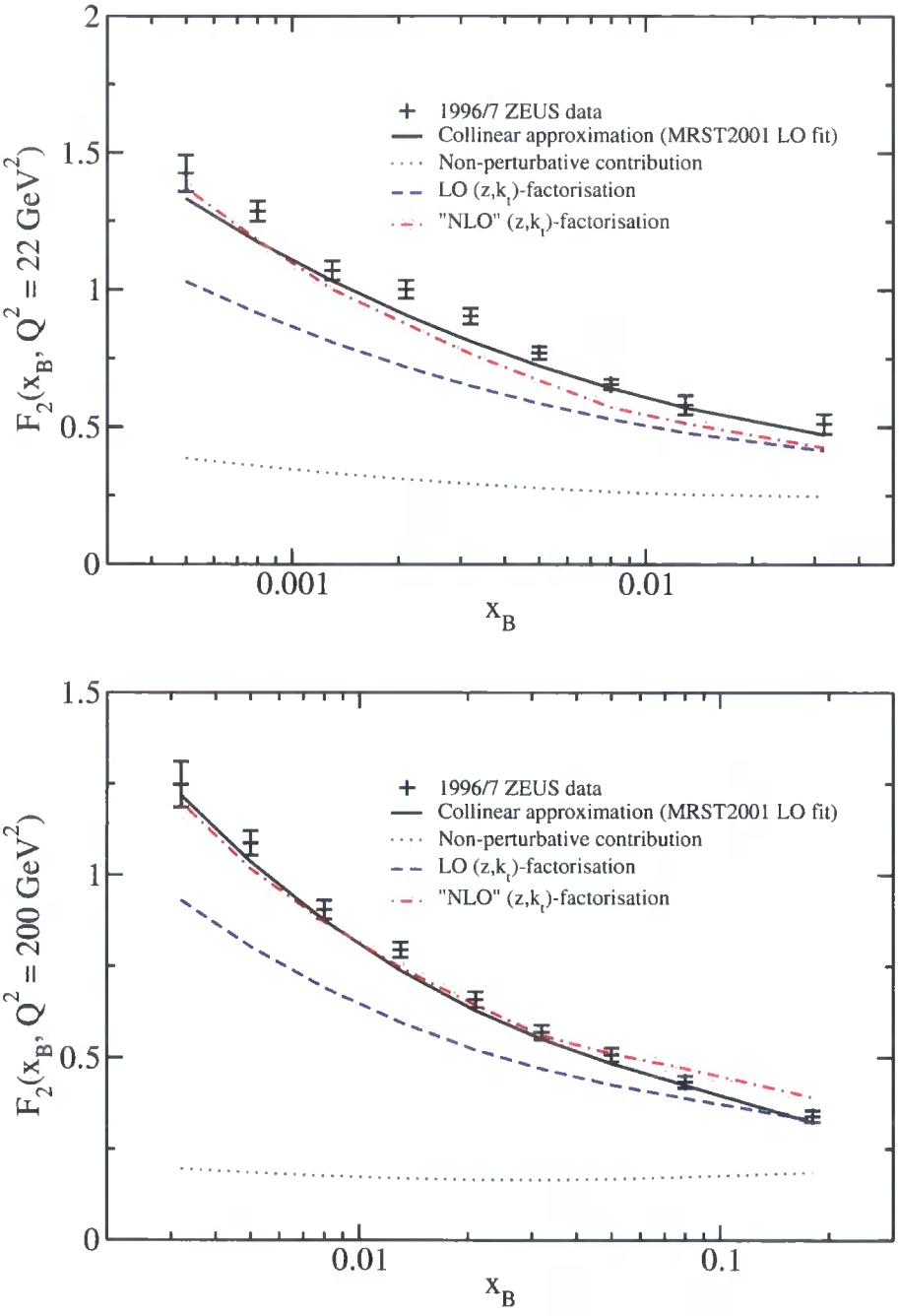

Figure 3.9: Predictions for $F_2(x_B, Q^2)$ at Q^2 values of 22 GeV^2 (top) and 200 GeV^2 (bottom) in the collinear approximation, where the 1996/97 ZEUS data [111] has been included in the MRST2001 LO fit [66], and in the (z, k_t)-factorisation approach using the same PDFs as input. The discrepancy between the data and the LO (z, k_t)-factorisation prediction can be eliminated by either refitting the input integrated PDFs or by adding some 'NLO' contribution.

3.4.2 Standard Model Higgs boson production at the LHC

The P_T distribution (3.30) for SM Higgs bosons of mass 125 GeV produced at the LHC ($\sqrt{s} = 14$ TeV) is shown in Fig. 3.10. To allow direct comparison with the results of [112], we do *not* account for top quark mass effects. Note that the peak in the Higgs P_T distribution is broader and occurs at a higher P_T than for vector boson production. This is primarily due to the enhanced $g \to gg$ colour factor ($C_A = 3$) compared to the $q \to qg$ colour factor ($C_F = 4/3$), resulting in a larger Sudakov suppression at low P_T. By the same reason the K-factor (3.37) is larger. For $P_T \lesssim M_H$, the P_T distribution is in good agreement with recent, more sophisticated, resummation predictions (see, for example, [112]), bearing in mind the spread in the various predictions available due to the different approaches and PDFs used, see Fig. 3.11. However, the peak occurs at a P_T about 1–2 GeV lower than the majority of the resummation predictions. Evaluating the total cross section by integrating over all P_T gives 38.6 pb, close to the NNLO QCD calculation which gives 39.4 pb [112].

Note that matrix-element corrections are necessary in parton shower simulations at large P_T. Without such corrections, the HERWIG parton shower prediction falls off dramatically at large $P_T \gtrsim M_H$ [113,114], see Fig. 3.11. The same effect is observed in HERWIG predictions for the P_T distributions of W and Z production [115], whereas we manage to describe the Tevatron data at large $P_T \gtrsim M_V$ without explicit matrix-element corrections. The fact that our predictions are much closer to the fixed-order results at large P_T than parton shower predictions suggests that we have successfully accounted for a large part of the sub-leading terms.

Off-shell matrix elements

The (z, k_t)-factorisation prescription involves calculating the squared matrix element $|\mathcal{M}|^2$ essentially *on-shell*, that is, with the incoming partons having momenta $k_i = x_i P_i$. This prescription was chosen so as to approximately reproduce the collinear factorisation calculation starting one rung down, for example, the $\mathcal{O}(\alpha_S^4)$ calculation for Higgs production at large P_T, where there are up to two hard emissions. However, we note from (2.28) that the non-factorisable 'beyond LLA' terms are proportional to the Sudakov variable β_i, confirmed by the explicit calculation of Section 2.3.1. Therefore, it is permissible to calculate $|\mathcal{M}|^2$ off-shell, that is, with the incoming partons having momentum $k_i = x_i P_i + k_{i\perp}$, as in the conventional k_t-factorisation prescription. Note however, that $|\mathcal{M}|^2$ *cannot* be calculated with the incoming partons having momentum $k_i = x_i P_i - \beta_i P_j + k_{i\perp}$, since in this case meaningless non-factorisable terms proportional to β_i would be obtained.

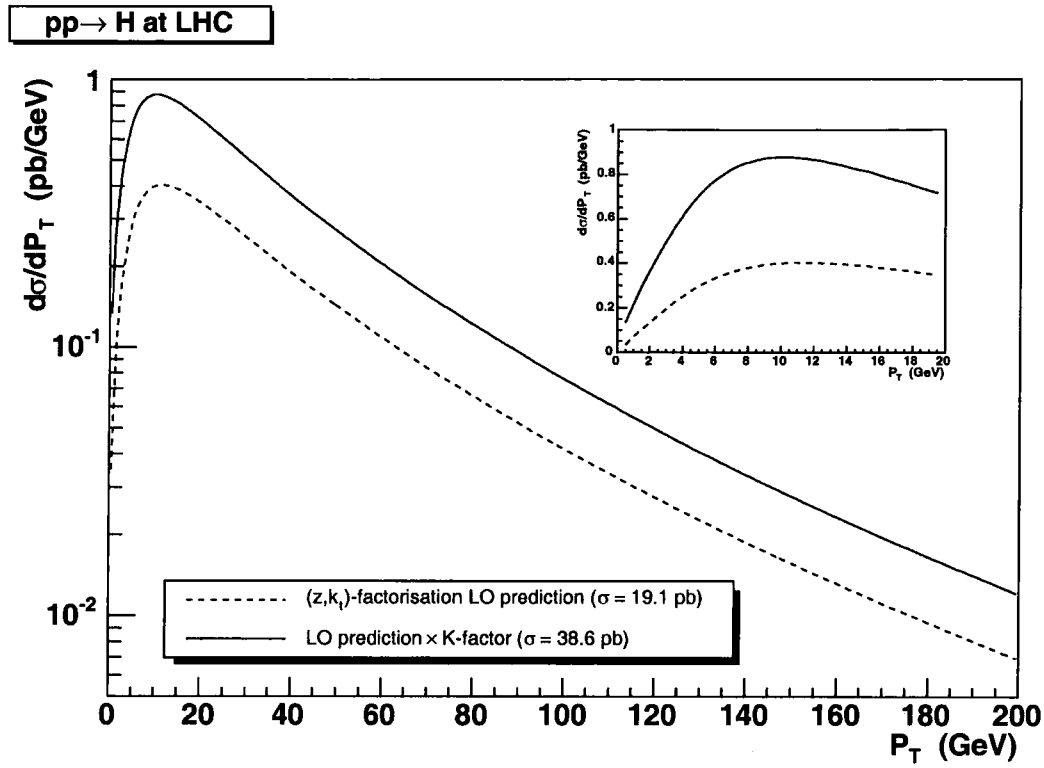

Figure 3.10: P_T distribution of SM Higgs bosons produced at the LHC with mass 125 GeV.

The squared matrix element $|\mathcal{M}(g_1^* g_2^* \to H)|^2$, given in the first line of (3.24), was evaluated with $k_i = x_i P_i + k_{i\perp}$ and the sums over gluon polarisations $d_{\mu\rho}(k_1, n)$ and $d_{\nu\sigma}(k_2, n)$ replaced by the BFKL-like polarisation tensors (1.66), as in the k_t-factorisation prescription. The difference with respect to the last line of (3.24) is an extra factor of $2\cos^2\phi$, where ϕ is the azimuthal angle between $\boldsymbol{k_{1,t}}$ and $\boldsymbol{k_{2,t}}$. This extra factor makes little difference to the P_T distribution shown in Figs. 3.10 and 3.11, except in the region of low $P_T \lesssim 10$ GeV where the cross section is slightly enhanced.

3.5 Summary

In this chapter we have extended the method of (z, k_t)-factorisation using DUPDFs to hadron-hadron collisions. The key idea is that the incoming partons to the subprocess have finite transverse momenta, which can be observed in the particles produced in the final state. This transverse momentum is generated perturbatively in the last evolution step, with a suitable extrapolation for the non-perturbative contribution. Virtual terms in the DGLAP equation are resummed into Sudakov form factors and angular-ordering constraints are applied which regulate soft gluon

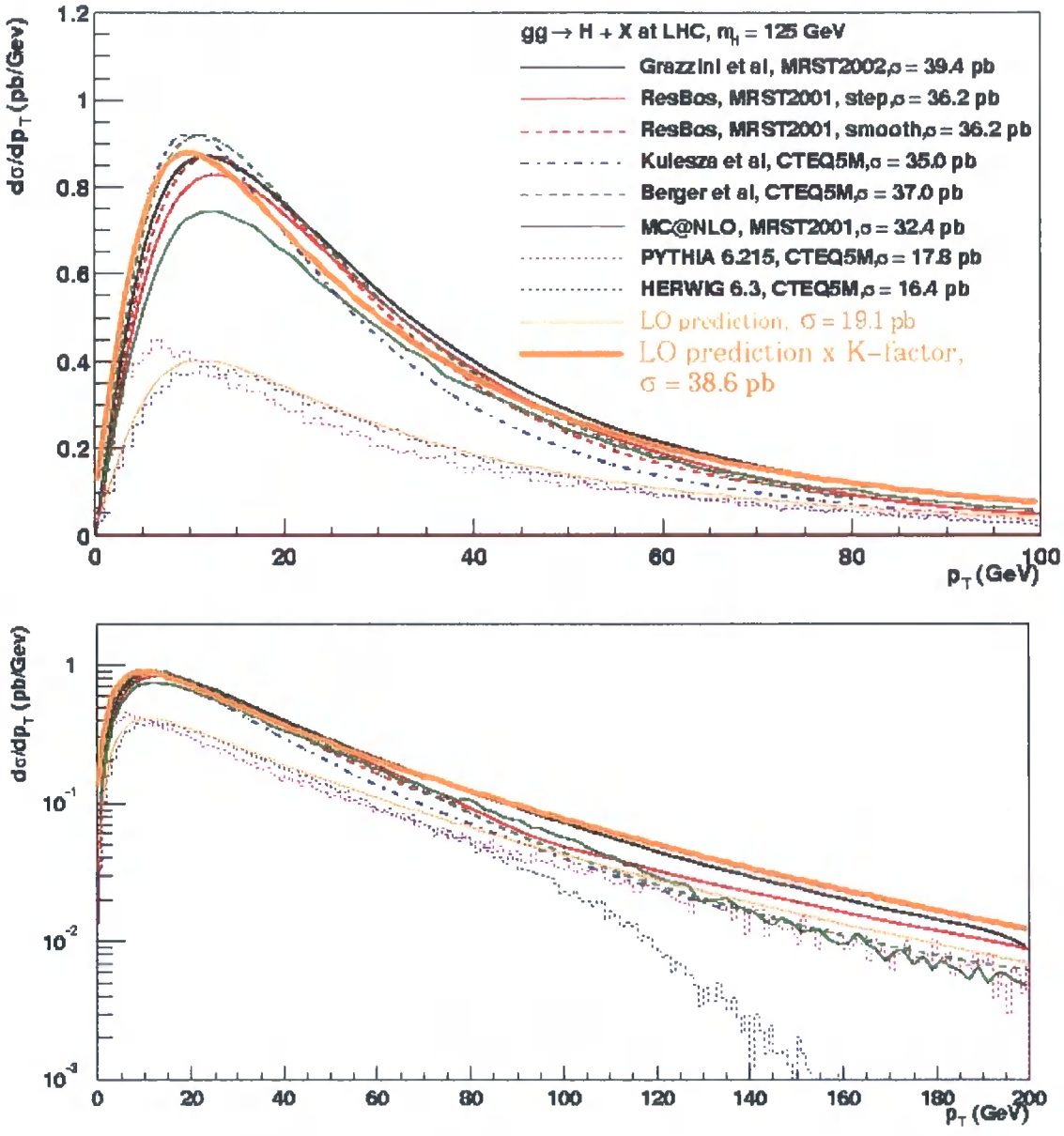

Figure 3.11: P_T distribution of SM Higgs bosons produced at the LHC with mass 125 GeV, compared to various resummed and parton shower predictions which are all matched to fixed-order calculations at large P_T (apart from HERWIG) [112].

emission. By accounting for the precise kinematics in the subprocess, together with these Sudakov form factors and angular-ordering constraints, we are able to include the main part of conventional higher order calculations.

We used this framework to calculate the P_T distributions of W and Z bosons produced at the Tevatron Run 1. The predictions gave a very good description of CDF and DØ data over the whole P_T range, after multiplying by an overall factor of 1.1–1.2, corresponding to multiplying each DUPDF by a factor $\lesssim 1.1$. We explained the origin of the need for this extra factor, which should not be regarded as a deficiency of our approach, but rather reflects the fact that the input integrated PDFs should themselves be determined from data using (z, k_t)-factorisation.

We also used the framework to calculate the P_T distribution for SM Higgs bosons of mass 125 GeV produced at the LHC. For $P_T \lesssim M_H$, our simple prescription was found to reproduce, to a fair degree, the predictions of more elaborate theoretical studies [112].

Part II

Diffractive parton distributions and absorptive corrections

Chapter 4

Diffractive deep-inelastic scattering

In this introductory chapter to Part II we begin by introducing the Pomeron in the context of Regge theory, and explain how it appears in diffractive processes, particularly in diffractive DIS. We describe one of the most popular descriptions of diffractive DIS, in which the Pomeron is treated as having PDFs just like a hadron. Finally, we explain how the Pomeron may be interpreted in QCD as two gluons or two sea quarks in a colour singlet, and we evaluate the corresponding Feynman diagrams at lowest order in α_S.

4.1 Regge theory

Before QCD emerged victorious as the theory of the strong interaction, the most promising candidate was Regge theory [116, 117], also known as the theory of complex angular momentum [118], which provided a natural framework to discuss particles scattering at high CM energies, $s \gg |t|$. Regge theory was founded on some very general properties of the S-matrix, namely Lorentz invariance, unitarity, and analyticity. Here, we briefly review a few key features of Regge phenomenology; for more details, see the textbooks [15–19].

In Regge theory, the scattering amplitude $\mathcal{A}(s,t)$ can be viewed as the exchange in the t-channel of a Regge trajectory or 'Reggeon' with 'angular momentum' $\alpha(t)$. The Reggeon is not a single particle, but rather a series of particles of different spins. For positive t the amplitude has poles corresponding to the exchange of physical particles of mass m_i and spin J_i, where $\alpha(m_i^2) = J_i$. Plotting the spins of

low-lying mesons against their masses squared gives a linear trajectory [117, 119],

$$\alpha(t) = \alpha(0) + \alpha' t, \tag{4.1}$$

with $\alpha(0) = 0.55$ and $\alpha' = 0.86$ GeV^{-2} for the ρ-trajectory [17]. The asymptotic behaviour of the total cross section for a scattering process dominated by a particular Regge trajectory is given by

$$\sigma_{\text{tot}} \propto s^{\alpha(0)-1}. \tag{4.2}$$

Therefore, a Regge trajectory with intercept $\alpha(0) < 1$ leads to a total cross section which falls as s increases. In fact a consequence of the Pomeranchuk theorem [120, 121], which proved that cross sections for particle–particle and particle–antiparticle scattering become equal at asymptotic energies, is that the cross section vanishes asymptotically for any scattering process with charge exchange. Conversely, if a cross section does *not* fall as s increases then that process must be dominated by the exchange of vacuum quantum numbers [122]. The fact that total cross sections are observed experimentally to slowly rise with increasing s may be attributed to an effective Reggeon with intercept $\alpha_{I\!P}(0) > 1$ and with the quantum numbers of the vacuum.[1] This effective Regge trajectory was called the Pomeron [123]. It has been claimed that glueball states lie on this trajectory when extrapolated to positive t, although this interpretation is controversial.

Donnachie and Landshoff [124] made a fit to total cross sections for pp and $p\bar{p}$ scattering:

$$\begin{aligned} \sigma_{pp} &= \left(21.7\, s^{0.08} + 56.1\, s^{-0.45}\right) \text{ mb}, \\ \sigma_{p\bar{p}} &= \left(21.7\, s^{0.08} + 98.4\, s^{-0.45}\right) \text{ mb}, \end{aligned} \tag{4.3}$$

with s in GeV^2. Here, the first term is the Pomeron ($I\!P$) contribution with intercept $\alpha_{I\!P}(0) = 1.08$, while the second term is a sub-leading Reggeon ($I\!R$) contribution with intercept $\alpha_{I\!R}(0) = 0.55$. Note that associating $\alpha_{I\!P}(0) = 1.08$ to a simple Regge pole would eventually lead to a violation of the Froissart-Martin bound [125, 126]:

$$\sigma_{\text{tot}} < C \ln^2 s, \tag{4.4}$$

where $C \sim 60$ mb. However, $\alpha_{I\!P}(0) = 1.08$ is only an effective Pomeron intercept which includes the effects of exchange of two or more Pomerons (so-called Regge cuts). For example, taking into account the $I\!P$-pole and the $I\!P \otimes I\!P$ cut (4.2) is

[1] Originally, a Reggeon with $\alpha_{I\!P}(0) = 1$ was introduced to account for the asymptotically constant total cross sections expected in the early 1960s.

modified to [18]

$$\sigma_{\rm tot} \sim A_{I\!P}\, s^{\alpha_{I\!P}(0)-1} - A_{I\!P\otimes I\!P}\, \frac{s^{2(\alpha_{I\!P}(0)-1)}}{\ln s}. \tag{4.5}$$

These multiple exchanges tame the asymptotic rise of the cross section leading to the ultimate preservation of unitarity. The success of the Donnachie-Landshoff fit (4.3) suggests that the reduction of the effective Pomeron intercept as the energy increases is very slow. In any case, with $\alpha_{I\!P}(0) = 1.08$ the Froissart-Martin bound (4.4) is not violated for CM energies less than the Planck scale.

In low-Q^2 DIS the $\gamma^* p$ CM energy W plays the rôle of $\sqrt{s}$ in hadronic cross sections. Hence, for $Q^2 \ll W^2$, then $x_B \simeq Q^2/W^2 \ll 1$ and we would expect the proton structure function to satisfy

$$\begin{aligned} F_2(x_B, Q^2 \lesssim 1\ {\rm GeV}^2) &\sim A_{I\!P}\, x_B^{1-\alpha_{I\!P}(0)} + A_{I\!R}\, x_B^{1-\alpha_{I\!R}(0)} \\ &\simeq A_{I\!P}\, x_B^{-0.08} + A_{I\!R}\, x_B^{0.45}, \end{aligned} \tag{4.6}$$

where we have taken the same intercepts as found in the Donnachie-Landshoff fit (4.3). At higher $Q^2 \gtrsim 1$ GeV^2, QCD evolution takes over modifying the x_B dependence. Indeed, parameterising the HERA data for $x_B < 0.1$ in the form $F_2(x_B, Q^2) = A(Q^2)\, x_B^{-\lambda}$ gives $\lambda \simeq 0.1$ at small $Q^2 \lesssim 1$ GeV^2, and $\lambda \simeq 0.3$ at large $Q^2 \sim$ 10–100 GeV^2. In terms of PDFs, the Pomeron is identified with the flavour-singlet sea quark and gluon distributions, while the sub-leading Reggeon is identified with the non-singlet valence quark distributions. Thus, the Regge theory predictions for the small-x and low $Q^2 \lesssim 1$ GeV^2 behaviour of the PDFs are

$$\begin{aligned} x q_V(x, Q^2) &\sim x^{1-\alpha_{I\!R}(0)} \simeq x^{0.45}, \\ x S(x, Q^2), x g(x, Q^2) &\sim x^{1-\alpha_{I\!P}(0)} \simeq x^{-0.08}. \end{aligned} \tag{4.7}$$

In Table 4.1 we compare these predictions with the $x \to 0$ behaviour of the MRST2001 NLO PDFs [127] at the input scale of $Q_0^2 = 1$ GeV^2. The valence quark distributions are roughly in line with the Regge theory expectations. However, the sea quark and gluon distributions behave very differently. The sea quark distribution increases with decreasing x while the gluon becomes increasingly negative with decreasing x. The negative gluon was introduced by MRST to achieve an acceptable fit to data; demanding a positive gluon would lead to a strongly valence-like input gluon distribution and to a much worse description of the data [127]. Such differing behaviour of the sea quark and gluon distributions is totally contradictory to Regge theory expectations. We will discuss this puzzle in more detail in Chapter 6.

	Regge theory	MRST2001 NLO
$xu_V(x,Q_0^2)$	$x^{0.45}$	$x^{0.25}$
$xd_V(x,Q_0^2)$	$x^{0.45}$	$x^{0.27}$
$xS(x,Q_0^2)$	$x^{-0.08}$	$x^{-0.26}$
$xg(x,Q_0^2)$	$x^{-0.08}$	$-x^{-0.33}$

Table 4.1: Regge theory expectations for the small-x behaviour of PDFs compared to the $x \to 0$ behaviour of the MRST2001 NLO PDFs [127] at $Q_0^2 = 1$ GeV^2.

4.2 What is diffraction?

The term 'diffraction' was introduced in nuclear high-energy physics in the 1950s, in analogy with the familiar optical phenomenon. Two equivalent definitions of what is meant by diffraction in high-energy physics are given in [18]. The first is due to Good and Walker [128]:

> A reaction in which no quantum numbers are exchanged between the colliding particles is, at high energies, a diffractive reaction.

The Reggeon which dominates at asymptotic energies is the Pomeron. Some secondary Reggeons, contributing to non-diffractive events, also have the quantum numbers of the vacuum, but are suppressed at high energies. It is often difficult to know experimentally whether or not the outgoing system has the same quantum numbers as the incoming particles. A more operational definition was given by Bjorken [129]:

> A diffractive reaction is characterised by a large, non-exponentially suppressed, rapidity gap in the final state.

The large rapidity gap, a region of the detector devoid of particles, arises from the fact that the colourless Pomeron does not radiate as it is exchanged. Again, the requirement purely of a large rapidity gap will include some contamination from non-diffractive events with secondary Reggeon exchange, but these contributions are exponentially suppressed as a function of the gap size.

Soft diffractive reactions, such as elastic hadron-hadron scattering and diffractive dissociation, are characterised by a scale of the order of the hadron size ($\sim$ 1 fm), and so are intrinsically non-perturbative and therefore unable to be described by perturbative QCD. Regge theory has had considerable phenomenological success[2] in describing such soft reactions, where there is no alternative theoretical framework available.

[2]Indeed, Donnachie and Landshoff [124] conclude their paper with the statement that "Regge theory remains one of the great truths of particle physics."

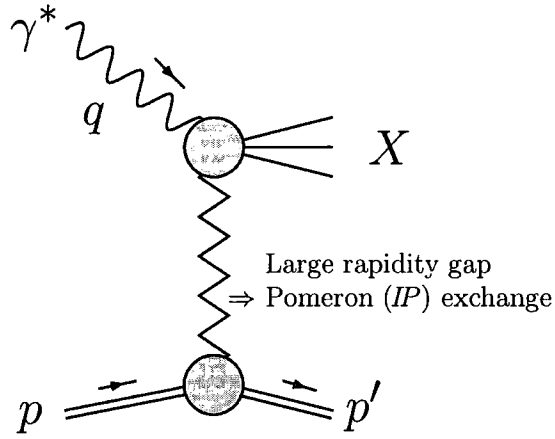

Figure 4.1: Diffractive DIS kinematics.

On the other hand, hard diffractive reactions are characterised by an additional 'hard' energy scale ($\gtrsim 1$ GeV^2) and thus they allow use of perturbative QCD to some extent. The ultimate goal is to translate Regge theory into QCD. We will play a small part towards achieving this goal in Chapter 5, where we present a QCD analysis of diffractive DIS. In this case, the hard energy scale is provided by the photon virtuality Q^2.

4.3 Diffractive DIS kinematics

A notable feature of deep-inelastic scattering is the existence of diffractive events, $\gamma^* p \to Xp$, in which the slightly deflected proton and the cluster X of outgoing hadrons are well-separated in rapidity; see Fig. 4.1. The large number and distinctive character of diffractive events discovered at HERA [130, 131] was somewhat surprising [132]. The large rapidity gap is believed to be associated with Pomeron exchange. The diffractive events make up an appreciable fraction ($\approx 10\%$) of all (inclusive) deep-inelastic events, $\gamma^* p \to X$. We will refer to the diffractive and inclusive processes as DDIS and DIS respectively.

First we define the basic kinematical variables in DDIS, without recourse to any specific theoretical model for the Pomeron. We use a Sudakov decomposition of the momenta of the incoming and outgoing protons:

$$p = P' + \alpha_p Q', \qquad p' = (1 - x_{I\!P})\, P' + \alpha_{p'} Q' + p'_\perp, \tag{4.8}$$

where P' and Q' are lightlike 4-vectors ($P'^2 = 0 = Q'^2$), and $p'_\perp$ is a spacelike 4-vector such that ${p'_\perp}^2 = -p'^2_t$. The on-shell conditions, $p^2 = m_p^2 = p'^2$, where m_p is

the proton mass, give

$$\alpha_p = \frac{m_p^2}{2\,P'\cdot Q'}, \qquad \alpha_{p'} = \frac{m_p^2 + {p'_t}^2}{2\,P'\cdot Q'\,(1-x_{I\!P})}, \tag{4.9}$$

leading to the squared momentum transferred by the Pomeron,

$$t \equiv (p-p')^2 = -\frac{x_{I\!P}^2\, m_p^2 + {p'_t}^2}{1-x_{I\!P}}. \tag{4.10}$$

The minimum value of $|t|$ occurs when $p'_t = 0$, that is,

$$t_{\min} = -\frac{x_{I\!P}^2\, m_p^2}{1-x_{I\!P}}. \tag{4.11}$$

Since most DDIS events occur for small values of $|t|$, and $x_{I\!P} \ll 1$, $m_p^2, |t| \ll Q^2, M_X^2, W^2$, we will make the approximations $m_p \simeq 0$ GeV and $t \simeq t_{\min} \simeq 0$ GeV^2 in our calculations. That is, we will assume that $p \simeq P'$ and $p' \simeq (1-x_{I\!P})P'$.

As usual in DIS, we define the photon virtuality, $q^2 \equiv -Q^2$, the $\gamma^* p$ CM energy squared, $W^2 \equiv (q+p)^2$, and the Bjorken-x variable,

$$x_B \equiv \frac{Q^2}{2p\cdot q} = \frac{Q^2}{Q^2+W^2}, \tag{4.12}$$

which gives the fraction of the proton's momentum carried by the struck quark. In DDIS we additionally define the invariant mass squared of the hadronic system X produced by the photon dissociation, $M_X^2 \equiv (q+p-p')^2$. This definition leads to

$$x_{I\!P} = \frac{Q^2+M_X^2}{Q^2+W^2}, \qquad \beta \equiv \frac{x_B}{x_{I\!P}} = \frac{Q^2}{Q^2+M_X^2}, \tag{4.13}$$

where $x_{I\!P}$ is the fraction of the proton's momentum carried by the Pomeron and β is the fraction of the Pomeron's momentum carried by the struck quark.

Neglecting the proton mass, the size of the rapidity gap between the outgoing proton and the hadronic system X is

$$\Delta\eta \equiv \eta(p') - \eta(q+p-p') \simeq \frac{1}{2}\ln\left(\frac{1-x_{I\!P}}{x_{I\!P}^2}\,\frac{Q^2}{|t|}\,\frac{1-\beta}{\beta}\right). \tag{4.14}$$

If $x_{I\!P} \ll 1$, $Q^2 \sim |t|$, $\beta \sim 0.5$, then $\Delta\eta \sim \ln(1/x_{I\!P})$.

4.4 Diffractive structure function

Recall from (1.20) that the ep cross section in DIS is related to the $\gamma^* p$ cross section by

$$\frac{\mathrm{d}^2\sigma^{ep}}{\mathrm{d}x_B\,\mathrm{d}Q^2} = \frac{\alpha_{\mathrm{em}}}{2\pi x_B Q^2}\left\{\left[1+(1-y)^2\right]\sigma^{\gamma^* p} - y^2\sigma_L^{\gamma^* p}\right\}, \tag{4.15}$$

where $\sigma^{\gamma^* p} = \sigma_T^{\gamma^* p} + \sigma_L^{\gamma^* p}$, $y = Q^2/(x_B s)$, and the ep CM energy squared, $s = 4E_e E_p$. Now consider the more specific case of DDIS. We have $x_B = \beta x_{I\!P}$, so (4.15) can be written

$$\frac{\mathrm{d}^2\sigma^{ep}}{\mathrm{d}x_{I\!P}\,\mathrm{d}Q^2} = \frac{\alpha_{\mathrm{em}}}{2\pi x_{I\!P} Q^2}\left\{\left[1+(1-y)^2\right]\sigma^{\gamma^* p} - y^2\sigma_L^{\gamma^* p}\right\}, \tag{4.16}$$

where σ are now the diffractive components of the ep or $\gamma^* p$ cross sections. The diffractive structure function, $F_2^{D(4)}(x_{I\!P}, \beta, Q^2, t)$, is defined via

$$\frac{\mathrm{d}^4\sigma^{ep}}{\mathrm{d}x_{I\!P}\,\mathrm{d}\beta\,\mathrm{d}Q^2\,\mathrm{d}t} = \frac{2\pi\alpha_{\mathrm{em}}^2}{\beta Q^4}\left\{\left[1+(1-y)^2\right]F_2^{D(4)} - y^2 F_L^{D(4)}\right\}. \tag{4.17}$$

For small y, or assuming that $F_L^{D(4)} \ll F_2^{D(4)}$, the last term may be neglected. By comparing (4.16) and (4.17), we obtain

$$F_2^{D(4)} = \frac{Q^2}{4\pi^2\alpha_{\mathrm{em}}}\frac{\beta}{x_{I\!P}}\frac{\mathrm{d}^2\sigma^{\gamma^* p}}{\mathrm{d}\beta\,\mathrm{d}t}. \tag{4.18}$$

Experimental measurements are usually integrated over t:

$$F_2^{D(3)}(x_{I\!P}, \beta, Q^2) = \int_{t_{\mathrm{cut}}}^{t_{\mathrm{min}}} \mathrm{d}t\; F_2^{D(4)}(x_{I\!P}, \beta, Q^2, t), \tag{4.19}$$

where $t_{\mathrm{cut}} = -1\ \mathrm{GeV}^2$ and $t_{\mathrm{min}} \simeq 0\ \mathrm{GeV}^2$.

4.5 Collinear factorisation in DDIS

Just as measurements of the DIS structure function $F_2(x_B, Q^2)$ are used to determine the PDFs of the proton, $a(x, Q^2) = xg(x, Q^2)$ or $xq(x, Q^2)$, so measurements of the DDIS structure function $F_2^{D(3)}(x_{I\!P}, \beta, Q^2)$ can be used to determine the *diffractive* PDFs (DPDFs) of the proton, $a^D(x_{I\!P}, \beta, Q^2) = \beta g^D(x_{I\!P}, \beta, Q^2)$ or $\beta q^D(x_{I\!P}, \beta, Q^2)$.[3]

In DDIS, the collinear factorisation formula for the $\gamma^* p$ cross section, analogous

[3]DPDFs are exactly the same as 'extended fracture functions' [133–135].

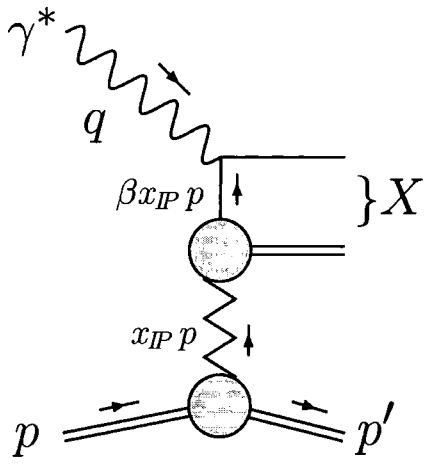

Figure 4.2: LO contribution to DDIS in the 'resolved' Pomeron model.

to (1.35), can be written

$$\frac{\mathrm{d}\sigma^{\gamma^* p}}{\mathrm{d}x_{I\!P}} = \sum_{a=q,g} \int_{\beta}^{1} \frac{\mathrm{d}\beta'}{\beta'}\, a^D(x_{I\!P}, \beta', Q^2)\, \hat{\sigma}^{\gamma^* a}, \tag{4.20}$$

where $a^D(x_{I\!P}, \beta', Q^2)$ satisfy DGLAP evolution in Q^2, and $\hat{\sigma}^{\gamma^* a}$ are the *same* partonic cross sections or hard-scattering coefficients as in DIS. Collinear factorisation was proven to hold for all DDIS processes by Collins [136, 137], but fails for diffractive hadron-hadron collisions, where an additional rapidity gap 'survival probability' [129] due to multi-Pomeron exchange is needed [138, 139]. The same factorisation breaking has recently been observed for the resolved photon component in diffractive dijet photoproduction [140, 141] and low-Q^2 DIS [142] at HERA.

4.6 'Resolved' Pomeron model

Ingelman-Schlein factorisation [143] is collinear factorisation together with 'Regge factorisation' for the Pomeron exchange, where the $x_{I\!P}$ dependence of the DPDFs factorises into a Pomeron flux factor, $f_{I\!P}(x_{I\!P})$, and the β and Q^2 dependence is given by the PDFs of the Pomeron, $a^{I\!P}(\beta, Q^2) = \beta g^{I\!P}(\beta, Q^2)$ or $\beta q^{I\!P}(\beta, Q^2)$. In this 'resolved' Pomeron model, the Pomeron is treated as having partonic structure just like a hadron; see Fig. 4.2 where the LO contribution to the Pomeron structure function is shown. Variations of this method have been used to fit DDIS data by many different groups (see, for example, [144–147]). Here, we summarise the procedure recently used by the H1 Collaboration [148], where Regge factorisation is

assumed,

$$a^D(x_{I\!P}, \beta, Q^2) = f_{I\!P}(x_{I\!P})\, a^{I\!P}(\beta, Q^2), \tag{4.21}$$

$$F_2^{D(3)}(x_{I\!P}, \beta, Q^2) = f_{I\!P}(x_{I\!P})\, F_2^{I\!P}(\beta, Q^2). \tag{4.22}$$

The Pomeron flux factor is taken from Regge phenomenology,

$$f_{I\!P}(x_{I\!P}) = \int_{t_{\rm cut}}^{t_{\rm min}} \mathrm{d}t \frac{\mathrm{e}^{B_{I\!P}\, t}}{x_{I\!P}^{2\alpha_{I\!P}(t)-1}}, \tag{4.23}$$

with $\alpha_{I\!P}(t) = \alpha_{I\!P}(0) + \alpha'_{I\!P}\, t$. The parameters $\alpha'_{I\!P}$ and $B_{I\!P}$ are taken from fits to soft hadron data, with

$$\alpha_{I\!P}(0) = 1.173 \pm 0.018(\text{stat.}) \pm 0.017(\text{syst.})^{+0.063}_{-0.035}(\text{model}) \tag{4.24}$$

determined from a fit to the DDIS data. Note that the only real use of the Pomeron in this analysis is as a label for a particular power law for the $x_{I\!P}$ dependence of diffractive cross sections, with the exponent actually being a free power. The value of $\alpha_{I\!P}(0)$ extracted from the DDIS data lies significantly above the Donnachie-Landshoff [124] value of 1.08, suggesting that there are large perturbative QCD contributions.

In the preliminary H1 analysis [148], the input Pomeron PDFs at a scale $Q_0^2 = 3$ GeV^2 are parameterised in the form

$$a^{I\!P}(\beta, Q_0^2) = \left[\sum_{j=0}^{2} C_j^a\, T_j(2\beta - 1)\right]^2 \exp\left(-\frac{0.01}{1-\beta}\right), \tag{4.25}$$

where C_j^a are free parameters, and $T_0(x) = 1$, $T_1(x) = x$, and $T_2(x) = 2x^2 - 1$ are the first three Chebyshev polynomials. The sum of orthonormal polynomials is used so that the input distributions are free to adopt the widest possible range of forms for a given number of parameters. The square of this sum is taken to ensure positivity. The exponential factor ensures that the Pomeron PDFs tend to 0 as $\beta \to 1$. No momentum sum rule is imposed on the Pomeron PDFs.

Although this type of description of $F_2^{D(3)}(x_{I\!P}, \beta, Q^2)$ is often referred to as a 'QCD fit', only the Q^2 dependence is actually described by QCD, with the $x_{I\!P}$ dependence being obtained by fitting a power law, and the β dependence taken to be completely arbitrary. Clearly, we would like to be able to use QCD to constrain the $x_{I\!P}$ and β dependence of $F_2^{D(3)}(x_{I\!P}, \beta, Q^2)$, as well as the Q^2 dependence.

In the H1 analysis [148], a secondary Reggeon contribution is also included of

a form similar to (4.22). The Reggeon flux factor is taken in the form (4.23) with $\alpha_{I\!R}(0) = 0.50$. The Reggeon PDFs are assumed to be the same as the pion PDFs [149]. This contribution is found to be significant only for $x_{I\!P} > 0.01$.

Since the Pomeron is not a particle, and so the concept of a 'Pomeron flux' is not well defined, the 'resolved' Pomeron model must be taken on a purely phenomenological basis.

4.7 The Pomeron in QCD

Attempts to understand the Pomeron in terms of QCD were first made by interpreting Pomeron exchange as *two-gluon* exchange [150, 151], two gluons being the minimum number needed to reproduce the quantum numbers of the vacuum. Accounting for all $\alpha_S \ln(1/x_B)$ terms, the BFKL Pomeron is a gluon ladder in a colour singlet configuration, as described in Section 1.4. The BFKL Pomeron is often called the 'hard' Pomeron in distinction to the 'soft' Pomeron with effective intercept $\alpha_{I\!P}(0) \simeq 1.08$ discussed in Section 4.1. The LL BFKL Pomeron has effective intercept $\alpha_{I\!P}(0) \simeq 1.5$ while the resummed NLL BFKL Pomeron has effective intercept $\alpha_{I\!P}(0) \simeq 1.3$ (see, for example, [47]), cf. the experimental value of $\simeq 1.3$ obtained from fitting F_2 data at large $Q^2 \sim 10$–100 GeV^2 (see Section 4.1). In naïve Regge theory, it was assumed that the Pomeron singularity is a simple pole in the complex angular momentum plane. By contrast, the BFKL Pomeron, consisting of a ladder of reggeised gluons, is a branch cut in the complex angular momentum plane [152]. Assuming that BFKL effects are not important at HERA energies, we will regard the QCD Pomeron as being a DGLAP ladder rather than a BFKL ladder.

In Section 4.7.1 we present calculations of the lowest order Feynman diagrams for the two-gluon Pomeron in DDIS using the dipole formalism, reproducing the results presented by Wüsthoff [153] in the limit of strongly-ordered transverse momenta. In Section 4.7.2 we extend the same formalism to calculate the lowest order Feynman diagrams for DDIS assuming that the Pomeron is represented by two sea quarks.

4.7.1 Two-gluon exchange

First we consider the kinematics of the quark dipole shown in Fig. 4.3(a). We use a Sudakov decomposition of the momentum k of the off-shell quark,

$$k = \alpha q' + \beta_k p + k_\perp, \tag{4.26}$$

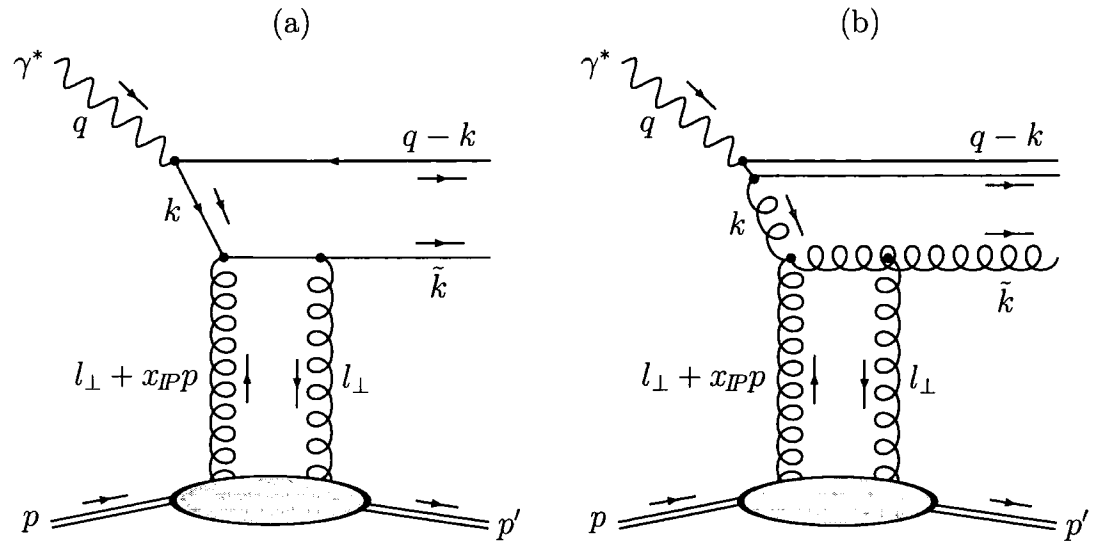

Figure 4.3: (a) Quark dipole and (b) effective gluon dipole interacting with the proton via a perturbative Pomeron represented by two t-channel gluons.

with $q' \equiv q + x_B\, p$, $q'^2 = 0 = p^2$, $k_\perp^2 = -k_t^2$. The two outgoing components of the dipole have momenta

$$q - k = (1-\alpha)\, q' + x_B \frac{k_t^2/Q^2}{1-\alpha}\, p - k_\perp, \tag{4.27}$$

$$\tilde{k} = k + x_{I\!P}\, p = \alpha\, q' + x_B \frac{k_t^2/Q^2}{\alpha}\, p + k_\perp, \tag{4.28}$$

where the on-shell conditions, $(q-k)^2 = 0$ and $\tilde{k}^2 = 0$, determine

$$\beta_k = -x_B \left(1 + \frac{k_t^2/Q^2}{1-\alpha}\right), \qquad x_{I\!P} = x_B \left(1 + \frac{k_t^2/Q^2}{\alpha(1-\alpha)}\right). \tag{4.29}$$

The invariant mass of the $q\bar{q}$ system is given by

$$M_X^2 = (q + x_{I\!P}\, p)^2 = \frac{k_t^2}{\alpha(1-\alpha)}. \tag{4.30}$$

Since $\beta = Q^2/(Q^2 + M_X^2)$, this can be written as

$$\alpha(1-\alpha)Q^2 = \beta \frac{k_t^2}{1-\beta} \equiv \beta\mu^2. \tag{4.31}$$

The off-shell quark with momentum k has virtuality

$$k^2 = -\frac{\mu^2}{1-\alpha} \simeq -\mu^2, \tag{4.32}$$

since $\alpha \ll 1$ in the approximation of strongly-ordered transverse momentum, $k_t^2 \ll Q^2$, to which we are working.[4]

Quark dipole with a transversely polarised photon

The differential $\gamma^* p$ cross section corresponding to Fig. 4.3(a) is given by a k_t-factorisation formula similar to that described in Section 1.4. It can be written in terms of photon wave functions $\Psi(\alpha, \boldsymbol{k_t})$, describing the fluctuation of the photon into a quark–antiquark dipole, convoluted over α and k_t with a dipole cross section $\hat{\sigma}$, describing the interaction of the dipole with the proton via two-gluon exchange. The dipole factorisation formula for Fig. 4.3(a) with a transversely polarised photon is

$$\left.\frac{\mathrm{d}\sigma_{T,q\bar{q}}^{\gamma^* p}}{\mathrm{d}t}\right|_{t=0} = \frac{N_C}{16\pi}\int_0^1 \mathrm{d}\alpha \int \frac{\mathrm{d}k_t^2}{2\pi} \sum_f e_f^2\, \alpha_{\mathrm{em}}\, \frac{1}{2} \sum_{\gamma=\pm 1} \sum_{h=\pm\frac{1}{2}} \left| \int \frac{\mathrm{d}^2\boldsymbol{l_t}}{\pi}\, D\Psi_h^\gamma \frac{\mathrm{d}\hat{\sigma}}{\mathrm{d}l_t^2} \right|^2, \quad (4.33)$$

cf. the corresponding result for DIS,[5]

$$\sigma_{T,q\bar{q}}^{\gamma^* p} = N_C \int_0^1 \mathrm{d}\alpha \int \frac{\mathrm{d}k_t^2}{2\pi} \sum_f e_f^2\, \alpha_{\mathrm{em}}\, \frac{1}{2} \sum_{\gamma=\pm 1} \sum_{h=\pm\frac{1}{2}} \int \frac{\mathrm{d}^2\boldsymbol{l_t}}{\pi} \left|\Psi_h^\gamma(\alpha, \boldsymbol{k_t}) - \Psi_h^\gamma(\alpha, \boldsymbol{k_t} + \boldsymbol{l_t})\right|^2 \frac{\mathrm{d}\hat{\sigma}}{\mathrm{d}l_t^2}. \quad (4.34)$$

The light-cone wave functions for the quark–antiquark dipole with a transversely polarised photon are [153]

$$\Psi_h^\gamma(\alpha, \boldsymbol{k_t}) = \frac{\sqrt{2}}{k_t^2 + \alpha(1-\alpha)Q^2} \times \begin{cases} (\alpha - 1)\,\boldsymbol{k_t} & : \quad \gamma = +1, h = +\frac{1}{2} \\ \alpha\,\boldsymbol{k_t} & : \quad \gamma = +1, h = -\frac{1}{2} \\ \alpha\,\boldsymbol{k_t}^* & : \quad \gamma = -1, h = +\frac{1}{2} \\ (\alpha - 1)\,\boldsymbol{k_t}^* & : \quad \gamma = -1, h = -\frac{1}{2} \end{cases}, \quad (4.35)$$

where γ and h denote the helicity of the photon and the quark respectively. Here, $\boldsymbol{k_t} = k_t^1 + \mathrm{i}\,k_t^2 = (k_t^1, k_t^2)$ and $\boldsymbol{k_t}^* = k_t^1 - \mathrm{i}\,k_t^2 = (k_t^1, -k_t^2)$. The denominator of these wave functions is the virtuality of the off-shell quark with momentum k:

$$k_t^2 + \alpha(1-\alpha)Q^2 = (1-\beta)\mu^2 + \beta\mu^2 = \mu^2 \simeq |k^2|. \quad (4.36)$$

Note that the wave functions are symmetric under $\alpha \to (1-\alpha)$ and $\boldsymbol{k_t} \to -\boldsymbol{k_t}$, corresponding to $q \leftrightarrow \bar{q}$, that is, (4.27) $\leftrightarrow$ (4.28), so we only need to sum over

[4] Actually, from (4.31), $k_t^2 \ll Q^2$ implies either $\alpha \ll 1$ or $(1-\alpha) \ll 1$, but it is conventional to take the former.

[5] Note the extra factor 2 in (4.34) compared to (7) of [153].

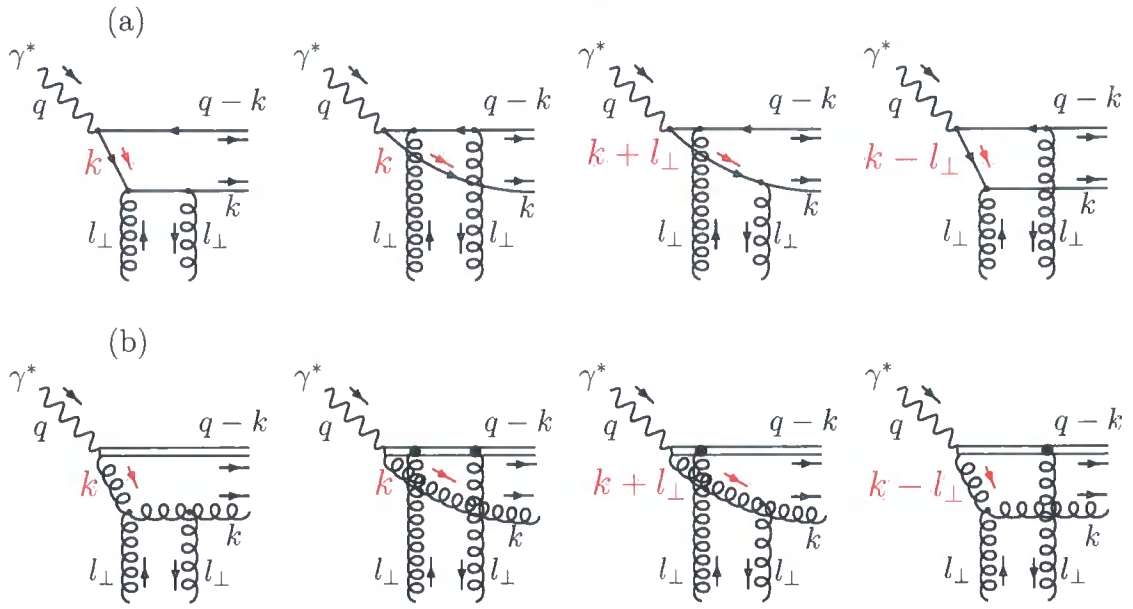

Figure 4.4: The four different permutations of the couplings of the two t-channel gluons to the two components of (a) the quark dipole and (b) the effective gluon dipole.

flavours in (4.33) and not over quarks and antiquarks separately.

The four different permutations of the couplings of the two t-channel gluons to the two components of the quark dipole, shown in Fig. 4.4(a), are obtained by simply shifting the argument of the wave function:

$$D\Psi(\alpha, \boldsymbol{k_t}, \boldsymbol{l_t}) \equiv 2\Psi(\alpha, \boldsymbol{k_t}) - \Psi(\alpha, \boldsymbol{k_t} + \boldsymbol{l_t}) - \Psi(\alpha, \boldsymbol{k_t} - \boldsymbol{l_t}). \tag{4.37}$$

We choose a basis where $\boldsymbol{k_t} = k_t\,(1,0)$ and $\boldsymbol{l_t} = l_t\,(\cos\phi, \sin\phi)$ and neglect the $x_{I\!P}\,p$ components of the momenta. We work in the approximation of strongly-ordered transverse momenta, $l_t \ll k_t \ll Q$, and expand $D\Psi$ in the limit $l_t \to 0$, only keeping the leading term proportional to l_t^2. After doing the azimuthal integral, we find

$$\int_0^{2\pi} \frac{\mathrm{d}\phi}{2\pi} D\Psi_h^\gamma(\alpha, \boldsymbol{k_t}, \boldsymbol{l_t}) = l_t^2 \frac{4\sqrt{2}\alpha(1-\alpha)Q^2}{\left[k_t^2 + \alpha(1-\alpha)Q^2\right]^3} \times \begin{cases} (\alpha-1)\,\boldsymbol{k_t} & : \quad \gamma = +1, h = +\frac{1}{2} \\ \alpha\,\boldsymbol{k_t} & : \quad \gamma = +1, h = -\frac{1}{2} \\ \alpha\,\boldsymbol{k_t}^* & : \quad \gamma = -1, h = +\frac{1}{2} \\ (\alpha-1)\,\boldsymbol{k_t}^* & : \quad \gamma = -1, h = -\frac{1}{2} \end{cases}, \tag{4.38}$$

cf. (21) of [153]. We need these expressions squared and summed over helicities.

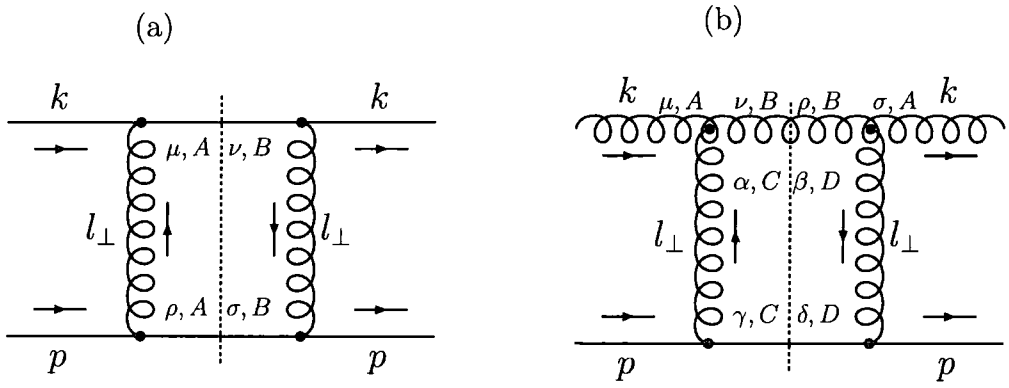

Figure 4.5: Cut diagrams giving the dipole cross sections for the two-gluon Pomeron: (a) $qq \to qq$ and (b) $gq \to gq$.

Neglecting a term $\mathcal{O}(k_t^2/Q^2)$ gives

$$\sum_{\gamma=\pm 1}\sum_{h=\pm\frac{1}{2}}\left|\int_0^{2\pi}\frac{\mathrm{d}\phi}{2\pi}D\Psi_h^{\gamma}(\alpha,\boldsymbol{k_t},\boldsymbol{l_t})\right|^2 = l_t^4\,\frac{64}{\mu^6}\,\beta^2(1-\beta). \tag{4.39}$$

The other necessary part of the calculation is the cross section for $qp \to qp$, obtained from the process $qq \to qq$ with t-channel gluon exchange, shown in Fig. 4.5(a). (Note that we could equally well obtain the cross section for $qp \to qp$ from $qg \to qg$, but the algebra is slightly easier for $qq \to qq$.) We assume that $k^2 \simeq 0$ and neglect the $x_{I\!P}\,p$ components of the momenta in these calculations.

First, we derive the differential cross section, $\mathrm{d}\hat{\sigma}/\mathrm{d}|\hat{t}|$, for a generic $2 \to 2$ scattering process. Let the incoming particles have momenta p_1 and p_2, while the outgoing particles have momenta p_3 and p_4. We write the momenta in the CM frame of the colliding particles as $p_1 = (E, 0, 0, E)$, $p_2 = (E, 0, 0, -E)$, $p_3 = (E_3, \boldsymbol{p_3})$, and $p_4 = (E_4, \boldsymbol{p_4})$, where $p_1^2 = p_2^2 = p_3^3 = p_4^2 = 0$. The phase space element is

$$\mathrm{d}\Phi = (2\pi)^4\,\delta^{(4)}\left(p_1 + p_2 - p_3 - p_4\right)\,\frac{\mathrm{d}^3\boldsymbol{p_3}}{2E_3\,(2\pi)^3}\,\frac{\mathrm{d}^3\boldsymbol{p_4}}{2E_4\,(2\pi)^3} \tag{4.40}$$

$$= \frac{1}{4\pi^2}\,\delta\left(2E - E_3 - E_4\right)\,\frac{\mathrm{d}^3\boldsymbol{p_3}}{4E_3E_4}, \tag{4.41}$$

with $\boldsymbol{p_3} = -\boldsymbol{p_4} \equiv (\boldsymbol{l_t}, p_z)$, $E_3 = E_4 = \sqrt{l_t^2 + p_z^2}$, and $\mathrm{d}^3\boldsymbol{p_3} = \mathrm{d}^2\boldsymbol{l_t}\,\mathrm{d}p_z = \pi\,\mathrm{d}l_t^2\,\mathrm{d}p_z$, so

$$\mathrm{d}\Phi = \frac{1}{8\pi}\,\delta\left(E - \sqrt{l_t^2 + p_z^2}\right)\,\frac{\mathrm{d}l_t^2\,\mathrm{d}p_z}{4E_3E_4} = \frac{1}{8\pi}\,\frac{E}{\sqrt{E^2 - l_t^2}}\,\frac{\mathrm{d}l_t^2}{4E^2}. \tag{4.42}$$

Taking the high-energy limit ($E \gg l_t$) we have $\hat{t} = (p_1 - p_3)^2 = (p_2 - p_4)^2 = -l_t^2$, and so, since $\hat{s} = (p_1 + p_2)^2 = (p_3 + p_4)^2 = 4E^2$, then $\mathrm{d}\Phi = \mathrm{d}|\hat{t}|/(8\pi\hat{s})$. Since

$\mathrm{d}\hat{\sigma} = \mathrm{d}\Phi\,|\mathcal{M}|^2 / F$, where $F = 2\hat{s}$, we have the differential cross section

$$\frac{\mathrm{d}\hat{\sigma}}{\mathrm{d}|\hat{t}|} = \frac{|\mathcal{M}|^2}{16\pi\hat{s}^2}. \tag{4.43}$$

We now return to the $qq \to qq$ process shown in Fig. 4.5(a), where $\hat{s} = 2\,k\cdot p = \alpha\,Q^2/x_B \simeq \mu^2/x_{I\!P}$ and $\hat{t} = -l_t^2$. The squared matrix element for $qq \to qq$ is

$$|\mathcal{M}|^2 = \frac{1}{4}\mathcal{C}\,\frac{g^4}{l_t^4}\,\mathrm{Tr}[\gamma^\mu \not{k}\gamma^\nu(\not{k}+\not{l}_\perp)]\,\mathrm{Tr}[\gamma^\rho \not{p}\gamma^\sigma(\not{p}-\not{l}_\perp)]\,(-g_{\mu\rho})(-g_{\nu\sigma}), \tag{4.44}$$

where the colour factor is

$$\mathcal{C}(qq \to qq) = \frac{1}{N_C^2}\mathrm{Tr}[t^A t^B]\mathrm{Tr}[t^A t^B] = \frac{2}{9}. \tag{4.45}$$

In the high-energy limit, where only the terms to leading $\mathcal{O}(\hat{s}/|\hat{t}|)$ are retained, that is, in the $l_t \to 0$ limit,

$$\frac{\mathrm{d}\hat{\sigma}}{\mathrm{d}l_t^2}(qq \to qq) = \frac{1}{l_t^4}\frac{8\pi}{9}\alpha_S(l_t^2)\alpha_S(\mu^2), \tag{4.46}$$

where appropriate scales for α_S have been chosen corresponding to the two different vertices in Fig. 4.5(a). The lower vertex in Fig. 4.5(a) may be considered as the first step of DGLAP evolution, which generates the unintegrated gluon distribution of the proton, $f_g(x_{I\!P}, l_t^2, \mu^2)$. Therefore, we obtain the cross section for $qp \to qp$ by making the replacement

$$\frac{\alpha_S(l_t^2)}{2\pi}x_{I\!P}P_{gq}(x_{I\!P})\Big|_{x_{I\!P}\ll 1} = \frac{\alpha_S(l_t^2)}{2\pi}2C_F = \frac{4}{3\pi}\alpha_S(l_t^2) \to f_g(x_{I\!P}, l_t^2, \mu^2). \tag{4.47}$$

This replacement accounts for more complicated diagrams than Fig. 4.5(a) which include the complete DGLAP evolution:

$$\frac{\mathrm{d}\hat{\sigma}}{\mathrm{d}l_t^2}(qp \to qp) = \frac{1}{l_t^4}\frac{2\pi^2}{3}\alpha_S(\mu^2) f_g(x_{I\!P}, l_t^2, \mu^2). \tag{4.48}$$

Combining (4.39) and (4.48) we obtain

$$\sum_{\gamma=\pm1}\sum_{h=\pm\frac{1}{2}}\left|\int\frac{\mathrm{d}^2\boldsymbol{l_t}}{\pi}\,D\Psi_h^\gamma\,\frac{\mathrm{d}\hat{\sigma}}{\mathrm{d}l_t^2}\right|^2 = \frac{64}{\mu^6}\beta^2(1-\beta)\left[\frac{2\pi^2}{3}\alpha_S(\mu^2)\int_0^{\mu^2}\frac{\mathrm{d}l_t^2}{l_t^2}f_g(x_{I\!P}, l_t^2, \mu^2)\right]^2$$
$$= \frac{256\pi^4}{9\mu^2}\left[\frac{\alpha_S(\mu^2)}{\mu^2}\,x_{I\!P}g(x_{I\!P}, \mu^2)\right]^2\beta^2(1-\beta), \tag{4.49}$$

where $g(x_{I\!P}, \mu^2)$ is the *integrated* gluon distribution of the proton. Strictly speaking, this last expression should be written in terms of the off-diagonal (or skewed) gluon distribution of the proton, since the left and right t-channel gluons in Fig. 4.3(a) carry different fractions of the proton momentum. At small $x_{I\!P}$, and assuming that $x_{I\!P}\, g(x_{I\!P}, \mu^2) \propto x_{I\!P}^{-\lambda}$, then the off-diagonal gluon distribution is given by the diagonal distribution multiplied by an overall constant factor [93],[6]

$$R_g(\lambda) = \frac{2^{2\lambda+3}}{\sqrt{\pi}} \frac{\Gamma(\lambda + 5/2)}{\Gamma(\lambda + 4)}. \tag{4.50}$$

Recall from (4.31) that

$$\alpha \simeq \beta \frac{\mu^2}{Q^2}, \qquad k_t^2 = \mu^2(1-\beta). \tag{4.51}$$

Changing variables from (α, k_t^2) to (β, μ^2) we have the Jacobian

$$\left|\frac{\partial(\alpha, k_t^2)}{\partial(\beta, \mu^2)}\right| \equiv \begin{vmatrix} \partial\alpha/\partial\beta & \partial k_t^2/\partial\beta \\ \partial\alpha/\partial\mu^2 & \partial k_t^2/\partial\mu^2 \end{vmatrix} = \begin{vmatrix} \mu^2/Q^2 & -\mu^2 \\ \beta/Q^2 & 1-\beta \end{vmatrix} = \frac{\mu^2}{Q^2}. \tag{4.52}$$

Assuming a t dependence of the form $\exp(B_D\, t)$, where the diffractive slope parameter $B_D \simeq 6$ GeV^{-2} from experiment, then

$$\sigma^{\gamma^* p} = \int_{t_{\rm cut}}^{t_{\rm min}} \mathrm{d}t\; \mathrm{e}^{B_D\, t} \left.\frac{\mathrm{d}\sigma^{\gamma^* p}}{\mathrm{d}t}\right|_{t=0} \simeq \frac{1}{B_D} \left.\frac{\mathrm{d}\sigma^{\gamma^* p}}{\mathrm{d}t}\right|_{t=0}. \tag{4.53}$$

Accounting for the skewed effect, the change of variables from (α, k_t^2) to (β, μ^2), and the t dependence, (4.33) becomes

$$\sigma_{T,q\bar{q}}^{\gamma^* p} = \frac{R_g^2}{B_D} \frac{N_C}{16\pi} \int_0^1 \mathrm{d}\beta \int \frac{\mathrm{d}\mu^2}{2\pi} \frac{\mu^2}{Q^2} \sum_f e_f^2\, \alpha_{\rm em}\, \frac{1}{2} \sum_{\gamma=\pm 1} \sum_{h=\pm\frac{1}{2}} \left| \int \frac{\mathrm{d}^2 \boldsymbol{l_t}}{\pi}\, D\Psi_h^\gamma\, \frac{\mathrm{d}\hat{\sigma}}{\mathrm{d}l_t^2} \right|^2. \tag{4.54}$$

From (4.18),

$$F_2^{D(3)} = \frac{Q^2}{4\pi^2 \alpha_{\rm em}} \frac{\beta}{x_{I\!P}} \frac{\mathrm{d}\sigma^{\gamma^* p}}{\mathrm{d}\beta}, \tag{4.55}$$

so after combining (4.49), (4.54), and (4.55), we finally obtain

$$F_{T,q\bar{q}}^{D(3)} = \int_{Q_0^2}^{Q^2} \mathrm{d}\mu^2\, \frac{1}{x_{I\!P}} \left[\frac{\alpha_S(\mu^2)}{\mu^2}\, x_{I\!P} g(x_{I\!P}, \mu^2) \right]^2 \sum_f e_f^2 \frac{R_g^2}{3B_D} \beta^3 (1-\beta), \tag{4.56}$$

which coincides with (22) of [153] (apart from the extra factor R_g^2/B_D). Since

[6] This factor is not seen in calculating Fig. 4.5(a) since it is absent in the limit $x_{I\!P} \to 0$ [154].

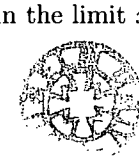

$\sum_f e_f^2 = n_f \langle e_f^2 \rangle$ (with $n_f = 3$), this can be written

$$F_{T,q\bar{q}}^{D(3)} = \int_{Q_0^2}^{Q^2} \mathrm{d}\mu^2 \, f_{I\!P=G}(x_{I\!P};\mu^2) \, \langle e_f^2 \rangle \, \beta\Sigma^{I\!P=G}(\beta,\mu^2;\mu^2), \tag{4.57}$$

where the 'Pomeron flux factor' is

$$f_{I\!P=G}(x_{I\!P};\mu^2) = \frac{1}{x_{I\!P}} \left[\frac{\alpha_S(\mu^2)}{\mu^2} \, x_{I\!P} g(x_{I\!P},\mu^2) \right]^2, \tag{4.58}$$

and the quark singlet distribution at a scale μ originating from a component of the Pomeron of size $1/\mu$ is

$$\beta\Sigma^{I\!P=G}(\beta,\mu^2;\mu^2) = c_{q/G}^{\mathrm{LO}} \, \beta^3(1-\beta), \tag{4.59}$$

with $c_{q/G}^{\mathrm{LO}} \equiv R_g^2/B_D$. The notation $I\!P = G$ is used to indicate that the perturbative Pomeron is represented by two t-channel gluons. Since only the combination of (4.58) and (4.59) is meaningful, all the numerical factors have been collected in (4.59). In the next chapter, we will use this formula (and others derived in the rest of the chapter) as the basis for a QCD analysis of DDIS data, after adding DGLAP evolution and NLO corrections to the Pomeron structure function, and replacing $c_{q/G}^{\mathrm{LO}}$ with a free parameter, $c_{q/G}$, to take account of these higher-order corrections.

Quark dipole with a longitudinally polarised photon

The dipole factorisation formula for Fig. 4.3(a) with a longitudinally polarised photon is

$$\left. \frac{\mathrm{d}\sigma_{L,q\bar{q}}^{\gamma^* p}}{\mathrm{d}t} \right|_{t=0} = \frac{N_C}{16\pi} \int_0^1 \mathrm{d}\alpha \int \frac{\mathrm{d}k_t^2}{2\pi} \sum_f e_f^2 \, \alpha_{\mathrm{em}} \sum_{h=\pm\frac{1}{2}} \left| \int \frac{\mathrm{d}^2\boldsymbol{l_t}}{\pi} \, D\Psi_h^{\gamma=0} \, \frac{\mathrm{d}\hat{\sigma}}{\mathrm{d}l_t^2} \right|^2, \tag{4.60}$$

where the light-cone wave functions for the quark–antiquark dipole with a longitudinally polarised photon are [153]

$$\Psi_h^{\gamma=0}(\alpha,\boldsymbol{k_t}) = 2\frac{\alpha(1-\alpha)Q}{k_t^2 + \alpha(1-\alpha)Q^2} \quad : \quad h = \pm\frac{1}{2}. \tag{4.61}$$

Taking the limit $l_t \to 0$ of the combination of wave functions (4.37) and doing the azimuthal integral gives[7]

$$\int_0^{2\pi} \frac{\mathrm{d}\phi}{2\pi} D\Psi_h^{\gamma=0}(\alpha, \boldsymbol{k_t}, \boldsymbol{l_t}) = l_t^2 \frac{\alpha(1-\alpha)Q^2 - k_t^2}{[k_t^2 + \alpha(1-\alpha)Q^2]^3} \, 4\alpha(1-\alpha)Q \quad : \quad h = \pm\frac{1}{2}. \tag{4.62}$$

Squaring this expression and summing over the quark helicities gives

$$\sum_{h=\pm\frac{1}{2}} \left| \int_0^{2\pi} \frac{\mathrm{d}\phi}{2\pi} D\Psi_h^{\gamma=0}(\alpha, \boldsymbol{k_t}, \boldsymbol{l_t}) \right|^2 = l_t^4 \frac{32}{\mu^6} \frac{\mu^2}{Q^2} \beta^2 (2\beta - 1)^2. \tag{4.63}$$

The dipole cross section, $\mathrm{d}\hat{\sigma}/\mathrm{d}l_t^2(qp \to qp)$, is the same as (4.48), giving

$$F_{L,q\bar{q}}^{D(3)} = \frac{Q^2}{4\pi^2 \alpha_{\mathrm{em}}} \frac{\beta}{x_{I\!P}} \frac{\mathrm{d}\sigma_{L,q\bar{q}}^{\gamma^* p}}{\mathrm{d}\beta} = \left(\int_{Q_0^2}^{Q^2} \mathrm{d}\mu^2 \, \frac{\mu^2}{Q^2} \, f_{I\!P=G}(x_{I\!P}; \mu^2) \right) c_{L/G}^{\mathrm{LO}} \, \beta^3 (2\beta - 1)^2, \tag{4.64}$$

where $c_{L/G}^{\mathrm{LO}} = 2R_g^2/(9B_D)$; this result is a factor of 2 different from (23) of [153], but is in agreement with [101]. Note that this term is twist-four due to the extra factor μ^2/Q^2 with respect to (4.57), and hence we should not add DGLAP evolution.

Gluon dipole with a transversely polarised photon

Now consider the kinematics of the $q\bar{q}g$ system shown in Fig. 4.3(b). Although this diagram has an extra factor α_S with respect to the $q\bar{q}$ system shown in Fig. 4.3(a), it is known to be dominant at large M_X (small β) due to the extra t-channel spin-1 gluon. Using a Sudakov parameterisation (4.26) of the momentum k of the off-shell gluon gives the momenta of the outgoing $q\bar{q}$ pair and gluon as

$$q - k = (1-\alpha)\, q' + \frac{x_B}{Q^2} \frac{k_t^2 + M_{q\bar{q}}^2}{1-\alpha} \, p - k_\perp, \tag{4.65}$$

$$\tilde{k} = k + x_{I\!P}\, p = \alpha\, q' + x_B \frac{k_t^2/Q^2}{\alpha} \, p + k_\perp, \tag{4.66}$$

respectively, where $M_{q\bar{q}}$ is the invariant mass of the $q\bar{q}$ system. The on-shell conditions, $(q-k)^2 = M_{q\bar{q}}^2$ and $\tilde{k}^2 = 0$, determine

$$\beta_k = -x_B \left(1 + \frac{k_t^2 + M_{q\bar{q}}^2}{(1-\alpha)Q^2} \right), \qquad x_{I\!P} = x_B \left(1 + \frac{k_t^2 + \alpha M_{q\bar{q}}^2}{\alpha(1-\alpha)Q^2} \right). \tag{4.67}$$

[7]Note the extra factor 2 in (4.62) compared to (21) of [153].

The invariant mass of the $q\bar{q}g$ system is given by

$$M_X^2 = (q + x_{I\!P}\, p)^2 = \frac{k_t^2 + \alpha M_{q\bar{q}}^2}{\alpha(1-\alpha)}. \tag{4.68}$$

The calculation is greatly simplified in the approximation $M_{q\bar{q}} \ll Q$, in addition to assuming strongly-ordered transverse momenta, $l_t \ll k_t \ll Q$. In this limit, the kinematics of the $(q\bar{q})g$ system is identical to the previously considered $q\bar{q}$ system of Fig. 4.3(a). The emitted $(q\bar{q})$ pair is localised in impact parameter space, and forms an effective 'gluon' conjugate in colour to the emitted gluon. The $(q\bar{q})g$ system can thus be considered as forming an effective gg dipole.

The dipole factorisation formula for Fig. 4.3(b) with a transversely polarised photon is then

$$\left.\frac{\mathrm{d}\sigma_{T,gg}^{\gamma^* p}}{\mathrm{d}t}\right|_{t=0} = \frac{N_C^2 - 1}{16\pi} \int_0^1 \mathrm{d}\alpha \int \frac{\mathrm{d}k_t^2}{2\pi} \sum_f e_f^2\, \alpha_{\mathrm{em}} \sum_{m,n=1,2} \left| \int \frac{\mathrm{d}^2 \boldsymbol{l_t}}{\pi}\, D\Psi^{mn}\, \frac{\mathrm{d}\hat{\sigma}}{\mathrm{d}l_t^2} \right|^2. \tag{4.69}$$

Again there are four different permutations of the couplings of the two gluons to the two components of the effective gluon dipole, shown in Fig. 4.4(b), which are obtained by shifting the argument of the wave function as in (4.37). The light-cone wave functions for the effective gluon dipole with a transversely polarised photon are [153]

$$\Psi^{mn}(\alpha, \boldsymbol{k_t}) = \frac{1}{\sqrt{\alpha(1-\alpha)Q^2}}\, \frac{k_t^2 \delta^{mn} - 2k_t^m k_t^n}{k_t^2 + \alpha(1-\alpha)Q^2} \quad : \quad m,n = 1,2. \tag{4.70}$$

Taking the limit $l_t \to 0$ of $D\Psi^{mn}$ and doing the azimuthal integral gives

$$\int_0^{2\pi} \frac{\mathrm{d}\phi}{2\pi} D\Psi^{mn}(\alpha, \boldsymbol{k_t}, \boldsymbol{l_t}) = l_t^2 \frac{2k_t^2}{\sqrt{\alpha(1-\alpha)Q^2}}\, \frac{3\alpha(1-\alpha)Q^2 + k_t^2}{\left[k_t^2 + \alpha(1-\alpha)Q^2\right]^3} \left(\delta^{mn} - \frac{2k_t^m k_t^n}{k_t^2}\right), \tag{4.71}$$

cf. (24) of [153]. Squaring this expression and summing over the indices $m, n = 1, 2$ gives

$$\sum_{m,n=1,2} \left| \int_0^{2\pi} \frac{\mathrm{d}\phi}{2\pi} D\Psi^{mn}(\alpha, \boldsymbol{k_t}, \boldsymbol{l_t}) \right|^2 = l_t^4 \frac{8}{\mu^6} (1-\beta)^2 (1+2\beta)^2 \frac{1}{\beta}. \tag{4.72}$$

The dipole cross section for $gp \to gp$ is obtained from the scattering process $gq \to gq$ with t-channel gluon exchange, shown in Fig. 4.5(b). Here, the squared

matrix element is

$$|\mathcal{M}|^2 = \frac{1}{4}C\,\frac{g^4}{l_t^4}\,\mathrm{Tr}[\not{p}\gamma^\gamma(\not{p}-\not{l}_\perp)\gamma^\delta]\;d_{\mu\sigma}(k,p)\;d_{\nu\rho}(k+l_\perp,p)\;(-g_{\alpha\gamma})\;(-g_{\beta\delta})$$
$$\times\left[(2k+l_\perp)^\alpha g^{\mu\nu}-(k+2l_\perp)^\mu g^{\nu\alpha}+(l_\perp-k)^\nu g^{\mu\alpha}\right]$$
$$\times\left[(2k+l_\perp)^\beta g^{\rho\sigma}-(k+2l_\perp)^\sigma g^{\rho\beta}+(l_\perp-k)^\rho g^{\sigma\beta}\right], \quad (4.73)$$

where the transverse polarisations of the incoming and outgoing gluons are summed in a light-cone gauge,

$$d_{\mu\sigma}(k,p) \equiv -g_{\mu\sigma}+\frac{k_\mu p_\sigma + p_\mu k_\sigma}{p\cdot k}, \quad (4.74)$$

and where the colour factor is

$$C(gq\to gq)=\frac{1}{N_C}\frac{1}{(N_C^2-1)}\,f^{ABC}f^{ABD}\,\mathrm{Tr}[t^Ct^D]=\frac{1}{2}. \quad (4.75)$$

In the high-energy limit, where only the terms to leading $\mathcal{O}(\hat{s}/|\hat{t}|)$ are retained, that is, in the $l_t \to 0$ limit,

$$\frac{\mathrm{d}\hat{\sigma}}{\mathrm{d}l_t^2}(gq\to gq)=\frac{1}{l_t^4}2\pi\alpha_S(l_t^2)\alpha_S(\mu^2), \quad (4.76)$$

where appropriate scales for α_S have been chosen corresponding to the two different vertices in Fig. 4.5(b). As before, we obtain the cross section for $gp \to gp$ by making the replacement (4.47), which gives

$$\frac{\mathrm{d}\hat{\sigma}}{\mathrm{d}l_t^2}(gp\to gp)=\frac{1}{l_t^4}\frac{3\pi^2}{2}\alpha_S(\mu^2)f_g(x_{I\!P},l_t^2,\mu^2). \quad (4.77)$$

Inserting (4.72) and (4.77) into (4.69), and accounting for the skewed effect, the change of variables from (α,k_t^2) to (β,μ^2), and the t dependence, we obtain

$$\frac{\mathrm{d}\sigma_{T,gg}^{\gamma^*p}}{\mathrm{d}\beta}=\frac{4\pi^2\alpha_{\mathrm{em}}}{Q^2}\int_{Q_0^2}^{Q^2}\mathrm{d}\mu^2\left[\frac{\alpha_S(\mu^2)}{\mu^2}\,x_{I\!P}g(x_{I\!P},\mu^2)\right]^2\sum_f e_f^2\frac{9R_g^2}{8B_D}(1-\beta)^2(1+2\beta)^2\frac{1}{\beta} \quad (4.78)$$

We must account for the fact that the off-shell gluon with momentum k in Fig. 4.3(b) does not interact directly with the photon, but first splits into a quark–antiquark pair forming the 'effective gluon' of the dipole. To do this, we replace $\beta \to \beta'$ in the previous formula and include the DGLAP splitting for $g \to q\bar{q}$, that

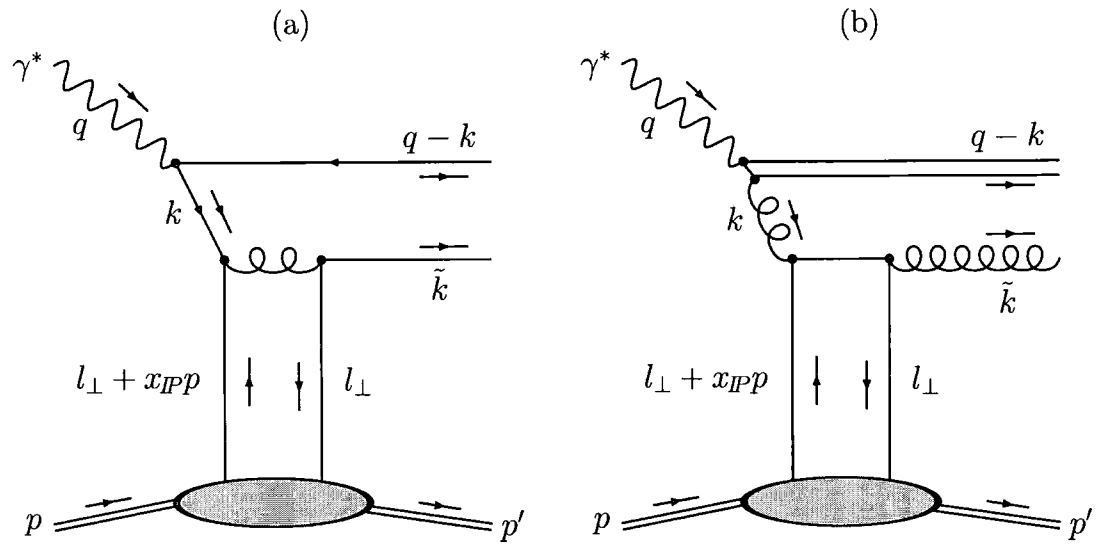

Figure 4.6: (a) Quark dipole and (b) effective gluon dipole interacting with the proton via a perturbative Pomeron represented by two t-channel sea quarks.

is,

$$\frac{\mathrm{d}\sigma^{\gamma^* p}_{T,(q\bar{q})g}}{\mathrm{d}\beta} = \frac{\alpha_S(Q^2)}{2\pi} \ln\left(\frac{Q^2}{\mu^2}\right) \int_\beta^1 \frac{\mathrm{d}\beta'}{\beta'} P_{qg}\left(\frac{\beta}{\beta'}\right) \frac{\mathrm{d}\sigma^{\gamma^* p}_{T,gg}}{\mathrm{d}\beta'}. \tag{4.79}$$

Putting everything together, we finally obtain

$$F^{D(3)}_{T,(q\bar{q})g} = \frac{Q^2}{4\pi^2 \alpha_{\mathrm{em}}} \frac{\beta}{x_{I\!P}} \frac{\mathrm{d}\sigma^{\gamma^* p}_{T,(q\bar{q})g}}{\mathrm{d}\beta} = \int_{Q_0^2}^{Q^2} \mathrm{d}\mu^2 \, f_{I\!P=G}(x_{I\!P};\mu^2) \, \langle e_f^2 \rangle \beta \Sigma^{I\!P=G}(\beta, Q^2; \mu^2), \tag{4.80}$$

where

$$\beta \Sigma^{I\!P=G}(\beta, Q^2; \mu^2) = 2 n_f \frac{\alpha_S(Q^2)}{2\pi} \ln\left(\frac{Q^2}{\mu^2}\right) \beta \int_\beta^1 \frac{\mathrm{d}\beta'}{\beta'^2} P_{qg}\left(\frac{\beta}{\beta'}\right) \beta' g^{I\!P=G}(\beta', \mu^2; \mu^2), \tag{4.81}$$

with

$$\beta' g^{I\!P=G}(\beta', \mu^2; \mu^2) = c^{\mathrm{LO}}_{g/G} \, (1-\beta')^2 (1+2\beta')^2, \tag{4.82}$$

where $c^{\mathrm{LO}}_{g/G} = 9R_g^2/(16B_D)$. Note the extra factor 2 compared to (25) of [153] (this was corrected in a later paper [155]).

4.7.2 Two-quark exchange

We now consider the Pomeron as being represented by two sea quarks rather than two gluons, and calculate the lowest order Feynman diagrams using the same formalism as in Section 4.7.1. As far as we are aware, this is a completely new idea which has not previously been proposed in the literature. The reason why a two-

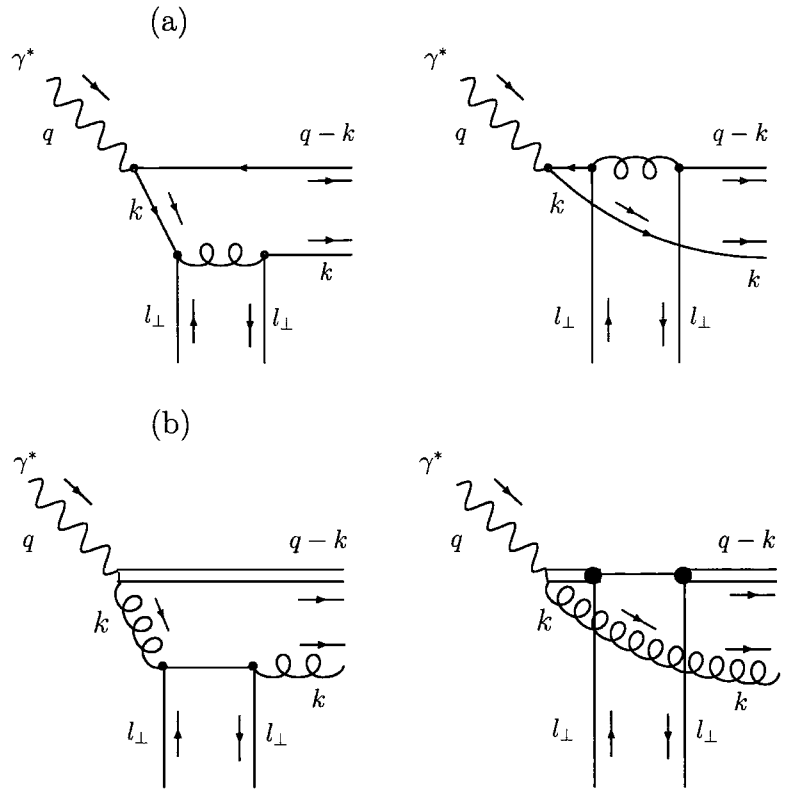

Figure 4.7: The two different permutations of the couplings of the two t-channel sea quarks to the two components of (a) the quark dipole and (b) the effective gluon dipole.

quark Pomeron is necessary is due to the valence-like shape of the gluon distribution of the proton at low scales; we will discuss this problem in more detail in the next two chapters. The quark dipole and effective gluon dipole interacting with the two-quark Pomeron are shown in Fig. 4.6. The light-cone wave functions of the photon, $\Psi(\alpha, \boldsymbol{k}_t)$, are the same as those given in Section 4.7.1. The two different permutations of the couplings of the two sea quarks to the two components of the dipole, shown in Fig. 4.7, are obtained with

$$D\Psi(\alpha, \boldsymbol{k}_t) \equiv 2\Psi(\alpha, \boldsymbol{k}_t), \tag{4.83}$$

that is, there are no terms with a shifted argument as for the two-gluon Pomeron. Since there is no $\boldsymbol{l}_t$ dependence here, the integrals over $\boldsymbol{l}_t$ in the dipole factorisation formulae can be done immediately.

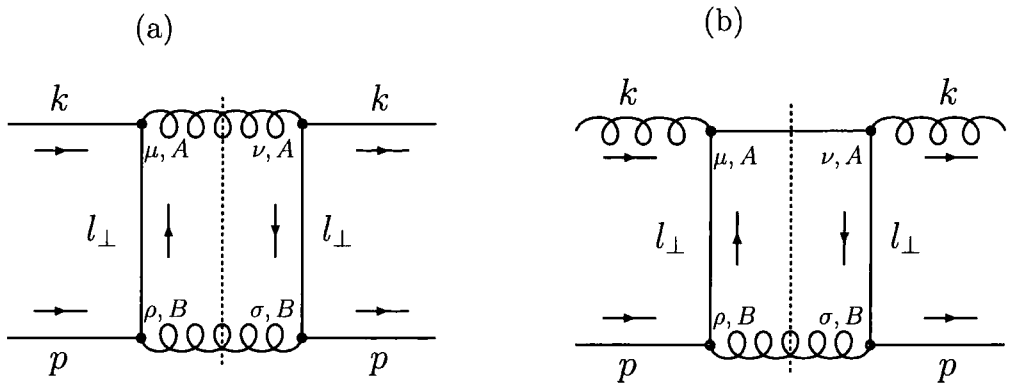

Figure 4.8: Cut diagrams giving the dipole cross sections for the two-quark Pomeron: (a) $qq \to gg$ and (b) $gq \to qg$.

Quark dipole with a transversely polarised photon

The dipole factorisation formula for Fig. 4.6(a) with a transversely polarised photon is

$$\left.\frac{\mathrm{d}\sigma^{\gamma^* p}_{T,q\bar{q}}}{\mathrm{d}t}\right|_{t=0} = \frac{N_C}{16\pi}\int_0^1 \mathrm{d}\alpha \int \frac{\mathrm{d}k_t^2}{2\pi} \sum_f e_f^2\, \alpha_{\mathrm{em}}\, \frac{1}{2} \sum_{\gamma=\pm 1} \sum_{h=\pm\frac{1}{2}} |D\Psi_h^\gamma|^2\, \hat{\sigma}^2, \tag{4.84}$$

where

$$\sum_{\gamma=\pm 1} \sum_{h=\pm\frac{1}{2}} |D\Psi_h^\gamma(\alpha, \boldsymbol{k_t})|^2 = \frac{16}{\mu^2}(1-\beta). \tag{4.85}$$

The dipole cross section for $qp \to gp$ is obtained from the scattering process $qq \to gg$ with t-channel sea quark exchange, shown in Fig. 4.8(a). Here, the squared matrix element is

$$|\mathcal{M}|^2 = \frac{1}{4}\mathcal{C}\,\frac{g^4}{l_t^4}\,\mathrm{Tr}[\gamma^\mu \not{k} \gamma^\nu \not{l}_\perp \gamma^\sigma \not{p} \gamma^\rho \not{l}_\perp]\, d_{\mu\nu}(k+l_\perp, p)\, d_{\rho\sigma}(p-l_\perp, k), \tag{4.86}$$

where the colour factor is

$$\mathcal{C}(qq \to qq) = \frac{1}{N_C^2}\mathrm{Tr}[t^A t^A t^B t^B] = \frac{16}{27}. \tag{4.87}$$

In the high-energy limit, where only the terms to leading $\mathcal{O}(\hat{s}/|\hat{t}|)$ are retained,

$$\frac{\mathrm{d}\hat{\sigma}}{\mathrm{d}l_t^2}(qq \to gg) = \frac{1}{l_t^2}\frac{32\pi}{27}\frac{x_{I\!P}}{\mu^2}\alpha_S(l_t^2)\alpha_S(\mu^2). \tag{4.88}$$

Note that this expression is suppressed by an extra factor $\mathcal{O}(|\hat{t}|/\hat{s})$ compared to the t-channel gluon exchange processes considered in Section 4.7.1, where $\hat{s} \simeq \mu^2/x_{I\!P}$

and $\hat{t} = -l_t^2$. We obtain the cross section for $qp \to gp$ by making the replacement

$$\frac{\alpha_S(l_t^2)}{2\pi} x_{I\!P} P_{qq}(x_{I\!P})\Big|_{x_{I\!P}\ll 1} = \frac{\alpha_S(l_t^2)}{2\pi}\, x_{I\!P}\, C_F = \frac{2}{3\pi} x_{I\!P}\alpha_S(l_t^2) \to f_q(x_{I\!P}, l_t^2, \mu^2), \quad (4.89)$$

where $f_q(x_{I\!P}, l_t^2, \mu^2)$ is the unintegrated quark distribution of the proton. This replacement gives

$$\hat{\sigma}(qp \to gp) = \frac{16\pi^2}{9}\frac{\alpha_S(\mu^2)}{\mu^2}\int_0^{\mu^2}\frac{\mathrm{d}l_t^2}{l_t^2} f_q(x_{I\!P}, l_t^2, \mu^2) = \frac{8\pi^2}{27}\frac{\alpha_S(\mu^2)}{\mu^2} x_{I\!P} S(x_{I\!P}, \mu^2), \quad (4.90)$$

where $S(x_{I\!P}, \mu^2)$ is the integrated sea quark distribution of the proton and we have assumed light quark flavour symmetry, $S(x_{I\!P}, \mu^2) = q(x_{I\!P}, \mu^2)/(2n_f)$, with $n_f = 3$. Again, we should really use the *skewed* quark distributions, which gives rise to an extra factor [93]

$$R_q(\lambda) = \frac{2^{2\lambda+3}}{\sqrt{\pi}}\frac{\Gamma(\lambda + 5/2)}{\Gamma(\lambda + 3)}, \quad (4.91)$$

assuming that $x_{I\!P}\, S(x_{I\!P}, \mu^2) \propto x_{I\!P}^{-\lambda}$ at small $x_{I\!P}$. The final result is

$$F_{T,q\bar{q}}^{D(3)} = \int_{Q_0^2}^{Q^2} \mathrm{d}\mu^2\, f_{I\!P=S}(x_{I\!P}; \mu^2)\, \langle e_f^2\rangle \beta\Sigma^{I\!P=S}(\beta, \mu^2; \mu^2), \quad (4.92)$$

where the 'Pomeron flux factor' is

$$f_{I\!P=S}(x_{I\!P}; \mu^2) = \frac{1}{x_{I\!P}}\left[\frac{\alpha_S(\mu^2)}{\mu^2}\, x_{I\!P} S(x_{I\!P}, \mu^2)\right]^2, \quad (4.93)$$

and the quark singlet distribution at a scale μ originating from a component of the Pomeron of size $1/\mu$ is

$$\beta\Sigma^{I\!P=S}(\beta, \mu^2; \mu^2) = c_{q/S}^{\mathrm{LO}}\, \beta(1-\beta), \quad (4.94)$$

with $c_{q/S}^{\mathrm{LO}} = 4R_q^2/(81B_D)$. The notation $I\!P = S$ is used to indicate that the perturbative Pomeron is represented by two t-channel sea quarks. In the next chapter we will add DGLAP evolution and NLO corrections to the Pomeron structure function in a QCD analysis of DDIS data.

Quark dipole with a longitudinally polarised photon

The dipole factorisation formula for Fig. 4.6(a) with a longitudinally polarised photon is

$$\left.\frac{\mathrm{d}\sigma^{\gamma^* p}_{L,q\bar{q}}}{\mathrm{d}t}\right|_{t=0} = \frac{N_C}{16\pi}\int_0^1 \mathrm{d}\alpha \int \frac{\mathrm{d}k_t^2}{2\pi} \sum_f e_f^2\, \alpha_{\mathrm{em}} \sum_{h=\pm\frac{1}{2}} \left|D\Psi_h^{\gamma=0}\right|^2 \hat{\sigma}^2, \tag{4.95}$$

where

$$\sum_{h=\pm\frac{1}{2}} \left|D\Psi_h^{\gamma=0}(\alpha, \boldsymbol{k_t})\right|^2 = \frac{32}{\mu^2}\frac{\mu^2}{Q^2}\beta^2, \tag{4.96}$$

leading to

$$F^{D(3)}_{L,q\bar{q}} = \frac{Q^2}{4\pi^2\alpha_{\mathrm{em}}}\frac{\beta}{x_{I\!P}}\frac{\mathrm{d}\sigma^{\gamma^* p}_{L,q\bar{q}}}{\mathrm{d}\beta} = \left(\int_{Q_0^2}^{Q^2} \mathrm{d}\mu^2\, \frac{\mu^2}{Q^2}\, f_{I\!P}(x_{I\!P};\mu^2)\right) c^{\mathrm{LO}}_{L/S}\, \beta^3, \tag{4.97}$$

where $c^{\mathrm{LO}}_{L/S} = 32R_q^2/(729B_D)$. Note that this term is twist-four due to the extra factor μ^2/Q^2 with respect to (4.92), and hence we should not add DGLAP evolution.

Gluon dipole with a transversely polarised photon

The dipole factorisation formula for Fig. 4.6(b) with a transversely polarised photon is

$$\left.\frac{\mathrm{d}\sigma^{\gamma^* p}_{gg,T}}{\mathrm{d}t}\right|_{t=0} = \frac{N_C^2-1}{16\pi}\int_0^1 \mathrm{d}\alpha \int \frac{\mathrm{d}k_t^2}{2\pi} \sum_f e_f^2\, \alpha_{\mathrm{em}} \sum_{m,n=1,2} |D\Psi^{m,n}|^2\, \hat{\sigma}^2, \tag{4.98}$$

where

$$\sum_{m,n=1,2} |D\Psi^{mn}(\alpha, \boldsymbol{k_t})|^2 = \frac{8}{\mu^2}(1-\beta)^2\frac{1}{\beta}. \tag{4.99}$$

The squared matrix element for $gq \to qg$, shown in Fig. 4.8(b), is

$$|\mathcal{M}|^2 \doteq \frac{1}{4}\mathcal{C}\,\frac{g^4}{l_t^4}\,\mathrm{Tr}[\gamma^\mu \not{l}_\perp \gamma^\rho \not{p} \gamma^\sigma \not{l}_\perp \gamma^\nu (\not{k} + \not{l}_\perp)]\; d_{\mu\nu}(k,p)\; d_{\rho\sigma}(p - l_\perp, k), \tag{4.100}$$

where the colour factor is

$$\mathcal{C}(gq \to gq) = \frac{1}{N_C}\frac{1}{N_C^2-1}\mathrm{Tr}[t^A t^A t^B t^B] = \frac{2}{9}. \tag{4.101}$$

The dipole cross section is then

$$\frac{\mathrm{d}\hat{\sigma}}{\mathrm{d}l_t^2}(gq \to qg) = \frac{1}{l_t^2}\frac{32\pi}{27}\frac{x_{I\!P}}{\mu^2}\alpha_S(l_t^2)\alpha_S(\mu^2), \tag{4.102}$$

so, making the replacement (4.89), the $gp \to qp$ cross section is

$$\hat{\sigma}(gp \to qp) = \frac{2\pi^2}{3}\frac{\alpha_S(\mu^2)}{\mu^2}\int_0^{\mu^2}\frac{\mathrm{d}l_t^2}{l_t^2}\sum_q f_q(x_{I\!P}, l_t^2, \mu^2) = \frac{2\pi^2}{3}\frac{\alpha_S(\mu^2)}{\mu^2}x_{I\!P}S(x_{I\!P}, \mu^2). \tag{4.103}$$

Again, we account for the $g \to q\bar{q}$ splitting using (4.79). The final result is

$$F_{T,(q\bar{q})g}^{D(3)} = \int_{Q_0^2}^{Q^2} \mathrm{d}\mu^2 \, f_{I\!P=S}(x_{I\!P}; \mu^2) \, \langle e_f^2 \rangle \beta\Sigma^{I\!P=S}(\beta, Q^2; \mu^2), \tag{4.104}$$

where

$$\beta\Sigma^{I\!P=S}(\beta, Q^2; \mu^2) = 2n_f\frac{\alpha_S(Q^2)}{2\pi}\ln\left(\frac{Q^2}{\mu^2}\right)\beta\int_\beta^1\frac{\mathrm{d}\beta'}{\beta'^2}P_{qg}\left(\frac{\beta}{\beta'}\right)\beta' g^{I\!P=S}(\beta', \mu^2; \mu^2), \tag{4.105}$$

with

$$\beta' g^{I\!P=S}(\beta', \mu^2; \mu^2) = c_{g/S}^{\mathrm{LO}}\,(1-\beta')^2, \tag{4.106}$$

where $c_{g/S}^{\mathrm{LO}} = R_q^2/(9B_D)$.

Chapter 5

A QCD analysis of diffractive deep-inelastic scattering data

A simple parameterisation based on the two-gluon exchange calculations presented in Section 4.7.1 was proposed by Bartels-Ellis-Kowalski-Wüsthoff (BEKW) in [156]. A slightly modified version of the BEKW parameterisation has been used by ZEUS to describe their recent DDIS data [157, 158]:

$$x_{I\!P} F_2^{D(3)}(x_{I\!P}, \beta, Q^2) = c_T \, F_{q\bar{q}}^T + c_L \, F_{q\bar{q}}^L + c_g \, F_{q\bar{q}g}^T, \tag{5.1}$$

where

$$F_{q\bar{q}}^T = \left(\frac{x_0}{x_{I\!P}}\right)^{n_T(Q^2)} \beta(1-\beta), \tag{5.2}$$

$$F_{q\bar{q}}^L = \left(\frac{x_0}{x_{I\!P}}\right)^{n_L(Q^2)} \frac{Q_0^2}{Q^2+Q_0^2} \ln^2\left(\frac{7}{4} + \frac{Q^2}{4\beta Q_0^2}\right) \beta^3(1-2\beta)^2, \tag{5.3}$$

$$F_{q\bar{q}g}^T = \left(\frac{x_0}{x_{I\!P}}\right)^{n_g(Q^2)} \ln\left(1+\frac{Q^2}{Q_0^2}\right) (1-\beta)^\gamma, \tag{5.4}$$

and $n(Q^2) = n_0 + n_1 \ln(1 + Q^2/Q_0^2)$. This parameterisation is rather far from the original perturbative QCD calculations of Section 4.7.1, with several parameters required to be determined from experiment.

In this chapter we perform a perturbative QCD analysis of the new high precision DDIS data, recently obtained by the ZEUS [157, 158] and H1 [148] Collaborations at HERA. The analysis is novel in that it treats individually the components of the Pomeron of different transverse size. The description of the DDIS data is based on a purely perturbative QCD framework. We take input forms of the PDFs of the Pomeron given by the calculation of the lowest-order QCD diagrams for $\gamma^* p \to Xp$

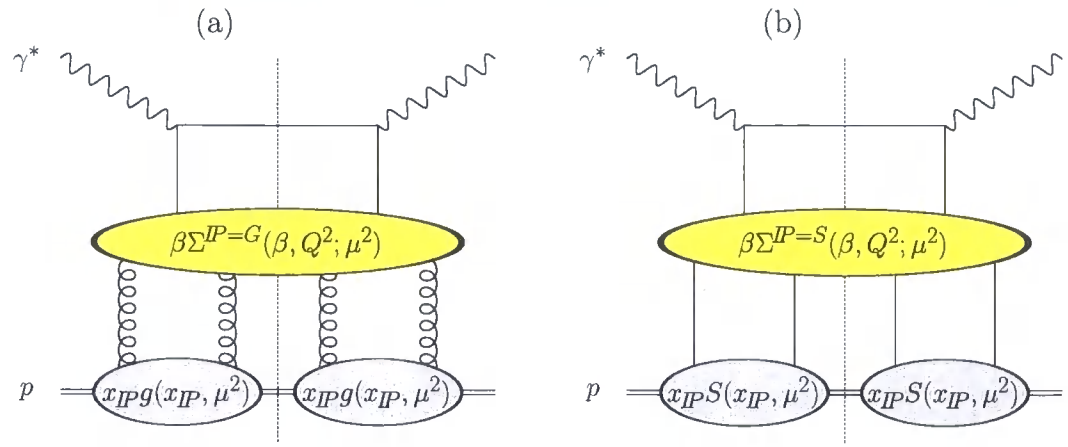

Figure 5.1: Cut diagrams illustrating the main ideas contained in (5.5). Each component of the perturbative Pomeron of size $1/\mu$ is represented by either (a) two t-channel gluons in a colour singlet or (b) sea quark–antiquark exchange. The perturbative Pomeron flux factors $f_{I\!P}(x_{I\!P}; \mu^2)$ are given in terms of the gluon and sea quark distributions of the proton, $g(x_{I\!P}, \mu^2)$ and $S(x_{I\!P}, \mu^2)$. The Pomeron structure function $F_2^{I\!P}(\beta, Q^2; \mu^2)$ is evaluated from the quark singlet, $\Sigma^{I\!P}(\beta, Q^2; \mu^2)$, and gluon, $g^{I\!P}(\beta, Q^2; \mu^2)$, distributions of the Pomeron.

(Section 4.7). In the 'resolved' Pomeron analyses described in Section 4.6, the Pomeron is treated as a hadron-like object of more or less fixed size. However, the microscopic structure of the Pomeron is different to that of a hadron. In perturbative QCD, it is known that the Pomeron singularity is not an isolated pole, but a branch cut, in the complex angular momentum plane [152]. The pole singularity corresponds to a single particle, whereas a branch cut may be regarded as a continuum series of poles. That is, the Pomeron wave function consists of a continuous number of components. Each component i has its own size, $1/\mu_i$. The QCD DGLAP evolution of a component should start from its own scale μ_i, provided that μ_i is large enough for the perturbative evolution to be valid. Therefore, the expression for the diffractive structure function $F_2^{D(3)}$ contains an integral over the Pomeron size, or rather over the scale μ. So to obtain $F_2^{D(3)}$ we evolve the input PDFs of each component of the Pomeron from their own starting scale μ up to the final scale Q. The extra integral over μ reflects the fact that the partonic structure of the Pomeron is more complicated than that of a normal hadron.

5.1 New perturbative QCD approach to DDIS

The fact that the Pomeron singularity is a cut rather than a pole implies an integral over the Pomeron scale, cf. (4.22),

$$F_{2,\mathrm{P}}^{D(3)}(x_{I\!P},\beta,Q^2) = \sum_{I\!P=G,S,GS} \int_{Q_0^2}^{Q^2} \mathrm{d}\mu^2 \, f_{I\!P}(x_{I\!P};\mu^2)\, F_2^{I\!P}(\beta,Q^2;\mu^2); \tag{5.5}$$

see Fig. 5.1. Here, the subscript P on $F_{2,\mathrm{P}}^{D(3)}$ is to indicate that this is the perturbative contribution with $\mu > Q_0 \sim 1$ GeV. The notation $I\!P = G, S, GS$ denotes that the perturbative Pomeron is represented by two t-channel gluons, two t-channel sea quarks, or the interference between these, respectively. The perturbative Pomeron flux factors are

$$f_{I\!P=G}(x_{I\!P};\mu^2) = \frac{1}{x_{I\!P}}\left[\frac{\alpha_S(\mu^2)}{\mu^2}\, x_{I\!P} g(x_{I\!P},\mu^2)\right]^2, \tag{5.6}$$

$$f_{I\!P=S}(x_{I\!P};\mu^2) = \frac{1}{x_{I\!P}}\left[\frac{\alpha_S(\mu^2)}{\mu^2}\, x_{I\!P} S(x_{I\!P},\mu^2)\right]^2, \tag{5.7}$$

$$f_{I\!P=GS}(x_{I\!P};\mu^2) = \frac{1}{x_{I\!P}}\left[\frac{\alpha_S(\mu^2)}{\mu^2}\right]^2 2\, x_{I\!P} g(x_{I\!P},\mu^2)\, x_{I\!P} S(x_{I\!P},\mu^2). \tag{5.8}$$

The Pomeron structure function, calculated at NLO, is

$$F_2^{I\!P}(\beta,Q^2;\mu^2) = \langle e_f^2\rangle \beta \Sigma^{I\!P}(\beta,Q^2;\mu^2) + \frac{\alpha_S(Q^2)}{2\pi}\beta\int_\beta^1 \frac{\mathrm{d}\beta'}{\beta'} \times \left[\langle e_f^2\rangle C_{2,q}^{\mathrm{NLO}}\left(\frac{\beta}{\beta'}\right)\Sigma^{I\!P}(\beta',Q^2;\mu^2) + \langle e_f^2\rangle C_{2,g}^{\mathrm{NLO}}\left(\frac{\beta}{\beta'}\right) g^{I\!P}(\beta',Q^2;\mu^2)\right], \tag{5.9}$$

where $\langle e_f^2\rangle = (1/n_f)\sum_f e_f^2$ (with $n_f = 3$), and where the coefficient functions $C_{2,q}^{\mathrm{NLO}}$ and $C_{2,g}^{\mathrm{NLO}}$ are calculated in the $\overline{MS}$ scheme [159]. The quark singlet, $\Sigma^{I\!P}(\beta,Q^2;\mu^2)$, and gluon, $g^{I\!P}(\beta,Q^2;\mu^2)$, distributions of the Pomeron are obtained by NLO DGLAP evolution up to Q^2 from input Pomeron PDFs parameterised at a starting scale μ^2:

$$\frac{\partial}{\partial \ln Q^2}\begin{pmatrix}\Sigma^{I\!P}(\beta,Q^2;\mu^2)\\ g^{I\!P}(\beta,Q^2;\mu^2)\end{pmatrix} = \frac{\alpha_S(Q^2)}{2\pi}\int_\beta^1\frac{\mathrm{d}\beta'}{\beta'} \times \begin{pmatrix} P_{qq}\left(\frac{\beta}{\beta'},\alpha_S(Q^2)\right) & 2n_f P_{qg}\left(\frac{\beta}{\beta'},\alpha_S(Q^2)\right)\\ P_{gq}\left(\frac{\beta}{\beta'},\alpha_S(Q^2)\right) & P_{gg}\left(\frac{\beta}{\beta'},\alpha_S(Q^2)\right)\end{pmatrix}\begin{pmatrix}\Sigma^{I\!P}(\beta',Q^2;\mu^2)\\ g^{I\!P}(\beta',Q^2;\mu^2)\end{pmatrix}. \tag{5.10}$$

The quark singlet distribution is $\Sigma^{I\!P} \equiv u^{I\!P} + d^{I\!P} + s^{I\!P} + \bar{u}^{I\!P} + \bar{d}^{I\!P} + \bar{s}^{I\!P}$, with $u^{I\!P} = d^{I\!P} = s^{I\!P} = \bar{u}^{I\!P} = \bar{d}^{I\!P} = \bar{s}^{I\!P}$, so that the non-singlet distributions are all zero. The

contributions of the charm and bottom quarks to $F_2^{I\!P}(\beta, Q^2; \mu^2)$ are calculated in the heavy quark fixed-flavour number scheme from the photon-gluon fusion process including NLO corrections [160]:

$$F_2^{I\!P,h\bar{h}}(\beta, Q^2; \mu^2) = \frac{\alpha_S(Q^2)}{2\pi} \left[e_h^2 \, C_{2,g}^{\mathrm{LO}} \otimes g^{I\!P} + \frac{\alpha_S(Q^2)}{2\pi} \right.$$
$$\left. \times \left(e_h^2 \, C_{2,g}^{\mathrm{NLO}} \otimes g^{I\!P} + e_h^2 \, C_{2,q}^{\mathrm{NLO}} \otimes \Sigma^{I\!P} + \langle e_f^2 \rangle \, \mathcal{D}_{2,q}^{\mathrm{NLO}} \otimes \Sigma^{I\!P} \right) \right], \quad (5.11)$$

where

$$C \otimes a^{I\!P} \equiv \int_{\beta\left(1+\frac{4m_h^2}{Q^2}\right)}^{1} \mathrm{d}\beta' \, C\left(\frac{\beta}{\beta'}, Q^2, m_h^2\right) a^{I\!P}(\beta', Q^2; \mu^2). \quad (5.12)$$

The input parameterisations for the Pomeron PDFs are obtained from the lowest-order Feynman diagrams (see Section 4.7):

$$\beta\Sigma^{I\!P=G}(\beta, \mu^2; \mu^2) = c_{q/G} \, \beta^3 (1-\beta), \quad (5.13)$$
$$\beta' g^{I\!P=G}(\beta', \mu^2; \mu^2) = c_{g/G} \, (1+2\beta')^2 (1-\beta')^2, \quad (5.14)$$
$$\beta\Sigma^{I\!P=S}(\beta, \mu^2; \mu^2) = c_{q/S} \, \beta (1-\beta), \quad (5.15)$$
$$\beta' g^{I\!P=S}(\beta', \mu^2; \mu^2) = c_{g/S} \, (1-\beta')^2, \quad (5.16)$$
$$\beta\Sigma^{I\!P=GS}(\beta, \mu^2; \mu^2) = c_{q/GS} \, \beta^2 (1-\beta), \quad (5.17)$$
$$\beta' g^{I\!P=GS}(\beta', \mu^2; \mu^2) = c_{g/GS} \, (1+2\beta') (1-\beta')^2. \quad (5.18)$$

Here, the coefficients $c_{a/I\!P}^{\mathrm{LO}}$ of Section 4.7, where $a = q, g$ and $I\!P = G, S, GS$, which implicitly include all the numerical factors arising from the lowest-order calculations, have been replaced by parameters $c_{a/I\!P}$. We will let these normalisations go free in fits to the DDIS data to account for higher-order QCD corrections (effective K-factors). Later on, we will discuss the size of these K-factors obtained from the fits. The normalisations of the interference terms between the two-gluon and the two-quark Pomerons is fixed by $c_{a/GS} = \sqrt{c_{a/G} \, c_{a/S}}$; that is, the K-factor is fixed for the amplitude rather than for the cross section.

In addition to the leading-twist contribution arising from the quark dipole calculation with a transversely polarised photon, there is an analogous twist-four contribution to $F_2^{D(3)}$ arising from a longitudinally polarised photon (see Section 4.7),

$$F_{L,\mathrm{P}}^{D(3)}(x_{I\!P}, \beta, Q^2) = \sum_{I\!P=G,S,GS} \left(\int_{Q_0^2}^{Q^2} \mathrm{d}\mu^2 \, \frac{\mu^2}{Q^2} \, f_{I\!P}(x_{I\!P}; \mu^2) \right) F_L^{I\!P}(\beta). \quad (5.19)$$

The twist-four nature of this longitudinal contribution is evident from the μ^2/Q^2

factor. The β dependences are again obtained from lowest-order perturbative QCD calculations (see Section 4.7):

$$F_L^{I\!P=G}(\beta) = c_{L/G}\,\beta^3\,(2\beta-1)^2, \tag{5.20}$$

$$F_L^{I\!P=S}(\beta) = c_{L/S}\,\beta^3, \tag{5.21}$$

$$F_L^{I\!P=GS}(\beta) = c_{L/GS}\,\beta^3\,(2\beta-1), \tag{5.22}$$

where, as before, the parameters $c_{L/I\!P}^{\rm LO}$ ($I\!P = G, S, GS$), which include all the numerical factors, have been replaced by free parameters, $c_{L/I\!P}$. Again, we fix $c_{L/GS} = \sqrt{c_{L/G}\,c_{L/S}}$.

We also include a non-perturbative (NP) Pomeron contribution (from scales $\mu < Q_0$) and a secondary Reggeon ($I\!R$) contribution to $F_2^{D(3)}(x_{I\!P}, \beta, Q^2)$, so that

$$F_2^{D(3)} = F_{2,\rm P}^{D(3)} + F_{2,\rm NP}^{D(3)} + F_{L,\rm P}^{D(3)} + F_{2,I\!R}^{D(3)}, \tag{5.23}$$

with

$$F_{2,\rm NP}^{D(3)}(x_{I\!P}, \beta, Q^2) = f_{I\!P=\rm NP}(x_{I\!P})\,F_2^{I\!P=\rm NP}(\beta, Q^2; Q_0^2), \tag{5.24}$$

$$F_{2,I\!R}^{D(3)}(x_{I\!P}, \beta, Q^2) = c_{I\!R}\,f_{I\!R}(x_{I\!P})\,F_2^{I\!R}(\beta, Q^2), \tag{5.25}$$

where $c_{I\!R}$ is taken to be a free parameter. Here, the non-perturbative Pomeron and Reggeon flux factors are[1]

$$f_i(x_{I\!P}) = \int_{t_{\rm cut}}^{t_{\rm min}} {\rm d}t \frac{{\rm e}^{B_i t}}{x_{I\!P}^{2\alpha_i(t)-1}} = \frac{x_{I\!P}^{1-2\alpha_i(0)}\left(1 - {\rm e}^{B_i t_{\rm cut}} x_{I\!P}^{-2\alpha_i' t_{\rm cut}}\right)}{B_i + 2\alpha_i' \ln(1/x_{I\!P})}, \tag{5.26}$$

with $i = I\!P$ and $I\!R$ respectively, and $\alpha_i(t) = \alpha_i(0) + \alpha_i' t$. The integration limits are taken to be $t_{\rm cut} = -1$ GeV^2 and $t_{\rm min} \simeq 0$ GeV^2. For the non-perturbative Pomeron, we fix $\alpha_{I\!P}(0) = 1.08$ [124], $\alpha_{I\!P}' = 0.26$ GeV^{-2} and $B_{I\!P} = 4.6$ GeV^{-2} [161], whereas for the Reggeon we take $\alpha_{I\!R}(0) = 0.50$ [162], $\alpha_{I\!R}' = 0.90$ GeV^{-2} [163] and $B_{I\!R} = 2.0$ GeV^{-2} [164]. Apart from $\alpha_{I\!P}(0)$, these are the same values used in the preliminary H1 analysis [148]. The Reggeon structure function, $F_2^{I\!R}(\beta, Q^2)$, is calculated at NLO from the GRV pionic PDFs [165]. For the non-perturbative Pomeron, the input quark singlet and gluon distributions, $\beta\Sigma^{I\!P=\rm NP}(\beta, Q_0^2; Q_0^2)$ and $\beta' g^{I\!P=\rm NP}(\beta', Q_0^2; Q_0^2)$, are taken to have the same β dependence as for the two-quark Pomeron (see (5.15) and (5.16)), with different normalisations $c_{q/\rm NP}$ and $c_{g/\rm NP}$. (Taking the same β dependence as for the two-gluon Pomeron, (5.13) and (5.14), gives a much worse

[1]The couplings of the Pomeron or Reggeon to the proton are absorbed into the parameters $c_{a/\rm NP}$ ($a = q, g$) and $c_{I\!R}$.

description of the data.)

An improvement to the treatment of the secondary Reggeon contribution described above might be to introduce a 'perturbative' contribution similar to the two-quark Pomeron, but depending on the valence quark distributions of the proton rather than the sea quark distributions. However, for the present analyses we adopt the same treatment of the secondary Reggeon contribution as H1 [148] to avoid introducing further additional parameters, and since there are rather few $F_2^{D(3)}$ data points at large $x_{I\!P} > 0.01$ where the secondary Reggeon contribution is important.

5.2 Description of DDIS data

We fit to the preliminary ZEUS [157,158] and H1 [148] DDIS data using (5.23), and varying the free parameters until an optimum description of the data is obtained. We impose a cut $M_X > 2$ GeV on the fitted data to exclude large contributions from vector meson production and other higher-twist effects, and a cut $y < 0.45$ so that we can assume that the measured reduced diffractive cross section $\sigma_r^{D(3)}$ is approximately equal to $F_2^{D(3)}$ (see (4.17)). The statistical and systematic experimental errors are added in quadrature.[2] The χ^2 is then

$$\chi^2 = \sum_i \frac{\left[(F_2^{D(3)})_i^{\text{exp.}} - (F_2^{D(3)})_i^{\text{th.}}\right]^2}{(\delta^2_{\text{stat.}} + \delta^2_{\text{sys.}})_i^{\text{exp.}}}, \tag{5.27}$$

where the sum is over all data points satisfying the cuts $y < 0.45$ and $M_X > 2$ GeV.

We use the QCDNUM program [166] to perform the NLO DGLAP evolution and the MINUIT program [167] to find the optimal parameters. The values of $\alpha_S(M_Z^2)$ and the charm and bottom quark masses are taken to be the same as in the MRST2001 NLO parton set [127]. Two sets of preliminary ZEUS data are fitted: those obtained using the leading proton spectrometer (LPS) [157][3], and those obtained using the so-called M_X method [158] which is based on the fact that diffractive and non-diffractive events have very different $\ln M_X^2$ distributions. For the latter data set, in addition to elastic proton scattering, proton dissociation up to mass $M_Y = 2.3$ GeV is included. Clearly the cross section will be larger in this case, so we allow for the overall normalisation of these data by multiplying (5.23) by a factor N_Z. An analogous normalisation, N_H, is applied for the preliminary H1 data [148], where diffractive events are selected on the basis of a large rapidity gap, and where proton

[2] In reality the various systematic errors are often strongly correlated; these correlations are accounted for in the H1 analysis [148] but are not publically available.

[3] This data set has since been published in [168].

dissociation up to mass $M_Y = 1.6$ GeV is included. The ZEUS M_X data [158] do not include secondary Reggeon contributions, therefore we omit the fourth term of (5.23) when fitting to these data. We fit to each data set separately, and then we perform fits to the three data sets combined.

5.2.1 ... with a 'dummy' gluon distribution

For our first study, we parameterise the perturbative Pomeron flux factor (5.6) using a simplified form for the gluon distribution of the proton,

$$x_{I\!P} g(x_{I\!P}, \mu^2) = x_{I\!P}^{-\lambda}, \tag{5.28}$$

where λ is independent of μ^2 and is determined by the fit to data.[4] The normalisation of (5.28) has been absorbed into the free parameters $c_{q/G}$, $c_{g/G}$, and $c_{L/G}$. The two-quark Pomeron is not included, that is, effectively $c_{q/S} = c_{g/S} = c_{L/S} = 0$.

Varying the Q_0 parameter, we find that the best fit to the combined ZEUS and H1 data sets is obtained with $Q_0^2 = 0.8$ GeV^2, which gives a χ^2/d.o.f. $= 1.05$ with $c_{g/\mathrm{NP}}$ going to zero. Later on, we will use the MRST2001 NLO [127] PDFs of the proton instead of the simplified form (5.28), where the minimum possible scale is 1 GeV. Using the form (5.28) with $Q_0^2 = 1$ GeV^2 gives only a slightly worse χ^2/d.o.f. $= 1.07$. Furthermore, fixing $c_{g/\mathrm{NP}} = 0$ makes little difference to the quality of the fit. Therefore, in all fits presented here, we take $Q_0^2 = 1$ GeV^2 and fix $c_{g/\mathrm{NP}} = 0$.

We find that each data set can be well described by this simple, perturbatively-motivated, approach. However, different values of λ and the other parameters are obtained from the ZEUS and H1 data, as can be seen from Table 5.1. In particular, the H1 data seem to have a flatter $x_{I\!P}$ dependence than the ZEUS data. This should be regarded as some inconsistency between the data sets, but not as a contradiction, since it is possible to obtain an adequate description of the combined data sets, as shown in Fig. 5.2 and by the results in the last column of Table 5.1.

Since the normalisation of the 'dummy' gluon distribution has been absorbed into the $c_{i/G}$ parameters ($i = q, g, L$) it is difficult to work out the effective 'K-factors' in this case, but we will do this in the next section.

[4]Strictly speaking, λ should depend on $\ln \mu^2$. We investigated this effect by taking $\lambda(\mu^2) = 0.08 + c_\lambda \ln(\mu^2/(0.45\,\mathrm{GeV}^2))$ with $Q_0 = 1$ GeV and $c_{g/\mathrm{NP}} = 0$. The combined fit to ZEUS and H1 DDIS data gave a χ^2/d.o.f. $= 1.12$ with $c_\lambda = 0.054 \pm 0.006$. This is consistent with the value found by H1 in a fit to inclusive F_2 data [169] of $c_\lambda = 0.0481 \pm 0.0013(\mathrm{stat.}) \pm 0.0037(\mathrm{syst.})$. Since the χ^2/d.o.f. was not improved compared to the corresponding fit which took λ to be independent of μ^2 (χ^2/d.o.f. $= 1.07$), we used the form (5.28) for simplicity.

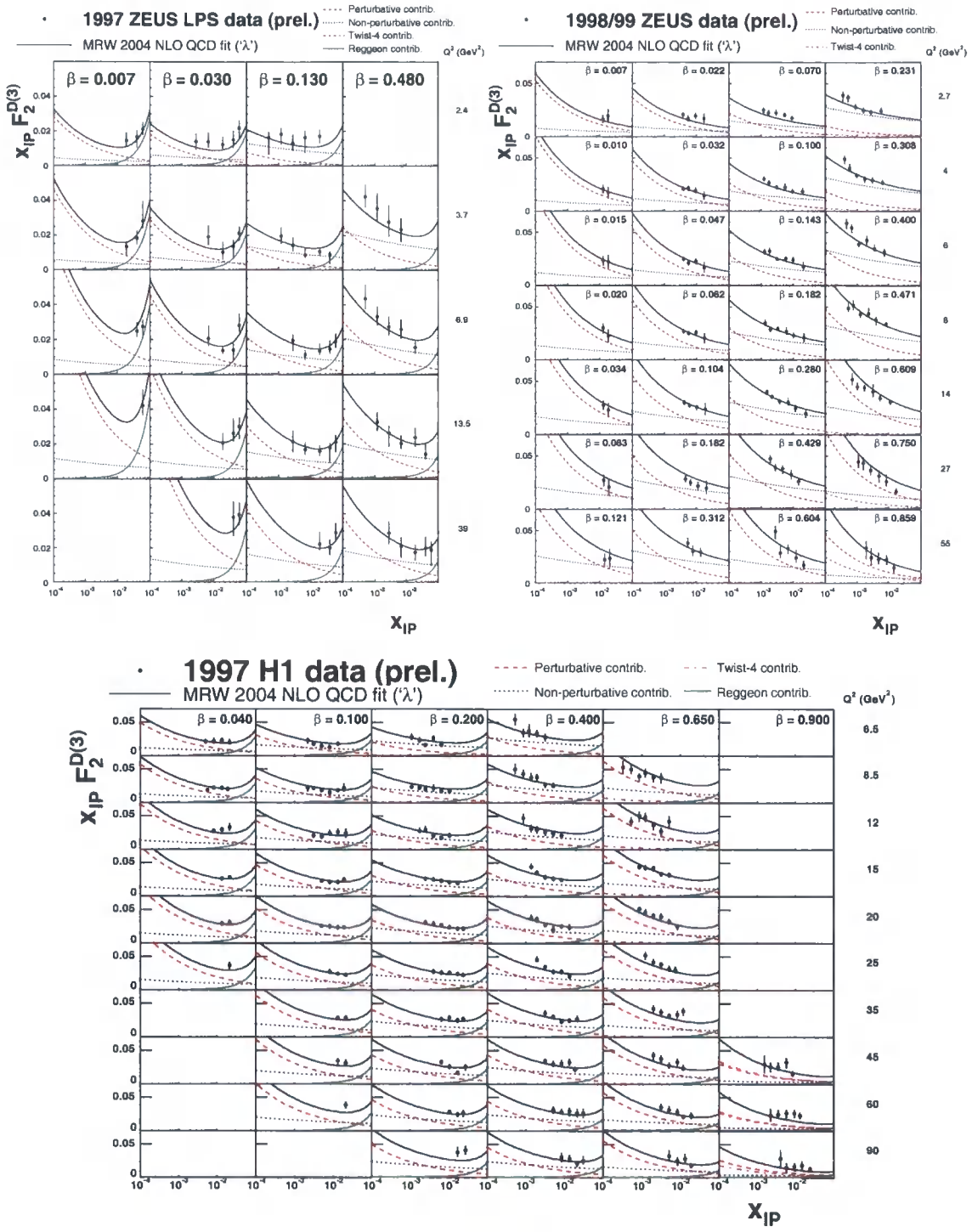

Figure 5.2: Fit to combined preliminary ZEUS [157, 158] and H1 [148] $F_2^{D(3)}$ data with a 'dummy' gluon distribution of the proton proportional to $x_{I\!P}^{-\lambda}$ (5.28). The curves show the four contributions to the total, as defined in (5.23). Only data points included in the fit are plotted.

Data sets fitted	ZEUS LPS[a]	ZEUS M_X	H1	ZEUS + H1
Number of points	69	121	214	404
χ^2/d.o.f.	0.67	0.78	1.08	1.08
$c_{q/G}$ (GeV^2)	0.71 ± 0.39	0.48 ± 0.12	2.2 ± 0.4	1.1 ± 0.2
$c_{g/G}$ (GeV^2)	0.11 ± 0.05	0.10 ± 0.02	0.26 ± 0.05	0.17 ± 0.02
$c_{L/G}$ (GeV^2)	0	0.20 ± 0.08	0.54 ± 0.17	0.36 ± 0.08
$c_{q/\mathrm{NP}}$ (GeV^{-2})	0.87 ± 0.13	1.22 ± 0.04	0.91 ± 0.05	1.09 ± 0.05
$c_{I\!R}$ (GeV^{-2})	6.7 ± 0.8	—	7.5 ± 2.0	6.2 ± 0.6
λ	0.23 ± 0.04	0.21 ± 0.02	0.13 ± 0.01	0.17 ± 0.01
N_Z	—	1.56 (fixed)	—	1.56 ± 0.06
N_H	—	—	1.26 (fixed)	1.26 ± 0.05
$R(6.5\,\mathrm{GeV}^2), R(90\,\mathrm{GeV}^2)$	0.60, 0.60	0.56, 0.57	0.54, 0.55	0.55, 0.56

Table 5.1: The values of the free parameters obtained in the fits to preliminary ZEUS [157, 158] and H1 [148] $F_2^{D(3)}$ data with a 'dummy' gluon distribution of the proton proportional to $x_{I\!P}^{-\lambda}$ (5.28). The last row $R(Q^2)$, defined in (5.33), gives the fraction of the Pomeron's (plus Reggeon's) momentum carried by gluons at $x_{I\!P} = 0.003$.

[a]Fitting to the published ZEUS LPS data [168], which is unchanged from the preliminary data fitted here apart from having smaller systematic errors, gives a χ^2/d.o.f. = 0.77.

5.2.2 ... with MRST gluon and sea quark distributions

These fits to the DDIS data imply that the growth of $F_2^{D(3)}$ with decreasing $x_{I\!P}$ comes from a gluon distribution which grows as $x_{I\!P}^{-\lambda}$ with $\lambda \simeq 0.17$. On the other hand, at low scales $\mu \sim Q_0 \sim 1$ GeV, which are dominant due to the $1/\mu^4$ factor in the Pomeron flux factor (5.6), the gluon distribution of the proton obtained from global analyses of DIS and related data is valence-like, or even negative, at small x, while the sea quark distribution grows as a negative power of x with decreasing x; see Fig. 5.3. Therefore, in order to describe the DDIS data we are forced to introduce a Pomeron comprised of two t-channel sea quarks, illustrated in Fig. 5.1(b).

The results of fits with this extended model, using the MRST2001 NLO [127] gluon and sea quark distributions of the proton, are shown in Table 5.2 and Fig. 5.4. We set $x_{I\!P}\, g(x_{I\!P}, \mu^2) = 0$ if it is negative. Again, good fits are obtained whether fitting ZEUS and H1 data separately or all together. However, the fit with only H1 data is dramatically different from the other three fits in Table 5.2, with a much larger two-gluon Pomeron contribution compared to the other three, which are dominated by the two-quark Pomeron. This difference can be traced to the flatter $x_{I\!P}$ dependence of the H1 data compared to the ZEUS data (see Table 5.1). Note that some parameters in Table 5.2 are consistent with zero, indicating some redundancy in this extended model.

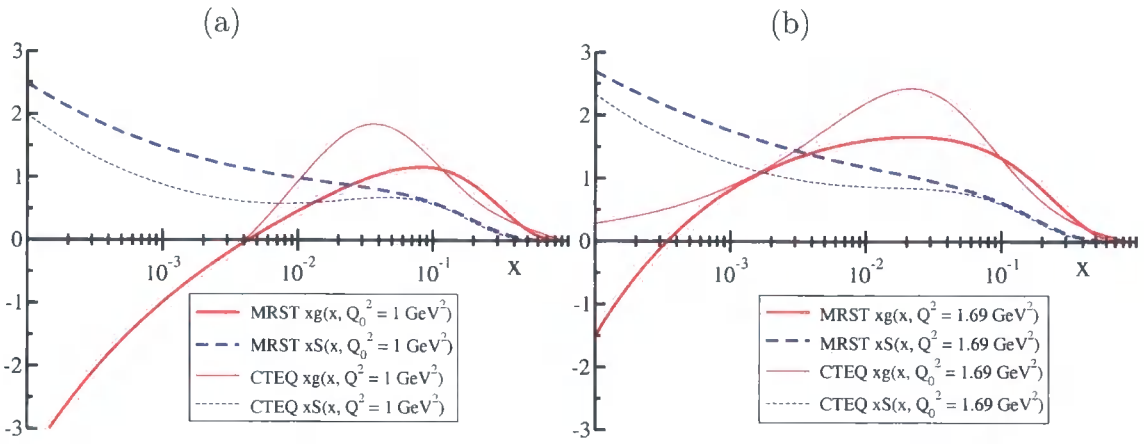

Figure 5.3: Comparison of MRST2001 NLO [127] and CTEQ6M [35] PDFs at their respective input scales of (a) 1 GeV^2 and (b) 1.69 GeV^2. The more recent MRST2002 [170] and MRST2004 [34] PDFs are similar to MRST2001. In (a) the CTEQ gluon distribution is set to zero if it is negative.

Data sets fitted	ZEUS LPS	ZEUS M_X	H1	ZEUS + H1
Number of points	69	121	214	404
χ^2/d.o.f.	0.79	0.96	0.71	1.14
$c_{q/G}$ (GeV^2)	0.001 ± 0.053	0.018 ± 0.023	0.36 ± 0.06	0.18 ± 0.04
$c_{g/G}$ (GeV^2)	0	0	0.37 ± 0.02	0
$c_{L/G}$ (GeV^2)	0.2 ± 1.5	0.050 ± 0.033	0.14 ± 0.03	0.064 ± 0.024
$c_{q/S}$ (GeV^2)	0.97 ± 0.40	0.49 ± 0.10	1.1 ± 0.1	0.58 ± 0.07
$c_{g/S}$ (GeV^2)	1.2 ± 0.2	1.23 ± 0.07	0	1.31 ± 0.07
$c_{L/S}$ (GeV^2)	0.41 ± 0.28	0.21 ± 0.09	0	0.11 ± 0.05
$c_{q/\mathrm{NP}}$ (GeV^{-2})	0.79 ± 0.22	1.16 ± 0.08	0.09 ± 0.11	0.92 ± 0.07
$c_{I\!R}$ (GeV^{-2})	6.6 ± 0.7	—	8.4 ± 1.8	6.4 ± 0.5
N_Z	—	1.54 (fixed)	—	1.54 ± 0.06
N_H	—	—	1.24 (fixed)	1.24 ± 0.04
$K_{q/G}$	0.006 ± 0.318	0.11 ± 0.14	2.2 ± 0.4	1.1 ± 0.2
$K_{g/G}$	0	0	3.9 ± 0.2	0
$K_{L/G}$	5 ± 41	1.4 ± 0.9	3.8 ± 0.8	1.7 ± 0.6
$K_{q/S}$	7.1 ± 2.9	3.6 ± 0.7	8.0 ± 0.7	4.2 ± 0.5
$K_{g/S}$	3.9 ± 0.7	4.0 ± 0.2	0	4.3 ± 0.2
$K_{L/S}$	3.4 ± 2.3	1.7 ± 0.7	0	0.9 ± 0.4
$R(6.5\,\mathrm{GeV}^2), R(90\,\mathrm{GeV}^2)$	0.57, 0.58	0.57, 0.59	0.60, 0.66	0.57, 0.57

Table 5.2: The values of the free parameters obtained in the fits to ZEUS [157, 158] and H1 [148] $F_2^{D(3)}$ data with MRST2001 NLO [127] gluon and sea quark distributions of the proton. The K-factors are defined in (5.29). The last row $R(Q^2)$, defined in (5.33), gives the fraction of the Pomeron's (plus Reggeon's) momentum carried by gluons at $x_{I\!P} = 0.003$.

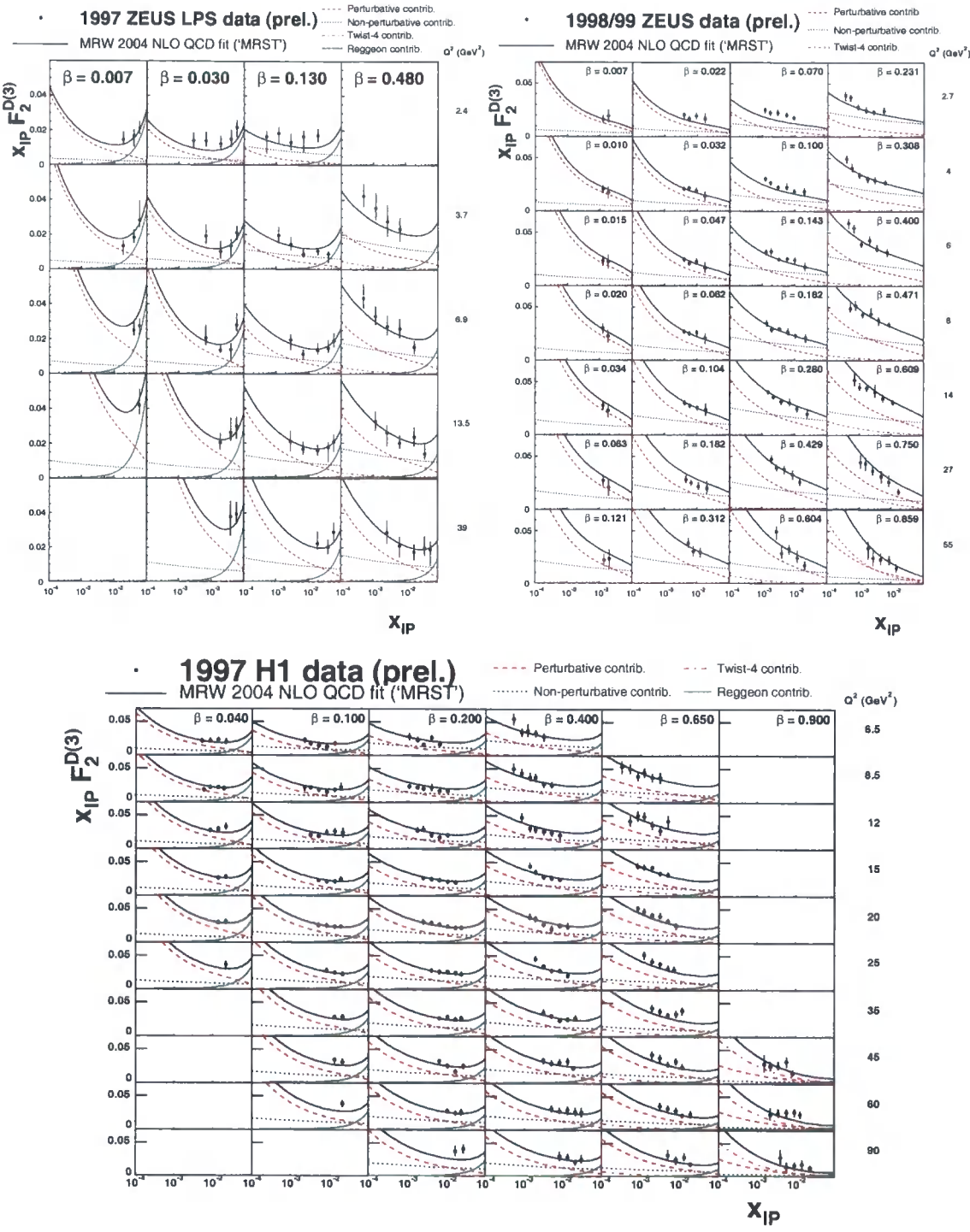

Figure 5.4: Fit to combined preliminary ZEUS [157, 158] and H1 [148] $F_2^{D(3)}$ data with MRST2001 NLO [127] gluon and sea quark distributions of the proton. The curves show the four contributions to the total, as defined in (5.23). Only data points included in the fit are plotted.

The experimental 'K-factors' given in Table 5.2 are defined as

$$K_{i/I\!P} \equiv \frac{c_{i/I\!P}}{c^{\rm LO}_{i/I\!P}}, \tag{5.29}$$

where $i = q, g, L$ and $I\!P = G, S$. The LO coefficients, $c^{\rm LO}_{i/I\!P}$, were derived in Section 4.7 and are collected below for convenience:

$$c^{\rm LO}_{q/G} = \frac{R_g^2}{B_D}, \qquad c^{\rm LO}_{g/G} = \frac{9R_g^2}{16B_D}, \qquad c^{\rm LO}_{L/G} = \frac{2R_g^2}{9B_D}, \tag{5.30}$$

$$c^{\rm LO}_{q/S} = \frac{4R_q^2}{81B_D}, \qquad c^{\rm LO}_{g/S} = \frac{R_q^2}{9B_D}, \qquad c^{\rm LO}_{L/S} = \frac{32R_q^2}{729B_D}. \tag{5.31}$$

In obtaining the numerical values of $K_{i/I\!P}$ presented in Table 5.2, we have used $B_D = 6$ GeV^{-2}, $R_g(\lambda = 0) = 1$ as given by (4.50), and $R_q(\lambda = 0.26) = 4.1$ as given by (4.91). These values of λ are obtained from the behaviour of the MRST2001 NLO PDFs at $Q^2 = 1$ GeV^2 as $x \to 0$, bearing in mind that we set the gluon distribution to zero if it is negative. It is remarkable that the K-factors turn out to be of typical size 1 to 4 (apart from $c_{g/G} = 0$) for the combined fit to ZEUS and H1 data; see also the values obtained later in Tables 6.1 and 6.3.

5.3 Diffractive parton distributions

From these fits to $F_2^{D(3)}$, we can extract the quark singlet and gluon DPDFs, $a^D(x_{I\!P}, \beta, Q^2) = \beta\Sigma^D(x_{I\!P}, \beta, Q^2)$ or $\beta g^D(x_{I\!P}, \beta, Q^2)$, from the three leading-twist contributions to (5.23):

$$a^D(x_{I\!P}, \beta, Q^2) = \sum_{I\!P=G,S,GS} \left(\int_{Q_0^2}^{Q^2} {\rm d}\mu^2 \, f_{I\!P}(x_{I\!P}; \mu^2) \, a^{I\!P}(\beta, Q^2; \mu^2) \right)$$
$$+ f_{I\!P={\rm NP}}(x_{I\!P}) \, a^{I\!P={\rm NP}}(\beta, Q^2; Q_0^2) + c_{I\!R} \, f_{I\!R}(x_{I\!P}) \, a^{I\!R}(\beta, Q^2). \tag{5.32}$$

The DPDFs calculated using (5.32) are plotted for the eight different fits of Tables 5.1 ('λ') and 5.2 ('MRST') in Fig. 5.5(a) for $x_{I\!P} = 0.003$ and $Q^2 = 6.5, 90$ GeV^2. The DPDFs extracted from the fits to the combined ZEUS and H1 data sets are shown as the solid lines. We also show the Pomeron PDFs from the preliminary H1 analysis [148] multiplied by $f_{I\!P}(x_{I\!P})$ (given by (5.26) with $\alpha_{I\!P}(0) = 1.173$) and normalised to the ZEUS LPS data by dividing by a factor 1.26 (from Table 5.1). Notice that the eight different fits of Tables 5.1 and 5.2 give similar DPDFs, especially at the higher Q^2 value, with the possible exception of the 'MRST' fit to only H1 data.

From Fig. 5.5(a), the diffractive quark singlet distribution obtained by H1 [148]

(a)

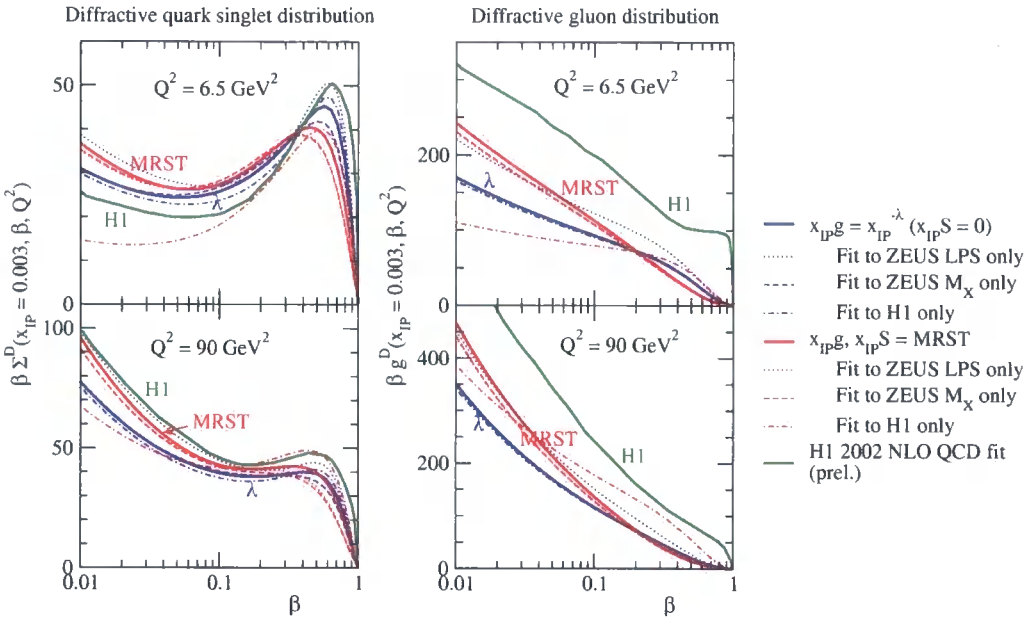

(b)

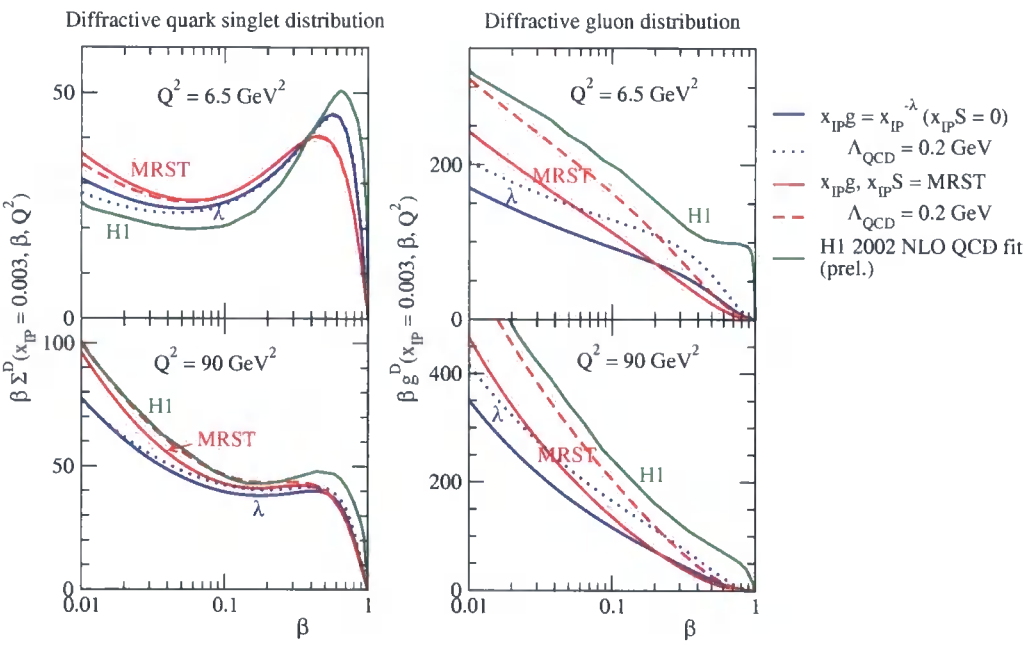

Figure 5.5: The solid lines labelled 'λ' and 'MRST' show the DPDFs extracted from the fits in Tables 5.1 and 5.2 to the combined preliminary ZEUS [157, 158] and H1 [148] data (compared to those obtained by H1 [148]). In (a) we also show the separate fits to the three different data sets of Tables 5.1 and 5.2. In (b) we also show fits to the combined ZEUS and H1 data using the same value of $\alpha_S(M_Z^2)$ as in the preliminary H1 analysis [148], corresponding to $\Lambda_{QCD} = 0.2$ GeV for 4 flavours.

has a slightly steeper Q^2 dependence than the fits presented here, and hence H1 obtain a larger diffractive gluon distribution. In addition, the smaller value of $\alpha_S(M_Z^2)$ used by H1 also enlarges their gluon density.[5] To demonstrate this, we repeated the combined fits to ZEUS and H1 data using the same value of $\alpha_S(M_Z^2)$ as in the preliminary H1 analysis [148]. The resulting DPDFs are shown by the dotted ('λ') and dashed ('MRST') lines in Fig. 5.5(b); the diffractive gluon distributions are much closer to the H1 diffractive gluon distribution, especially for the 'MRST' fit, but there is still some discrepancy. In our analysis, all the input Pomeron PDFs vanish as either $(1-\beta)$ or $(1-\beta)^2$ as $\beta \to 1$. As $\beta \to 1$, the only non-zero contribution to $F_2^{D(3)}$ comes from a twist-four component arising from longitudinally polarised photons. This contribution was not included in the H1 analysis [148], and hence rather large DPDFs were obtained by H1 for β close to 1, with an unphysical 'bump' in the diffractive gluon distribution (see Fig. 5.5).

In Fig. 5.6 we show the breakdown of the five separate components of (5.32) for the 'λ' and 'MRST' fits to the combined data sets. Note the large contribution from the two-quark component of the Pomeron for the 'MRST' fit.

We define the fraction of the Pomeron's (plus Reggeon's) momentum carried by gluons at $x_{I\!P} = 0.003$ as

$$R(Q^2) \equiv \frac{\int_{0.01}^{1} \mathrm{d}\beta\ \beta g^D(x_{I\!P}=0.003,\beta,Q^2)}{\int_{0.01}^{1} \mathrm{d}\beta\ [\beta\Sigma^D(x_{I\!P}=0.003,\beta,Q^2)+\beta g^D(x_{I\!P}=0.003,\beta,Q^2)]}, \tag{5.33}$$

which is given for Q^2 values of 6.5 and 90 GeV^2 in the last rows of Tables 5.1 and 5.2. The gluon momentum fraction, $R(Q^2)$, is consistently 55–60% and is almost independent of Q^2. Taking the same $\alpha_S(M_Z^2)$ as in the preliminary H1 analysis would increase this value to $\approx 65\%$, compared to the value found by H1 of $75 \pm 15\%$ [148].

Note, from Fig. 5.4, that the perturbative Pomeron contribution to $F_2^{D(3)}$ (from scales $\mu > Q_0 = 1$ GeV) is not small; as a rule it is more than half the total contribution. The comparison of the separate fits to the ZEUS and H1 data presented in Table 5.2 demonstrates that there is a strong correlation between the pairs of parameters $c_{i/G}$ and $c_{i/S}$, where $i = q, g, L$. That is, with the present accuracy of the data, it is hard to distinguish between partons which originate from the two-gluon and two-quark components of the Pomeron.[6] Nevertheless, the final DPDFs are similar for the different fits. This stability increases confidence in these distri-

[5] In the preliminary H1 analysis [148], $\Lambda_{\rm QCD} = 0.2$ GeV for 4 flavours, corresponding to $\alpha_S(M_Z^2) = 0.1085$, whereas we take $\alpha_S(M_Z^2) = 0.1190$ from the MRST2001 NLO parton set [127]; cf. the world average, $\alpha_S(M_Z^2) = 0.1187(20)$, from the PDG [171].

[6] The combined analysis of DDIS data with a more exclusive diffractive process, such as diffractive J/ψ production at HERA, which is sensitive to the two-gluon component of the Pomeron, may help to resolve this problem.

(a)

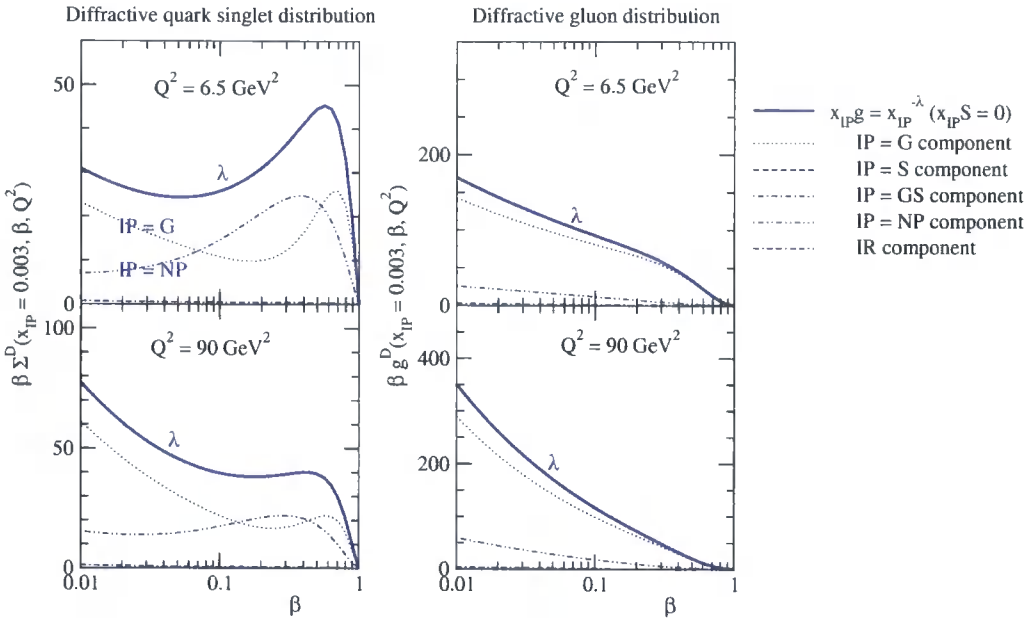

(b)

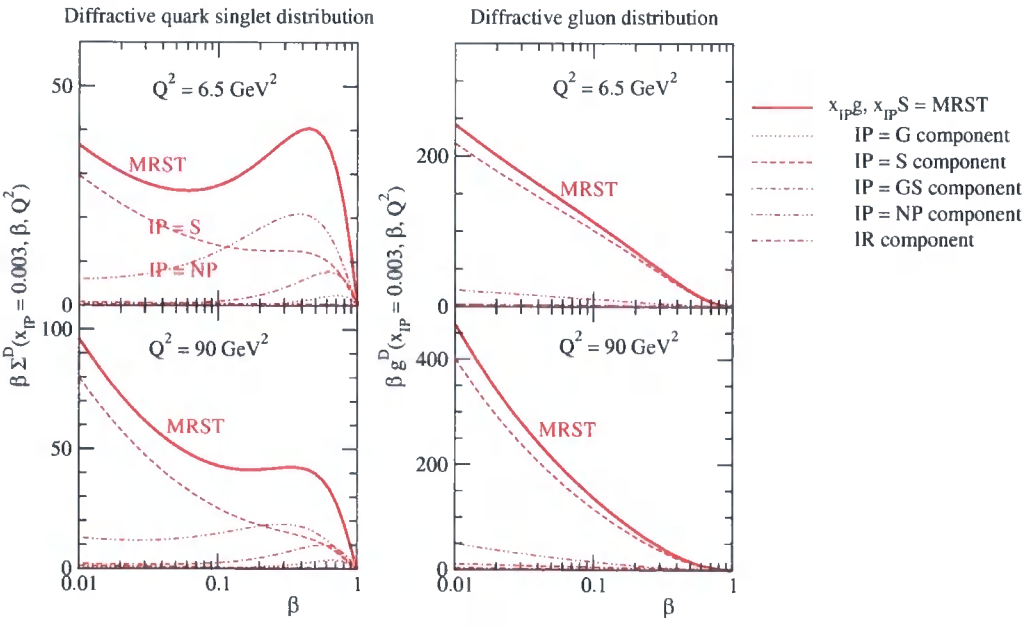

Figure 5.6: The breakdown of the five separate components of (5.32) for (a) the 'λ' fit of Table 5.1 and (b) the 'MRST' fit of Table 5.2. In both cases, the fit to the combined ZEUS and H1 data is shown.

butions, so that they can be used in the description of other diffractive processes at HERA and the Tevatron. Of course, we must include the probability that the rapidity gap survives the soft rescattering of the colliding hadrons or 'hadron-like' states [138–142].

It has been demonstrated by H1 that their preliminary DPDFs [148] can be used to describe final state observables in DDIS, namely dijet and D^* meson production cross sections [172]. Before our DPDFs can be taken seriously we need to demonstrate the same thing. The DPDFs can be then be used to calculate the diffractive structure function of the antiproton, defined as

$$\tilde{F}_{jj}^{D}(\beta) = \frac{1}{\xi_{\text{max}} - \xi_{\text{min}}} \int_{\xi_{\text{min}}}^{\xi_{\text{max}}} \mathrm{d}\xi \left[\beta g^{D}(\xi, \beta, Q^2) + \frac{4}{9} \beta \Sigma^{D}(\xi, \beta, Q^2) \right]. \tag{5.34}$$

Comparison to CDF diffractive dijet data measured at the Tevatron [173] will allow checks to be made of the rapidity gap 'survival probability' [138, 139], which is an important ingredient in calculations of diffractive Higgs production at the LHC [91].

Chapter 6

Absorptive corrections in deep-inelastic scattering

A long-standing question concerns the treatment of diffractive events in a global parton analysis of DIS and related hard-scattering data. Are they already included in the input distributions or must some account be taken of them in the DGLAP evolution? The present chapter addresses this question. We show that DDIS is partially included in the starting distributions and partially must be allowed for in the DGLAP evolution.

The advantage of describing the DDIS data using an approach where the dependence on the Pomeron scale μ is explicit, as in the last chapter, is the possibility to use the results to evaluate the absorptive corrections $\Delta F_2^{\rm abs}$ to the inclusive structure function F_2. Indeed, as we shall describe below, the application of the Abramovsky-Gribov-Kancheli (AGK) cutting rules [174, 175] gives[1]

$$\Delta F_2^{\rm abs}(x_B, Q^2; \mu^2) = -F_2^D(x_B, Q^2; \mu^2), \tag{6.1}$$

where $F_2^D(x_B, Q^2; \mu^2)$ is the contribution to the diffractive structure function $F_2^{D(3)}$ (integrated over $x_{I\!P}$) which originates from a perturbative component of the Pomeron of size $1/\mu$. Since the equality (6.1) is valid for each component, μ, of the perturbative Pomeron, we can separate the screening corrections coming from low $\mu < Q_0$ (which are included in the input parameterisations) from the absorptive effects at small distances ($\mu > Q_0$) which occur during the DGLAP evolution in the analysis of DIS data. Clearly, the inclusion of these absorptive effects will modify the parton distributions obtained from the DIS analysis. Not surprisingly, we find that by

[1] Actually, to extract the 'data' appropriate for a pure DGLAP fit of $F_2(x_B, Q^2)$ we have to include the absorptive corrections $\Delta F_2^{\rm abs}$ integrated over μ^2 in the whole evolution interval from Q_0^2 to Q^2.

accounting for these 'Glauber-type' shadowing corrections we enhance the small-x input gluon distribution.

6.1 Gluon recombination at small x

At very small values of x it is expected that the number density of partons within the proton becomes so large that they begin to recombine with each other. This phenomenon of parton recombination is also referred to in the literature by a plethora of other names, such as absorptive corrections, non-linear effects, screening, shadowing, unitarity corrections, multiple scattering, multiple interactions, or saturation effects. Here, we will usually refer to 'absorptive corrections'.

The first perturbative QCD calculations describing the fusion of two Pomeron ladders into one were made within the DLLA by Gribov-Levin-Ryskin (GLR) [23] and by Mueller-Qiu (MQ) [176]. The GLRMQ equations add an extra non-linear term, quadratic in the gluon density, to the usual DGLAP equations for the gluon and sea quark evolution:

$$\frac{\partial xg(x,Q^2)}{\partial \ln Q^2} = \left.\frac{\partial xg(x,Q^2)}{\partial \ln Q^2}\right|_{\text{DGLAP}} - 3\,\frac{\alpha_S^2(Q^2)}{R^2Q^2}\int_x^1 \frac{\mathrm{d}x'}{x'}\left[x'g(x',Q^2)\right]^2, \tag{6.2}$$

$$\frac{\partial xS(x,Q^2)}{\partial \ln Q^2} = \left.\frac{\partial xS(x,Q^2)}{\partial \ln Q^2}\right|_{\text{DGLAP}} - \frac{1}{10}\,\frac{\alpha_S^2(Q^2)}{R^2Q^2}\left[xg(x,Q^2)\right]^2, \tag{6.3}$$

where R is of the order of the proton radius. The Balitsky-Kovchegov (BK) [177–179] equation generalises the non-linear term of the GLRMQ equations to single $\ln(1/x)$ accuracy. It is equivalent to the LL BFKL equation with an additional non-linear term. However, NLL BFKL contributions are not accounted for, which are known to have a large numerical effect.

A phenomenological investigation using the GLRMQ equations based on NLO DGLAP evolution was made in [180], before the advent of the HERA data. The input gluon and sea quark distributions were assumed to have a small-x behaviour of the form $xg, xS \sim x^{-0.5}$ at an input scale of $Q_0^2 = 4$ GeV^2. Since the small-x gluon distribution is now known to be valence-like at low Q^2 from the HERA data, the shadowing corrections due to gluon recombination are correspondingly reduced, as found by MRST in [181]. At low Q^2 the sea quarks are the dominant partons at small x, and hence sea quark recombination should be considered in addition to gluon recombination.

On the other hand, Eskola *et al.* [182] have found that taking input gluon and sea quark distributions at $Q^2 = 1.4$ GeV^2, then evolving upwards with the GLRMQ

equation based on LO DGLAP evolution, improves the agreement with F_2 data at small x and low Q^2 compared to the standard CTEQ sets. In [182] the input distributions were obtained by interpolating between three results: CTEQ5L [81] PDFs at $Q^2 = 5$ GeV^2, CTEQ6L [35] PDFs at $Q^2 = 10$ GeV^2, and CTEQ6L PDFs at $Q^2 = 3$ GeV^2, each evolved downwards to $Q^2 = 1.4$ GeV^2 using the GLRMQ equation based on LO DGLAP evolution. This procedure of obtaining the input by averaging over different CTEQ PDFs is clearly strange, but is necessary since simply obtaining the input distributions by evolving the CTEQ6L PDFs at $Q^2 = 5$ GeV^2 downwards to $Q_0^2 = 1.4$ GeV^2 gave a worse description of the data at small x than the CTEQ6L result. This approach assumes that the PDFs evolved with the GLRMQ equation should be unchanged at large Q^2 from the conventional DGLAP-evolved sets. However, as we will show later, this is not the case, as observed by MQ [176]:

> The correction term to the usual DGLAP equation is of higher twist as a factor of $1/Q^2$ explicitly appears. This does not mean that shadowing effects go away as $1/Q^2$. On the contrary, in order to determine $g(x, Q^2)$ in terms of, say, $g(x', Q_0^2)$ one must integrate the DGLAP equation between Q_0^2 and Q^2. If the correction term is effective anywhere in that interval shadowing effects will have been included.

Therefore the CTEQ PDFs, with input scale $Q_0^2 = 1.69$ GeV^2, will not be free of the effects of absorptive corrections even at large Q^2 and so they should not be taken as input to GLRMQ evolution. It is necessary to refit the input PDFs in a global parton analysis, preferably using NLO QCD rather than just LO QCD.

Using the GLRMQ equation to study absorptive corrections has several limitations. The non-linear terms in the evolution equation lead to a violation of momentum conservation. There is some uncertainty in the two-gluon distribution, taken to be [176]

$$x^2 G^{(2)}(x, Q^2) = \frac{2}{3\pi R^2} \left[x g(x, Q^2) \right]^2 \tag{6.4}$$

in (6.2) and (6.3), and in the value of the R parameter. In the next section, we show that the absorptive corrections to F_2 can be extracted from DDIS data using the formalism of Chapter 5. We will then perform a NLO QCD parton analysis of F_2 including these absorptive corrections, originating from sea quark recombination as well as gluon recombination.

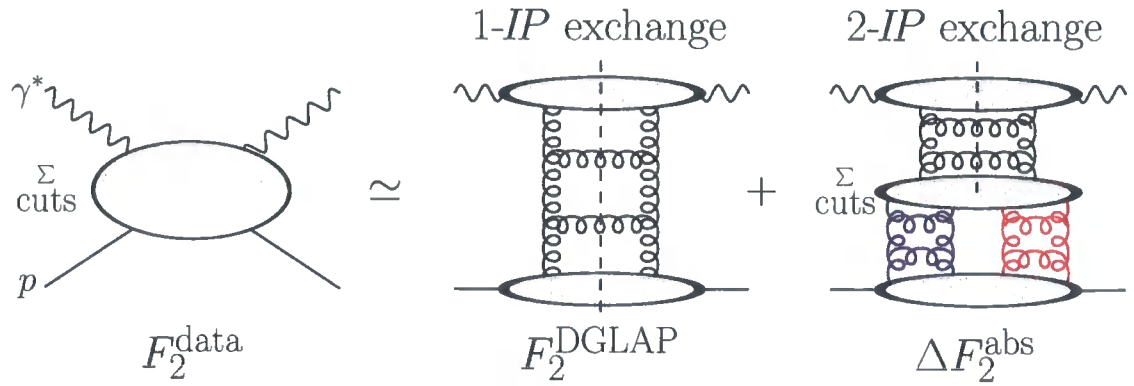

Figure 6.1: The total F_2, measured by experiment, can be approximated by the sum of the one-Pomeron and two-Pomeron exchange contributions.

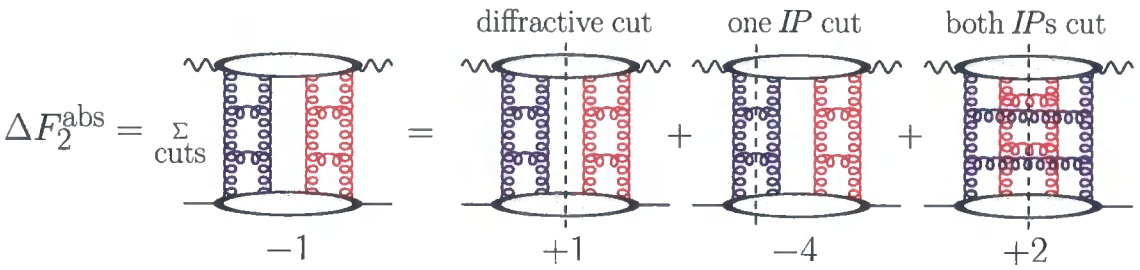

Figure 6.2: The two-Pomeron exchange contribution to F_2. The equality shows the application of the AGK cutting rules, and the relative magnitudes of the cut diagrams. All the permutations of the two gluon ladders (forming Pomeron exchange) are implied.

6.2 Absorptive corrections to F_2

The total proton structure function, $F_2^{\text{data}}(x_B, Q^2)$, as measured by experiment, can be approximately written as a sum of the one-Pomeron[2] (DGLAP) contribution and absorptive corrections due to two-Pomeron exchange. That is,

$$F_2^{\text{data}}(x_B, Q^2) \simeq F_2^{\text{DGLAP}}(x_B, Q^2) + \Delta F_2^{\text{abs}}(x_B, Q^2), \tag{6.5}$$

illustrated in Fig. 6.1. A brief insight into the equality (6.1) may be obtained from Fig. 6.2, which shows the leading absorptive correction (the two-Pomeron exchange contribution) to F_2. For simplicity, the upper parton ladder, shown in the right-hand diagram of Fig. 6.1, is hidden inside the upper blob in each diagram of Fig. 6.2. Applying the AGK cutting rules [174] to the $IP \otimes IP$ contribution, we obtain the relative contributions of $+1$, -4, and $+2$ according to whether neither Pomeron, one Pomeron, or both Pomerons are cut. The first contribution is just F_2^D, which

[2]Here, we are interpreting the perturbative Pomeron to be a NLO DGLAP parton ladder, rather than the more usual interpretation of the QCD Pomeron as being a BFKL gluon ladder.

enters with the same magnitude, but the opposite sign, in the total $\Delta F_2^{\rm abs}$. Hence the equality shown in (6.1). In this way, we are able to estimate the absorptive corrections, $\Delta F_2^{\rm abs}(x_B, Q^2; \mu^2)$, as a function of μ, from the perturbative component of $F_2^{D(3)}$ determined from the fit to the DDIS data. Integrating (6.1) over μ^2 from Q_0^2 to Q^2 we obtain

$$\Delta F_2^{\rm abs}(x_B, Q^2) = -\int_{Q_0^2}^{Q^2} {\rm d}\mu^2 \; F_2^D(x_B, Q^2; \mu^2). \tag{6.6}$$

That is, the leading absorptive correction is given by *minus* the diffractive component arising from Pomeron scales greater than Q_0, where Q_0 is the scale that the input PDFs are parameterised at in a DGLAP fit to DIS data. (Note that the same negative sign was given in (4.5) for the $I\!P \otimes I\!P$ contribution in Regge theory.) The $\mu < Q_0$ contributions to the absorptive corrections are already included in the input parameterisations. To fit F_2 purely using the DGLAP formalism, we first need to 'correct' the data for absorptive corrections,

$$\begin{aligned} F_2^{\rm DGLAP}(x_B, Q^2) &\simeq F_2^{\rm data}(x_B, Q^2) - \Delta F_2^{\rm abs}(x_B, Q^2) \\ &= F_2^{\rm data}(x_B, Q^2) + |\Delta F_2^{\rm abs}(x_B, Q^2)|. \end{aligned} \tag{6.7}$$

Basically, the (negative) screening corrections have to be subtracted from the F_2 data, before the DGLAP analysis is performed. At small x_B, the effective F_2 'data' are therefore appreciably enhanced. Notice that the original fit to the DDIS data in Chapter 5 required knowledge of the gluon and sea quark distributions, $x_{I\!P}\, g(x_{I\!P}, \mu^2)$ and $x_{I\!P}\, S(x_{I\!P}, \mu^2)$, in the perturbative Pomeron flux factors. Since the new DIS fit yields modified parton distributions, we therefore have to repeat the fit to the DDIS data. Fortunately, the successive iterations between the DDIS and DIS fits rapidly converge, as we shall demonstrate.

6.2.1 Connection to GLRMQ approach

It is illuminating to show how our approach of 'correcting' the data then performing linear DGLAP evolution is related to the GLRMQ approach of including a non-linear term in the evolution equation.

Assuming that Q_0^2, the scale that the input PDFs are taken at, has the same value as that used in Chapter 5 to separate the perturbative and non-perturbative contributions to DDIS, then the absorptive corrections are

$$\Delta F_2^{\rm abs}(x_B, Q^2) = -\int_{x_B}^{1} {\rm d}x_{I\!P} \left[F_{2,{\rm P}}^{D(3)}(x_{I\!P}, \beta, Q^2) + F_{L,{\rm P}}^{D(3)}(x_{I\!P}, \beta, Q^2) \right], \tag{6.8}$$

where $F_{2,\mathrm{P}}^{D(3)}$ is the leading-twist contribution (5.5) and $F_{L,\mathrm{P}}^{D(3)}$ is the twist-four contribution (5.19). Recall that the notation $I\!P = G, S, GS$ denotes that the perturbative Pomeron is represented by two t-channel gluons, two t-channel sea quarks, or the interference between these, respectively. Considering only the $I\!P = G$ contribution, then

$$F_{2,\mathrm{P}}^{D(3)}(x_{I\!P}, \beta, Q^2) = \int_{Q_0^2}^{Q^2} \frac{\mathrm{d}\mu^2}{\mu^4} \frac{1}{x_{I\!P}} \left[\alpha_S(\mu^2)\, x_{I\!P} g(x_{I\!P}, \mu^2) \right]^2 F_2^{I\!P=G}(\beta, Q^2; \mu^2), \quad (6.9)$$

$$F_{L,\mathrm{P}}^{D(3)}(x_{I\!P}, \beta, Q^2) = \frac{1}{Q^2} \int_{Q_0^2}^{Q^2} \frac{\mathrm{d}\mu^2}{\mu^2} \frac{1}{x_{I\!P}} \left[\alpha_S(\mu^2)\, x_{I\!P} g(x_{I\!P}, \mu^2) \right]^2 F_L^{I\!P=G}(\beta), \quad (6.10)$$

where $F_2^{I\!P=G}(\beta, Q^2; \mu^2)$ and $F_L^{I\!P=G}(\beta)$ are defined in (5.9) and (5.20) respectively. Neglecting the logarithmic scaling violations of $F_2^{I\!P=G}(\beta, Q^2; \mu^2)$ and differentiating (6.5) with respect to $\ln Q^2$ we obtain

$$\frac{\partial F_2^{\mathrm{data}}}{\partial \ln Q^2} \simeq \frac{\partial F_2^{\mathrm{DGLAP}}}{\partial \ln Q^2} - \frac{\alpha_S^2(Q^2)}{Q^2} \int_{x_B}^1 \frac{\mathrm{d}x_{I\!P}}{x_{I\!P}} \left[x_{I\!P} g(x_{I\!P}, Q^2) \right]^2 \left\{ F_2^{I\!P=G}(\beta, Q^2; Q^2) + F_L^{I\!P=G}(\beta) \right\}. \quad (6.11)$$

This equation could be used to derive a more precise form of the GLRMQ equation, where the non-linear terms were calculated in the DLLA, that is, assuming that $\beta \ll \beta' \ll 1$ where $\beta \equiv x_B/x_{I\!P} \to 0$. In this limit,

$$\beta \Sigma^{I\!P=G}(\beta, Q^2; Q^2) \to 0, \quad (6.12)$$

$$\beta' g^{I\!P=G}(\beta', Q^2; Q^2) \to c_{g/G}, \quad (6.13)$$

$$F_L^{I\!P=G}(\beta) \to 0, \quad (6.14)$$

so the Pomeron structure function (5.9) is

$$\begin{aligned} F_2^{I\!P}(\beta, Q^2; Q^2) &= \frac{\alpha_S}{2\pi} \beta \int_\beta^1 \frac{\mathrm{d}\beta'}{\beta'^2} \langle e_f^2 \rangle C_{2,g}^{\mathrm{NLO}}\left(\frac{\beta}{\beta'}\right) c_{g/G} \\ &= \frac{\alpha_S}{2\pi} x_B \int_{x_B}^1 \frac{\mathrm{d}x}{x^2} \langle e_f^2 \rangle C_{2,g}^{\mathrm{NLO}}\left(\frac{x_B}{x}\right) c_{g/G}, \end{aligned} \quad (6.15)$$

since $\beta' = x/x_{I\!P}$. A similar equation holds for the proton structure function, assuming that gluons give the dominant contribution at small x. Neglecting the scale dependence of $\alpha_S(Q^2)$ and differentiating with respect to $\ln Q^2$ gives

$$\frac{\partial F_2}{\partial \ln Q^2} = \frac{\alpha_S}{2\pi} x_B \int_{x_B}^1 \frac{\mathrm{d}x}{x^2} \langle e_f^2 \rangle C_{2,g}^{\mathrm{NLO}}\left(\frac{x_B}{x}\right) \frac{\partial\, x g(x, Q^2)}{\partial \ln Q^2}. \quad (6.16)$$

Hence (6.11) becomes

$$\frac{\partial x g(x,Q^2)}{\partial \ln Q^2} \simeq \frac{\partial x g(x,Q^2)}{\partial \ln Q^2}\bigg|_{\text{DGLAP}} - c_{g/G}\,\frac{\alpha_S^2(Q^2)}{Q^2}\int_x^1 \frac{\mathrm{d}x_{I\!P}}{x_{I\!P}}\left[x_{I\!P} g(x_{I\!P},Q^2)\right]^2, \quad (6.17)$$

which is the GLRMQ equation for the gluon evolution (6.2) with $c_{g/G} = 3/R^2$.

The GLRMQ equation for the sea quark evolution (6.3) can be obtained from (6.11) by assuming light quark flavour symmetry and neglecting valence quarks (since we are assuming small x_B),

$$\frac{\partial F_2(x_B,Q^2)}{\partial \ln Q^2} = \langle e_f^2\rangle\,\frac{\partial x_B S(x_B,Q^2)}{\partial \ln Q^2}, \quad (6.18)$$

and replacing the Pomeron structure function in (6.11) with[3]

$$\left\{F_2^{I\!P=G}(\beta,Q^2;Q^2) + F_L^{I\!P=G}(\beta)\right\} \;\to\; \langle e_f^2\rangle\,\beta\,\delta(1-\beta)\,\frac{1}{10\,R^2}, \quad (6.19)$$

assuming that the struck quark carries all the Pomeron's momentum. Then (6.11) becomes

$$\begin{aligned}\frac{\partial x_B S(x_B,Q^2)}{\partial \ln Q^2} &\simeq \frac{\partial x_B S(x_B,Q^2)}{\partial \ln Q^2}\bigg|_{\text{DGLAP}} - \frac{1}{10}\,\frac{\alpha_S^2(Q^2)}{R^2Q^2}\int_{x_B}^1 \frac{\mathrm{d}\beta}{\beta}\left[x_{I\!P} g(x_{I\!P},Q^2)\right]^2 \beta\,\delta(1-\beta)\\ &= \frac{\partial x_B S(x_B,Q^2)}{\partial \ln Q^2}\bigg|_{\text{DGLAP}} - \frac{1}{10}\,\frac{\alpha_S^2(Q^2)}{R^2Q^2}\left[x_B g(x_B,Q^2)\right]^2.\end{aligned} \quad (6.20)$$

While our approach is qualitatively equivalent to the GLRMQ approach it goes beyond the DLLA keeping the full β dependence in the Pomeron structure function and introducing sea quark recombination in addition to gluon recombination.

We repeat that the factor of $1/Q^2$ in the non-linear term of the evolution equations does *not* mean that shadowing effects disappear at large Q^2. The absorptive corrections accumulate evolving from a scale Q_0^2 up to Q^2; however, the *increase* in absorptive corrections *does* fall off as $1/\mu^2$ as the scale μ increases. Thus, the commonly held belief that the PDFs obtained from a parton analysis are independent of the input scale Q_0^2 that they are parameterised at is incorrect for a fit which neglects absorptive corrections; larger absorptive corrections will be obtained the smaller the value of Q_0^2. This fact might explain why MRST, who take $Q_0^2 = 1$ GeV^2, obtain a smaller gluon distribution at small x than CTEQ, who take $Q_0^2 = 1.69$ GeV^2; see, for example, Fig. 5.3. It is interesting that this hypothesis is further corroborated

[3]This replacement is needed to reproduce the GLRMQ equation for the sea quark evolution (6.3). Keeping the exact β dependence would give a more precise version of the GLRMQ equation.

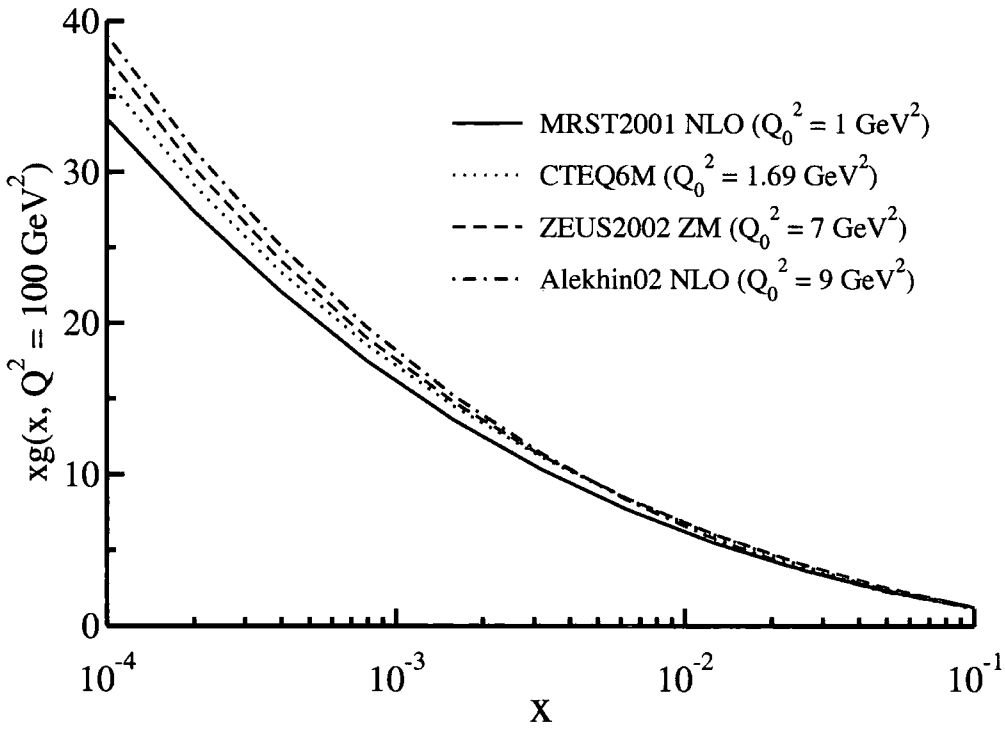

Figure 6.3: Gluon distribution at $Q^2 = 100$ GeV^2 from four different PDF sets. The size at small x increases with the input scale Q_0^2.

by considering the ZEUS2002 PDFs [183] with $Q_0^2 = 7$ GeV^2 and the Alekhin02 PDFs [184] with $Q_0^2 = 9$ GeV^2. The gluon distributions at $Q^2 = 100$ GeV^2 are compared in Fig. 6.3. It is seen that the ordering of the size of the small-x gluon distribution,

$$\mathrm{MRST} < \mathrm{CTEQ} < \mathrm{ZEUS} < \mathrm{Alekhin}, \tag{6.21}$$

reflects the ordering in Q_0^2. However, since there are many other differences between these four parton analyses besides the value of Q_0^2 taken, a controlled study of the effect of absorptive corrections is called for.

6.3 Theoretical calculation of F_2^{DGLAP}

Having explained how the data can be corrected for absorptive effects to extract the 'experimental' F_2^{DGLAP}, we now explain how the theoretical F_2^{DGLAP} is calculated at NLO. Heavy quarks are treated in the light quark variable flavour number scheme. The DGLAP equation for the evolution of the quark singlet and gluon distributions

of the proton is

$$\frac{\partial}{\partial \ln Q^2}\begin{pmatrix}\Sigma(x,Q^2)\\ g(x,Q^2)\end{pmatrix} = \frac{\alpha_S(Q^2)}{2\pi}\int_x^1 \frac{\mathrm{d}z}{z} \times \begin{pmatrix}P_{qq}\left(z,\alpha_S(Q^2)\right) & 2\,n_f\,P_{qg}\left(z,\alpha_S(Q^2)\right)\\ P_{gq}\left(z,\alpha_S(Q^2)\right) & P_{gg}\left(z,\alpha_S(Q^2)\right)\end{pmatrix}\begin{pmatrix}\Sigma\left(\frac{x}{z},Q^2\right)\\ g\left(\frac{x}{z},Q^2\right)\end{pmatrix}, \quad (6.22)$$

where the quark singlet distribution is

$$\Sigma(x,Q^2) = \sum_{f=u,d,s,c,b}\left[q(x,Q^2)+\bar{q}(x,Q^2)\right], \quad (6.23)$$

with $s=\bar{s}$, $c=\bar{c}$ and $b=\bar{b}$. The non-singlet distributions $q^{\pm}(x,Q^2)$ are defined as

$$q_V(x,Q^2) \equiv q^-(x,Q^2) = q(x,Q^2)-\bar{q}(x,Q^2), \quad (6.24)$$

$$q^+(x,Q^2) = q(x,Q^2)+\bar{q}(x,Q^2)-\frac{1}{n_f}\Sigma(x,Q^2). \quad (6.25)$$

Since $q(x,Q^2)$, $\bar{q}(x,Q^2)$, and $\Sigma(x,Q^2)$ are continuous functions of Q^2, the change in n_f across flavour thresholds must be compensated by a discontinuity in $q^+(x,Q^2)$. It follows that

$$q^+(x,m_c^2)\big|_{n_f=4} = q^+(x,m_c^2)\big|_{n_f=3}+\frac{1}{12}\Sigma(x,m_c^2), \quad (6.26)$$

$$q^+(x,m_b^2)\big|_{n_f=5} = q^+(x,m_b^2)\big|_{n_f=4}+\frac{1}{20}\Sigma(x,m_b^2). \quad (6.27)$$

The heavy quarks do not contribute below the relevant flavour threshold, that is,

$$c^+(x,Q^2) = \begin{cases}-\frac{1}{3}\Sigma(x,Q^2) & : \quad Q<m_c\\ -\frac{1}{4}\Sigma(x,Q^2) & : \quad Q=m_c\end{cases}, \quad (6.28)$$

$$b^+(x,Q^2) = \begin{cases}-\frac{1}{4}\Sigma(x,Q^2) & : \quad Q<m_b\\ -\frac{1}{5}\Sigma(x,Q^2) & : \quad Q=m_b\end{cases}. \quad (6.29)$$

The evolution of the non-singlet distributions does not depend on the gluon distribution:

$$\frac{\partial q^{\pm}(x,Q^2)}{\partial \ln Q^2} = \frac{\alpha_S(Q^2)}{2\pi}\int_x^1 \frac{\mathrm{d}z}{z}\,P_{\pm}\left(z,\alpha_S(Q^2)\right)\,q^{\pm}\left(\frac{x}{z},Q^2\right). \quad (6.30)$$

We define

$$q^{\gamma^* p}(x,Q^2) = \sum_f e_f^2\left[q(x,Q^2)+\bar{q}(x,Q^2)\right] = \langle e_f^2\rangle\Sigma(x,Q^2)+q_{ns}^{\gamma^* p}(x,Q^2), \quad (6.31)$$

where $\langle e_f^2 \rangle = (1/n_f) \sum_f e_f^2$, and

$$q_{ns}^{\gamma^* p}(x, Q^2) = \sum_f e_f^2 \, q^+(x, Q^2). \tag{6.32}$$

Again, $q_{ns}^{\gamma^* p}(x, Q^2)$ is discontinuous across the flavour thresholds:

$$q_{ns}^{\gamma^* p}(x, m_c^2)\big|_{n_f=4} = q_{ns}^{\gamma^* p}(x, m_c^2)\big|_{n_f=3} - \frac{1}{18}\Sigma(x, m_c^2), \tag{6.33}$$

$$q_{ns}^{\gamma^* p}(x, m_b^2)\big|_{n_f=5} = q_{ns}^{\gamma^* p}(x, m_b^2)\big|_{n_f=4} + \frac{1}{30}\Sigma(x, m_b^2). \tag{6.34}$$

The proton structure function is then

$$F_2^{\rm DGLAP}(x_B, Q^2) = q^{\gamma^* p}(x_B, Q^2) + \frac{\alpha_S(Q^2)}{2\pi} x_B \int_{x_B}^1 \frac{{\rm d}x}{x} \times \left[C_{2,q}^{\rm NLO}\left(\frac{x_B}{x}\right) q^{\gamma^* p}\left(x, Q^2\right) + \langle e_f^2 \rangle C_{2,g}^{\rm NLO}\left(\frac{x_B}{x}\right) g\left(x, Q^2\right) \right], \tag{6.35}$$

where the coefficient functions $C_{2,q}^{\rm NLO}$ and $C_{2,g}^{\rm NLO}$ are calculated in the $\overline{MS}$ scheme [159], as in (5.9).

Since we are primarily interested in the effect of absorptive corrections, it is sufficient to consider the description of the small x_B data. We therefore fit to the ZEUS [111, 185] and H1 [186–188] inclusive $F_2(x_B, Q^2)$ data with $x_B < 0.01$, $2 < Q^2 < 500$ GeV^2 and $W^2 > 12.5$ GeV^2. These are the same HERA data sets fitted in the MRST2001 NLO analysis [127]. We take MRST-like parametric forms [127] for the starting gluon and sea quark distributions at $Q_0^2 = 1$ GeV^2:

$$xg(x, Q_0^2) = A_g \, x^{-\lambda_g}(1-x)^{3.70}(1 + \epsilon_g\sqrt{x} + \gamma_g x) - A_- \, x^{-\delta_-}(1-x)^{10}, \tag{6.36}$$

$$xS(x, Q_0^2) = A_S \, x^{-\lambda_S}(1-x)^{7.10}(1 + \epsilon_S\sqrt{x} + \gamma_S x), \tag{6.37}$$

where the powers of the $(1-x)$ factors are taken from [127], together with the valence quark distributions, u_V and d_V, and $\Delta \equiv \bar{d} - \bar{u}$:

$$xu_V(x, Q_0^2) = 0.157\, x^{0.25}\,(1-x)^{3.33}\,(1 + 5.61\sqrt{x} + 55.49x), \tag{6.38}$$

$$xd_V(x, Q_0^2) = 0.041\, x^{0.27}\,(1-x)^{3.88}\,(1 + 52.73\sqrt{x} + 30.65x), \tag{6.39}$$

$$x\Delta(x, Q_0^2) = 1.201\, x^{1.24}\,(1-x)^{9.10}\,(1 + 14.05x - 45.52x^2). \tag{6.40}$$

The λ_g, ϵ_g, A_-, δ_-, A_S, λ_S, and ϵ_S are taken as free parameters, γ_g and γ_S are fixed at zero since they are unconstrained by the small x_B data, and A_g is determined

from the momentum sum rule,

$$\int_0^1 \mathrm{d}x \, \left[x\Sigma(x,Q_0^2) + xg(x,Q_0^2)\right] = 1, \tag{6.41}$$

where $\Sigma = S + u_V + d_V$. The integral (6.41) can be done analytically, with the solution expressed in terms of gamma functions. At the initial scale Q_0, the flavour structure of the light quark sea is taken to be $2\bar{u} = 0.4S - \Delta$, $2\bar{d} = 0.4S + \Delta$ and $2s = 2\bar{s} = 0.2S$. The values of $\alpha_S(M_Z^2)$ and the charm and bottom quark masses are taken to be the same as in the MRST2001 NLO parton set [127]. Since we do not fit to DIS data with $x_B > 0.01$, we constrain the gluon and sea quark distributions to agree with the MRST2001 NLO parton set [127] at $x = 0.2$. This is done by including the value of these parton distributions at $x = 0.2$ in the DIS fit with an error of 10%.

As in Chapter 5 we use the QCDNUM program [166] to perform the NLO DGLAP evolution and calculate the structure functions, and the MINUIT program [167] to find the optimal parameters.

6.4 Simultaneous QCD analysis of DDIS and DIS data

The 'simultaneous' fit of DDIS and DIS data proceeds as follows:

(i) Start by fitting ZEUS [111, 185] and H1 [186–188] F_2 data (279 points) with no absorptive corrections, similar to the MRST2001 NLO analysis [127].

(ii) Fit ZEUS [157, 158] and H1 [148] $F_2^{D(3)}$ data (404 points) using $g(x_{I\!P},\mu^2)$ and $S(x_{I\!P},\mu^2)$ from the previous F_2 fit.

(iii) Fit $F_2^{\mathrm{DGLAP}} = F_2^{\mathrm{data}} + \left|\Delta F_2^{\mathrm{abs}}\right|$, with $\Delta F_2^{\mathrm{abs}}$ from the previous $F_2^{D(3)}$ fit.

(iv) Go to (ii).

As we will demonstrate, convergence is achieved after only a few iterations. In practice, we allow four iterations of steps (ii) and (iii) for all the results presented in this chapter. To allow for the contribution of proton dissociation in (6.6) we take

$$\Delta F_2^{\mathrm{abs}}(x_B,Q^2) = -2\int_{Q_0^2}^{Q^2} \mathrm{d}\mu^2 \, F_{2,\mathrm{el}}^D(x_B,Q^2;\mu^2) \equiv -2\,F_{2,\mathrm{el}}^D(x_B,Q^2), \tag{6.42}$$

where the factor 2 enhancement of the (elastic) proton contribution was estimated from the normalisation factors found in fitting to DDIS data in Chapter 5. It

accounts for absorptive corrections due to diffractive events involving proton dissociation with $M_Y \lesssim 6$ GeV. Events with a large amount of proton dissociation will have a small rapidity gap such that $I\!P \to I\!P \otimes I\!P$ contributions could become important and so our formalism, which only accounts for $I\!P \otimes I\!P \to I\!P$ contributions, would not apply. This factor 2 is justified by a ZEUS comparison [189] of LPS data with M_X data; the M_X data allowed proton dissociation with $M_Y < 6$ GeV and a relative normalisation factor of 1.85 ± 0.38(stat.) was found compared to the LPS data. Of course, there is some uncertainty in this factor 2, but the precise amount is difficult to justify. The (elastic) proton contribution is obtained by normalising to the ZEUS LPS data [157], for which there is no proton dissociation.

Since we have taken $Q_0 = 1$ GeV, the same value as used in Chapter 5 to separate the perturbative and non-perturbative contributions to DDIS, then

$$F_{2,\mathrm{el}}^{D}(x_B, Q^2) = \Theta(0.1 - x_B) \int_{x_B}^{0.1} \mathrm{d}x_{I\!P} \left[F_{2,\mathrm{P}}^{D(3)}(x_{I\!P}, \beta, Q^2) + F_{L,\mathrm{P}}^{D(3)}(x_{I\!P}, \beta, Q^2) \right], \tag{6.43}$$

where $F_{2,\mathrm{P}}^{D(3)}$ is the leading-twist contribution (5.5) and $F_{L,\mathrm{P}}^{D(3)}$ is the twist-four contribution (5.19). The upper cutoff of $x_{I\!P} = 0.1$ is necessary since the simple formula we have used for the absorptive corrections is invalid for large $x_{I\!P}$ (small rapidity gaps) where secondary Reggeon contributions become more important.

In Fig. 6.4 we show a contour plot showing $\left|\Delta F_2^{\mathrm{abs}}\right| / F_2^{\mathrm{data}}$ as a percentage. The F_2 data points [111, 185–188] have been put in 20 bins along each axis and $\left|\Delta F_2^{\mathrm{abs}}\right| / F_2^{\mathrm{data}}$ is averaged over each bin. A percentage increase of more than 50% would violate the unitarity limit, but this does not happen for any of the data points. By definition $|\Delta F_2^{\mathrm{abs}}|$ is zero at the input scale of 1 GeV^2 and grows to an approximately constant value at large Q^2. Since F_2^{data} increases at large Q^2, this means that the fractional size of the absorptive corrections relative to the data falls away at large Q^2. This behaviour can be seen more clearly in Fig. 6.5, which shows the F_2 data at the smallest x_B values, before and after the absorptive corrections have been applied. The predictions of the corresponding fits, shown by the solid and dashed lines, respectively, are also plotted. The data points have been binned according to the nearest value of x_B (in the last bin only data with $x_B \leq 3.6 \times 10^{-4}$ are included).

In Fig. 6.6 we illustrate the convergence of the 'simultaneous' fit to DDIS and DIS data by showing the input parton distributions obtained from a fit to F_2 with no absorptive corrections, then after each of 4 iterations with absorptive corrections. The input gluon and sea quark distributions obtained after the third and after the fourth iteration are almost identical.

	no absorp. corr.	with absorp. corr.
F_2 : χ^2/d.o.f.	1.15	1.09
A_g	10.6	10.1
λ_g	-0.50 ± 0.17	-0.49 ± 0.10
ϵ_g	-1.1 ± 0.2	-1.2 ± 0.1
γ_g	0 (fixed)	0 (fixed)
A_-	$(6 \pm 8) \times 10^{-2}$	$(2 \pm 6) \times 10^{-3}$
δ_-	0.47 ± 0.15	0.74 ± 0.30
A_S	0.10 ± 0.02	0.14 ± 0.03
λ_S	0.33 ± 0.02	0.30 ± 0.02
ϵ_S	10 ± 3	9.0 ± 2.6
γ_S	0 (fixed)	0 (fixed)
$F_2^{D(3)}$: χ^2/d.o.f.	1.14	1.15
$c_{q/G}$ (GeV^2)	0.14 ± 0.03	0.18 ± 0.04
$c_{g/G}$ (GeV^2)	0	0
$c_{L/G}$ (GeV^2)	0.051 ± 0.021	0.074 ± 0.032
$c_{q/S}$ (GeV^2)	0.70 ± 0.09	0.37 ± 0.07
$c_{g/S}$ (GeV^2)	1.41 ± 0.09	1.14 ± 0.07
$c_{L/S}$ (GeV^2)	0.16 ± 0.05	0.027 ± 0.033
$c_{q/\mathrm{NP}}$ (GeV^{-2})	0.87 ± 0.08	1.00 ± 0.07
$c_{I\!R}$ (GeV^{-2})	6.8 ± 0.5	6.5 ± 0.5
N_Z	1.54 ± 0.07	1.55 ± 0.06
N_H	1.24 ± 0.05	1.24 ± 0.04
$K_{q/G}$	0.84 ± 0.18	1.08 ± 0.24
$K_{g/G}$	0	0
$K_{L/G}$	1.4 ± 0.6	2.0 ± 0.9
$K_{q/S}$	4.3 ± 0.6	2.5 ± 0.5
$K_{g/S}$	3.9 ± 0.2	3.4 ± 0.2
$K_{L/S}$	1.1 ± 0.3	0.2 ± 0.2
$R(6.5\,\mathrm{GeV}^2), R(90\,\mathrm{GeV}^2)$	0.57,0.58	0.56, 0.57

Table 6.1: The parameter values of the 'simultaneous' fits to the inclusive F_2 and $F_2^{D(3)}$ data measured by the ZEUS [111, 157, 158, 185] and H1 [148, 186–188] Collaborations. The parameters for the F_2 fit are defined in (6.36) and (6.37), while the parameters for the $F_2^{D(3)}$ fit are defined in Chapter 5. The K-factors (5.29) are evaluated using $R_g(\lambda = 0) = 1$ as given by (4.50) and $R_q(\lambda = \lambda_S) = 4$ as given by (4.91). The last row $R(Q^2)$, defined in (5.33), gives the fraction of the Pomeron's (plus Reggeon's) momentum carried by gluons at $x_{I\!P} = 0.003$. Sample parton distributions are shown in Fig. 6.7.

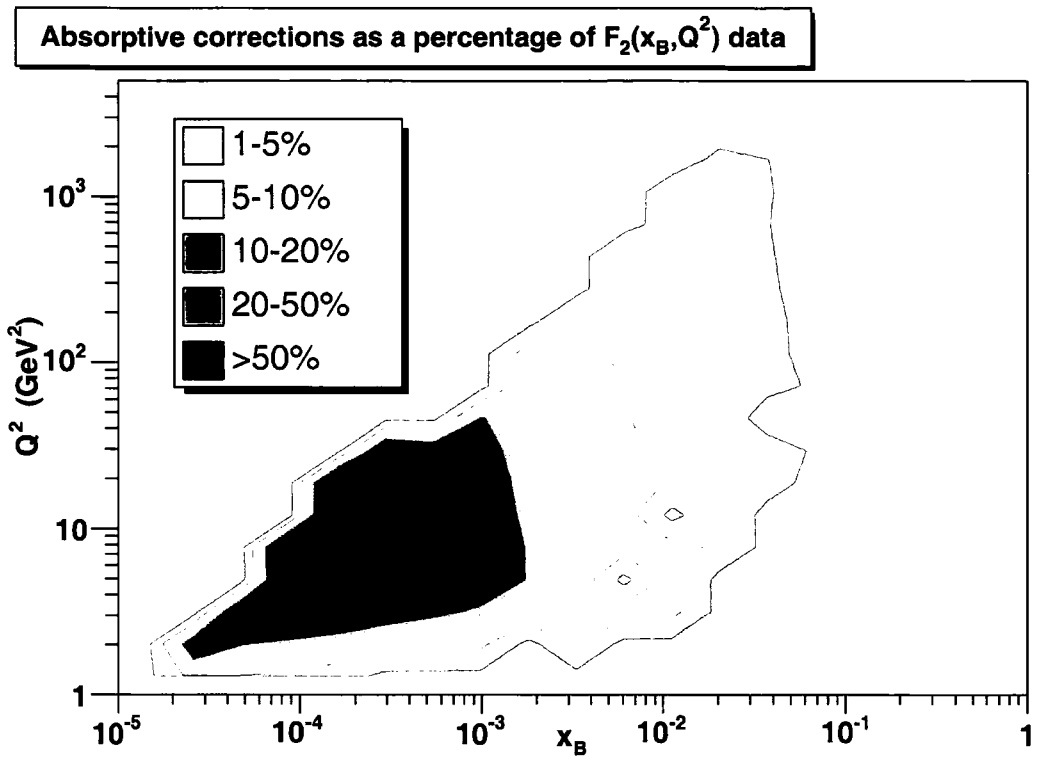

Figure 6.4: Contour plot of the absorptive corrections as a percentage of $F_2(x_B, Q^2)$ data [111, 185–188].

The parameter values of this combined description of the DIS and DDIS data are given in Table 6.1. The thin solid curves in Fig. 6.7 show the parton distributions obtained from the fit before the absorptive corrections have been included; they are very similar to those from the MRST2001 NLO parton set [127] shown by the dotted curves in Fig. 6.7, with the input gluon distribution going negative at small $x \lesssim 5 \times 10^{-3}$. The small differences between the solid and dotted curves arise due to the small differences between our analysis of F_2 and the MRST2001 global analysis, such as the treatment of heavy quarks (MRST use the Thorne-Roberts [190] variable flavour number scheme), the fact that we fit only the small-x_B HERA F_2 data, the fact that we fix the parameters $\gamma_g = \gamma_S = 0$, and due to the large uncertainty in the A_- parameter, as shown in Table 6.1.[4]

The dashed curves in Fig. 6.7 show the final input parton distributions obtained after four iterations between the fits to the DIS and DDIS data, and also the gluon

[4] After the completion of this work, it was realised that MRST let the normalisation of the ZEUS F_2 data [111, 185] go to its lower limit of 98% in [127], whereas all the fits in this chapter were obtained assuming that the ZEUS and H1 F_2 data have the same normalisation. Repeating the fits presented in Table 6.1 multiplying the ZEUS F_2 data [111, 185] by a factor 0.98 gives χ^2/d.o.f. values of 0.92 and 0.88 for the fits to F_2 without and with absorptive corrections. The parton distributions obtained from the F_2 fit are practically unchanged.

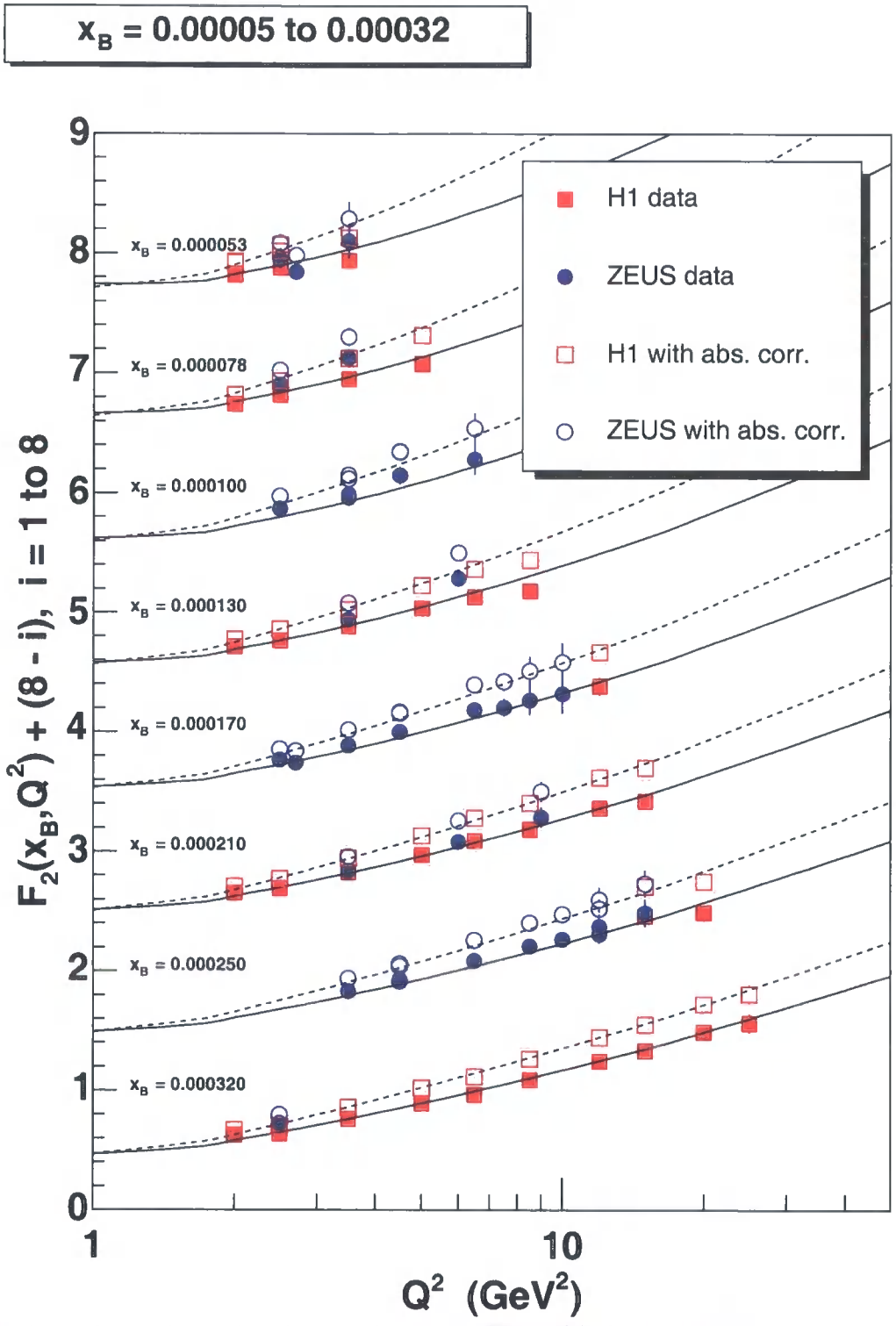

Figure 6.5: $F_2(x_B, Q^2)$ data [111, 185–188] before and after absorptive corrections have been included. Only data points included in the fits, shown by the solid and dashed lines, are plotted.

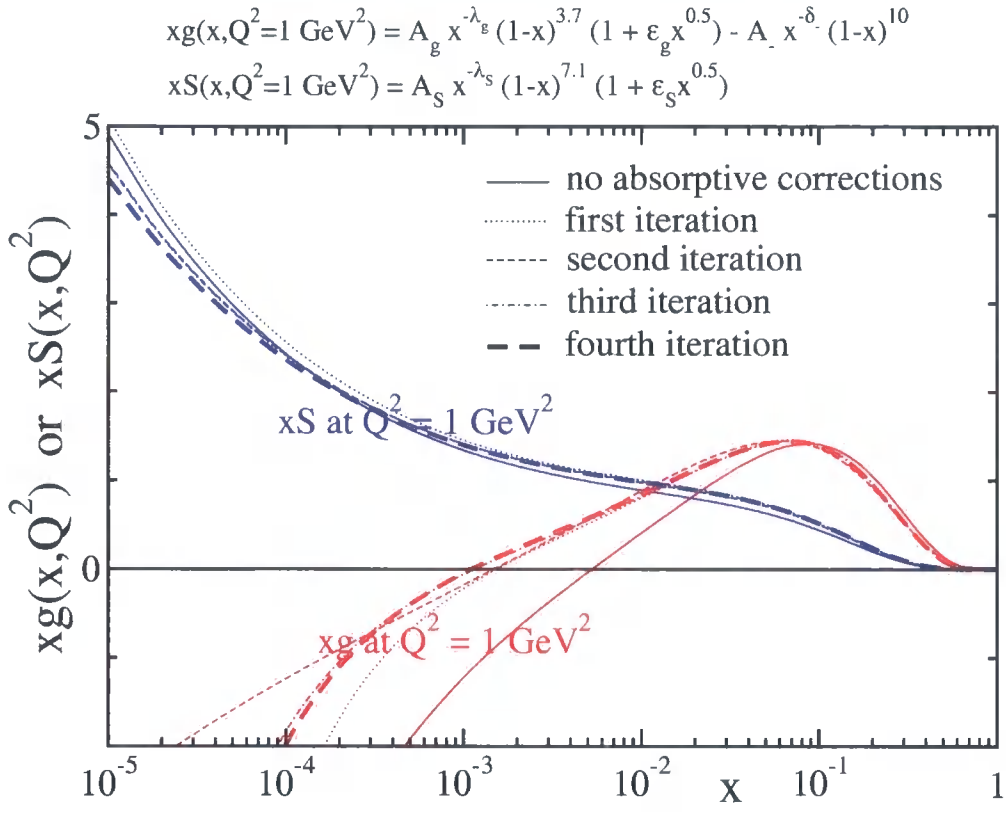

Figure 6.6: Convergence of the 'simultaneous' fit to DDIS and DIS data.

distribution when evolved up to higher scales. These dashed curves show that the inclusion of absorptive effects yield an input gluon distribution which is much less negative, whereas the input sea quark distribution is largely unaffected. Indeed, the absorptive effects crucially change the input gluon distribution for $x \lesssim 10^{-3}$. They change the input sea quark distribution much less, due to the smaller colour charge of the quark and, phenomenologically, due to the fact that the quark distributions are measured directly by F_2, whereas only scaling violations and NLO contributions constrain the gluon distribution. Thus small changes in the quark distributions can be accompanied by large changes in the gluon distribution.

In Fig. 6.8 we show the percentage increase in the gluon and sea quark distributions as a contour plot in the x–Q^2 plane. For the gluon distribution, which goes negative for small x and low Q^2, the modulus of the denominator has been taken. The black region of the upper plot in Fig. 6.8, indicating an increase of more than 50% in the gluon distribution, is where the gluon changes sign from negative to positive. Even for quite moderate x and Q^2 the inclusion of absorptive corrections has a significant effect on the PDFs obtained.

A study of the uncertainties due to PDFs on the NLO cross section for SM Higgs boson production at the LHC has been made in [191]. For Higgs boson production

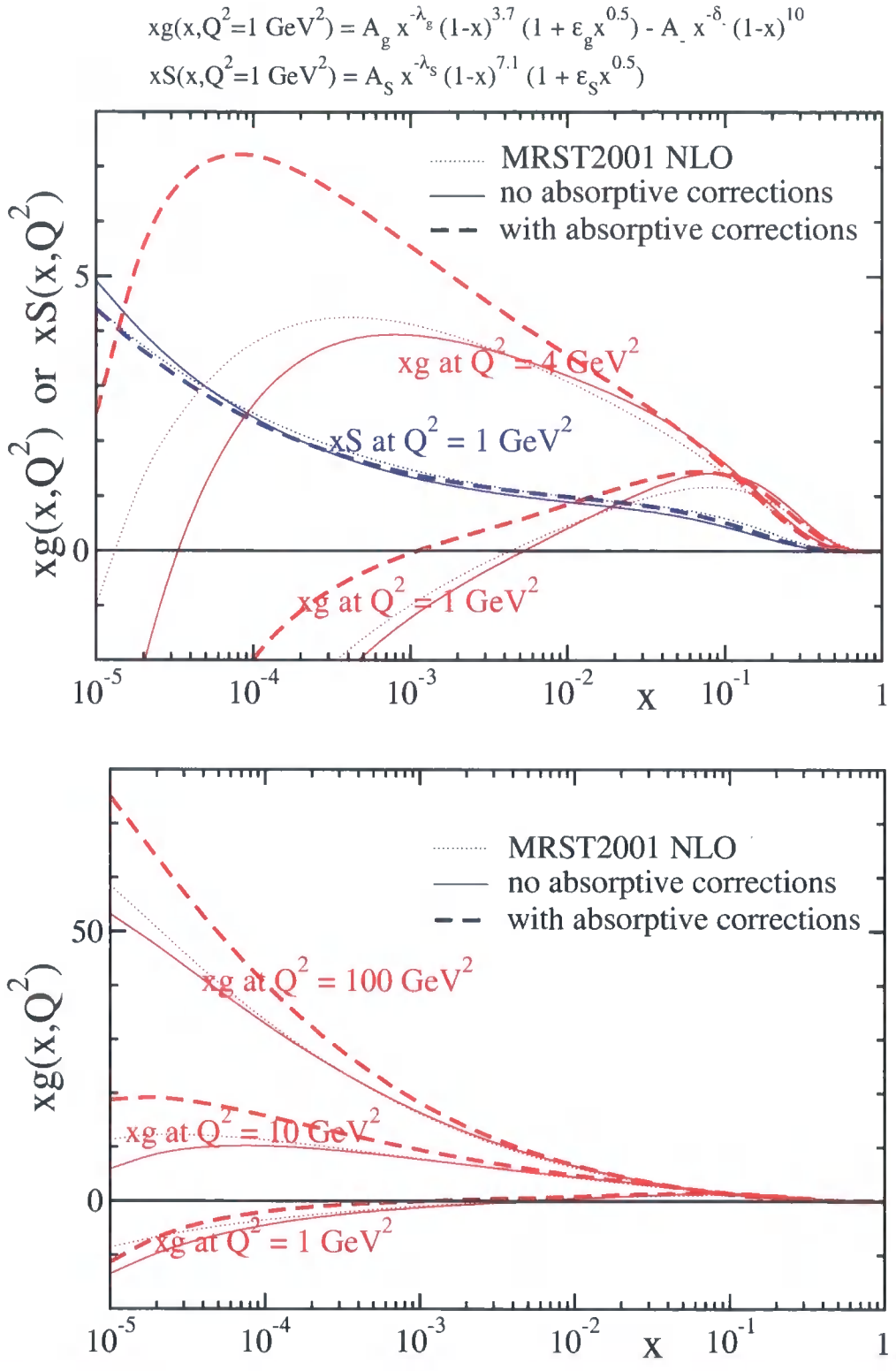

Figure 6.7: The gluon and sea quark distributions obtained from a NLO DGLAP fit to F_2, before and after absorptive corrections have been included. The input at $Q_0^2 = 1$ GeV^2 has been chosen to have 'MRST-like' parametric forms, with an explicit term included in the gluon distribution to allow it to go negative, see (6.36).

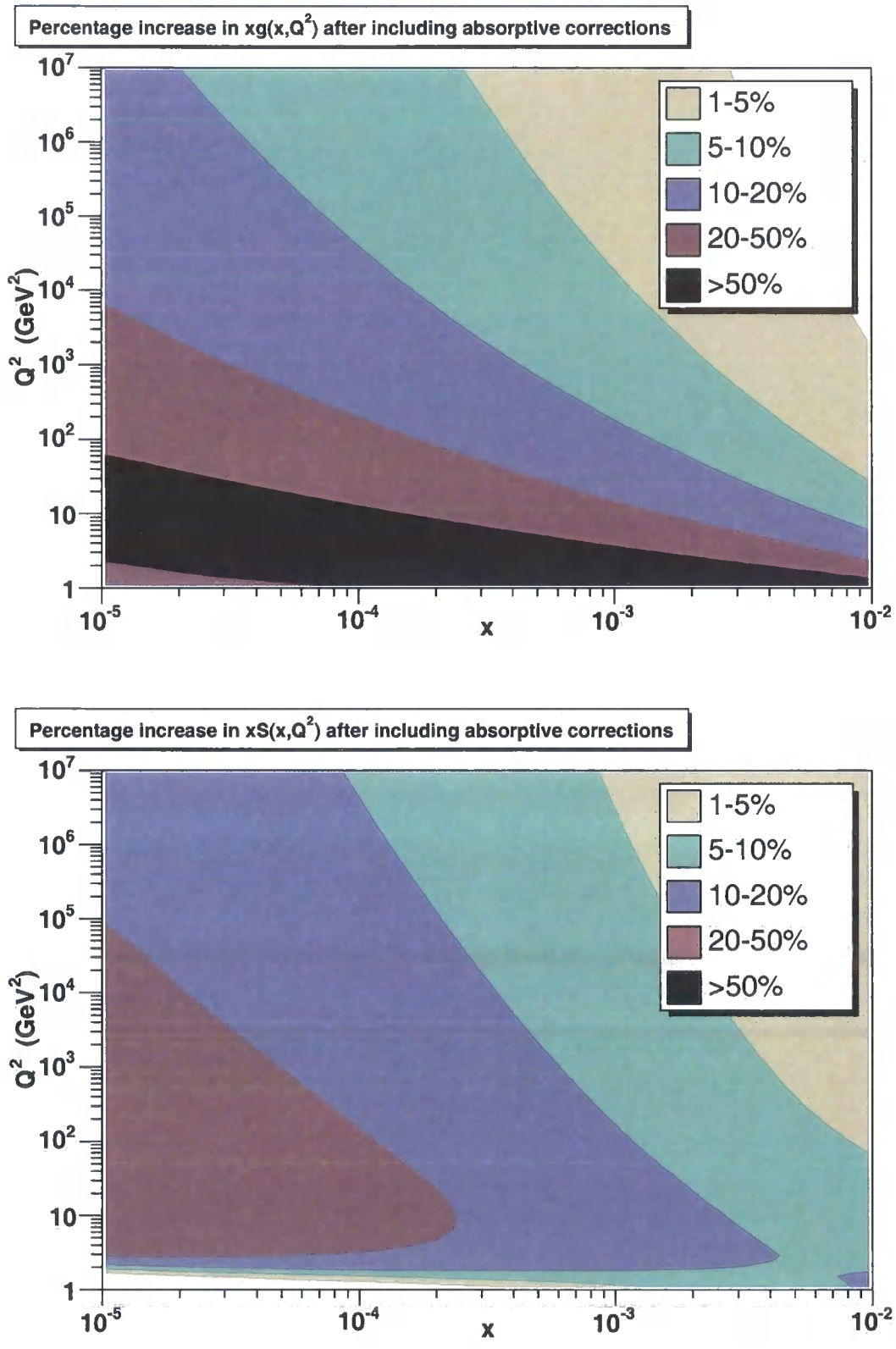

Figure 6.8: Contour plots of the percentage increase in the gluon and sea quark distributions obtained from a NLO DGLAP fit to F_2 after absorptive corrections have been included.

PDF set	$\sigma(gg \to H)$ (pb)
MRST2001 NLO	33.48
no absorptive corrections	37.11
with absorptive corrections	37.09

Table 6.2: NLO cross section for SM Higgs boson production ($M_H = 125$ GeV) at the LHC via gluon fusion. The results were obtained using the HIGLU [192] program with different PDFs.

via gluon fusion, uncertainties of $\mathcal{O}(5\%)$ were found for $M_H \lesssim 300$ GeV. To study the effect of absorptive corrections on final state observables we used the HIGLU program [192] to compute the NLO total cross section at the LHC for SM Higgs bosons ($M_H = 125$ GeV) produced via gluon fusion. This program includes the full dependence of the top and bottom quark masses of the NLO cross section, not only the result in the infinite top quark mass limit. The code was run first with the standard MRST2001 NLO PDFs, then with the PDFs obtained from the two fits of Table 6.1 (without and with absorptive corrections). The results are shown in Table 6.2. The MRST2001 NLO result of 33.5 pb is slightly higher than the MC@NLO [193] result of 32.4 pb given in Fig. 3.11, since the latter was obtained in the infinite top quark mass limit. The results using the two PDF sets of Table 6.2 are almost identical (37.1 pb). This particular observable is mainly driven by the gluon distribution at moderate $x \sim M_H/\sqrt{s} \sim 0.01$, where the effect of the absorptive corrections is small, and where our PDF sets are relatively unconstrained since we only fit the F_2 data at small $x_B < 0.01$. Therefore, the absolute value of the cross section obtained with our PDFs is not as reliable as with the MRST2001 PDFs. An accurately known experimental observable which is sensitive to the small-x PDFs would play an important rôle in testing the PDFs obtained with absorptive corrections. One possibility is the production of Drell-Yan pairs at large rapidity. For further study, it would also be better to incorporate the absorptive corrections into a *global* parton analysis rather than the restricted analysis we have performed here.

6.5 Diversion: Multi-Pomeron exchange

It is tempting to investigate the effect of absorptive corrections due to more than two Pomerons being exchanged. Unfortunately, the application of the AGK cutting rules is not as simple in this case. A speculative estimate of the size of multi-Pomeron contributions is given here using an eikonal formula.

At high energies, the s-channel unitarity relation is diagonal in the impact pa-

rameter ($\boldsymbol{b_t}$) basis, such that

$$2\,\mathrm{Im}\,T_{\mathrm{el}}(s,\boldsymbol{b_t}) = |T_{\mathrm{el}}(s,\boldsymbol{b_t})|^2 + G_{\mathrm{inel}}(s,\boldsymbol{b_t}), \tag{6.44}$$

with $\sigma_{\mathrm{tot}} = 2\int \mathrm{d}^2\boldsymbol{b_t}\ \mathrm{Im}\,T_{\mathrm{el}}(s,\boldsymbol{b_t})$, $\sigma_{\mathrm{el}} = \int \mathrm{d}^2\boldsymbol{b_t}\ |T_{\mathrm{el}}(s,\boldsymbol{b_t})|^2$. Neglecting the real part of the elastic scattering amplitude, then

$$T_{\mathrm{el}}(s,\boldsymbol{b_t}) = \mathrm{i}\left[1 - \exp\left(-\Omega(s,\boldsymbol{b_t})/2\right)\right], \tag{6.45}$$

$$G_{\mathrm{inel}}(s,\boldsymbol{b_t}) = 1 - \exp\left(-\Omega(s,\boldsymbol{b_t})\right), \tag{6.46}$$

where $\Omega \geq 0$ is the opacity (optical density) or eikonal. For some average value of the impact parameter $\langle \boldsymbol{b_t} \rangle$[5], the ratio of the diffractive component of F_2 to the total F_2 is given by

$$\frac{F_2^D}{F_2^{\mathrm{data}}} = \frac{|T_{\mathrm{el}}(s,\langle \boldsymbol{b_t}\rangle)|^2}{2\,\mathrm{Im}\,T_{\mathrm{el}}(s,\langle \boldsymbol{b_t}\rangle)} = \frac{1}{2}\left[1 - \exp\left(-\Omega(s,\langle \boldsymbol{b_t}\rangle)/2\right)\right], \tag{6.47}$$

where $F_2^D = |\Delta F_2^{\mathrm{abs}}|$ with $\Delta F_2^{\mathrm{abs}}$ given by (6.42). Solving for $\Omega/2$ gives

$$\Omega/2 = -\ln\left(1 - \frac{2\,F_2^D}{F_2^{\mathrm{data}}}\right). \tag{6.48}$$

The requirement $2\,F_2^D/F_2^{\mathrm{data}} < 1$ is the unitarity limit. The one-Pomeron (DGLAP) contribution to F_2 divided by the multi-Pomeron contribution is given by

$$\frac{F_2^{\mathrm{DGLAP}}}{F_2^{\mathrm{data}}} = \frac{\Omega/2}{1 - \exp(-\Omega/2)}, \tag{6.49}$$

so that

$$F_2^{\mathrm{DGLAP}} = F_2^{\mathrm{data}}\,\frac{\Omega/2}{1 - \exp(-\Omega/2)}, \tag{6.50}$$

with $\Omega/2$ given by (6.48). It is a useful check to take the limit of small absorptive corrections $2\,F_2^D/F_2^{\mathrm{data}} \ll 1 \iff \Omega/2 \ll 1$, then

$$\frac{\Omega/2}{1 - \exp(-\Omega/2)} = \frac{\Omega/2}{\Omega/2 - \frac{1}{2!}(\Omega/2)^2 + \ldots} \approx 1 + \frac{1}{2}(\Omega/2), \tag{6.51}$$

and from (6.48):

$$\Omega/2 = -\ln\left(1 - \frac{2\,F_2^D}{F_2^{\mathrm{data}}}\right) \approx \frac{2\,F_2^D}{F_2^{\mathrm{data}}}, \tag{6.52}$$

[5] An alternative approach would be to assume some functional form for $\Omega(s,\boldsymbol{b_t})$, such as a Gaussian distribution in $\boldsymbol{b_t}$.

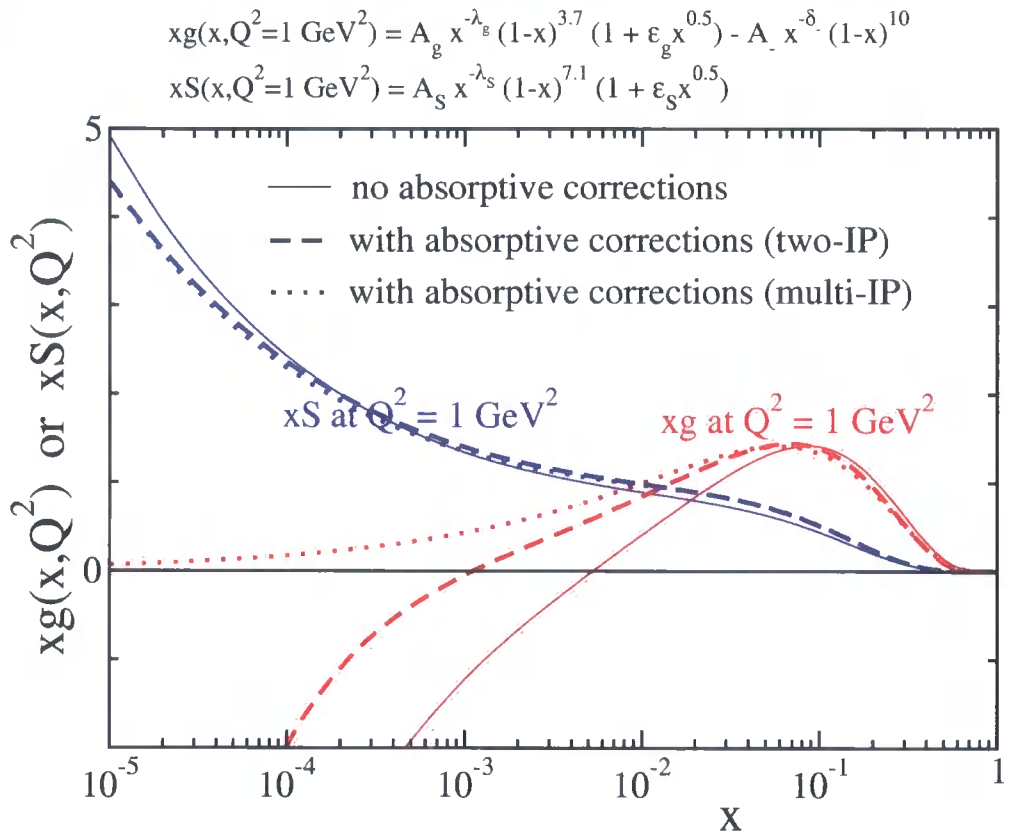

Figure 6.9: The gluon and sea quark distributions obtained from a NLO DGLAP fit to F_2, before and after two-Pomeron and multi-Pomeron absorptive corrections have been included.

so (6.50) becomes

$$F_2^{\rm DGLAP} \approx F_2^{\rm data}\left(1+\frac{F_2^D}{F_2^{\rm data}}\right) = F_2^{\rm data} + F_2^D, \tag{6.53}$$

that is, we recover the two-Pomeron exchange formula (6.7).

Repeating the 'simultaneous' fit to DDIS and DIS data with the absorptive corrections given by (6.50) instead of (6.7), we obtain the input PDFs shown by the dotted curves in Fig. 6.9. The A_- parameter controlling the negative term in the input gluon distribution has gone to zero, resulting in a positive small-x input gluon distribution. The final χ^2/d.o.f. for the F_2 fit is 0.86 and for the $F_2^{D(3)}$ fit is 1.15; cf. the values 1.09 and 1.15 given in Table 6.1. Since the two-Pomeron exchange absorptive corrections, computed using the AGK cutting rules, are on a sounder theoretical footing, we return to using (6.7) for the remainder of this chapter.

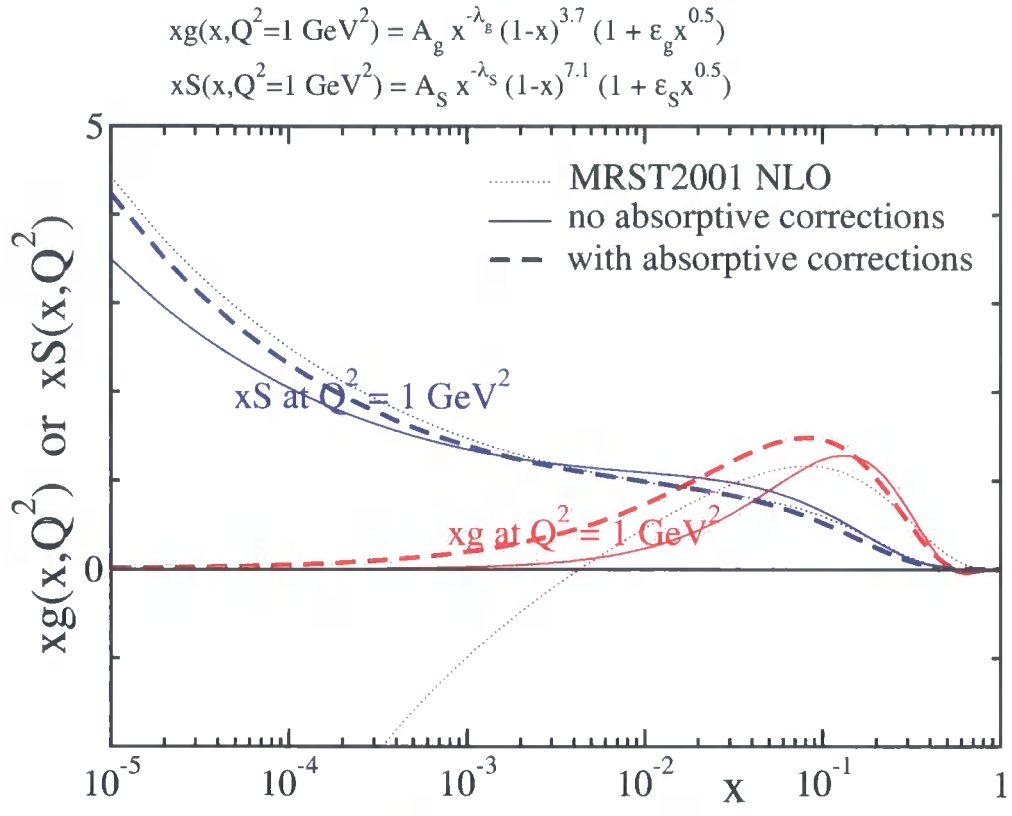

Figure 6.10: The input gluon and sea quark distributions obtained from a NLO DGLAP fit to F_2, before and after absorptive corrections have been included, and taking a positive input gluon parameterisation. For reference the MRST2001 NLO input PDFs are also shown.

6.6 Positive input gluons at 1 GeV^2

We now return to using the two-Pomeron exchange formula for the absorptive corrections (6.7). Note, from Table 6.1, that the parameter A_- is consistent with zero. Indeed, repeating the fits with a fixed $A_- = 0$ gives a description of the F_2 data which is almost as good (χ^2/d.o.f. = 1.11, compared to 1.09 for a negative input gluon). By contrast, without any absorptive corrections, the fit to F_2 is much worse with a fixed $A_- = 0$ (χ^2/d.o.f. = 1.57, compared to 1.15 for a negative input gluon). We conclude that absorptive corrections remove the need for a negative gluon distribution at $Q^2 = 1$ GeV^2. The fit parameters are shown in Table 6.3 and the input PDFs are plotted in Fig. 6.10.

	no absorp. corr.	with absorp. corr.
F_2 : χ^2/d.o.f.	1.57	1.11
A_g	38	16
λ_g	-1.06 ± 0.09	-0.63 ± 0.07
ϵ_g	-1.39 ± 0.04	-1.33 ± 0.06
γ_g	0 (fixed)	0 (fixed)
A_-	0 (fixed)	0 (fixed)
δ_-	—	—
A_S	0.16 ± 0.05	0.15 ± 0.03
λ_S	0.27 ± 0.03	0.29 ± 0.02
ϵ_S	12 ± 4	8.7 ± 2.3
γ_S	0 (fixed)	0 (fixed)
$F_2^{D(3)}$: χ^2/d.o.f.	1.17	1.14
$c_{q/G}$ (GeV^2)	0.45 ± 0.12	0.25 ± 0.07
$c_{g/G}$ (GeV^2)	0	0
$c_{L/G}$ (GeV^2)	0.15 ± 0.03	0.11 ± 0.05
$c_{q/S}$ (GeV^2)	0.25 ± 0.12	0.28 ± 0.08
$c_{g/S}$ (GeV^2)	1.04 ± 0.06	1.14 ± 0.07
$c_{L/S}$ (GeV^2)	$(3 \pm 8) \times 10^{-5}$	$(1 \pm 20) \times 10^{-3}$
$c_{q/\mathrm{NP}}$ (GeV^{-2})	1.11 ± 0.12	1.06 ± 0.07
$c_{I\!R}$ (GeV^{-2})	5.2 ± 0.6	6.2 ± 0.5
N_Z	1.54 ± 0.06	1.55 ± 0.06
N_H	1.23 ± 0.04	1.24 ± 0.04
$K_{q/G}$	2.7 ± 0.7	1.5 ± 0.4
$K_{g/G}$	0	0
$K_{L/G}$	4.1 ± 0.8	3.0 ± 1.4
$K_{q/S}$	1.8 ± 0.9	1.9 ± 0.5
$K_{g/S}$	3.3 ± 0.2	3.5 ± 0.2
$K_{L/S}$	$(2 \pm 6) \times 10^{-4}$	$(1 \pm 15) \times 10^{-2}$
$R(6.5\,\mathrm{GeV}^2), R(90\,\mathrm{GeV}^2)$	0.53, 0.53	0.56, 0.56

Table 6.3: The parameter values of the 'simultaneous' fits to the inclusive F_2 and $F_2^{D(3)}$ data taking a positive input gluon parameterisation in the F_2 fit. The K-factors (5.29) are evaluated using $R_g(\lambda = 0) = 1$ as given by (4.50) and $R_q(\lambda = \lambda_S) = 4$ as given by (4.91). The last row $R(Q^2)$, defined in (5.33), gives the fraction of the Pomeron's (plus Reggeon's) momentum carried by gluons at $x_{I\!P} = 0.003$.

6.7 Pomeron-like sea quarks but valence-like gluons?

The inclusion of absorptive corrections have enabled the DGLAP-based description of F_2 to give a more physical small-x gluon distribution. That is, there is now no need for a negative input gluon distribution at 1 GeV^2. However, absorptive corrections have not removed a long-standing puzzle of the behaviour of parton distributions at small x and low scales. That is, we still have a valence-like gluon distribution, whereas the sea quark distribution increases with decreasing x. That is, since the HERA F_2 data have become available, we have had a 'Pomeron-like' sea quark distribution. Indeed, this feature has been present in all the parton analyses from GRV94 [194] and MRS(A) [195] in 1994, up to the present MRST [34] and CTEQ [35] global fits. On the other hand, as described in Section 4.1, according to Regge theory the high energy (small x) behaviour of both gluons and sea quarks is controlled by the same rightmost singularity in the complex angular momentum plane, and so we would expect

$$\lambda_g = \lambda_S, \tag{6.54}$$

where the λ_i are defined in (6.36) and (6.37). If we impose such an equality on the λ_i values, we obtain a very poor description of the F_2 data. We have studied several possibilities of obtaining a satisfactory fit with this equality imposed, including saturation-motivated parameterisations or including inverse transverse momentum ordering (which appears at NNLO) using the calculations of Section 2.3.3, but none overcame the problem. The only modification which appears consistent with the data (and with the $\lambda_g = \lambda_S$ equality) is the inclusion of power-like corrections. There may be higher-twist corrections due to the exchange of four gluons in colour antisymmetric states, which are not connected to F_2^D by the AGK cutting rules, and also more complicated higher-twist corrections caused by renormalons etc. Here we exploit the fact that such power-like corrections may slow down the DGLAP evolution at low Q^2. Indeed, it has been argued [196–199] that such corrections must inhibit the growth of α_S and slow down the speed of evolution as Q^2 decreases below about 1 or 2 GeV^2. At present, there is no precise formula to implement this effect. As noted in Section 3.4, Guffanti and Smye [107] observed that part of the non-perturbative power corrections to the W and Z P_T distributions, calculated using the dispersive approach [200], could be interpreted as a shift in the scale at which the parton distributions are evaluated. We therefore mimic the effect of a flatter behaviour of α_S at low scales by shifting the scale in $F_2(x_B, Q^2)$ from Q^2 to

$Q^2 + m^2$, where $m^2 = 1$ GeV^2.[6] To be consistent we must make the same shift in the $F_2^{D(3)}$ fit, so that (5.5), (5.19), (5.24), and (5.25) become

$$\begin{aligned}
F_{2,\mathrm{P}}^{D(3)}(x_{I\!P}, \beta, Q^2) &= \sum_{I\!P=G,S,GS} \int_{Q_0^2}^{Q^2} \mathrm{d}\mu^2 \, f_{I\!P}(x_{I\!P}; \mu^2 + m^2) \, F_2^{I\!P}(\beta, Q^2 + m^2; \mu^2 + m^2), \\
F_{L,\mathrm{P}}^{D(3)}(x_{I\!P}, \beta, Q^2) &= \sum_{I\!P=G,S,GS} \left(\int_{Q_0^2}^{Q^2} \mathrm{d}\mu^2 \, \frac{\mu^2 + m^2}{Q^2 + m^2} \, f_{I\!P}(x_{I\!P}; \mu^2 + m^2) \right) F_L^{I\!P}(\beta), \\
F_{2,\mathrm{NP}}^{D(3)}(x_{I\!P}, \beta, Q^2) &= f_{I\!P=\mathrm{NP}}(x_{I\!P}) \, F_2^{I\!P=\mathrm{NP}}(\beta, Q^2 + m^2; Q_0^2 + m^2), \\
F_{2,I\!R}^{D(3)}(x_{I\!P}, \beta, Q^2) &= c_{I\!R} \, f_{I\!R}(x_{I\!P}) \, F_2^{I\!R}(\beta, Q^2 + m^2).
\end{aligned} \tag{6.55}$$

This simplified prescription enables us to obtain a satisfactory simultaneous description of the DIS and DDIS data, with the same asymptotic behaviour, $\lambda_g = \lambda_S$ $(= 0)$, of the input gluon and sea quark distributions at a 'physical' $Q^2 = 0$ GeV^2 corresponding to a 'shifted' $Q^2 = (0 + 1)$ GeV^2, as shown in Fig. 6.11; the corresponding parameter values are listed in Table 6.4. However, we do not have a solid theoretical justification for fixing $\lambda_g = \lambda_S = 0$ or for the value of $m^2 = 1$ GeV^2 that we shift the scales by. A more detailed, and more theoretically-motivated, investigation of the effect of power corrections in DIS is called for.

6.8 Back to diffractive PDFs

Since the PDFs are modified after including absorptive corrections then so are the DPDFs, which depend on the square of the PDFs. In Fig. 6.12(a) we show the final DPDFs obtained from the three fits in Tables 6.1 ('Negative gluon'), 6.3 ('Positive gluon'), and 6.4 ('Shift scale'), compared to the 'MRST' fit of Chapter 5 and the DPDFs from the preliminary H1 analysis [148]. The DPDFS from the 'Negative gluon' and 'Positive gluon' fits are almost unchanged from those obtained from the 'MRST' fit, because the fit to DDIS data is driven by the sea quark distribution at low scales $\mu^2 \sim Q_0^2 \sim 1$ GeV^2, and this is almost unchanged after including absorptive corrections. The DPDFs labelled 'Shift scale' are defined as

$$\begin{aligned}
a^D(x_{I\!P}, \beta, Q^2) = \sum_{I\!P=G,S,GS} &\left(\int_{Q_0^2}^{Q^2} \mathrm{d}\mu^2 \, f_{I\!P}(x_{I\!P}; \mu^2 + m^2) \, a^{I\!P}(\beta, Q^2 + m^2; \mu^2 + m^2) \right) \\
&+ f_{I\!P=\mathrm{NP}}(x_{I\!P}) \, a^{I\!P=\mathrm{NP}}(\beta, Q^2 + m^2; Q_0^2 + m^2) + c_{I\!R} \, f_{I\!R}(x_{I\!P}) \, a^{I\!R}(\beta, Q^2 + m^2).
\end{aligned} \tag{6.56}$$

[6] Taking moments involves a factor $(Q^2 + m^2)^\gamma = (Q^2)^\gamma(1 + \gamma m^2/Q^2 + \ldots)$, where γ is the anomalous dimension, and so we see the power corrections suppressed by $1/Q^2$.

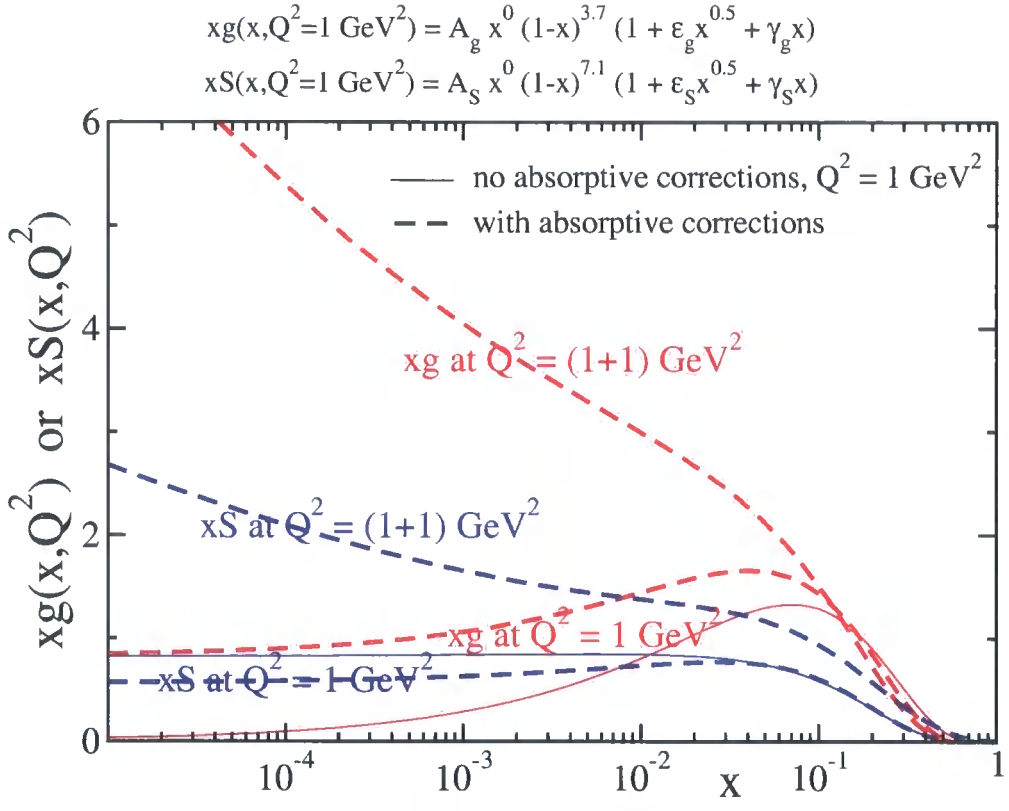

Figure 6.11: The input gluon and sea quark distributions, (6.36) and (6.37), in which the parameter $A_- = 0$ and the equality $\lambda_g = \lambda_S$ $(= 0)$ is imposed, as required by Regge theory. We now include γ_i as free parameters in (6.36) and (6.37). To obtain a satisfactory fit it is necessary to shift the scale in $F_2(x_B, Q^2)$ from Q^2 to $Q^2 + m^2$, where $m^2 = 1$ GeV^2. As before, the continuous and dashed curves show the parton distributions before and after absorptive corrections are included. We also show the 'shifted' parton distributions, at $Q^2 = (1 + 1)$ GeV^2.

	no absorp. corr.	with absorp. corr.
F_2 : χ^2/d.o.f.	1.45	1.15
A_g	3.4×10^{-6}	0.82
λ_g	0 (fixed)	0 (fixed)
ϵ_g	$(2.7 \pm 1.2) \times 10^6$	10 ± 1
γ_g	$(-3.2 \pm 1.4) \times 10^6$	-15 ± 2
A_-	0 (fixed)	0 (fixed)
δ_-	—	—
A_S	0.82 ± 0.03	0.56 ± 0.04
λ_S	0 (fixed)	0 (fixed)
ϵ_S	0.72 ± 0.46	4.0 ± 1.2
γ_S	2.8 ± 1.5	-0.04 ± 2.42
$F_2^{D(3)}$: χ^2/d.o.f.	1.30	1.29
$c_{q/G}$ (GeV^2)	0.57 ± 0.15	0.37 ± 0.03
$c_{g/G}$ (GeV^2)	$(1 \pm 31) \times 10^{-4}$	$(3 \pm 5) \times 10^{-3}$
$c_{L/G}$ (GeV^2)	0.099 ± 0.026	0.072 ± 0.017
$c_{q/S}$ (GeV^2)	0.028 ± 0.064	0.032 ± 0.007
$c_{g/S}$ (GeV^2)	4.6 ± 0.8	3.9 ± 0.7
$c_{L/S}$ (GeV^2)	0	0
$c_{q/\mathrm{NP}}$ (GeV^{-2})	1.40 ± 0.07	1.38 ± 0.05
$c_{I\!R}$ (GeV^{-2})	5.6 ± 0.5	5.7 ± 0.5
N_Z	1.52 ± 0.06	1.53 ± 0.06
N_H	1.20 ± 0.04	1.20 ± 0.04
$R(6.5\,\mathrm{GeV}^2), R(90\,\mathrm{GeV}^2)$	0.62, 0.65	0.63, 0.67

Table 6.4: The parameter values of the 'simultaneous' fits to the inclusive F_2 and $F_2^{D(3)}$ data with $\lambda_g = \lambda_S = 0$ imposed and shifting the scale by 1 GeV^2 to simulate the effect of power corrections. The last row $R(Q^2)$, defined in (5.33), gives the fraction of the Pomeron's (plus Reggeon's) momentum carried by gluons at $x_{I\!P} = 0.003$.

It is interesting that the DPDFs obtained from this fit are closer to the H1 DPDFs, especially at the higher Q^2 value shown in Fig. 6.12(a); however, the reader should bear in mind the effect of taking the same value of $\alpha_S(M_Z^2)$ as H1, as shown in Fig. 5.5(b). In Fig. 6.12(b) we show the breakdown of the DPDFs from the 'Shift scale' fit. Notice that the two-quark Pomeron contribution is still the dominant one, although the two-gluon Pomeron contribution is non-negligible, cf. Fig. 5.6(b). As discussed at the end of Section 5.3, the description of final state observables in DDIS will help to discriminate between the various DPDFs.

6.9 Discussion and summary

A reasonably satisfactory simultaneous description of DDIS and DIS data was originally obtained using the dipole saturation model [155, 201, 202]. However, the description of the new more precise DDIS data using the BGK model [202] is less good, with the model predictions tending to lie slightly below the data, especially at low β [157, 168]. Moreover, the DGLAP evolution of the Pomeron parton distributions is not accounted for. In the dipole approach, the best fit to DIS data also has a valence-like input gluon distribution [202, 203]. This indicates that we need to account for the sea quark contribution to the perturbative Pomeron flux factor in DDIS; indeed, this was one of the new ingredients of the analysis made in Chapter 5. Note that within dipole saturation models the sea quarks are generated solely from the gluon and therefore both have the same high-energy behaviour. In order to obtain a good fit to DIS data, the authors of [202, 203] were forced to shift the scale of the gluon distribution by $\mu_0^2 \simeq 1$ GeV^2, the same value we used in (6.55).

Finally, a comment on why we consider partons at low scales. It might be argued that $Q^2 \sim 1$ GeV^2 is too low a scale to work in terms of quarks and gluons. (Recall that we only fit F_2 data with $Q^2 > 2$ GeV^2.) However, we emphasise that $Q^2 \sim 1$ GeV^2 is the region where the description in terms of hadronic and quark–gluon degrees of freedom should be matched to each other. Therefore, we would like to obtain input parton distributions at $Q_0^2 = 1$ GeV^2 which are consistent with Regge theory. An alternative approach is to adopt a hadronic description for $Q^2 \sim 1$ GeV^2 (see, for example, [204]); however, this does not confront the issue. Note that within the OPE, the leading-twist parton distributions are well-defined quantities even at low scales. Of course, at such low Q^2, higher-order α_S corrections, power corrections and other non-perturbative effects are not negligible and need to be accounted for. Indeed, it was one of the goals of this chapter to see if absorptive (and power) corrections could cure the anomalous behaviour of the gluon at low Q^2 and small x.

(a)

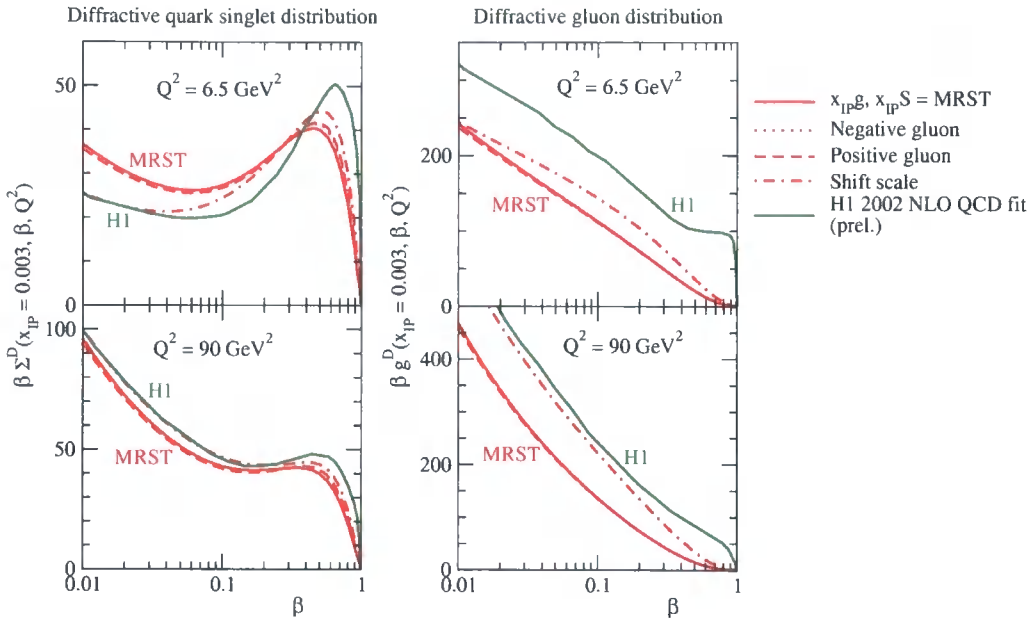

(b)

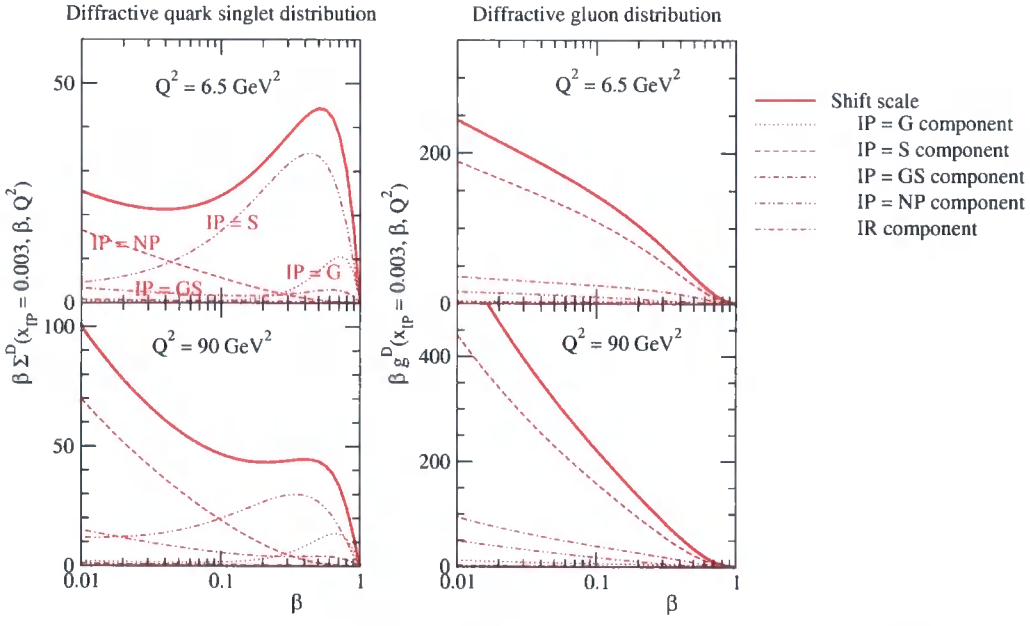

Figure 6.12: (a) DPDFs obtained from the three 'simultaneous' fits in Tables 6.1 ('Negative gluon'), 6.3 ('Positive gluon'), and 6.4 ('Shift scale'), compared to the 'MRST' fit of Chapter 5 and the DPDFs from the preliminary H1 analysis [148]. (b) Breakdown of the five separate components of (6.56) for the 'Shift scale' fit.

Note that the characteristic size of instantons, which are a typical example of the non-perturbative contribution, is about 0.4 GeV^2 (see, for example, [205]), and down to this scale it looks reasonable to work with quark and gluon degrees of freedom. The relevant hadronic (confinement) scale μ_h is smaller. It is driven by $\Lambda_{\rm QCD}$ and the constituent quark mass, that is, $\mu_h^2 \sim 0.1$ GeV^2.

In summary, we have achieved a good simultaneous description of all the DDIS and small-x_B inclusive DIS data, in which the absorptive corrections in the description of the latter data have been identified and incorporated. In this way a more physical input gluon distribution at $Q_0^2 = 1$ GeV^2 has been obtained, which no longer needs to be negative at small x. However, there remains an outstanding dilemma in small-x DIS. Either, contrary to expectations, the non-perturbative Pomeron does not couple to gluons, or DGLAP evolution is frozen at low Q^2, perhaps by power corrections. Note, however, that in both scenarios we still have the puzzle that the secondary Reggeon couples more to gluons than to sea quarks.

Bibliography

[1] V. N. Gribov and L. N. Lipatov, "e^+e^- pair annihilation and deep-inelastic ep scattering in perturbation theory," Yad. Fiz. **15** (1972) 1218 [Sov. J. Nucl. Phys. **15** (1972) 675].

[2] V. N. Gribov and L. N. Lipatov, "Deep-inelastic ep scattering in perturbation theory," Yad. Fiz. **15** (1972) 781 [Sov. J. Nucl. Phys. **15** (1972) 438].

[3] L. N. Lipatov, "The parton model and perturbation theory," Sov. J. Nucl. Phys. **20** (1975) 94 [Yad. Fiz. **20** (1974) 181].

[4] G. Altarelli and G. Parisi, "Asymptotic freedom in parton language," Nucl. Phys. B **126** (1977) 298.

[5] Y. L. Dokshitzer, "Calculation of the structure functions for deep-inelastic scattering and e^+e^- annihilation by perturbation theory in quantum chromodynamics," Sov. Phys. JETP **46** (1977) 641 [Zh. Eksp. Teor. Fiz. **73** (1977) 1216].

[6] M. E. Peskin and D. V. Schroeder, "An introduction to quantum field theory," Reading, USA: Addison-Wesley (1995).

[7] F. Halzen and A. D. Martin, "Quarks and leptons: An introductory course in modern particle physics," New York, USA: Wiley (1984).

[8] R. K. Ellis, W. J. Stirling and B. R. Webber, "QCD and collider physics," Cambridge Monogr. Part. Phys. Nucl. Phys. Cosmol. **8** (1996) 1.

[9] R. D. Field, "Applications of perturbative QCD," Redwood City, USA: Addison-Wesley (1989).

[10] A. H. Mueller (ed.), "Perturbative quantum chromodynamics," Singapore, Singapore: World Scientific (1989).

[11] Y. L. Dokshitzer, V. A. Khoze, A. H. Mueller and S. I. Troian, "Basics of perturbative QCD," Gif-sur-Yvette, France: Ed. Frontieres (1991).

[12] G. Altarelli, "The development of perturbative QCD," Singapore, Singapore: World Scientific (1994).

[13] R. G. Roberts, "The structure of the proton: Deep-inelastic scattering," Cambridge, UK: Univ. Pr. (1990).

[14] R. Devenish and A. Cooper-Sarkar, "Deep-inelastic scattering," Oxford, UK: Univ. Pr. (2004).

[15] P. D. B. Collins, "An introduction to Regge theory and high-energy physics," Cambridge, UK: Univ. Pr. (1977).

[16] V. N. Gribov, "The theory of complex angular momenta: Gribov lectures on theoretical physics," Cambridge, UK: Univ. Pr. (2003).

[17] J. R. Forshaw and D. A. Ross, "Quantum chromodynamics and the Pomeron," Cambridge, UK: Univ. Pr. (1997).

[18] V. Barone and E. Predazzi, "High-energy particle diffraction," Heidelberg, Germany: Springer-Verlag (2002).

[19] S. Donnachie, G. Dosch, O. Nachtmann and P. Landshoff, "Pomeron physics and QCD," Cambridge, UK: Univ. Pr. (2002).

[20] R. Brock *et al.* [CTEQ Collaboration], "Handbook of perturbative QCD: Version 1.0," Rev. Mod. Phys. **67** (1995) 157.

[21] Y. L. Dokshitzer, D. Diakonov and S. I. Troian, "Hard processes in quantum chromodynamics," Phys. Rept. **58** (1980) 269.

[22] G. Altarelli, "Partons in quantum chromodynamics," Phys. Rept. **81** (1982) 1.

[23] L. V. Gribov, E. M. Levin and M. G. Ryskin, "Semihard processes in QCD," Phys. Rept. **100** (1983) 1 .

[24] D. E. Soper, "Basics of QCD perturbation theory," arXiv:hep-ph/0011256.

[25] G. Sterman, "Partons, factorization and resummation," arXiv:hep-ph/9606312.

[26] B. Andersson *et al.* [Small x Collaboration], "Small x phenomenology: Summary and status," Eur. Phys. J. C **25** (2002) 77 [arXiv:hep-ph/0204115].

[27] J. R. Andersen *et al.* [Small x Collaboration], "Small x phenomenology: Summary and status 2002," Eur. Phys. J. C **35** (2004) 67 [arXiv:hep-ph/0312333].

[28] G. Leibbrandt, "Introduction to noncovariant gauges," Rev. Mod. Phys. **59** (1987) 1067.

[29] J. C. Collins, D. E. Soper and G. Sterman, "Factorization of hard processes in QCD," Adv. Ser. Direct. High Energy Phys. **5** (1988) 1 [arXiv:hep-ph/0409313].

[30] S. Moch, J. A. M. Vermaseren and A. Vogt, "The three-loop splitting functions in QCD: The non-singlet case," Nucl. Phys. B **688** (2004) 101 [arXiv:hep-ph/0403192].

[31] A. Vogt, S. Moch and J. A. M. Vermaseren, "The three-loop splitting functions in QCD: The singlet case," Nucl. Phys. B **691** (2004) 129 [arXiv:hep-ph/0404111].

[32] J. C. Collins, "What exactly is a parton density?," Acta Phys. Polon. B **34** (2003) 3103 [arXiv:hep-ph/0304122].

[33] D. E. Soper, "Parton distribution functions," Nucl. Phys. Proc. Suppl. **53** (1997) 69 [arXiv:hep-lat/9609018].

[34] A. D. Martin, R. G. Roberts, W. J. Stirling and R. S. Thorne, "Physical gluons and high-E_T jets," Phys. Lett. B **604** (2004) 61 [arXiv:hep-ph/0410230].

[35] J. Pumplin, D. R. Stump, J. Huston, H. L. Lai, P. Nadolsky and W. K. Tung, "New generation of parton distributions with uncertainties from global QCD analysis," JHEP **0207** (2002) 012 [arXiv:hep-ph/0201195].

[36] G. Corcella *et al.*, "HERWIG 6.5 release note," arXiv:hep-ph/0210213.

[37] T. Sjostrand, L. Lonnblad, S. Mrenna and P. Skands, "PYTHIA 6.3 physics and manual," arXiv:hep-ph/0308153.

[38] E. A. Kuraev, L. N. Lipatov and V. S. Fadin, "Multi-reggeon processes in the Yang-Mills theory," Sov. Phys. JETP **44** (1976) 443 [Zh. Eksp. Teor. Fiz. **71** (1976) 840].

[39] E. A. Kuraev, L. N. Lipatov and V. S. Fadin, "The Pomeranchuk singularity in nonabelian gauge theories," Sov. Phys. JETP **45** (1977) 199 [Zh. Eksp. Teor. Fiz. **72** (1977) 377].

[40] I. I. Balitsky and L. N. Lipatov, "The Pomeranchuk singularity in quantum chromodynamics," Sov. J. Nucl. Phys. **28** (1978) 822 [Yad. Fiz. **28** (1978) 1597].

[41] S. Catani, M. Ciafaloni and F. Hautmann, "High-energy factorization and small x heavy flavour production," Nucl. Phys. B **366** (1991) 135.

[42] J. C. Collins and R. K. Ellis, "Heavy quark production in very high-energy hadron collisions," Nucl. Phys. B **360** (1991) 3.

[43] E. M. Levin, M. G. Ryskin, Y. M. Shabelski and A. G. Shuvaev, "Heavy quark production in semihard nucleon interactions," Sov. J. Nucl. Phys. **53** (1991) 657 [Yad. Fiz. **53** (1991) 1059].

[44] V. S. Fadin and L. N. Lipatov, "BFKL pomeron in the next-to-leading approximation," Phys. Lett. B **429** (1998) 127 [arXiv:hep-ph/9802290].

[45] M. Ciafaloni and G. Camici, "Energy scale(s) and next-to-leading BFKL equation," Phys. Lett. B **430** (1998) 349 [arXiv:hep-ph/9803389].

[46] V. A. Khoze, A. D. Martin, M. G. Ryskin and W. J. Stirling, "The spread of the gluon k_t-distribution and the determination of the saturation scale at hadron colliders in resummed NLL BFKL," Phys. Rev. D **70** (2004) 074013 [arXiv:hep-ph/0406135].

[47] G. P. Salam, "An introduction to leading and next-to-leading BFKL," Acta Phys. Polon. B **30** (1999) 3679 [arXiv:hep-ph/9910492].

[48] J. C. Collins, "Light-cone variables, rapidity and all that," arXiv:hep-ph/9705393.

[49] M. Ciafaloni, "Coherence effects in initial jets at small Q^2/s," Nucl. Phys. B **296** (1988) 49.

[50] S. Catani, F. Fiorani and G. Marchesini, "QCD coherence in initial state radiation," Phys. Lett. B **234** (1990) 339.

[51] S. Catani, F. Fiorani and G. Marchesini, "Small x behaviour of initial state radiation in perturbative QCD," Nucl. Phys. B **336** (1990) 18.

[52] G. Marchesini, "QCD coherence in the structure function and associated distributions at small x," Nucl. Phys. B **445** (1995) 49 [arXiv:hep-ph/9412327].

[53] H. Jung and G. P. Salam, "Hadronic final state predictions from CCFM: The hadron-level Monte Carlo generator CASCADE," Eur. Phys. J. C **19** (2001) 351 [arXiv:hep-ph/0012143].

[54] G. Marchesini and B. R. Webber, "Simulation of QCD initial state radiation at small x," Nucl. Phys. B **349** (1991) 617.

[55] G. Marchesini and B. R. Webber, "Final states in heavy quark leptoproduction at small x," Nucl. Phys. B **386** (1992) 215.

[56] H. Jung, "The CCFM Monte Carlo generator CASCADE," Comput. Phys. Commun. **143** (2002) 100 [arXiv:hep-ph/0109102].

[57] B. Andersson, G. Gustafson and J. Samuelsson, "The linked dipole chain model for DIS," Nucl. Phys. B **467** (1996) 443.

[58] H. Kharraziha and L. Lonnblad, "The linked dipole chain Monte Carlo," JHEP **9803** (1998) 006 [arXiv:hep-ph/9709424].

[59] H. Jung, "k_t-factorization and CCFM: The solution for describing the hadronic final states — everywhere?," Mod. Phys. Lett. A **19** (2004) 1 [arXiv:hep-ph/0311249].

[60] M. A. Kimber, A. D. Martin and M. G. Ryskin, "Unintegrated parton distributions and prompt photon hadroproduction," Eur. Phys. J. C **12** (2000) 655 [arXiv:hep-ph/9911379].

[61] M. A. Kimber, A. D. Martin and M. G. Ryskin, "Unintegrated parton distributions," Phys. Rev. D **63** (2001) 114027 [arXiv:hep-ph/0101348].

[62] M. A. Kimber, "Unintegrated parton distributions," Ph.D. thesis, University of Durham, 2001.

[63] M. A. Kimber, J. Kwiecinski, A. D. Martin and A. M. Stasto, "The unintegrated gluon distribution from the CCFM equation," Phys. Rev. D **62** (2000) 094006 [arXiv:hep-ph/0006184].

[64] J. Kwiecinski, "Unintegrated gluon distributions from the transverse coordinate representation of the CCFM equation in the single loop approximation," Acta Phys. Polon. B **33** (2002) 1809 [arXiv:hep-ph/0203172].

[65] J. Kwiecinski, A. D. Martin and A. M. Stasto, "A unified BFKL and GLAP description of F_2 data," Phys. Rev. D **56** (1997) 3991 [arXiv:hep-ph/9703445].

[66] A. D. Martin, R. G. Roberts, W. J. Stirling and R. S. Thorne, "NNLO global parton analysis," Phys. Lett. B **531** (2002) 216 [arXiv:hep-ph/0201127].

[67] A. D. Martin, R. G. Roberts, W. J. Stirling and R. S. Thorne, "Parton distributions and the LHC: W and Z production," Eur. Phys. J. C **14** (2000) 133 [arXiv:hep-ph/9907231].

[68] J. A. Vermaseren, "New features of FORM," arXiv:math-ph/0010025.

[69] D. Graudenz, "DISASTER++ version 1.0," arXiv:hep-ph/9710244.

[70] S. Catani and M. H. Seymour, "A general algorithm for calculating jet cross sections in NLO QCD," Nucl. Phys. B **485** (1997) 291 [Erratum-ibid. B **510** (1997) 503] [arXiv:hep-ph/9605323], DISENT available from `http://hepwww.rl.ac.uk/theory/seymour/nlo/`.

[71] B. Potter, "JetViP 2.1: The HBOOK version," Comput. Phys. Commun. **133** (2000) 105 [arXiv:hep-ph/9911221].

[72] E. Mirkes and D. Zeppenfeld, "Dijet production at HERA in next-to-leading order," Phys. Lett. B **380** (1996) 205 [arXiv:hep-ph/9511448].

[73] Z. Nagy and Z. Trocsanyi, "Multi-jet cross sections in deep inelastic scattering at next-to-leading order," Phys. Rev. Lett. **87** (2001) 082001 [arXiv:hep-ph/0104315].

[74] J. M. Butterworth, J. P. Couchman, B. E. Cox and B. M. Waugh, "KTJET: A C++ implementation of the $K_\perp$ clustering algorithm," Comput. Phys. Commun. **153** (2003) 85 [arXiv:hep-ph/0210022].

[75] L. Lonnblad, "CLHEP: A project for designing a C++ class library for high-energy physics," Comput. Phys. Commun. **84** (1994) 307, available from `http://wwwinfo.cern.ch/asd/lhc++/clhep/`.

[76] M. Galassi *et al.*, "GNU Scientific Library reference manual (2nd Ed.)", available from `http://www.gnu.org/software/gsl/`.

[77] G. P. Lepage, "VEGAS: An adaptive multidimensional integration program," CLNS-80/447.

[78] S. Chekanov *et al.* [ZEUS Collaboration], "Inclusive jet cross sections in the Breit frame in neutral current deep-inelastic scattering at HERA and determination of α_S," Phys. Lett. B **547** (2002) 164 [arXiv:hep-ex/0208037].

[79] C. Adloff *et al.* [H1 Collaboration], "Measurement and QCD analysis of jet cross sections in deep-inelastic positron-proton collisions at $\sqrt{s}$ of 300 GeV," Eur. Phys. J. C **19** (2001) 289 [arXiv:hep-ex/0010054].

[80] C. Adloff *et al.* [H1 Collaboration], "Measurement of inclusive jet cross sections in deep-inelastic *ep* scattering at HERA," Phys. Lett. B **542** (2002) 193 [arXiv:hep-ex/0206029].

[81] H. L. Lai *et al.* [CTEQ Collaboration], "Global QCD analysis of parton structure of the nucleon: CTEQ5 parton distributions," Eur. Phys. J. C **12** (2000) 375 [arXiv:hep-ph/9903282].

[82] L. Motyka and N. Timneanu, "Unintegrated gluon in the photon and heavy quark production," Eur. Phys. J. C **27** (2003) 73 [arXiv:hep-ph/0209029].

[83] R. K. Ellis and S. Veseli, "W and Z transverse momentum distributions: Resummation in q_T-space," Nucl. Phys. B **511** (1998) 649 [arXiv:hep-ph/9706526]; and references therein.

[84] C. Balazs and C. P. Yuan, "Soft gluon effects on lepton pairs at hadron colliders," Phys. Rev. D **56** (1997) 5558 [arXiv:hep-ph/9704258]; and references therein.

[85] A. Gawron and J. Kwiecinski, "Resummation effects in Higgs boson transverse momentum distribution within the framework of unintegrated parton distributions," Phys. Rev. D **70** (2004) 014003 [arXiv:hep-ph/0309303].

[86] J. Kwiecinski and A. Szczurek, "Unintegrated CCFM parton distributions and transverse momentum of gauge bosons," Nucl. Phys. B **680** (2004) 164 [arXiv:hep-ph/0311290].

[87] M. A. Dobbs *et al.*, "Les Houches guidebook to Monte Carlo generators for hadron collider physics," arXiv:hep-ph/0403045.

[88] C. Balazs, J. Huston and I. Puljak, "Higgs production: A comparison of parton showers and resummation," Phys. Rev. D **63** (2001) 014021 [arXiv:hep-ph/0002032].

[89] E. Thome, "Perturbative and nonperturbative effects in transverse momentum generation," arXiv:hep-ph/0401121.

[90] J. Huston, I. Puljak, T. Sjostrand and E. Thome, "Resummation and shower studies," arXiv:hep-ph/0401145.

[91] V. A. Khoze, A. D. Martin and M. G. Ryskin, "Prospects for new physics observations in diffractive processes at the LHC and Tevatron," Eur. Phys. J. C **23** (2002) 311 [arXiv:hep-ph/0111078].

[92] A. Shuvaev, "Solution of the off-forward leading logarithmic evolution equation based on the Gegenbauer moments inversion," Phys. Rev. D **60** (1999) 116005 [arXiv:hep-ph/9902318].

[93] A. G. Shuvaev, K. J. Golec-Biernat, A. D. Martin and M. G. Ryskin, "Off-diagonal distributions fixed by diagonal partons at small x and ξ," Phys. Rev. D **60** (1999) 014015 [arXiv:hep-ph/9902410].

[94] A. D. Martin and M. G. Ryskin, "Unintegrated generalised parton distributions," Phys. Rev. D **64** (2001) 094017 [arXiv:hep-ph/0107149].

[95] A. J. Askew, J. Kwiecinski, A. D. Martin and P. J. Sutton, "Properties of the BFKL equation and structure function predictions for HERA," Phys. Rev. D **49** (1994) 4402 [arXiv:hep-ph/9310261].

[96] J. R. Ellis, M. K. Gaillard and D. V. Nanopoulos, "A phenomenological profile of the Higgs boson," Nucl. Phys. B **106** (1976) 292.

[97] M. A. Shifman, A. I. Vainshtein, M. B. Voloshin and V. I. Zakharov, "Low-energy theorems for Higgs boson couplings to photons," Sov. J. Nucl. Phys. **30** (1979) 711 [Yad. Fiz. **30** (1979) 1368].

[98] G. Parisi, "Summing large perturbative corrections in QCD," Phys. Lett. B **90** (1980) 295.

[99] G. Curci and M. Greco, "Large infrared corrections in QCD processes," Phys. Lett. B **92** (1980) 175.

[100] L. Magnea and G. Sterman, "Analytic continuation of the Sudakov form-factor in QCD," Phys. Rev. D **42** (1990) 4222.

[101] E. M. Levin, A. D. Martin, M. G. Ryskin and T. Teubner, "Diffractive open charm production at HERA," Z. Phys. C **74** (1997) 671 [arXiv:hep-ph/9606443].

[102] A. Kulesza and W. J. Stirling, "Sudakov logarithm resummation in transverse momentum space for electroweak boson production at hadron colliders," Nucl. Phys. B **555** (1999) 279 [arXiv:hep-ph/9902234].

[103] T. Affolder *et al.* [CDF Collaboration], "The transverse momentum and total cross section of e^+e^- pairs in the Z boson region from $p\bar{q}$ collisions at $\sqrt{s} = 1.8$ TeV," Phys. Rev. Lett. **84** (2000) 845 [arXiv:hep-ex/0001021].

[104] B. Abbott *et al.* [DØ Collaboration], "Measurement of the inclusive differential cross section for Z bosons as a function of transverse momentum in $\bar{p}p$ collisions at $\sqrt{s} = 1.8$ TeV," Phys. Rev. D **61** (2000) 032004 [arXiv:hep-ex/9907009].

[105] B. Abbott *et al.* [DØ Collaboration], "Differential cross section for W boson production as a function of transverse momentum in $p\bar{p}$ collisions at $\sqrt{s} = 1.8$ TeV," Phys. Lett. B **513** (2001) 292 [arXiv:hep-ex/0010026].

[106] K. Hagiwara *et al.* [Particle Data Group Collaboration], "Review of particle physics," Phys. Rev. D **66** (2002) 010001.

[107] A. Guffanti and G. E. Smye, "Non-perturbative effects in the W and Z transverse momentum distribution," JHEP **0010** (2000) 025 [arXiv:hep-ph/0007190].

[108] J. C. Collins, D. E. Soper and G. Sterman, "Transverse momentum distribution in Drell-Yan pair and W and Z boson production," Nucl. Phys. B **250** (1985) 199.

[109] P. M. Nadolsky, D. R. Stump and C. P. Yuan, "Phenomenology of multiple parton radiation in semi-inclusive deep-inelastic scattering," Phys. Rev. D **64** (2001) 114011 [arXiv:hep-ph/0012261].

[110] S. Berge, P. Nadolsky, F. Olness and C. P. Yuan, "Transverse momentum resummation at small x for the Tevatron and LHC," arXiv:hep-ph/0410375.

[111] S. Chekanov *et al.* [ZEUS Collaboration], "Measurement of the neutral current cross section and F_2 structure function for deep inelastic e^+p scattering at HERA," Eur. Phys. J. C **21** (2001) 443 [arXiv:hep-ex/0105090].

[112] C. Balazs, M. Grazzini, J. Huston, A. Kulesza and I. Puljak, "A comparison of predictions for SM Higgs boson production at the LHC," arXiv:hep-ph/0403052; and references therein.

[113] G. Corcella and S. Moretti, "Matrix-element corrections to parton shower simulations for Higgs hadroproduction," Phys. Lett. B **590** (2004) 249 [arXiv:hep-ph/0402146].

[114] G. Corcella and S. Moretti, "Matrix-element corrections to gg / $q\bar{q} \to$ Higgs in HERWIG," arXiv:hep-ph/0402149.

[115] G. Corcella and M. H. Seymour, "Initial state radiation in simulations of vector boson production at hadron colliders," Nucl. Phys. B **565** (2000) 227 [arXiv:hep-ph/9908388].

[116] T. Regge, "Introduction to complex orbital momenta," Nuovo Cim. **14** (1959) 951.

[117] G. F. Chew and S. C. Frautschi, "Principle of equivalence for all strongly interacting particles within the S-matrix framework," Phys. Rev. Lett. **7** (1961) 394.

[118] V. N. Gribov, "Possible asymptotic behavior of elastic scattering," JETP Lett. **41** (1961) 667.

[119] G. F. Chew and S. C. Frautschi, "Regge trajectories and the principle of maximum strength for strong interactions," Phys. Rev. Lett. **8** (1962) 41.

[120] I. Y. Pomeranchuk, "The conservation of isotropic spin and the scattering of antinucleons by nucleons," Sov. Phys. JETP **3** (1956) 306 [Zh. Eksp. Teor. Fiz. **30** (1956) 423].

[121] L. B. Okun and I. Y. Pomeranchuk, "The conservation of isotropic spin and the cross section of the interaction of high-energy π-mesons and nucleons with nucleons," Sov. Phys. JETP **3** (1986) 307 [Zh. Eksp. Teor. Fiz. **30** (1956) 424].

[122] L. L. Foldy and R. F. Peierls, "Isotopic spin of exchanged systems," Phys. Rev. **130** (1963) 1585.

[123] I. Y. Pomeranchuk, "Equality of the nucleon and antinucleon total interaction cross section at high energies," Sov. Phys. JETP **7** (1958) 499 [Zh. Eksp. Teor. Fiz. **34** (1958) 725].

[124] A. Donnachie and P. V. Landshoff, "Total cross sections," Phys. Lett. B **296** (1992) 227 [arXiv:hep-ph/9209205].

[125] M. Froissart, "Asymptotic behavior and subtractions in the Mandelstam representation," Phys. Rev. **123** (1961) 1053.

[126] A. Martin, "Unitarity and high-energy behavior of scattering amplitudes," Phys. Rev. **129** (1963) 1432.

[127] A. D. Martin, R. G. Roberts, W. J. Stirling and R. S. Thorne, "MRST2001: Partons and α_S from precise deep-inelastic scattering and Tevatron jet data," Eur. Phys. J. C **23** (2002) 73 [arXiv:hep-ph/0110215].

[128] M. L. Good and W. D. Walker, "Diffraction disssociation of beam particles," Phys. Rev. **120** (1960) 1857.

[129] J. D. Bjorken, "Rapidity gaps and jets as a new physics signature in very high energy hadron-hadron collisions," Phys. Rev. D **47** (1993) 101.

[130] M. Derrick *et al.* [ZEUS Collaboration], "Observation of events with a large rapidity gap in deep-inelastic scattering at HERA," Phys. Lett. B **315** (1993) 481.

[131] T. Ahmed *et al.* [H1 Collaboration], "Deep-inelastic scattering events with a large rapidity gap at HERA," Nucl. Phys. B **429** (1994) 477.

[132] W. J. Stirling, "The return of the Pomeron," Physics World **7N4** (1994) 30.

[133] L. Trentadue and G. Veneziano, "Fracture functions: An improved description of inclusive hard processes in QCD," Phys. Lett. B **323** (1994) 201.

[134] M. Grazzini, L. Trentadue and G. Veneziano, "Fracture functions from cut vertices," Nucl. Phys. B **519** (1998) 394 [arXiv:hep-ph/9709452].

[135] D. de Florian and R. Sassot, "QCD analysis of diffractive and leading proton DIS structure functions in the framework of fracture functions," Phys. Rev. D **58** (1998) 054003 [arXiv:hep-ph/9804240].

[136] J. C. Collins, "Proof of factorization for diffractive hard scattering," Phys. Rev. D **57** (1998) 3051 [Erratum-ibid. D **61** (2000) 019902] [arXiv:hep-ph/9709499].

[137] J. C. Collins, "Factorization in hard diffraction," J. Phys. G **28** (2002) 1069 [arXiv:hep-ph/0107252].

[138] V. A. Khoze, A. D. Martin and M. G. Ryskin, "Soft diffraction and the elastic slope at Tevatron and LHC energies: A multi-pomeron approach," Eur. Phys. J. C **18** (2000) 167 [arXiv:hep-ph/0007359].

[139] A. B. Kaidalov, V. A. Khoze, A. D. Martin and M. G. Ryskin, "Probabilities of rapidity gaps in high energy interactions," Eur. Phys. J. C **21** (2001) 521 [arXiv:hep-ph/0105145].

[140] M. Klasen and G. Kramer, "Factorization breaking in diffractive photoproduction of dijets," arXiv:hep-ph/0401202.

[141] M. Klasen and G. Kramer, "Factorization breaking in diffractive dijet photoproduction," Eur. Phys. J. C **38** (2004) 93 [arXiv:hep-ph/0408203].

[142] M. Klasen and G. Kramer, "Evidence for factorization breaking in diffractive low-Q^2 dijet production," arXiv:hep-ph/0410105.

[143] G. Ingelman and P. E. Schlein, "Jet structure in high mass diffractive scattering," Phys. Lett. B **152** (1985) 256.

[144] G. Ingelman and K. Prytz, "The Pomeron structure in DIS and gluon recombination effects," Z. Phys. C **58** (1993) 285.

[145] K. Golec-Biernat and J. Kwiecinski, "QCD analysis of deep inelastic diffractive scattering at HERA," Phys. Lett. B **353** (1995) 329 [arXiv:hep-ph/9504230].

[146] T. Gehrmann and W. J. Stirling, "Deep-inelastic electron-Pomeron scattering at HERA," Z. Phys. C **70** (1996) 89 [arXiv:hep-ph/9503351].

[147] L. Alvero, J. C. Collins, J. Terron and J. J. Whitmore, "Diffractive production of jets and weak bosons, and tests of hard-scattering factorization," Phys. Rev. D **59** (1999) 074022 [arXiv:hep-ph/9805268].

[148] H1 Collaboration, "Measurement and NLO DGLAP QCD interpretation of diffractive deep-inelastic scattering at HERA," paper 089 submitted to EPS 2003, Aachen.

[149] J. F. Owens, "Q^2 dependent parametrizations of pion parton distribution functions," Phys. Rev. D **30** (1984) 943.

[150] F. E. Low, "A model of the bare Pomeron," Phys. Rev. D **12** (1975) 163.

[151] S. Nussinov, "Colored quark version of some hadronic puzzles," Phys. Rev. Lett. **34** (1975) 1286.

[152] L. N. Lipatov, "The bare Pomeron in quantum chromodynamics," Sov. Phys. JETP **63** (1986) 904 [Zh. Eksp. Teor. Fiz. **90** (1986) 1536].

[153] M. Wüsthoff, "Large rapidity gap events in deep-inelastic scattering," Phys. Rev. D **56** (1997) 4311 [arXiv:hep-ph/9702201].

[154] J. Bartels and M. Loewe, "The nonforward QCD ladder diagrams," Z. Phys. C **12** (1982) 263.

[155] K. Golec-Biernat and M. Wusthoff, "Saturation in diffractive deep-inelastic scattering," Phys. Rev. D **60** (1999) 114023 [arXiv:hep-ph/9903358].

[156] J. Bartels, J. R. Ellis, H. Kowalski and M. Wüsthoff, "An analysis of diffraction in deep-inelastic scattering," Eur. Phys. J. C **7** (1999) 443 [arXiv:hep-ph/9803497].

[157] ZEUS Collaboration, "Dissociation of virtual photons in events with a leading proton at HERA," paper 540 submitted to EPS 2003, Aachen.

[158] ZEUS Collaboration, "Deep-inelastic diffractive scattering with the ZEUS forward plug calorimeter using 1998–1999 Data," paper 538 submitted to EPS 2003, Aachen.

[159] W. Furmanski and R. Petronzio, "Lepton-hadron processes beyond leading order in quantum chromodynamics," Z. Phys. C **11** (1982) 293.

[160] S. Riemersma, J. Smith and W. L. van Neerven, "Rates for inclusive deep inelastic electroproduction of charm quarks at HERA," Phys. Lett. B **347** (1995) 143 [arXiv:hep-ph/9411431]; and references therein.

[161] F. Abe *et al.* [CDF Collaboration], "Measurement of small angle antiproton-proton elastic scattering at $\sqrt{s} = 546$ and 1800 GeV," Phys. Rev. D **50** (1994) 5518.

[162] C. Adloff *et al.* [H1 Collaboration], "Inclusive measurement of diffractive deep-inelastic ep scattering," Z. Phys. C **76** (1997) 613 [arXiv:hep-ex/9708016].

[163] W. D. Apel *et al.* [Serpukhov-CERN Collaboration], "Reaction $\pi^- p \to \pi^0 n$ In The 15–40 GeV Momentum Range," Nucl. Phys. B **154** (1979) 189 [Yad. Fiz. **30** (1979) 373].

[164] A. B. Kaidalov, "Diffractive production mechanisms," Phys. Rept. **50** (1979) 157.

[165] M. Gluck, E. Reya and A. Vogt, "Pionic parton distributions," Z. Phys. C **53** (1992) 651.

[166] M. Botje, QCDNUM version 16.12, ZEUS Note 97-066 (unpublished), available from `http://www.nikhef.nl/~h24/qcdcode/`.

[167] F. James and M. Roos, MINUIT version 94.1, "A system for function minimization and analysis of the parameter errors and correlations," Comput. Phys. Commun. **10** (1975) 343.

[168] S. Chekanov *et al.* [ZEUS Collaboration], "Dissociation of virtual photons in events with a leading proton at HERA," arXiv:hep-ex/0408009.

[169] C. Adloff *et al.* [H1 Collaboration], "On the rise of the proton structure function F_2 towards low x," Phys. Lett. B **520** (2001) 183 [arXiv:hep-ex/0108035].

[170] A. D. Martin, R. G. Roberts, W. J. Stirling and R. S. Thorne, "Uncertainties of predictions from parton distributions. I: Experimental errors," Eur. Phys. J. C **28** (2003) 455 [arXiv:hep-ph/0211080].

[171] S. Eidelman *et al.* [Particle Data Group Collaboration], "Review of particle physics," Phys. Lett. B **592** (2004) 1.

[172] H1 Collaboration, "Comparison at NLO between predictions from QCD fits to F_2^D and diffractive final state observables at HERA," paper 113 submitted to EPS 2003, Aachen.

[173] T. Affolder *et al.* [CDF Collaboration], "Diffractive dijets with a leading antiproton in $\bar{p}p$ collisions at $\sqrt{s} = 1800$ GeV," Phys. Rev. Lett. **84** (2000) 5043.

[174] V. A. Abramovsky, V. N. Gribov and O. V. Kancheli, "Character of inclusive spectra and fluctuations produced in inelastic processes by multi-Pomeron exchange," Yad. Fiz. **18** (1973) 595 [Sov. J. Nucl. Phys. **18** (1974) 308].

[175] J. Bartels and M. G. Ryskin, "The space-time picture of the wee partons and the AGK cutting rules in perturbative QCD," Z. Phys. C **76** (1997) 241 [arXiv:hep-ph/9612226].

[176] A. H. Mueller and J. w. Qiu, "Gluon recombination and shadowing at small values of x," Nucl. Phys. B **268** (1986) 427.

[177] I. Balitsky, "Operator expansion for high-energy scattering," Nucl. Phys. B **463** (1996) 99 [arXiv:hep-ph/9509348].

[178] Y. V. Kovchegov, "Small-x F_2 structure function of a nucleus including multiple pomeron exchanges," Phys. Rev. D **60** (1999) 034008 [arXiv:hep-ph/9901281].

[179] Y. V. Kovchegov, "Unitarization of the BFKL pomeron on a nucleus," Phys. Rev. D **61** (2000) 074018 [arXiv:hep-ph/9905214].

[180] J. Kwiecinski, A. D. Martin, W. J. Stirling and R. G. Roberts, "Parton distributions at small x," Phys. Rev. D **42** (1990) 3645.

[181] A. D. Martin, R. G. Roberts, W. J. Stirling and R. S. Thorne, "Uncertainties of predictions from parton distributions. II: Theoretical errors," Eur. Phys. J. C **35** (2004) 325 [arXiv:hep-ph/0308087].

[182] K. J. Eskola, H. Honkanen, V. J. Kolhinen, J. w. Qiu and C. A. Salgado, "Nonlinear corrections to the DGLAP equations in view of the HERA data," Nucl. Phys. B **660** (2003) 211 [arXiv:hep-ph/0211239].

[183] S. Chekanov *et al.* [ZEUS Collaboration], "A ZEUS next-to-leading order QCD analysis of data on deep-inelastic scattering," Phys. Rev. D **67** (2003) 012007 [arXiv:hep-ex/0208023].

[184] S. Alekhin, "Parton distributions from deep-inelastic scattering data," Phys. Rev. D **68** (2003) 014002 [arXiv:hep-ph/0211096].

[185] J. Breitweg *et al.* [ZEUS Collaboration], "ZEUS results on the measurement and phenomenology of F_2 at low x and low Q^2," Eur. Phys. J. C **7** (1999) 609 [arXiv:hep-ex/9809005].

[186] C. Adloff *et al.* [H1 Collaboration], "Deep-inelastic inclusive ep scattering at low x and a determination of α_S," Eur. Phys. J. C **21** (2001) 33 [arXiv:hep-ex/0012053].

[187] C. Adloff *et al.* [H1 Collaboration], "Measurement of neutral and charged current cross sections in electron proton collisions at high Q^2," Eur. Phys. J. C **19** (2001) 269 [arXiv:hep-ex/0012052].

[188] C. Adloff *et al.* [H1 Collaboration], "Measurement of neutral and charged current cross-sections in positron proton collisions at large momentum transfer," Eur. Phys. J. C **13** (2000) 609 [arXiv:hep-ex/9908059].

[189] S. Chekanov *et al.* [ZEUS Collaboration], "Measurement of the Q^2 and energy dependence of diffractive interactions at HERA," Eur. Phys. J. C **25** (2002) 169 [arXiv:hep-ex/0203039].

[190] R. S. Thorne and R. G. Roberts, "A practical procedure for evolving heavy flavour structure functions," Phys. Lett. B **421** (1998) 303 [arXiv:hep-ph/9711223].

[191] A. Djouadi and S. Ferrag, "PDF uncertainties in Higgs production at hadron colliders," Phys. Lett. B **586** (2004) 345 [arXiv:hep-ph/0310209].

[192] M. Spira, "HIGLU: A program for the calculation of the total higgs production cross section at hadron colliders via gluon fusion including QCD corrections," arXiv:hep-ph/9510347, available from `http://people.web.psi.ch/spira/higlu/`.

[193] S. Frixione and B. R. Webber, "The MC@NLO 2.3 event generator," arXiv:hep-ph/0402116.

[194] M. Gluck, E. Reya and A. Vogt, "Dynamical parton distributions of the proton and small x physics," Z. Phys. C **67** (1995) 433.

[195] A. D. Martin, W. J. Stirling and R. G. Roberts, "Parton distributions of the proton," Phys. Rev. D **50** (1994) 6734 [arXiv:hep-ph/9406315].

[196] G. E. Smye, "Power corrections to flavour-singlet structure functions," Nucl. Phys. B **546** (1999) 315 [arXiv:hep-ph/9810292].

[197] G. E. Smye, "Power corrections in flavor-singlet deep inelastic scattering," Nucl. Phys. B **613** (2001) 260 [arXiv:hep-ph/0105015].

[198] D. M. Howe and C. J. Maxwell, "All-orders infrared freezing of observables in perturbative QCD," Phys. Rev. D **70** (2004) 014002 [arXiv:hep-ph/0303163].

[199] P. Hoyer and S. Peigné, "Dressing the quark with QCD condensates," arXiv:hep-ph/0304010.

[200] Y. L. Dokshitzer, G. Marchesini and B. R. Webber, "Dispersive approach to power-behaved contributions in QCD hard processes," Nucl. Phys. B **469** (1996) 93 [arXiv:hep-ph/9512336].

[201] K. Golec-Biernat and M. Wusthoff, "Saturation effects in deep-inelastic scattering at low Q^2 and its implications on diffraction," Phys. Rev. D **59** (1999) 014017 [arXiv:hep-ph/9807513].

[202] J. Bartels, K. Golec-Biernat and H. Kowalski, "A modification of the saturation model: DGLAP evolution," Phys. Rev. D **66** (2002) 014001 [arXiv:hep-ph/0203258].

[203] H. Kowalski and D. Teaney, "An impact parameter dipole saturation model," Phys. Rev. D **68** (2003) 114005 [arXiv:hep-ph/0304189].

[204] J. Alwall and G. Ingelman, "Interpretation of electron proton scattering at low Q^2," Phys. Lett. B **596** (2004) 77 [arXiv:hep-ph/0402248].

[205] T. Schafer and E. V. Shuryak, "Instantons in QCD," Rev. Mod. Phys. **70** (1998) 323 [arXiv:hep-ph/9610451].